KiwiSpec: The Design and Performance of a High Resolution Échelle Spectrograph for Astronomy

by

Steven R. Gibson

Department of Physics and Astronomy
University of Canterbury
Christchurch, New Zealand

A thesis submitted to the University of Canterbury
in partial fulfilment of the requirements for the degree of
Doctor of Philosophy

Abstract

This document describes the design, analysis, construction and testing of KiwiSpec, a fibre-fed, high resolution astronomical spectrograph of an asymmetric white pupil design. The instrument employs an R4, 31.6 groove mm^{-1} échelle grating for primary dispersion and a 725 lines mm^{-1} volume phase holographic (VPH) based grism for cross-dispersion. Two versions of the prototype were designed and constructed: an 'in-air' prototype, and a prototype featuring a vacuum chamber (to increase the stability of the instrument).

The KiwiSpec optical design is introduced, as well as a description of the theory behind a cross-dispersed échelle spectrograph. The results of tolerancing the optical design are reported for alignment, optical fabrication, and optical surface quality groups of parameters. The optical windows of an iodine cell are also toleranced.

The opto-mechanical mounts of both prototypes are described in detail, as is the design of the vacuum chamber system. Given the goal of 1 m/s radial velocity stability, analyses were undertaken to determine the allowable amount of movement of the vacuum windows, and to determine the allowable changes in temperature and pressure within and outside of the vacuum chamber.

The spectral efficiency of the instrument was estimated through a predictive model; this was calculated for the as-built instrument and also for an instrument with ideal, high-efficiency coatings. Measurements of the spectral efficiency of various components of the instrument are reported, as well as a description of the measurement system developed to test the efficiency of VPH gratings. On-sky efficiency measurements from use of KiwiSpec on the 1-m McLellan telescope at Mt John University Observatory are reported.

Two possible exposure meter locations are explored via an efficiency model, and also through the measurement of the zero-order reflectivity of the échelle grating.

Various stability aspects of the design are investigated. These include the stability of the optical mounts with temperature changes, and also the effect of the expansion and contraction of the supporting optical tables. As well, the stability of the in-air prototype was determined through measurement of the movement of thorium-argon emission lines within spectra as the temperature, atmospheric pressure and relative humidity (naturally) varied. Current and planned testing for determining the stability of the vacuum chamber prototype is discussed.

Contents

List of Figures

List of Tables

ACKNOWLEDGMENTS

I would like to take this opportunity to thank several people who have helped me to complete this work.

First of all, to my wife Annemarie for her continuous support, and for convincing me to undertake this project in the first place. Thank you to our two little children, Madeleine and Ross, for wonderfully distracting me from this work.

Thank you to both of our families for being so positive about this opportunity when it presented itself, which made the difficult decision to stay in New Zealand much easier. My parents, Don and Georgia Gibson, have always supported and encouraged me in my interests in telescope making and astronomy. Thank you to my in-laws, Mark and Jean Hoffmann, who made several trips to New Zealand to help us at home while I was busy writing this thesis.

Thank you to my advisor, John Hearnshaw, for his enthusiasm towards this project, for providing much advice, and for his excellent book "Astronomical Spectrographs and their History," from which I learned a great deal.

Thank you to the KiwiStar Optics team for many interesting and exciting discussions about optics and instrument design. In particular, to Dave Cochrane for always being willing to lend a helping hand or to answer any question; and to Deon Grobler for design advice, and for commiserating on the process of designing and building an astronomical spectrograph.

Thank you also to Stuart Barnes, from whom I learned a lot about spectrographs and their design and use.

Several other people and groups deserve mention: Kathryn Nield, (the original leader of the commercial side of the project); Damien Jones, for help with the tolerancing of optical systems; the mechanical workshop, who manufactured the components for both of the KiwiSpec prototypes; and the Photometry and Radiometry group of the Measurement Standards Laboratory of New Zealand for help with various spectrophotometric tests and questions.

This research has made use of NASA's Astrophysics Data System.

DISCLAIMER

The work presented within this thesis is that of the author, except where indicated within this section or within the main text of the thesis.

The core optical design of the KiwiSpec prototype (from the entrance slit to the detector) was developed by Dr. Stuart Barnes.

The detailed design of the vacuum chamber was a collaboration between Deon Grobler, Dave Cochrane (both of KiwiStar Optics), kanDO Innovation (Auckland, NZ), Dr. Stuart Barnes (Stuart Barnes Optical Design), and the author. kanDO Innovation was responsible for the computer-aided drafting (CAD) work. Both the author and kanDO Innovation performed the finite element analysis (FEA) simulations required during the design process.

The reduction and wavelength calibration of the on-sky spectra was performed by Dr. Stuart Barnes.

The design of the KiwiSpec control and monitoring software was developed by the author, although the actual LabView code was written by Dr. Shaun Hurd.

The radial velocity analysis of the on-sky spectra obtained with an iodine reference cell was performed by Dr. Mike Endl.

The work within this thesis is commercial-in-confidence and will be embargoed from public access by the University of Canterbury library for a period of two years.

Chapter 1

Introduction

> "To design an efficient stellar spectrograph is not an altogether simple matter..." Merrill (1931)

Eighty years later, this quote still holds true. While modern tools and computer analyses have made aspects of the design process easier, they have also greatly increased the complexity possible with astronomical instrumentation. Driving the process, just as in Merrill's day, is astronomy's demand for the most stable and technologically advanced instruments possible.

KiwiSpec is a high resolution, fibre-fed astronomical spectrograph. The author's task was to take the core optical design (developed by Stuart Barnes), and develop and test a working prototype of the spectrograph. This work included: the optical design of the input relay and the calibration light system; a tolerancing study of the entire spectrograph optical design; the complete opto-mechanical design of two versions of the prototype; the development of a vacuum chamber system; the modelling and measurement of instrument efficiency; the development of an exposure meter system; and the testing of the stability of the instrument.

The first KiwiSpec prototype was built 'in-air' (i.e. without any environmental stability) in order to quickly prove the concept of the instrument. After completion, this in-air prototype was then transported to Mt John University Observatory for two weeks of on-sky testing with the 1-m McLellan telescope. Following the successful on-sky testing period, work began on re-designing the instrument to include a vacuum chamber (the goal being increased stability for radial-velocity measurements). At the time of writing, the sub-components of the vacuum chamber prototype have been designed and manufactured, and the assembly of this second version of the KiwiSpec instrument is underway.

1.1 KiwiSpec Optical Design Overview

The optical layout of the KiwiSpec prototype is shown in Figure 1.1. Light from an optical fibre is collected and focused onto the entrance slit of the

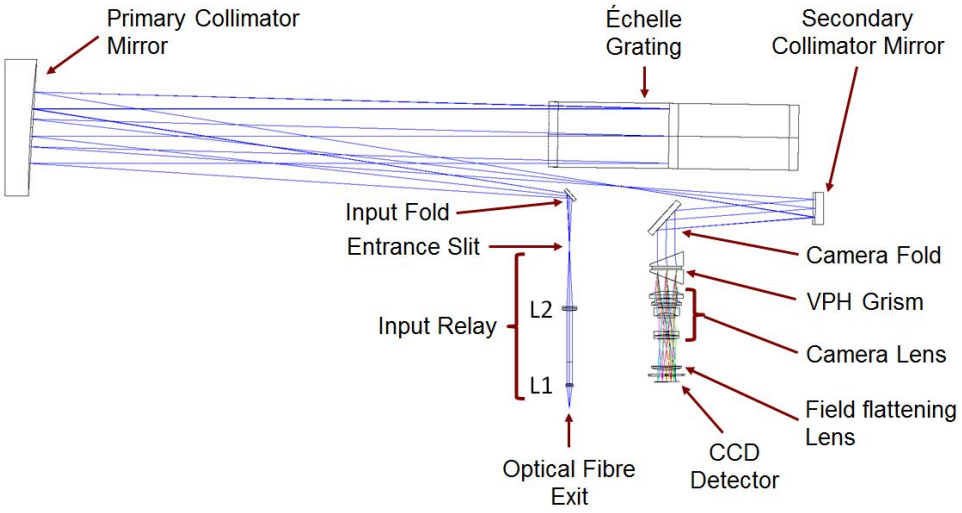

Figure 1.1: The optical layout of the KiwiSpec prototype, with key components labelled.

spectrograph by an input relay system, which takes the approximately f/4 diverging beam from the fibre exit and converts it to a converging f/10 beam. After passing through the entrance slit, the light diverges and reflects off the input fold mirror, a flat mirror employed to redirect the beam for mechanical convenience. The light then reflects from (and is collimated by) the primary collimator mirror, an off-axis paraboloid. This collimated beam is then incident on the primary disperser, an échelle grating. Post-diffraction from the échelle, the diverging monochromatic beams reflect from the primary collimator a second time. Because the échelle grating is rotated slightly about a vertical axis (the échelle 'γ' angle, to be described more in Section 2.2), the dispersed light does not return along the same path, which separates the pre- and post-diffraction beams. Therefore, after reflecting from the collimator the second time, the dispersed light forms an intermediate focus just to the side of the échelle, and does not return to the entrance slit. After the intermediate focus, the diverging monochromatic beams are collimated by the secondary collimator mirror. Because the focal length of this mirror is one-third that of the primary collimator, there is a 3:1 reduction in beam diameter following the secondary collimator.

After reflecting from the secondary collimator mirror, collimated beams reflect from the camera fold mirror, which is a flat mirror employed to steer the light path away from the input relay.

As KiwiSpec employs an échelle grating for primary dispersion, some form of cross-dispersion is required to separate the échelle orders. Within the KiwiSpec design, a volume phase holographic (VPH) grating is employed between a pair of symmetric prisms, forming what is known as a 'grism' (a term derived from a simplification of 'grating prism').

Immediately following the VPH grism is the camera lens. Somewhat unique for astronomical spectrographs, the KiwiSpec prototype camera is an of-the-shelf Hasselblad 150-mm focal length medium-format camera lens. This choice provided the obvious benefits of expediency and cost during the construction of the prototype spectrograph - while at the same time the Hasselblad lens afforded excellent performance to prove the capabilities of the KiwiSpec design. Just after the Hasselblad lens is an off-the-shelf meniscus field flattening lens to trim up the final image quality.

Finally the light falls on the detector, which is a backside-illuminated, midband-coated 2k $\times$ 2k CCD with 13.5-μm pixels.

The optical design of KiwiSpec follows the classical white pupil concept. This design approach was first introduced by Baranne (Baranne, 1965; Baranne and Duchesne, 1972) as a technique to avoid large beam footprints and diverging angles of incidence on the cross-disperser and camera. The benefits of such a design include smaller cross-dispersion and camera optical elements.

Within a white pupil design, following the secondary collimator the monochromatic collimated beams converge towards a common point on the the optical axis of the spectrograph, shown schematically in Figure 1.2. The term 'white pupil' thus refers to the recombining of the wavelength-dispersed beams. The white pupil also represents an image of the illumination on the échelle grating. Placing the cross-disperser at the white pupil allows for the smallest possible grating, prism, or grism to be used.

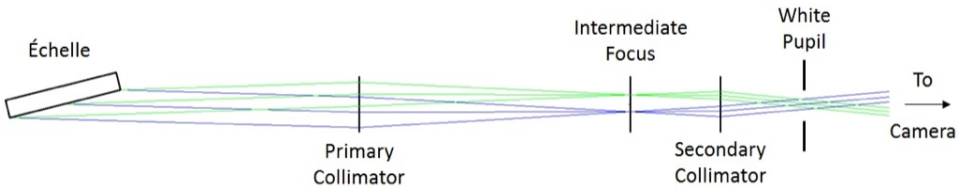

Figure 1.2: Paraxial schematic of the KiwiSpec design (following the échelle) with two wavelengths shown to illustrate the white pupil concept. For clarity, the primary and secondary collimator mirrors are shown here as paraxial lenses.

Within a symmetrical white pupil design, the focal lengths of the primary and secondary collimators are equal. In an asymmetric variation of the design, a smaller secondary collimator focal length leads to a demagnification of the collimated beam, as shown in Figure 1.3.

The relationship between the beam diameters and the focal lengths of the primary and secondary collimator mirrors within Figure 1.3 is given by:

$$B = A \cdot \frac{f_{\mathrm{s.coll}}}{f_{\mathrm{p.coll}}}. \tag{1.1}$$

An advantage of the asymmetric approach is that the reduced beam diameter following the secondary collimator mirror allows for smaller cross-

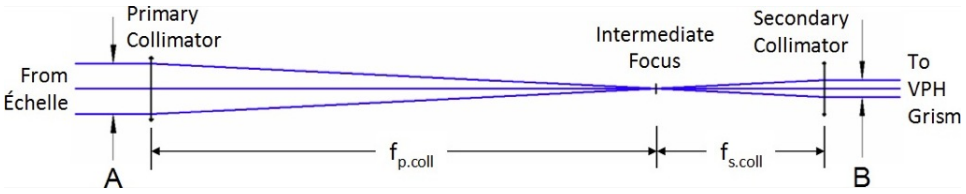

Figure 1.3: An unfolded paraxial schematic of the KiwiSpec optical design after the échelle grating, showing the asymmetry and beam reduction as described in the text. For clarity, the primary and secondary collimator mirrors are shown here as paraxial lenses.

disperser and camera optics. For example, the 3:1 reduction within the KiwiSpec design means the grism and camera optics are at least three times smaller than possible with a symmetrical design – meaning a significant saving in size, mass and cost. However, these benefits are offset by a larger angular divergence of the monochromatic beams, which has implications for the design form of the camera. Another factor influenced by the choice of asymmetry factor is the linear dispersion. Asymmetric design parameters will be discussed in more detail in Section 3.2.

The KiwiSpec prototype optical design is fundamentally composed of three relay systems, which are shown schematically in Figure 1.4. The magnification m of a relay system is set by the ratio of the focal lengths of the first and second optical elements (f_1 and f_2):

$$m = \frac{f_2}{f_1}, \tag{1.2}$$

with the magnification of several relays in series being:

$$m_{\text{total}} = m_1 \cdot m_2 \cdot m_3. \tag{1.3}$$

Therefore, for the KiwiSpec prototype, the magnification factor for the image of the fibre exit at the detector (in the absence of aberrations) is given by:

$$m_{\text{KiwiSpec}} = \frac{f_{\text{L2}}}{f_{\text{L1}}} \frac{f_{\text{p.coll}}}{f_{\text{p.coll}}} \frac{f_{\text{cam}}}{f_{\text{s.coll}}} = \frac{f_{\text{L2}}}{f_{\text{L1}}} \frac{f_{\text{cam}}}{f_{\text{s.coll}}}. \tag{1.4}$$

1.2 Adaptability

While the prototype is a single-channel instrument, the KiwiSpec design is quite versatile and allows for multiple channels to increase the wavelength coverage. A dual channel design for KiwiSpec is shown in Figure 1.5. As shown in the figure, each channel would contain a cross-disperser grism, a camera, and a detector - with each element being optimized for throughput and image quality over the channel's wavelength range.

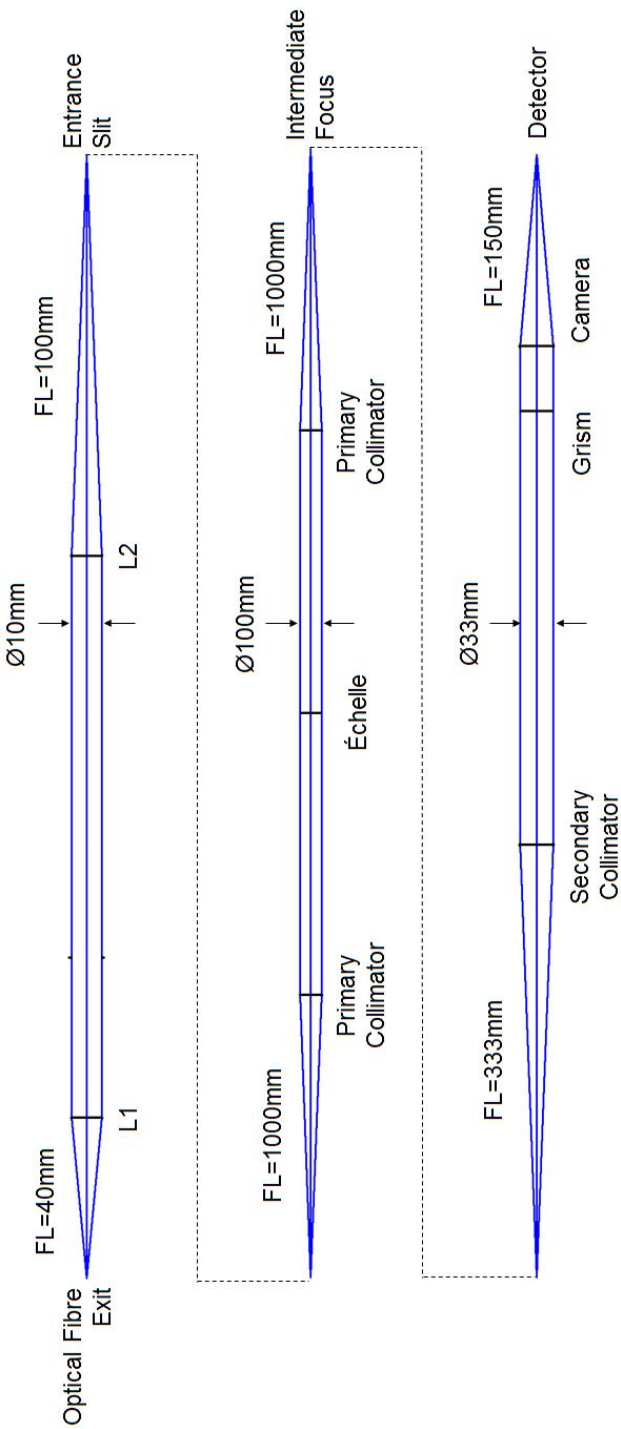

Figure 1.4: Paraxial representation of the three relays within the KiwiSpec instrument. Note that the three relays are not to scale with each other, as indicated by the collimated beam diameters.

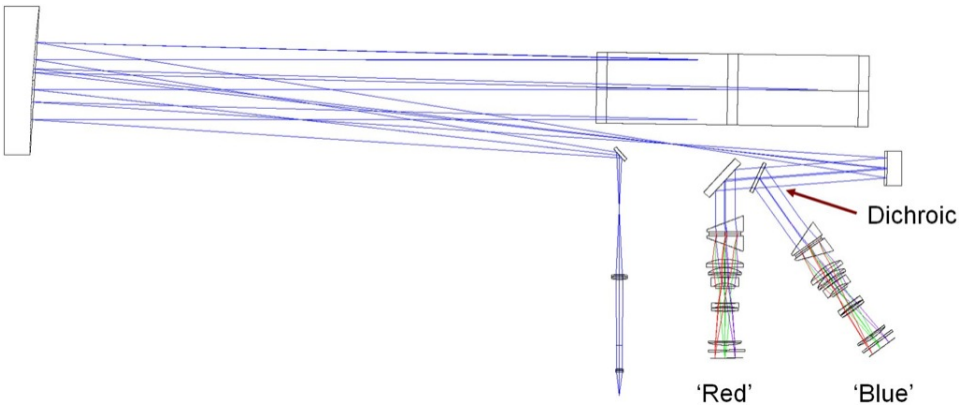

Figure 1.5: Optical layout of a dual channel KiwiSpec, in which a dichroic beam-splitter is used to reflect the blue wavelengths towards the first channel, and transmit the red wavelengths to the second channel.

1.3 Prototype Configuration

The various parameters chosen for the prototype configuration are listed in Table 1.1.

Table 1.1: The KiwiSpec prototype parameters.

Configuration:	single-channel instrument
	designed assuming 1-m telescope
	100-mm collimated beam diameter
Optical Fibre:	100-μm fibre, Polymicro FBP
Échelle:	R4, 31.6 grooves/mm
Cross-dispersion:	VPH grism (725 lines/mm)
Camera:	off-the-shelf camera (150 mm FL Hasselblad)
	off-the-shelf field flattening lens
Detector:	e2v CCD (2k $\times$ 2k, 13.5-μm pixels)
	backside-illuminated
	Spectral Instruments 850S detector body

The wavelength coverage of the KiwiSpec design is a function of cross-dispersion grating, camera, and CCD parameters. With the prototype parameters given in Table 1.1, it covers the wavelength range from 420 nm to 660 nm over 51 (échelle) diffraction orders.

The KiwiSpec prototype resolving power with a 100-μm fibre and no slit in place is $R \approx 40,000$, and the resolution element on the detector measures approximately 6 pixels wide. Theoretically, in the prototype configuration the KiwiSpec design could achieve $R \approx 100,000$ with three-pixel sampling. In practice, this could be accomplished through the use of an image slicer to re-arrange the circular fibre output into a near-rectangular shape, or by

employing a smaller fibre or an entrance slit (albeit at a loss of light throughput). It is also reasonable to assume that with a custom-designed camera or input relay the resolving power would increase (with no loss of throughput), owing to the optimized image quality of the purpose-built systems.

Two spectra obtained with the prototype instrument are shown in Figures 1.6 and 1.7: a thorium-argon calibration spectrum and a stellar spectrum of α CenA.

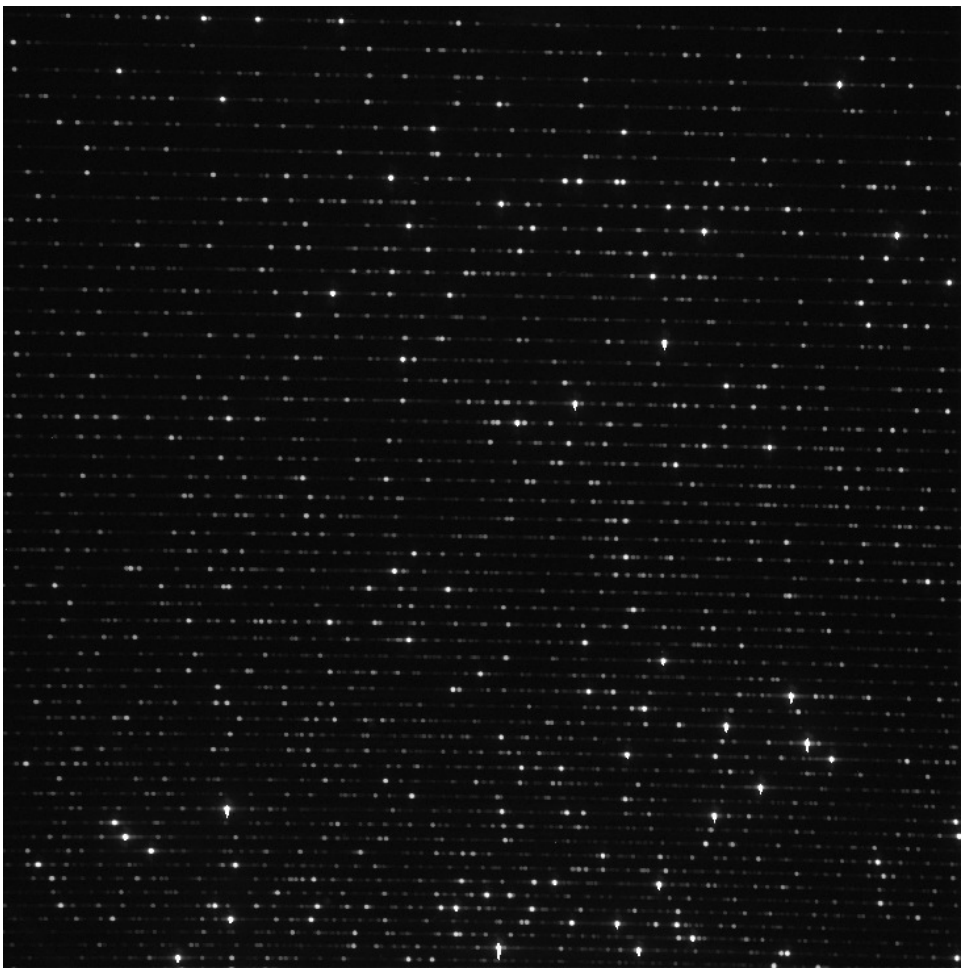

Figure 1.6: KiwiSpec spectrum of a thorium-argon calibration source lamp (exposure time = 30 seconds).

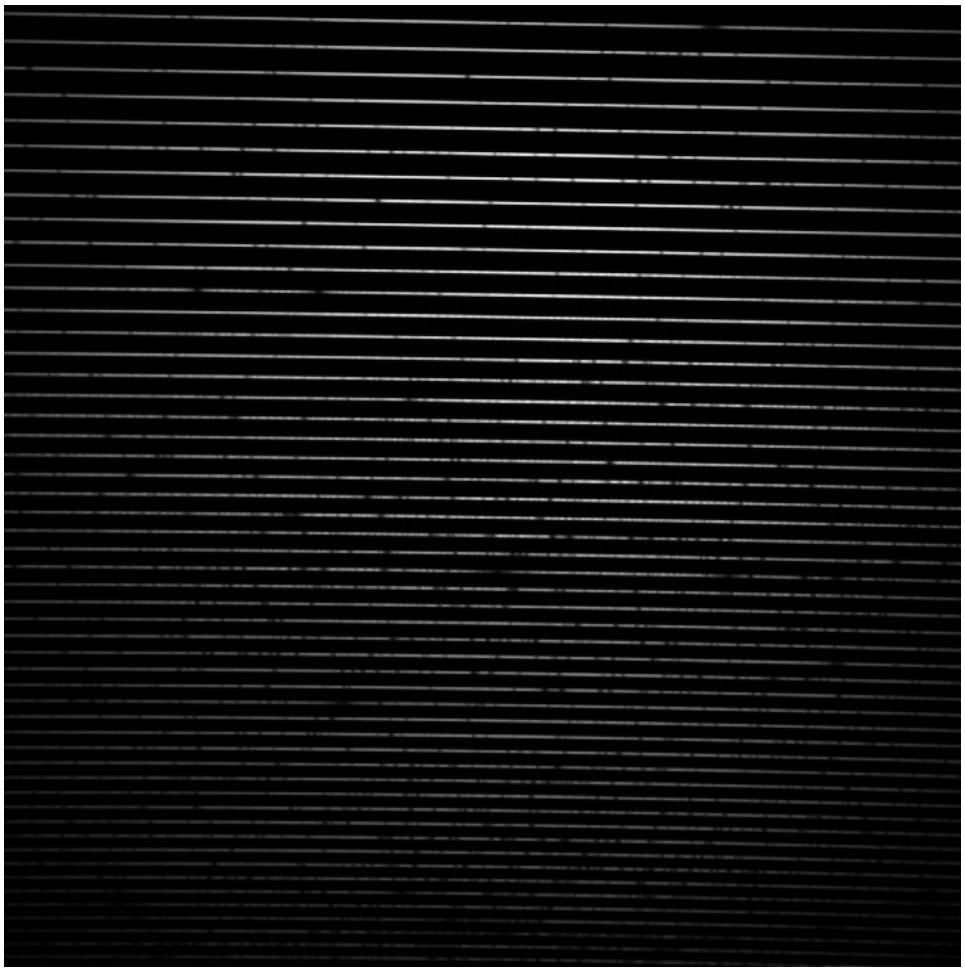

Figure 1.7: KiwiSpec spectrum of α CenA (exposure time = 30 seconds). The sodium D lines are located above and to the left of centre, and the Hα line is located at the top right (within the last order). An iodine reference cell was used during this observation.

1.4 Science Context

Astronomical spectrographs are the observational tool of choice within many areas of astrophysics. Such observations include: determining what the stars are made of (abundance or metallicity analyses); measuring the radial velocities of galaxies (redshift surveys); detecting unseen stellar companions (spectroscopic binaries); observing stellar pulsations to infer the internal construction of stars (astroseismology); measuring the movement of stars through space (radial velocities); detecting the presence of planets around other stars (precision radial velocities).

KiwiSpec was designed to be a versatile instrument that can be configured for the above fields of research (with the possible exception of redshift surveys of galaxies, for which multi-object spectrographs are typically employed). Given that precision radial velocity work imposes the strongest demands and requirements on a spectrograph (especially with respect to stability), that field became the primary science case for the KiwiSpec prototype during the development of the instrument.

1.5 Historical Context

The KiwiSpec design builds on over one hundred years of astronomical spectrograph development. This section will describe the historical context of a high resolution, high stability, échelle grating-based astronomical spectrograph.

1.5.1 Diffraction gratings

Early spectrographs were built around prisms as the main dispersing element. To obtain higher resolution, some spectrographs contained multiple prisms in order to increase the amount of dispersion (such as the three-prism Cassegrain spectrograph on the 60-inch telescope at Mt Wilson (Adams, 1912)). However, each additional prism led to a loss of throughput due to absorbed or scattered light (especially at blue and UV wavelengths), or reflected light from the uncoated prism entrance and exit faces. A further problem with prismatic dispersion is the changing angular dispersion, which is less for red wavelengths than for blue wavelengths. One method to counteract the decreased red angular dispersion was to increase the linear dispersion at the photographic plate through the use of a long focal length camera. This technique led to very large spectrographs, which utilized large photographic plates as detectors.

Despite the shortcomings of prisms, astronomers were slow to adopt diffraction gratings as an alternative dispersing element. The primary reason was that early diffraction gratings were not blazed and therefore suffered from very low efficiencies. Early gratings also generated aberrations and

ghosts due to the very difficult task of ruling straight, equally spaced grooves with the technology of the time (Loewen and Popov, 1997).

Several factors led to the rise of diffraction gratings as the prominent dispersing element within astronomical spectrographs. Rowland, in an 1882 article, described a major improvement to his ruling engine realized by removing the error from the lead screw, which greatly diminished the periodic errors that resulted in ghosts (Rowland, 1882). A further advance came with the development of blazed gratings by Wood in 1910 (Hearnshaw, 2009), meaning that the direction and intensity of the diffracted light could be controlled through asymmetric grooves. Blazed gratings led to much higher efficiencies than had been attained previously, with the benefit that the majority of the diffracted light could now be largely contained within a desired direction or diffraction order.

The development of evaporated coatings under vacuum by Strong in the 1930s (Strong, 1934) allowed for gratings to be ruled in very thin layers of aluminium deposited on low-expansion glass substrates such as pyrex. According to Loewen and Popov (1997), aluminium is the ideal material for grating ruling, as it is soft enough to deform plastically and can be deposited in thick, uniform layers on (and adheres strongly to) the glass substrate. Another advance occurred in 1945, when Harrison, (following a concept devised earlier by Michelson (Loewen and Popov, 1997)), introduced interferometric methods to monitor a ruling engine while generating a grating. This feedback system effectively removed the lead screw as the critical mechanical component of the ruling process, and led to a great increase in accuracy.

However, gratings remained expensive and in high demand, largely due to the time and care required to rule a new grating. By the 1950's, however, a replica process had been developed which made gratings less expensive and more widely available (Palmer and Loewen, 2005). This process involves making a cast of a mechanically ruled grating in a resin applied to a glass substrate, after which the resin is cured and coated with aluminium. In the case of échelle gratings, a further benefit is that a first-generation replica has a higher efficiency than the master grating. This is because the mechanical ruling process produces grooves with sharp troughs and smooth peaks, but the replica groove profile, (being the inverse of the master grating profile), exhibits sharp peaks and smooth troughs.

1.5.2 Grating-based Spectrographs

One of the earliest successful grating-based astronomical spectrographs was a Cassegrain instrument at Mount Wilson, described by Merrill (1931). As reported in that article, observers were very pleased with the new blazed grating-based instrument, which overcame the decreased red dispersion problem of prisms and also allowed for shorter exposures. The increased red dispersion of the grating removed the need for a long focal length camera,

resulted in a more compact and more stable instrument, and allowed Merrill and others to undertake new survey work at near-infrared wavelengths (Hearnshaw, 2009).

Other early uses of diffraction gratings in astronomical spectroscopy involved retrofitting plane gratings into existing prism spectrographs. This was the case for the 100-inch coudé spectrograph at Mt Wilson, where a blazed plane grating was employed in 1935 with a "great concentration of light in the red of the first order and the ultraviolet of the second" (Adams, 1941). The term 'coudé', (from the French for 'elbow'), represents a spectrograph design for which the light path from the telescope to the instrument is 'bent' by several fold mirrors, so as to reach a stable and mechanically immobile slit and spectrograph. Notably, during the prism-to-grating conversion of the 100-inch telescope coudé spectrograph, several of the then-new Schmidt cameras were developed for the instrument. These cameras provided a marked improvement in image quality and wavelength coverage over what could be achieved with traditional spectrograph cameras at the time.

Many spectrographs contained a suite of several different cameras within the instrument, allowing the observer to choose a camera giving the proper dispersion and wavelength range for the observing project at hand. This could be accomplished with either interchangeable cameras (Merrill, 1931), or by rotating the grating to send the diffracted light to different cameras fixed on the same support structure (Adams, 1941). The Hale telescope coudé, for example, allowed the observer to choose between five different cameras (Bowen, 1952).

Starting with the Mt Wilson 60-inch coudé, for several decades the coudé spectrograph was the adopted solution for obtaining high resolution and instrument stability. Typically, coudé spectrographs sat within a basement room under the observatory dome to increase the thermal and mechanical stability of the instrument. For example, the Hale telescope coudé was described as being located in a "constant-temperature room directly south of the telescope" (Anderson, 1948), and the Mt Wilson 100-inch coudé was "completely inclosed [*sic*] in an insulated wooden house, and the temperature is controlled by a series of heating coils" (Adams, 1941).

However, while mechanical stability and dispersion of the spectrograph were increased, efficiency suffered owing to the extra mirror reflections required to get the light from the telescope to the spectrograph. In the case of the Hale telescope coudé, up to four extra mirrors could be required, depending on the altitude of the object under observation (Anderson, 1948; Bowen, 1952).

Nonetheless, at that time period the coudé spectrograph design gave the highest dispersion possible, and the 100-inch coudé instrument "... became the standard instrument against which all other high resolving power spectrographs were judged for the next four decades." (Hearnshaw, 2009).

Coudé instruments, despite their success, were very large and expensive instruments, with long focal length cameras and large plane diffraction gratings. Conversely, the advent of the échelle grating led to instruments with high dispersion in a small package at a reasonable cost. For these reasons, the échelle grating would eventually replace the plane grating as the primary disperser in high resolution astronomical spectrographs.

1.5.3 Échelle gratings

An échelle grating is a diffraction grating with a coarse groove spacing, operating at high angles of incidence and diffraction, and as such, at high order numbers. Prior to the introduction of the échelle grating, the approach for attaining high dispersion involved large spectrographs employing gratings with high line densities. For example, the coudé spectrograph of the 100-inch Hooker telescope at Mt Wilson (Adams, 1941) employed a grating with a line spacing of 14,000 grooves per inch (551.2 grooves per mm), and the coudé spectrograph of the 200-inch Hale telescope at Mt Palomar (Bowen, 1952) used a grating with 10,000 grooves per inch (393.7 grooves per mm).

With respect to these instruments, Harrison (1949) mentioned that:

> The difficulty of producing such gratings, arising largely from the requirement of ruling such large numbers of equally spaced grooves, combined with the magnitude of the task of operating so large a spectrograph, makes consideration of alternative methods desirable.

Within the same paper, Harrison went further and introduced the theory behind the échelle grating, and also suggested its name (after the French term for "a ladder, scale, or pair of steps"). Harrison's realization with respect to angular dispersion that led to the concept of an échelle grating is described in more detail in Section 2.5.1.

The échelle grating offers many advantages over other primary disperser choices for spectrographs. Operating in high orders means that in any one direction there are many orders overlapping one another (a 'cross disperser' is typically employed to separate the overlapping orders, as will be discussed in Section 2.15). This has the advantage that the grating blaze angle, (which is designed to direct light into a given direction), efficiently directs the light into many different orders, giving a high efficiency across a large wavelength range. This is in contrast to a traditional grating, which was typically blazed for one or two orders. For example, the Mt Palomar coudé spectrograph grating was blazed for the third order in the violet and the second order for red wavelengths (Bowen, 1952).

Furthermore, échelle grating based spectrographs offer very high dispersion in a compact package, as the high angular dispersion of the grating

removes the need for long focal length cameras. For example, (and although admittedly not a direct comparison), the KiwiSpec prototype camera has a focal length of 150 mm, whereas the focal length of the highest-dispersion camera on the Hale Telescope coudé spectrograph had a focal length of 3,658 mm (144 inches) (Bowen, 1952).

Although Harrison introduced the échelle grating in 1949, stellar spectroscopists were slow to embrace the new type of grating within their instruments. Harrison et al. (1952) reports building a laboratory-based échelle spectrograph, but not for astronomical research. Solar spectroscopists were quick to adopt the new échelle grating, however, with Pierce, McMath and Mohler reporting use of an échelle-based solar spectrograph as early as 1951 (Pierce et al., 1951).

Some of the first échelle-based stellar spectrographs were adaptations of existing coudé instruments, modified for use with an échelle grating. A series of these were commissioned in the Ukraine, Japan, United States and Australia from the mid-1960s to early 1970s (Hearnshaw, 2009).

Échelle gratings allowed for a series of smaller spectrographs to be developed from the late 1960s through the 1980s that were once again placed at the focal plane of the telescope. Although the mechanical and temperature stability problems encountered during the days of prism spectrographs were still present, they were somewhat mitigated by the predominant telescope form having changed from long refractors to shorter, more rigid Cassegrain-type reflectors. The Cassegrain format allows for a strong mounting arrangement, with the spectrograph attached to the mechanically robust mirror cell. The échelle grating therefore allowed high resolution stellar spectroscopy - previously the sole domain of large coudé instruments - to be achievable on metre-class telescopes. One further benefit of a Cassegrain-based instrument is the increased efficiency at blue and UV wavelengths, which was greatly diminished in coudé instruments owing to the extra fold-mirror reflections required to get the light from the telescope to the spectrograph.

Finally, the development of the CCD detector from the mid-1970s to the present has also heavily favoured échelle-based instruments. The spectral format of an échelle spectrograph is perfectly matched to this small yet highly efficient device, meaning a large amount of spectral information can be recorded in a single exposure.

1.5.4 Stability

A major scientific driver behind spectrograph development in the last three decades has been precision radial-velocity work, and specifically exoplanet detection. Such research, which is based on detecting very small (as small as 1 m/s) variations in stellar radial velocities through Doppler-based measurements, has put a tremendous emphasis on instrument stability.

Measurements at this level of precision require that not only instrumental stability be addressed, but also various aspects of stellar atmospheres. Fundamentally this is because the light that has reached the spectrograph has travelled through and emanated from the atmosphere of the star. Therefore, movements (or changes in brightness) within the stellar atmosphere itself can skew the measurement of the radial velocity of the centre of mass of the star. Such effects include (from Dumusque et al., 2012): granulation (convection can impart positive or negative radial velocity signatures); rotational activity (variations of intensity across the stellar surface can create a radial velocity signal at the rotational period of the star); and the magnetic activity cycle (which influences the number of spots on the stellar surface, as well as the intensity of convection). Furthermore, the positional coordinates of the observed star must be known precisely, in order to obtain a correct barycentric correction factor (to account for the motion of the Earth during an observation).

With respect to the stability of the spectrograph itself, three methods are described here that enable an increase in instrument stability or measurement precision. The first two involve increasing the absolute stability of the instrument: the use of an optical fibre to link the telescope and spectrograph; and placing the instrument within a vacuum chamber. A third technique, based on imprinting a reference spectrum onto the stellar spectrum, does not rely on absolute instrument stability, but instead monitors the instrument instability during an observation and then removes it from the data afterwards.

1.5.4.1 Optical Fibres

The use of optical fibres in astronomy was introduced by Angel et al. (1977). The techniques behind fibre-fed spectrographs were initially developed by Ramsey and others in the late 1970s and early 1980s (i.e. Ramsey et al. (1985), Ramsey and Huenemoerder (1986)), and the success of the concept has meant development continues to this day. With respect to stability concerns, the benefits of mechanically decoupling the telescope and spectrograph are two-fold. First, the instrument can be removed from the telescope and placed within a thermally-isolated and vibration-free environment. Therefore, the instrument, being removed from the back end of the telescope, does not have to endure the changing temperatures of the night-time air or the induced flexure from a changing gravity vector as the telescope moves around the sky. Secondly, in a traditional spectrograph, if the star image wanders across the slit owing to seeing or imperfect guiding, the instrumental profile can change and introduce Doppler measurement errors (Butler et al., 1996). One benefit of optical fibres is that they are efficient 'scramblers', meaning that variations in the light intensity at the input end are not perfectly preserved at the output end (Queloz et al., 1999).

However, this scrambling effect is more pronounced in the azimuthal direction than the radial direction, so that if the star image centroid is located off-centre on the fibre entrance, the fibre output intensity tends to be ring-shaped (Queloz et al., 1999). A recent development to overcome this issue is the use of octagonal-section fibres, which provide a more uniform scrambling effect. For example, Perruchot et al. (2011) have demonstrated octagonal fibres to be six times less sensitive than circular fibres to seeing, guiding, and centering errors at the telescope focal plane.

1.5.4.2 Vacuum Chamber

Another solution employed to stabilize a spectrograph is to place it within a vacuum chamber. As will be shown in Section 6.1.1, temperature and atmospheric pressure changes lead to changes in the refractive index of air, which can have a very large effect on the radial-velocity stability of a spectrograph. By placing the instrument within a vacuum chamber, the spectrograph is decoupled from its environment and will experience a constant (vacuum) pressure and also be less sensitive to air temperature changes, resulting in an increase in instrument stability.

In the early 1950s, McMath (a solar spectroscopist) realized that a vacuum-based spectrograph would have many advantages: it would be free of resolution-degrading air currents; it would have high stability to ensure repeatability between measurements; it would be isolated from changing atmospheric pressure; and it would reduce reactions to temperature changes (McMath, 1956). Of note is the scale of the instrument he developed, which was contained within a vacuum tank 4 feet (1.2 m) in diameter and 52 feet (15.8 m) long.

Despite the success of solar spectrographs within vacuum chambers, stellar spectroscopists were slow to follow the lead of their solar spectroscopy colleagues with vacuum chamber-based instruments. However, several spectrographs currently in use or in development employ vacuum chambers, including HERCULES (Hearnshaw et al., 2002), HARPS (Mayor et al., 2003), HARPS-N (Cosentino et al., 2012) and SALT-HRS (Bramall et al., 2012).

1.5.4.3 Reference Spectrum

A third solution exists for increasing the Doppler precision of a spectrograph: the reference cell technique. This approach does not require the spectrograph to be absolutely stable, but instead uses an absorption spectrum, imprinted on the stellar spectrum, to act as a reference to monitor instrumental instability. As employed today, the reference spectrum is typically iodine (I_2) vapour, contained within a transparent glass tube or cell that is placed in the beam before the light enters the spectrograph. During an observation, instrument instabilities will cause both the stellar spectrum

and the iodine spectrum to shift. During the complicated reduction process (Marcy and Butler, 1992), careful monitoring of the shift of the iodine lines means that the instrument-induced movement can be determined. Removing the instrument-induced shift from the stellar spectrum then leaves the radial velocity movement of the star alone.

The absorption cell technique was pioneered by Campbell and Walker (Campbell and Walker, 1979), who introduced the concept and also conducted a landmark radial velocity survey of 21 stars (Campbell et al., 1988). Those authors chose hydrogen fluoride (HF) due to its strong and widely-separated absorption lines (which helped when separating the HF spectrum from the stellar spectrum). Campbell and Walker (1979) demonstrated a marked improvement in radial velocity stability with this technique, achieving 15 m/s precision in an era when 500 m/s was a common radial velocity precision measurement. However, despite its success as a reference material, major practical disadvantages of HF include: the vapour is highly corrosive (it reacts with glass); it can form hydrofluoric acid on combination with water; and it is toxic to humans (Wright and Gaudi, 2013).

Butler et al. (1996) would refine this technique, through the use of an iodine cell and sophisticated data reduction techniques. Those authors chose iodine over hydrogen fluoride due to the greater number of absorption features located over a broader spectral range.

As will be seen in the following chapters, the KiwiSpec prototype employs all three of these stability techniques.

Chapter 2

Échelle Spectrograph Theory

2.1 Introduction

Within this chapter the theory behind the design and operation of échelle spectrographs is discussed. The material presented has been influenced by the work of Loewen and Popov (1997), Schroeder (2000), Palmer and Loewen (2005) and Hearnshaw (2009).

2.2 Diffraction and the Grating Equation

A diffraction grating consists of a repeating pattern of parallel, equally spaced grooves. In use, each groove acts as a single slit and generates a characteristic sinc^2 diffraction pattern. The diffracted light from all of the grooves in the grating then interfere and cause dispersion of the light by wavelength. Note that diffraction gratings may be reflective or transmissive in nature.

Figure 2.1 shows light within a collimated beam incident on a diffraction grating. The two rays strike the centres of two adjacent grooves on the grating, and travel through different path lengths as shown in the diagram. Light in the two rays will interfere constructively when the path length difference between them is equal to an integral number of wavelengths of the incident light.

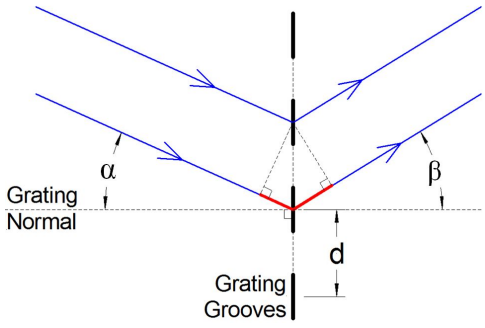

Figure 2.1: Schematic diagram of a transmission diffraction grating showing the path difference (in red) between rays of a common wavefront falling on adjacent grooves. In the case of a reflection grating, both the incident and diffracted beams would lie on the same side of the grating surface.

The relationship between wavelength and angle is known as the grating equation:

$$m\lambda = d(\sin\alpha \pm \sin\beta), \tag{2.1}$$

where:

m	=	diffraction order (0, ± 1, ± 2, ...)	[integer];
λ	=	wavelength	[nm];
d	=	width of grooves	[nm];
α	=	angle of incidence (in plane)	[degrees];
β	=	angle of diffraction (in plane)	[degrees].

Within this equation, the $(\sin\alpha + \sin\beta)$ scenario applies to reflection gratings, whereas the $(\sin\alpha - \sin\beta)$ scenario applies to transmission gratings. Note that when $\alpha = -\beta$ for a reflection grating, traditional reflection occurs, and when $\alpha = \beta$ for a transmission grating, transmission without diffraction occurs. Both of these special cases are known as 'zero order' diffraction.

Although the grating equation contains a parameter for the groove spacing, it gives no constraint on the *shape* of the grooves. A 'blazed' grating is one for which the groove profile has been designed to direct the majority of the diffracted light in a specific direction. In low-order gratings, this has the effect of increasing the efficiency of a given diffraction order. In high-order gratings, such as échelles, it is employed to direct the diffracted intensity back towards the direction of the incident light. Therefore, owing to the effect of overlapping diffraction orders with an échelle grating, the high efficiency of the blaze direction is distributed among many orders.

As such, the blaze angle, θ_B, is an important grating parameter as it indicates the direction of maximum diffracted efficiency. The schematic in Figure 2.2 shows the fundamental grating equation parameters and the blaze angle for an échelle grating. The échelle grating will be introduced in more detail in the Section 2.3.

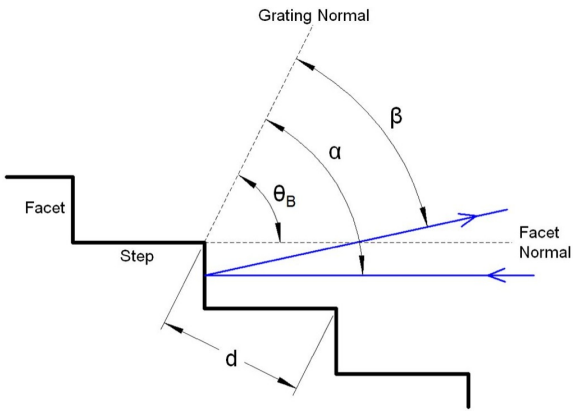

Figure 2.2: Fundamental échelle grating parameters and angles. Diffraction occurs at the grating facets, and the blaze angle, θ_B, gives the angle of the facet normal with respect to the grating normal.

Equation 2.1 assumes that the diffraction occurs within a plane oriented perpendicular to the grating grooves. However, in practice, gratings can be employed slightly 'out of plane', in which the incident and diffracted ray paths do not intersect, but are separated by an angle γ (see Figure 2.3).

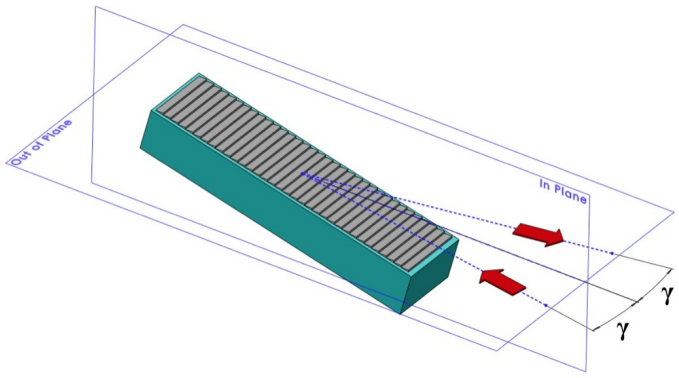

Figure 2.3: The out-of-plane angle, γ. The vertical plane in this diagram represents 'in plane' diffraction, which occurs in a plane perpendicular to the grating grooves. The gamma angle measures how far 'out of plane' the diffraction occurs.

Considering the out of plane situation, a more complete version of the grating equation is given by:

$$m\lambda G = (\sin\alpha + \sin\beta)\cos\gamma, \tag{2.2}$$

where:

G	=	grooves per nm ($= \frac{1}{d}$)	[nm^{-1}];
γ	=	angle of incidence (out of plane)	[degrees].

A useful rearrangement of the grating equation, for determining the angle of diffraction for a given wavelength and order, is given by:

$$\beta(\lambda) = \sin^{-1}\left[\frac{m\lambda G}{\cos\gamma} - \sin\alpha\right]. \tag{2.3}$$

2.3 Échelle Gratings

As introduced in Chapter 1, an échelle grating is a diffraction grating with a coarse groove spacing, operating at high angles of incidence and diffraction, and as such, at high order numbers.

Échelles are typically described by two parameters: G and the 'R-number'. The parameter G, the number of lines per mm, has been introduced above. Of historical interest is how the set of groove spacings for échelle gratings originated (i.e. 31.6 grooves/mm, 79 grooves/mm), as reported by Loewen and Popov (1997):

> "These odd frequencies derive from the ruling history at MIT, where at one time it was considered safer to make the spacing integral multiples of the He-Ne laser wavelength used to control the [ruling] engine."

The second échelle parameter, the R-number, is defined as the tangent of the blaze angle:

$$R = \tan \theta_{\mathrm{B}}. \tag{2.4}$$

This value, as will be shown in Section 2.5.1, is a convenient descriptor as it provides a direct comparison between the dispersive powers of different gratings.

2.4 Quasi-Littrow Configuration

The 'Littrow configuration' refers to a spectrograph design concept in which the diffracted light from the grating travels back in the same direction as the incident light. The name is derived from the Littrow spectroscope in which light travelled through a prism, was reflected within the prism by a silvered face, and then retraced its path back through the prism and the collimator optics (Hearnshaw, 2009).

In the Littrow mode the angle of incidence α equals the angle of diffraction β. In the so-called 'quasi-Littrow' configuration, $\alpha \simeq \beta$, but the grating is offset from the true Littrow condition by a small angle, θ (as shown in Figure 2.4).

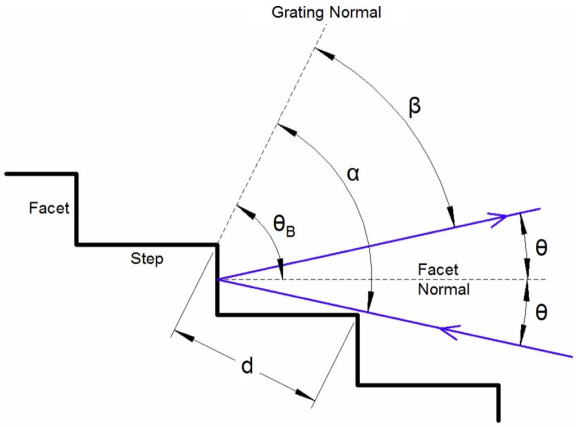

Figure 2.4: Échelle grating parameters and angles for the quasi-Littrow configuration.

The relations between α, β and θ for the quasi-Littrow configuration (at the centre of a diffraction order, and with respect to the grating blaze angle θ_{B}), are:

$$\alpha = \theta_{\mathrm{B}} + \theta; \tag{2.5}$$

$$\beta = \theta_{\mathrm{B}} - \theta. \tag{2.6}$$

Substituting these equations into the grating equation (Equation 2.2) leads to the quasi-Littrow version of that equation:

$$m\lambda G = 2 \sin\theta_{\mathrm{B}} \cos\theta \cos\gamma. \tag{2.7}$$

The blaze wavelength is important as it lies at the centre of a diffraction order, and is also the position of peak diffracted efficiency within the order. A slight rearrangement then provides a useful equation for calculating the blaze wavelength of a given diffraction order:

$$\lambda_{\mathrm{blaze}} = \frac{2 \sin\theta_{\mathrm{B}} \cos\theta \cos\gamma}{Gm}. \tag{2.8}$$

This equation can be further simplified, as many échelle spectrographs are designed with small θ and γ angles:

$$\lambda_{\mathrm{blaze}} \simeq \frac{2 \sin\theta_{\mathrm{B}}}{Gm}. \tag{2.9}$$

Small, positive, θ values are typically chosen as they offer the highest efficiency, as will be described in Section 2.16.

The value of θ also plays a role in the required length, L, of a grating, as shown by the geometry in Figure 2.5 and by the equation:

$$A_{\mathrm{coll}} = L \cos\alpha = L \cos(\theta_{\mathrm{B}} + \theta). \tag{2.10}$$

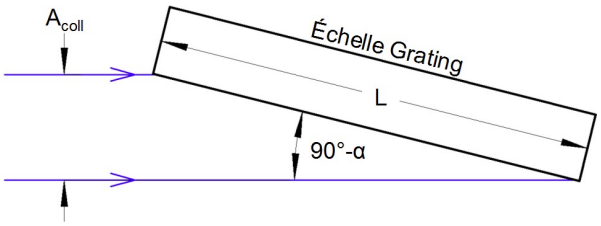

Figure 2.5: The relationship between the collimated beam diameter and grating length.

Table 2.1, which was determined using Equation 2.10, indicates that as θ increases, so does the required length of the grating. This is especially true of R4 gratings, for which the required length becomes impractically long with a θ value of only a few degrees.

However, in practice L is not a free design parameter, as one is usually constrained to choose the grating aspect ratios available from the manufacturer.

Table 2.1: Length-to-width ratios for several échelle gratings and various θ values.

	$\boldsymbol{\theta}$			
R-value	0°	0.1°	3°	5°
2	2.24	2.24	2.50	2.72
3	3.16	3.18	3.76	4.30
4	4.12	4.15	5.22	6.37

2.5 Dispersion

Two types of dispersion are considered: angular dispersion, which depends upon the grating parameters only, and linear dispersion, which also considers the focal length of the spectrograph camera.

2.5.1 Angular Dispersion

The angular dispersion, or the change of diffraction angle with wavelength, is given by $\frac{d\beta}{d\lambda}$, and is calculated by differentiating the grating equation with constant α.

Exploring two versions of this result is instructive. First:

$$\frac{d\beta}{d\lambda} = \frac{mG}{\cos\beta\cos\gamma}. \tag{2.11}$$

This equation shows that *for a given angle of diffraction*, increasing either the order number or the number of grooves per mm will increase the angular dispersion.

Secondly, substituting in the grating equation (Equation 2.2, solved for mG), gives:

$$\frac{d\beta}{d\lambda} = \frac{\sin\alpha + \sin\beta}{\lambda\cos\beta}. \tag{2.12}$$

This equation shows that *for a given wavelength* the dispersion of a grating depends only on the angles of incidence and diffraction. This finding was reported by Harrison (1949) in the paper in which he introduced the échelle grating. However, given that the equality of Equations 2.11 and 2.12 must be maintained for the given wavelength and angles of incidence and diffraction, m and G are not both free parameters. Because the ratio mG must remain constant, as G is decreased the order number, m, for the given wavelength must increase.

Other re-arrangements of the equation are useful as well. For the simplified case of the the quasi-Littrow configuration, α and β are replaced by

Equations 2.5 and 2.6, and after simplification Equation 2.12 becomes:

$$\frac{d\beta}{d\lambda} = \frac{2\tan\theta_{\mathrm{B}}}{\lambda(1-\tan\theta_{\mathrm{B}}\tan\theta)}. \tag{2.13}$$

Finally, considering the quasi-Littrow configuration ($\alpha \simeq \beta \simeq \theta_{\mathrm{B}}$), Equation 2.12 simplifies to:

$$\frac{d\beta}{d\lambda} \simeq \frac{2\tan\theta_{\mathrm{B}}}{\lambda_{\mathrm{blaze}}}. \tag{2.14}$$

Given that $R = \tan\theta_{\mathrm{B}}$, this equation shows that échelle R-numbers provide a convenient comparison value between gratings, as for a given wavelength a change in R-number means a change in angular dispersion (i.e. an R4 grating provides twice the angular dispersion of an R2 grating).

2.5.2 Linear Dispersion

An important parameter of a spectrograph is the linear size of the spectrum produced by the instrument. One measure of this, the linear dispersion at the detector, is the product of the angular dispersion of the grating and the focal length of the spectrograph camera lens:

$$\frac{dx}{d\lambda} = f_{\mathrm{trad.cam}} \cdot \frac{d\beta}{d\lambda}, \tag{2.15}$$

where:

x	=	linear distance on detector	[mm];
$f_{\mathrm{trad.cam}}$	=	focal length of camera within a traditional spectrograph design	[mm].

This equation is valid for collimated light falling on the grating, which is the usual situation in astronomical spectrographs. It gives the linear dispersion of a 'traditional' spectrograph, or one in which the camera system follows the grating with no change in beam (de)magnification between them.

A more practical version of Equation 2.15 is its reciprocal. This is known as the reciprocal linear dispersion, or plate scale, P:

$$P = \left(f_{\mathrm{trad.cam}} \cdot \frac{d\beta}{d\lambda} \right)^{-1}, \tag{2.16}$$

which has units of wavelength per detector dimension (i.e. nm/mm or nm/pixel).

Substituting in the angular dispersion for the general case (Equation 2.11), this becomes:

$$P = \frac{\cos\beta}{mGf_{\mathrm{trad.cam}}}. \tag{2.17}$$

This equation shows that the plate scale is not constant across a given order, but rather varies as $\cos\beta$. To investigate this further, the plate scale of an actual KiwiSpec spectrum is shown in Figure 2.6. The figure shows the change in plate scale (nm/pixel) across three échelle orders (located at the boundaries and centre of the spectral format).

The figure confirms the $\frac{1}{m}$ dependence of plate scale on order number, as the red orders (with lower order numbers) display higher overall plate scales. As well, the plate scale at the blue end of an order is higher, owing to the smaller β value (and therefore higher $\cos\beta$ value).

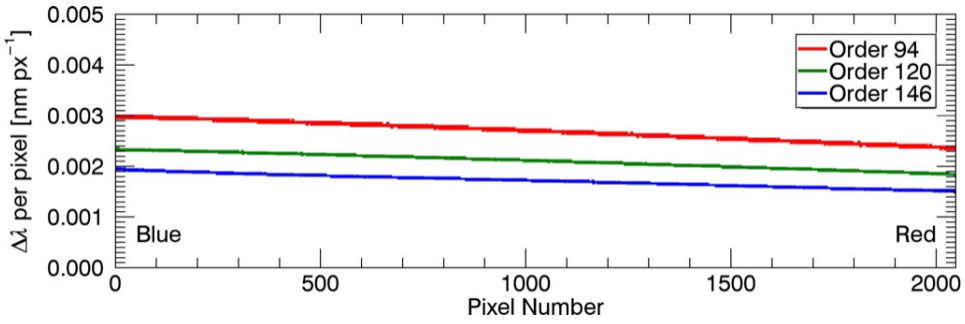

Figure 2.6: Wavelength change per pixel across three échelle orders, as extracted from a reduced KiwiSpec spectrum. The blue end within the orders is to the left; the red end within the orders is to the right.

Calculation of the plate scale can be simplified if one employs the quasi-Littrow expression for the angular dispersion:

$$P \simeq \frac{\lambda_{\text{blaze}}}{2 f_{\text{trad.cam}} \tan\theta_{\text{B}}}. \tag{2.18}$$

This equation gives the plate scale at the blaze wavelength, which would typically be placed at the centre of an order on the detector (i.e. near pixel 1024 in Figure 2.6). As such, although the plate scale will change across an order, Equation 2.18 gives an approximate average plate scale for the order containing λ_{blaze}.

Within the KiwiSpec design, the equations above give the plate scale of the échelle dispersion at the intermediate focus. Because of the magnification change due to the relay formed by the secondary collimator and camera lens (as described in Section 1.1), the following substitution is required for the KiwiSpec case:

$$f_{\text{trad.cam}} = f_{\text{p.coll}} \frac{f_{\text{KiwiSpec.cam}}}{f_{\text{s.coll}}}. \tag{2.19}$$

Finally, the plate scale values in Figure 2.6 allow one to estimate the amount of spectral movement that equates to a 1 m/s radial velocity Doppler

shift. The non-relativistic Doppler equation, (where c represents the speed of light), is given by:

$$v = \frac{\Delta\lambda \cdot c}{\lambda}. \tag{2.20}$$

From Figure 2.6, for order 120, at the centre of the order ($\lambda = 509.7\,\text{nm}$), the plate scale is 0.0021 nm/pixel. Employing these values within Equation 2.20 gives the following relationship:

$$1 \text{ pixel} = 1236 \text{ m/s}. \tag{2.21}$$

Or, in terms of a radial velocity shift:

$$1 \text{ m/s} = 8.1 \times 10^{-4} \text{ pixels} \approx \frac{1}{1000} \text{ pixel}. \tag{2.22}$$

This very small number highlights why high instrumental stability is required for precision radial-velocity measurements.

2.6 Free Spectral Range

Although the various diffraction orders of a grating overlap, for a given order there is a subset of wavelengths that do not overlay the same wavelengths in a neighbouring order. For each order, this set of wavelengths is known as the free spectral range ($\Delta\lambda_{\text{FSR}}$). Equivalently, it can be defined as the change in wavelength between adjacent orders for a given angle of diffraction.

Given that the parameters α, β and G within the grating equation are common to two adjacent orders, mathematically the situation can be expressed as:

$$m(\lambda + \Delta\lambda) = (m+1)\lambda; \text{ or} \tag{2.23}$$

$$\Delta\lambda = \Delta\lambda_{\text{FSR}} = \frac{\lambda}{m}. \tag{2.24}$$

With respect to échelle gratings, one is typically interested in the free spectral range of the blaze wavelengths (λ_{blaze}).

Equation 2.24 indicates that traditional gratings operating in low orders (i.e. $m = 1$) have large free spectral ranges; whereas échelle gratings operating at high orders (i.e. $m > 90$ in the KiwiSpec case) have short free spectral ranges. The equation also shows that orders at red wavelengths have longer free spectral ranges than orders at blue wavelengths.

The linear extent of a free spectral range on the detector can be determined by dividing Equation 2.24 by the plate scale of the spectrograph. This can be useful for determining the minimum detector size required (based on the longest free spectral range within the wavelength range of interest).

The free spectral range can also be expressed in terms of the grating groove spacing. Substituting the qausi-Littrow version of the grating equation (Equation 2.9, solved for m) into Equation 2.24, and employing the geometry of Figure 2.7 gives:

$$\Delta\lambda_{\mathrm{FSR}} \simeq \frac{\lambda^2 G}{2\sin\theta_{\mathrm{B}}} \simeq \frac{\lambda^2}{2s} \simeq \frac{2s}{m^2}. \tag{2.25}$$

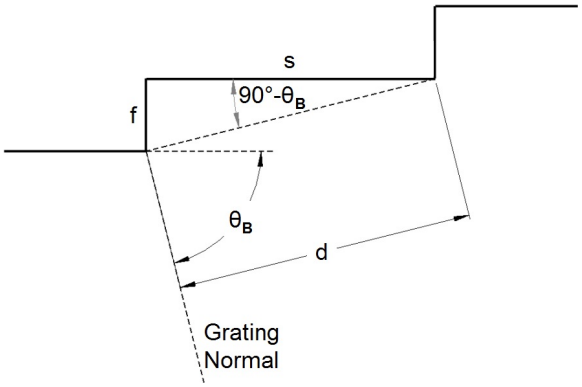

Figure 2.7: How the facet size (f) and step size (s) for a diffraction grating are set by the blaze angle (θ_{B}) and groove spacing (d). The diagram shows that $s = d\sin\theta_{\mathrm{B}}$ and $f = d\cos\theta_{\mathrm{B}}$.

Table 2.2 gives the calculated free spectral ranges for the four R4 gratings offered by Richardson Gratings. Within the table, the free spectral range is calculated for 560 nm, which is at the centre of the wavelength range of the KiwiSpec prototype. With respect to échelle spectrographs, shorter free spectral ranges are generally more desirable, as they lead to more compact spectra which require smaller (and hence less expensive) cameras and detectors.

Table 2.2: Calculated free spectral ranges ($\Delta\lambda_{\mathrm{FSR}}$) for the groove spacings of R4 échelle gratings available from Richardson Gratings (the KiwiSpec échelle is an R4, 31.6 grooves per mm grating). Free spectral ranges are calculated for 560 nm, which is the central wavelength of the KiwiSpec prototype spectral format.

G [grooves per mm]	**$\Delta\lambda_{\mathrm{FSR}}$ [nm at 560 nm]**
31.6	5.1
41.59	6.7
85.84	13.9
154.51	25.0

2.7 Anamorphic Magnification

Although the incident beam on the échelle grating is circular, the shape of the diffracted beam changes with the angle of diffraction. This change is known as anamorphic magnification and is illustrated in Figure 2.8. As shown in the figure, the diffracted beam shape changes in one direction only (in the direction perpendicular to the grating grooves). In the direction parallel to the grating grooves the beam size does not change following diffraction.

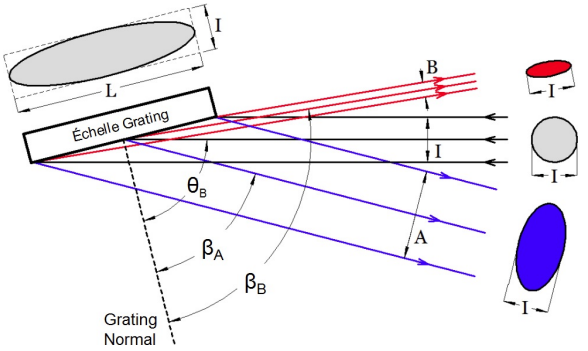

Figure 2.8: The shape of the diffracted beam changes with diffraction angle owing to anamorphic magnification. Beam profiles are also shown on the right hand side of the figure, and the illumination pattern on the échelle itself shown at the top left. Large diffraction angles were chosen for clarity; actual diffraction angles within KiwiSpec are within ± 1.5° of the blaze angle.

The anamorphic magnification, r, is given by:

$$r = \frac{\cos\alpha}{\cos\beta}. \tag{2.26}$$

Figure 2.9, derived using this equation, indicates the dimensional change of the collimated beam diameter (following the échelle) across an order. Figure 2.10 shows a picture of beam footprints at the secondary collimator, noticed during alignment of the instrument with a red HeNe laser.

In general, anamorphic magnification causes the resolution element (the image of the entrance slit) to change shape across an échelle diffraction order, and hence causes a change in wavelength resolution across the order.

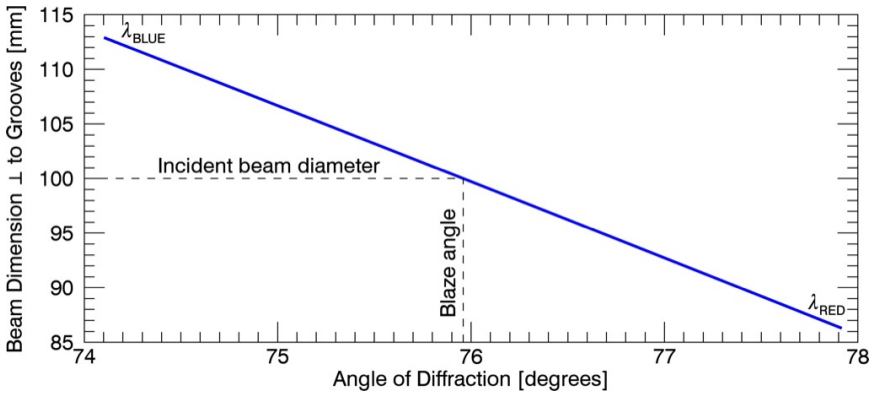

Figure 2.9: How the diffracted beam diameter changes with diffraction angle across a diffraction order. Moving across an order from blue wavelengths to red, the anamorphic magnification causes the beam size to decrease and the wavelength resolution correspondingly to increase. The plot was calculated for order 93 ($\lambda_{\text{blaze}} = 660\,\text{nm}$).

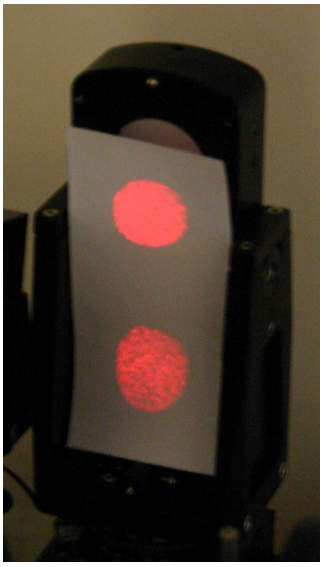

Figure 2.10: Beam footprints on the secondary collimator mirror from a red HeNe laser (632.8 nm) used for alignment. Although the two beam footprints are of the same wavelength, they are from orders 96 (bottom) and 97 (top), and hence have diffracted from the échelle at different angles. The difference in shape between the two beamprints is clearly seen.

2.8 Spectrograph Layout and Parameters

The following two sections describe parameters of 'direct' and fibre-fed spectrographs. A 'direct spectrograph' is defined here as a spectrograph which is directly fed by the telescope, meaning the f/ratio is preserved on either side of the slit. A fibre-fed spectrograph is connected to the telescope via a flexible optical fibre, which operates as a light pipe to transport light from the telescope to the spectrograph. This allows the spectrograph to be mechanically de-coupled from the telescope and placed within a mechanically and environmentally stable environment. However, the fibre does not preserve the input f/ratio, but instead modifies it to a smaller f/ratio through a process known as focal ratio degradation.

2.8.1 Direct Spectrographs

A schematic diagram of a direct spectrograph is shown in Figure 2.11.

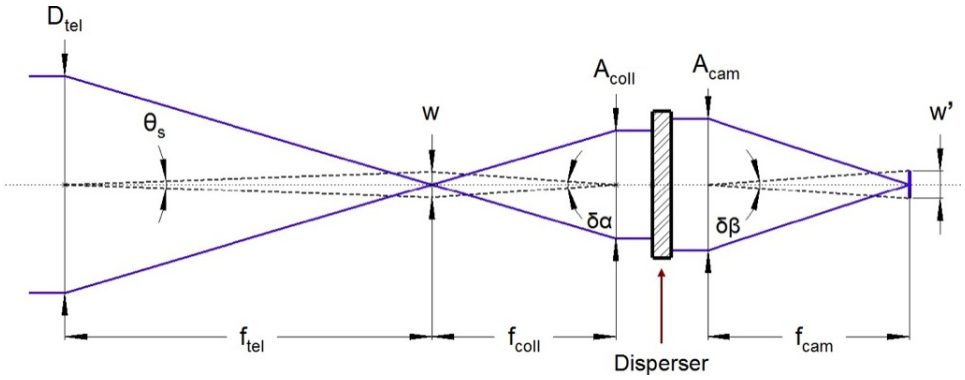

Figure 2.11: Schematic diagram of a direct spectrograph (i.e. one fed directly by a telescope). Shown is the plane of échelle dispersion; the spatial (non-dispersed) plane is normal to the page. The difference between $A_{\rm coll}$ and $A_{\rm cam}$ is due to anamorphic magnification. Diagram adapted from Schroeder (2000).

This diagram highlights several relationships important to spectrograph design. First, the angular size of the slit (of width w) projected onto the sky is given by:

$$\theta_{\rm s} = \frac{w}{f_{\rm tel}} \ \ [\text{radians}] = \frac{w}{f_{\rm tel}} \cdot 206,265 \ \ [\text{arcsec}]. \tag{2.27}$$

Secondly, the focal ratio is conserved on either side of the slit, giving the following relationship:

$$\frac{D_{\rm tel}}{f_{\rm tel}} = \frac{A_{\rm coll}}{f_{\rm coll}}. \tag{2.28}$$

And finally, the geometry of the figure provides the dimensions of the slit image at the detector. The size of the slit image (in the absence of aberrations) in the échelle dispersion direction is given by:

$$w' = rw\frac{f_{\rm cam}}{f_{\rm coll}}, \tag{2.29}$$

where r is the anamorphic magnification. For the spatial (non-dispersed) direction, the image length, h', of the physical slit length, h, becomes:

$$h' = h\frac{f_{\rm cam}}{f_{\rm coll}}. \tag{2.30}$$

2.8.2 Fibre-fed Spectrographs

A schematic diagram of a fibre-fed spectrograph is shown in Figure 2.12.

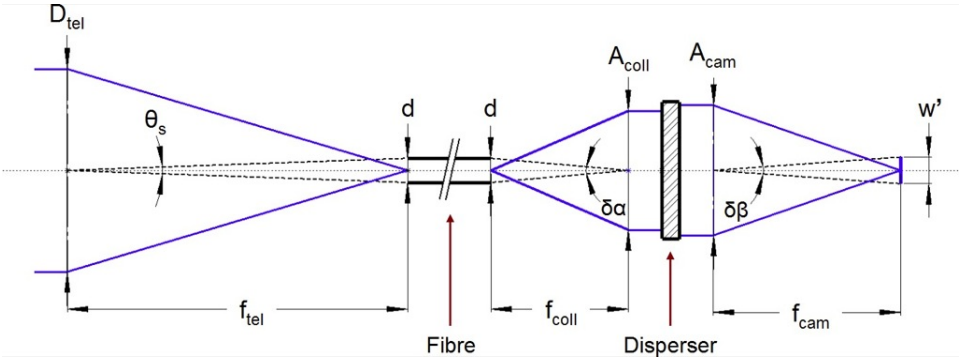

Figure 2.12: Schematic diagram of a fibre-fed spectrograph. Shown is the dispersion plane; the spatial (non-dispersed) plane is normal to the page. The difference between $A_{\rm coll}$ and $A_{\rm cam}$ is due to anamorphic magnification. Diagram adapted from Schroeder (2000).

Assuming the fibre end is used as the entrance slit for the spectrograph, the angular size of the fibre (of diameter d) projected onto the sky is given by:

$$\theta_{\rm s} = \frac{d}{f_{\rm tel}} \ \ [\text{radians}] = \frac{d}{f_{\rm tel}} \cdot 206,265 \ \ [\text{arcsec}]. \tag{2.31}$$

The major difference between a direct and a fibre-fed spectrograph is that the fibre does not preserve the f/ratio between the input beam (telescope side) and the output beam (spectrograph side). This effect is known as focal ratio degradation (FRD), and if light is fed into a fibre via a converging cone of light of angle θ, as a result of FRD it will emerge as a diverging cone of light of angle $\theta + \Delta\theta$. Expressed in terms of f/ratios, this becomes:

$$\text{FRD} = \rho = \frac{f/\text{ratio}_{\rm in}}{f/\text{ratio}_{\rm out}}. \tag{2.32}$$

FRD (ρ) is always a positive value greater than unity, and generally $\rho < 1.1$. With respect to Figure 2.12, the coupling between telescope and spectrograph becomes:

$$\frac{A_{\text{coll}}}{f_{\text{coll}}} = \rho \frac{D_{\text{tel}}}{f_{\text{tel}}}. \tag{2.33}$$

Murphy et al. (2008), in a summary of the current understanding of the sources of FRD, indicated that the following affect the FRD characteristics of fibres (in order of decreasing importance): surface quality on the end of the fibre; immersion (coupling the end of a fibre with a cover plate improves FRD); mounting and handling of the fibre (sharp bending and mounting-induced stress can increase FRD); length of fibre; and fibre type. Murphy et al. (2008) and others (Ramsey, 1988) have found little evidence that FRD is wavelength-dependent. Horton et al. (2011) indicate that the fibre core geometry (i.e. circular, square or octagonal) can have an effect on FRD characteristics. Also, Haynes et al. (2012) show that adding a tapered section to the fibre can have a minimal effect on FRD characteristics.

As reported by Angel et al. (1977), Ramsey (1988), and Murphy et al. (2008), FRD is minimized when fibres are fed with fast input beams. Murphy et al. (2008) found that f/ratios below f/4 are largely immune to FRD effects caused by bending of the fibre (after tests of bend radii from 250 to 10 mm).

2.9 Wavelength Resolution

Fundamentally, the spectrum produced by a spectrograph is composed of monochromatic images of the entrance slit. This slit image is known as the resolution element of the spectrograph, as it represents the smallest element or feature that can be detected within a spectrum. The wavelength resolution of a spectrograph is tied to the size of the spectrograph's resolution element, and therefore both parameters provide a measure of the fineness of detail discernible within the spectrum.

One of the more common measures of wavelength resolution is the Rayleigh criterion, which states that two neighbouring spectral features will be just resolved if the principal maximum of one coincides with the first minimum of the neighbouring feature. This is illustrated in Figure 2.13, for the case of two projected slit image profiles represented by sinc^2 functions. The wavelength resolution of a spectrograph is typically given as $\delta\lambda$ (the difference in wavelengths between the two just-resolved spectral features).

When the Rayleigh criterion is satisfied, the wavelength resolution is equivalent to the size of the resolution element (i.e., the projected slit width, w'). Therefore, the projected slit width and the spectrograph plate scale (P) at the detector can be used to develop an equation for the wavelength

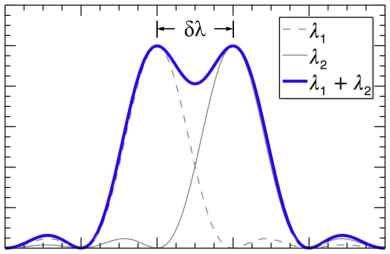

Figure 2.13: According to the Rayleigh criterion, two neighbouring spectral features are just resolved if the maximum value of one lies over the minimum value of the other (as shown here for two sinc^2 functions).

resolution in terms of spectrograph parameters, as shown in Equations 2.34 through 2.36. Note that this approach assumes that the slit width is the limiting factor in terms of wavelength resolution (the typical situation for astronomical spectrographs):

$$\delta\lambda = Pw'; \tag{2.34}$$

$$\delta\lambda = \left(f_{\text{cam}} \cdot \frac{d\beta}{d\lambda}\right)^{-1} \frac{r\theta_{\text{s}} D_{\text{tel}} f_{\text{cam}}}{A_{coll}}; \tag{2.35}$$

$$\delta\lambda = \frac{r}{\frac{d\beta}{d\lambda}} \cdot \frac{\theta_{\text{s}} D_{\text{tel}}}{A_{coll}}. \tag{2.36}$$

The numerator of Equation 2.36 shows that increasing the projected slit size (θ_{s}) leads to an increase in $\delta\lambda$, as does increasing the size of the telescope (which increases the size of the stellar images at the focal plane).

Within Equation 2.36 the échelle-based parameters have been separated to the left. This arrangement of the equation emphasizes that in order for a given échelle grating to have the same wavelength resolution on different telescopes, the parameter $\frac{\theta_{\text{s}} D_{\text{tel}}}{A_{coll}}$ must remain constant. Therefore, for a given slit width (projected on the sky), as the telescope diameter increases, so must the collimated beam diameter in order to maintain a given wavelength resolution.

2.10 Resolving Power

The resolving power of a spectrograph (a dimensionless quantity) is an alternative measure of the the amount of detail present in a spectrum. For two wavelengths just resolved, λ_1 and λ_2, it is given by:

$$R = \frac{\lambda}{\delta\lambda} = \frac{\frac{\lambda_1+\lambda_2}{2}}{\lambda_2 - \lambda_1}. \tag{2.37}$$

Although there are no discrete boundaries, 'low resolution' astronomical spectrographs may have resolving powers of several hundred to several thousand, whereas 'high resolution' astronomical spectrographs may have resolving powers of $40,000 - 100,000$. 'Ultra-high' resolution instruments

also exist; for example the Ultra-High Resolution Facility (UHRF) at the Anglo-Australian Telescope can achieve resolving powers of approximately 1,000,000 (Diego et al., 1995).

The resolving power can be limited in a spectrograph by either diffraction effects, the width of the slit or the size of the detector pixels. Diffraction-limited and slit-limited resolving powers are discussed below. Spectrographs are normally designed to be slit-limited, and the physical slit width is generally chosen as a compromise between wavelength resolution and the amount of light entering the spectrograph. Detector-limited spectrographs are not desirable (and therefore not discussed further), as in such a situation the detector is not recording all of the information that the instrument is capable of producing.

2.10.1 Diffraction-limited

The diffraction-limited resolving power of a diffraction grating is given by:

$$R = mGL = mN, \tag{2.38}$$

where:

L	=	grating length (perpendicular to grooves)	[mm];
N	=	total number of illuminated grating grooves	[unitless].

Therefore the theoretical resolving power of a grating depends only on the order number and the number of illuminated grooves. Increasing either parameter will lead to an increase in resolving power. For a given collimated beam diameter, the diffraction limited resolving power can be increased by illuminating more grooves by moving to a longer grating operating at a higher angle of incidence. Another method would be to choose a grating with a higher groove density.

The theoretical or diffraction-limited resolving power of a grating is many times more than the resolving power realized by placing the grating within an instrument (where an extended entrance aperture such as a slit or fibre exit is used instead of a point source). For example, for the KiwiSpec échelle grating, at order 120 (at the centre of the prototype spectral format), the diffraction limited resolving power is 1,547,136 (120 x 31.6 grooves/mm x 408 mm). For comparison, the resolving power calculated for the slit (fibre) limited prototype instrument was approximately 40,000.

2.10.2 Slit-limited Direct Spectrographs

Within Section 2.9, Equation 2.36 was developed to provide an expression for the slit-limited wavelength resolution, $\delta\lambda$. Substituting that result into

Equation 2.37 gives an expression for the slit-limited resolving power:

$$R_{\text{slit}} = \frac{\lambda}{\delta\lambda} = \frac{\frac{d\beta}{d\lambda} A_{coll}}{r\theta_{\text{s}} D_{\text{tel}}}. \tag{2.39}$$

Given the quasi-Littrow configuration, (where the anamorphic magnification, r, approximates to unity,) and employing Equation 2.13 for the angular dispersion term, the above equation becomes:

$$R_{\text{slit}} \simeq \frac{2A_{\text{coll}} \tan\theta_{\text{B}}}{\theta_{\text{s}} D_{\text{tel}}(1 - \tan\theta_{\text{B}} \tan\theta)}. \tag{2.40}$$

Assuming the further simplified case of $\theta \simeq 0$, the angular dispersion term can instead be replaced by Equation 2.14 to give:

$$R_{\text{slit}} \simeq \frac{2A_{\text{coll}}}{\theta_{\text{s}} D_{\text{tel}}} \tan\theta_{\text{B}}. \tag{2.41}$$

Another form of the equation can be produced by using the geometry in Figure 2.11, namely that $\frac{A_{\text{coll}}}{D_{\text{tel}}} = \frac{f_{\text{coll}}}{f_{\text{tel}}}$ and $\theta_{\text{s}} = \frac{w}{f_{\text{tel}}}$:

$$R_{\text{slit}} \simeq \frac{2f_{\text{coll}}}{w} \tan\theta_{\text{B}}. \tag{2.42}$$

And finally, Equation 2.41 can be rewritten using the relationship between the collimated beam diameter and the length of the échelle grating ($A_{\text{coll}} = L\cos\theta_{\text{B}}$) to give:

$$R_{\text{slit}} \simeq \frac{2L}{\theta_{\text{s}} D_{\text{tel}}} \sin\theta_{\text{B}}. \tag{2.43}$$

Note that in the final equation, the parameter L represents the length of a grating that would be filled by the collimated beam used (which might be larger than the actual grating if the grating is purposely overfilled).

Also of note is that Equation 2.43 indicates that the slit-limited resolving power is proportional to $\frac{L}{D_{\text{tel}}}$. Therefore, to maintain high resolving powers as telescope diameters increase, the length of the grating (or equivalently the diameter of the collimated beam) must increase as well.

The above equations for R_{slit} indicate several methods available to increase the resolving power of a traditional spectrograph:

- increase collimator focal length
- increase collimated beam diameter
- increase length of grating
- increase grating blaze angle
- decrease slit size
- decrease telescope size

The first three items are related through the common factor of the collimator focal ratio, meaning that as one increases, the other two increase as well. Increasing these three parameters to achieve high resolving powers was the basis behind traditional coudé spectrographs. The fourth item, increasing the grating blaze angle, represents the échelle solution to achieving high resolving powers. The fifth item, (decreasing the slit size), is a technique that can be employed on any spectrograph, although at the expense of a loss of throughput. Finally, the point about telescope size is owing to the fact that smaller telescopes produce smaller stellar images at their focal planes (and therefore require a narrower slit than a larger telescope).

2.10.3 Fibre-limited, Fibre-fed Spectrographs

In order to apply to a fibre-fed spectrograph, the slit-limited resolving power equations in the previous section need to be modified to account for FRD, using the relationship given in Equation 2.33.

The result is the introduction of an FRD term, ρ, in the denominator of Equations 2.39, 2.40, 2.41 and 2.43. For example, for a fibre-fed spectrograph, the resolving power becomes:

$$R = \frac{2A_{\rm coll}\tan\theta_{\rm B}}{\rho\theta_{\rm S}D_{\rm tel}(1-\tan\theta_{\rm B}\tan\theta)}. \tag{2.44}$$

2.11 Resolution-Throughput Product

For a given spectrograph there is a balance between throughput and resolution, in that increasing one parameter leads to a decrease in the other. For example, increasing the entrance slit size allows more light into the spectrograph, but it also leads to an increase in the size of the resolution element. The larger resolution elements then overlap more in the resulting spectrum, and hence lead to a decrease in the resolving power of the instrument.

A rearrangement of Equation 2.44 gives the balance between resolving power and throughput mathematically:

$$R\theta_{\rm s} = \frac{2A_{\rm coll}\tan\theta_{\rm B}}{\rho D_{\rm tel}(1-\tan\theta_{\rm B}\tan\theta)}. \tag{2.45}$$

Multiplying the result of this equation by 206,265 gives the $R\theta_{\rm s}$ product in units of arcsec, as it is usually expressed.

This parameter is a constant for a given spectrograph, which has implications if a spectrograph is moved to a larger telescope. For a fibre-fed spectrograph, maintaining the fibre diameter when moving to a larger telescope means that the resolving power, R, remains unchanged. However, the increased focal length of the larger telescope causes the angle subtended by

the fibre on the sky to decrease, and hence less light will enter the fibre compared to smaller telescope. Conversely, if one increases the fibre diameter to maintain throughput on the larger telescope, the resolving power of the spectrograph will decrease owing to the increased diameter of the fibre exit.

2.12 Overfilling

As was shown in Section 2.11, increasing the width of the entrance slit leads to a loss in resolution, as the resolution element (the monochromatic image of the slit) increases as well. Tull (1972) and Diego and Walker (1985) describe an approach that allows the lost resolution to be reclaimed through adjustment of the focal ratio of the beam incident on the entrance slit.

The theory of the technique can be illustrated by the equation for the size of the slit image at the detector (w'):

$$w' = r\theta_{\rm s} D_{\rm tel} \frac{f_{\rm cam}}{A_{\rm coll}} = r \frac{w}{f_{\rm tel}} D_{\rm tel} \frac{f_{\rm cam}}{A_{\rm coll}}. \tag{2.46}$$

For a given telescope-spectrograph combination, most of these parameters are fixed and not easily changed. However, the slit size (w) is mechanically adjustable, and the telescope focal length ($f_{\rm tel}$) can be adjusted with a focal reducer or extender. As shown in the geometry of Figure 2.11, changing $f_{\rm tel}$ leads to a change in the collimated beam diameter, $A_{\rm coll}$, through the preservation of the beam f/ratio on either side of the entrance slit. Equation 2.46 shows that increasing $A_{\rm coll}$ leads to a decrease in the size of the resolution element, and hence an increase in the spectrograph's resolving power.

In practice, with this technique one adjusts the slit width for a given seeing, and then compensates for the new slit width by adjusting the focal ratio of the beam entering the spectrograph with some kind of focal reducer or extender. With this approach, one can optimize throughput and at the same time maintain the nominal resolving power of the instrument. Some light may be lost by overfilling the grating; however, Tull (1972) and Diego and Walker (1985) calculated that such a loss is more than compensated for by the increased slit width.

One would want to place the focal reducer or extender on the telescope side of the slit, as the introduction of the optic would require a refocus (which is more easily accomplished with the telescope than the spectrograph). The introduction of the focal reducer/extender will also change the plate scale of the telescope, and hence the size of the projected slit on the sky will change, which needs to be taken into account.

2.13 Detector Sampling

In modern spectrographs, the detector that records the spectrum is invariably a CCD. Given that a CCD image is composed of thousands or millions of discrete pixels, care must be taken to ensure that the pixel-sampled image is accurately recording the continuously-varying information within the spectrum.

To meet the well-known Nyquist criterion, one must match the smallest detail present within the spectrum (i.e. the size of the resolution element) with two pixels on the detector. With modern low-noise detectors, where readout noise is minimal, this is sometimes expanded to three-pixel sampling.

Over-sampling is not desirable as the flux contained within each resolution element is then spread out over more pixels, resulting in each pixel having a lower signal-to-noise ratio. As well, since each pixel contributes readout noise, having more pixels covering the resolution element means more noise in the image (spectrum). Under-sampling is also not desirable as it means the spectrograph has become detector-limited and therefore information present in the spectrum is not being recorded.

During the design of a spectrograph, the camera focal length, pixel size, and overall detector size are typically adjusted to ensure that both the Nyquist theorem is satisfied and the spectrum fills the CCD. This trade-off study is guided by the finite number of device options available from CCD manufacturers (i.e. pixel sizes, detector dimensions).

The camera focal length required to meet the Nyquist sampling theorem for a direct spectrograph can be shown to be:

$$f_{\text{trad.cam}} = \frac{2\Delta s_{\text{px}} L \cos\beta}{\theta_{\text{s}} D_{\text{tel}}}, \tag{2.47}$$

where Δs_{px} is the size of a pixel on the detector. For the KiwiSpec case, the above equation needs to be modified to account for focal ratio degradation and the magnification factors of the relays described in Section 1.1:

$$f_{\text{KiwiSpec.cam}} = \frac{2\Delta s_{\text{px}} L \cos\beta}{\rho\theta_{\text{s}} D_{\text{tel}}} \frac{f_{\text{L1}} f_{\text{s.coll}}}{f_{\text{L2}} f_{\text{p.coll}}}. \tag{2.48}$$

Review of Equation 2.47 shows that: large gratings (large L) require long focal length cameras; échelle gratings (large β) require cameras with shorter focal lengths than conventional gratings; small slit widths (small θ_{s}) require long focal length cameras; and larger telescopes lead to shorter focal length cameras. With respect to the final point, this means that given the large beam diameter also required for large telescopes, spectrograph cameras on large telescopes are of small f/number.

2.14 Line Tilt

As described in Section 2.1, échelle gratings can be employed out-of-plane by an angle γ, which separates the incident and diffracted ray paths by an angle 2γ. This can be preferable to using the Littrow angle θ to separate the beams, a method which results in efficiency losses (to be described in Section 2.16). A consequence, however, of using an échelle grating out-of-plane is line tilt, which increases as γ increases.

Line tilt is effectively a change in the angle of diffraction β with γ, the angle 'across' an order (that is, perpendicular to the échelle dispersion). Mathematically this can be expressed by differentiating the full form of the grating equation (Equation 2.2):

$$\frac{d\beta}{d\gamma} = \left(\frac{\sin\alpha + \sin\beta}{\cos\beta}\right)\tan\gamma, \tag{2.49}$$

which, after substituting in the quasi-Littrow relationships of $\alpha = \theta_{\mathrm{B}} + \theta$ and $\beta = \theta_{\mathrm{B}} - \theta$ and simplifying, the line tilt at the blaze wavelength becomes:

$$\frac{d\beta}{d\gamma} \simeq 2\tan\theta_{\mathrm{B}}\tan\gamma. \tag{2.50}$$

Given the geometry of Figure 2.14, the amount of tilt, ϕ, can be expressed by:

$$\frac{d\beta}{d\gamma} = \tan\phi \simeq 2\tan\theta_{\mathrm{B}}\tan\gamma. \tag{2.51}$$

This equation can be further simplified as ϕ and γ are typically small values. As such, $\tan\phi \simeq \phi$ and $\tan\gamma \simeq \gamma$, and therefore:

$$\phi \simeq 2\tan\theta_{\mathrm{B}}\,\gamma. \tag{2.52}$$

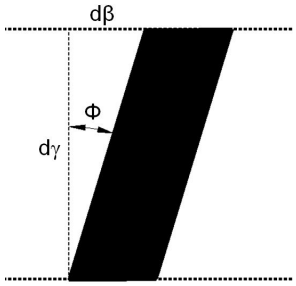

Figure 2.14: A tilted 'line' (resolution element of a rectangular entrance slit) within an échelle order (delineated by dashed horizontal lines).

The presence of the échelle R-number ($\tan\theta_{\mathrm{B}}$) in the equation shows that R4 gratings exhibit twice the line tilt of R2 gratings for a given γ angle.

Note that a cross-disperser (to be described more in Section 2.15) can also introduce line tilt, which can increase or decrease the 'native' line tilt

(depending on the relative signs of the effects). Note also that the angle of the slit can also be rotated to help compensate for the native line tilt.

In the case of a fibre-fed spectrograph, the circular exit face of the fibre is often used as the entrance slit of the spectrograph. For this situation, Barnes (2004) showed that the circular image of the fibre, which is extended into an ellipse of height h_e and width w_e (due to anamorphic magnification) is then tilted (or sheared) through an angle ϕ_e, calculated with the equation:

$$\tan \phi_\mathrm{e} = \tan \left(\frac{h_\mathrm{e}}{w_\mathrm{e}} \tan \phi \right). \tag{2.53}$$

2.15 Cross-Dispersion

Given that the échelle grating generates many diffraction orders overlying one another in the direction of the blaze angle, a second dispersive element is required to separate the orders to extract useful information from the spectrum. This second disperser is known as a cross-disperser, as its dispersive action is oriented orthogonal to, or across, the échelle dispersion direction. One of the reasons that échelle gratings have become popular is that the combination of the overlapping orders of short free spectral range, combined with a cross-disperser, allows for effective use of small detectors such as CCDs.

The ability to easily remove the échelle grating and cross-dispersion grism from the KiwiSpec prototype allowed a series of images to be taken to illustrate the separate and combined effects of the two dispersive elements. For these images, shown in Figures 2.15 to 2.18, the KiwiSpec monochrome CCD detector was removed and replaced by a Canon colour DSLR camera body, to capture the colours present in the spectra. As explained in the captions, the figures show the spectra that result from the removal of one (or both) of the dispersers in an échelle spectrograph.

The required dispersive power of the cross-disperser is much less than required for the primary disperser, and as such prisms or diffraction gratings (operating in the first order) are typically used for cross-dispersion. A combination of a grating and prism, known as a 'grism' can also be employed. Note that a narrow-band filter could also be used to separate out a single order. This technique is employed within the Hectochelle instrument (a 240-fibre multi-object spectrograph), and allows the observer to choose the échelle diffraction order of interest via a suite of 11 interference filters (Szentgyorgyi et al., 2011). However, while of benefit for multi-object spectrographs, order-separating filters are rarely used in single-fibre, large-wavelength-coverage instruments as they sacrifice the information contained in all other échelle orders.

The cross-disperser can be placed in several locations within the instrument: before the échelle (i.e. UCLES (Walker and Diego, 1985)) in single

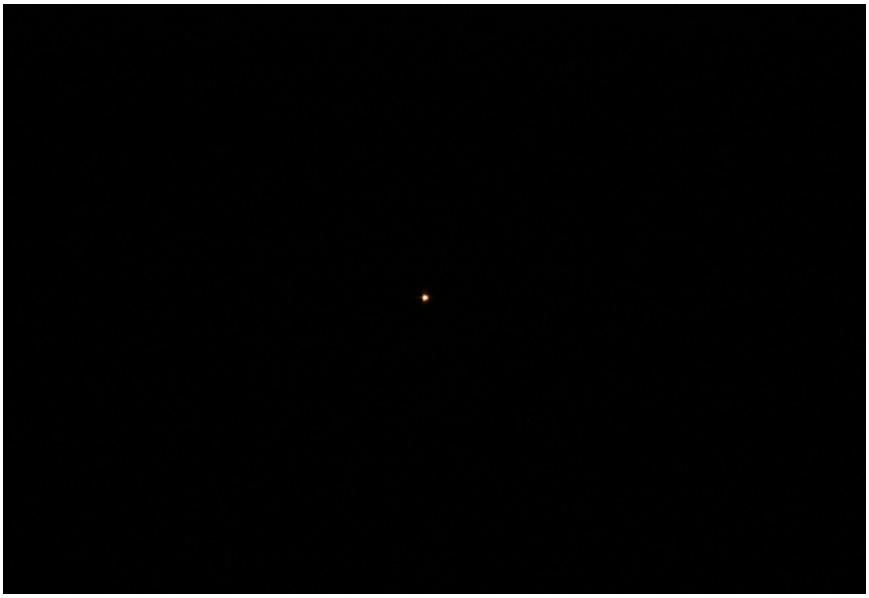

Figure 2.15: The KiwiSpec prototype resolution element (the image of the fibre exit). To create this image, the échelle grating was removed from the instrument and replaced by a flat mirror. The cross-dispersion grism was also removed, and the prototype CCD detector was removed and replaced by a Canon colour DSLR camera body.

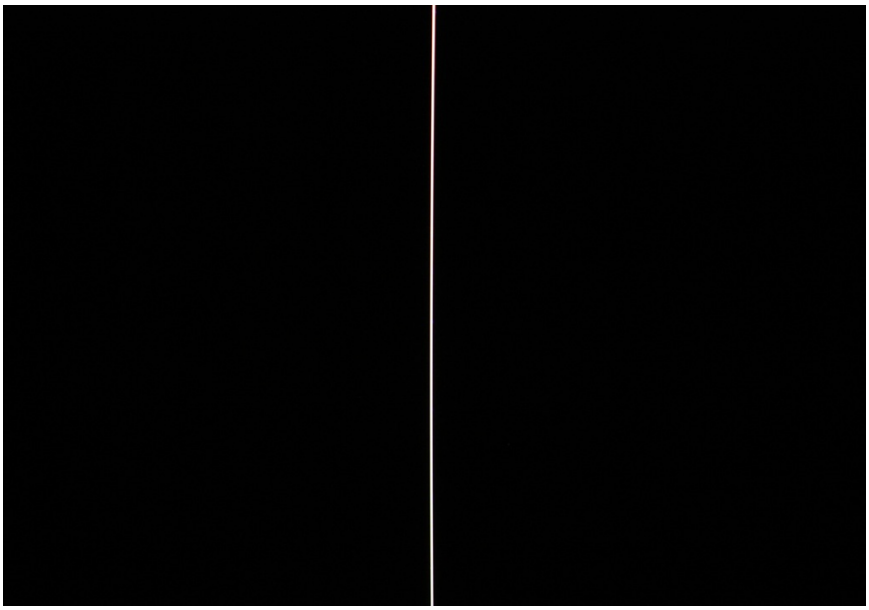

Figure 2.16: The effect of échelle dispersion. For this image, the échelle grating was installed in the KiwiSpec prototype, but the cross-disperser was removed. Shown are over 100 échelle diffraction orders (within the range 350 nm to 1000 nm), all overlaid on top of one another. This image was taken by placing a Canon colour DSLR camera body at the spectrograph focal plane.

Figure 2.17: The effect of cross-dispersion. For this image, the échelle grating was removed from the KiwiSpec prototype and replaced with a flat mirror. Therefore, the cross-dispersion grism was the only dispersive element in the instrument. Note the direction of dispersion is orthogonal to the échelle dispersion, and also the low amount of dispersion (the blue to red transition in the spectrum implies a wavelength coverage of approximately 300 nm). This image was taken by placing a Canon colour DSLR camera body at the spectrograph focal plane.

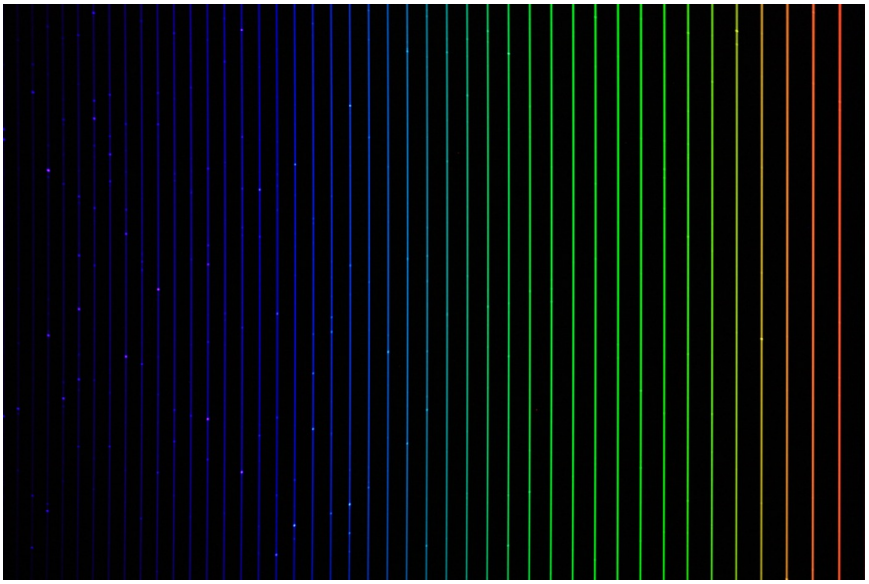

Figure 2.18: The effect of both échelle and cross-dispersion. For this image, the prototype CCD detector was removed and replaced by a Canon colour DSLR camera body. The light sources included a tungsten lamp (producing the continous spectrum) and a thorium-argon lamp (responsible for the bright emission lines visible thoughout the spectrum).

pass; close to the échelle in double-pass (i.e. HERCULES (Hearnshaw et al., 2002)); or between the échelle and camera (i.e. KiwiSpec). Double-pass cross-dispersers are invariably prisms, to avoid the larger throughput losses incurred by a grating in double-pass.

If the cross-disperser is placed before the échelle, the light will be pre-dispersed out-of-plane when it strikes the échelle. This introduces a change of γ angle with wavelength, and leads to a variable line tilt across the final spectrum (which can complicate the reduction procedure).

The actions of the cross-disperser and the échelle dispersion are not completely independent. Owing to the change in wavelength along an échelle order, the effect of cross-dispersion is not constant across an order. This introduces a tilt ψ to the orders, as shown in Figure 2.19. In the case of prism cross-dispersion, this effect can create significant curvature in the orders, which can make the analysis of the spectrum more difficult.

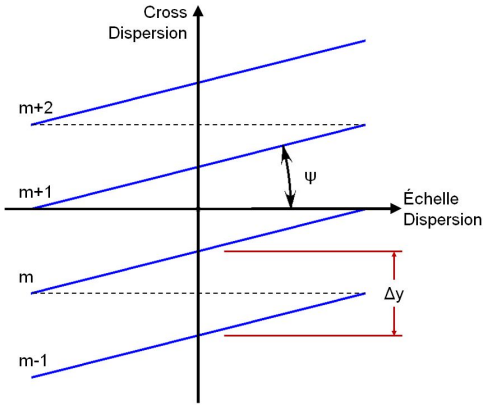

Figure 2.19: The effect of cross-dispersion on an échelle spectrum. Diagonal lines represent the échelle diffraction orders, and the dashed horizontal lines indicate lines of constant wavelength. After Schroeder (2000).

As shown in Figure 2.19, $\tan\psi$ is the ratio between the angular dispersions of the cross-disperser and the échelle:

$$\tan\psi = \left(\frac{d\beta}{d\lambda}_{\text{cross}}\right)\left(\frac{d\beta}{d\lambda}_{\text{échelle}}\right)^{-1}. \tag{2.54}$$

The inter-order separation Δy is set by the camera focal length f_{cam}, the angular dispersion of the cross-dispersion $\frac{d\beta}{d\lambda}_{\text{cross}}$, and the free spectral range $\Delta\lambda_{\text{FSR}}$. It is expressed by the following equation, which is essentially the linear dispersion equation for the cross-disperser:

$$\Delta y = f_{\text{cam}}\Delta\lambda_{\text{FSR}}\frac{d\beta}{d\lambda}_{\text{cross}} \tag{2.55}$$

This equation shows that the change in order separation across a spectrum is determined by the combination of the échelle free spectral range (which increases towards red orders), and the wavelength dependence of the angular dispersion of the cross-disperser. Note that the free spectral range

not only gives the length of the orders, but also the separation (in échelle wavelength space) between the blaze wavelengths in successive orders.

Other factors being equal, the resulting wavelength dependence of the order tilt and order separation for grating and prism cross-dispersers are compared in Table 2.3. The table shows that order tilt is more strongly affected by a prism than a grating, and that the change in order separation with wavelength is less variable with a prism than with a grating.

Table 2.3: Wavelength dependence of order tilt and order separation for grating and prism cross-dispersion methods.

	Grating	**Prism**
Order tilt:	$\tan\psi \propto \lambda_{\rm B}$	$\tan\psi \propto \lambda_{\rm B}^{-2}$
Order separation:	$\Delta y \propto \lambda_{\rm B}^{2}$	$\Delta y \propto \lambda_{\rm B}^{-1}$

In the following three sections, the use of prism, grating, and grism cross-dispersion will be discussed in turn.

2.15.1 Prism Cross-Dispersion

Although surpassed by diffraction gratings as primary dispersers, prisms remain in common use as a cross-disperser for échelle grating spectrographs (for example: HERCULES (Hearnshaw et al., 2002), FEROS (Kaufer et al., 1997), CHIRON (Schwab et al., 2010), HERMES (Raskin et al., 2011)). Within an instrument requiring a large wavelength range, prisms offer higher and more constant spectral efficiency than grating cross-dispersers.

The dispersing power of a prism depends on the beam diameter, the glass type and the size of the prism. More specifically, it depends on how the refractive index of the glass changes with wavelength, and the length, t, of the light ray closest to the prism base (within the glass). For the case of minimum deviation, the dispersing power of a prism is:

$$\frac{d\theta}{d\lambda} = \frac{t}{A}\frac{dn}{d\lambda}, \tag{2.56}$$

where:

θ	=	angular deviation of beam after prism	[degrees];
t	=	length of light ray closest to base	[mm];
A	=	incident beam diameter	[mm];
$\frac{dn}{d\lambda}$	=	change of index with wavelength	[nm^{-1}].

In order to obtain the required dispersion, multiple prisms in series can be used, forming a prism 'train'. This approach is usually appealing as multiple smaller prisms are easier to manufacture (and hence are less expensive) than a single, large prism. In order to calculate the dispersion of

multiple, identical prisms, the result of Equation 2.56 is simply multiplied by the number of prisms.

Advantages of prism-based over grating-based cross-dispersion include a more uniform order separation, and a greater separation between blue orders. Prisms also offer a higher average throughput over a broader wavelength range than gratings (or grisms), as shown in Figure 2.20.

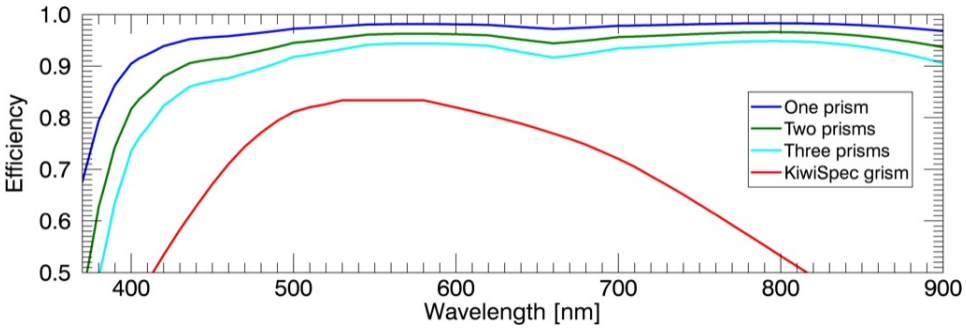

Figure 2.20: Comparison between the efficiencies of prism and grism cross-dispersers. The prism curves were calculated assuming F2 glass with a base length of 150 mm, and assume a high-efficiency anti-reflection coating on each air-to-glass surface. The effect of using multiple prisms (or passes through the same prism) is also illustrated. The grism curve represents measurement data of the actual KiwiSpec grism.

Disadvantages compared to gratings include greater order curvature, less order separation at red wavelengths, and a possible increase in size of the instrument if more than one prism is required. Furthermore, the design of the prisms is limited by the finite number of suitable glass types; a number which becomes smaller if large prisms are required (due to availability of glass) or if UV transmission is required (due to internal transmission characteristics). Another disadvantage is that owing to the (typical) long path length through a cross-dispersion prism, the glass used is required to be extremely homogeneous with respect to refractive index, stress, strain and impurities (bubbles, inclusions and striae). Such requirements, especially for large pieces of glass, greatly increase the cost of the prisms. Given that most spectrograph designs would require at least two prisms to achieve the required amount of cross-dispersion, these losses are multiplied by the number of prisms used. Another disadvantage of multiple prisms is that the overall throughput decreases by $T(\lambda)^n$, where $T(\lambda)$ is the transmissivity of a single prism and n is the number of prisms used (or the number of passes through the same prism). The efficiency loss due to multiple prisms (or multiple passes) is illustrated in Figure 2.20.

To investigate the effect of prism cross-dispersion, within Zemax the nominal KiwiSpec grism cross-disperser was replaced by a prism train, as shown in Figure 2.21. Three F2 prisms in series were required to obtain a

similar amount of cross-dispersion as the grism with a 150 mm focal length camera lens. However, several factors make this design impractical. First, the mechanical footprint of the instrument becomes much larger. Secondly, the flexibility of the design is diminished, as it would be very difficult to add a second channel to the instrument to increase the wavelength range. Thirdly, as shown in Figure 2.22, each prism must be larger than the one it follows, owing to the beam footprint increasing in size as one moves away from the white pupil. Finally, because of the greater footprint size, the camera aperture must be much greater (180 mm diameter vs. 58 mm diameter for the prototype Hasselblad lens). Maintaining the 150 mm focal length with such an aperture will also make the lens design more difficult, as the camera will be operating at a much smaller f/number.

A more practical arrangement would be to change the échelle to an R2 grating. This would halve the angular spread of monochromatic beams following the white pupil, and lead to smaller optical components. Because an R2 grating has half the angular dispersion of an R4 grating, the camera focal length would need to double to 300 mm to maintain the linear dispersion at the detector. However, that would mean that the amount of cross-dispersion could be halved, meaning at least one prism could be removed from the instrument. It is perhaps for these reasons that the prism cross-dispersed instruments listed at the start of this section are all based around R2 échelle gratings.

A spectral format for the instrument layout of Figure 2.21 is shown in Figure 2.23. The order curvature is readily apparent, as is the reduction in inter-order spacing for red orders. This figure should be compared against the corresponding spectral formats for grating and grism cross-dispersion (Figures 2.26 and 2.29).

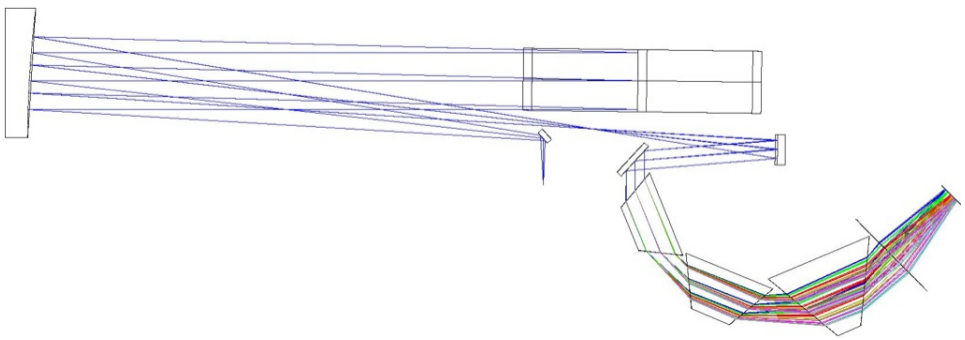

Figure 2.21: The KiwiSpec core R4 design with three F2 prisms for cross-dispersion, and a 150 mm paraxial camera lens. As explained in the text, this is an impractical design for several reasons.

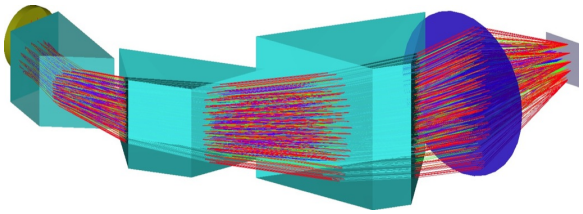

Figure 2.22: Shaded model of the prism train within the layout of Figure 2.21, showing how the beam widens in the vertical direction as the distance from the white pupil (located within the first prism) increases. Note also the large diameter of the (paraxial) camera lens.

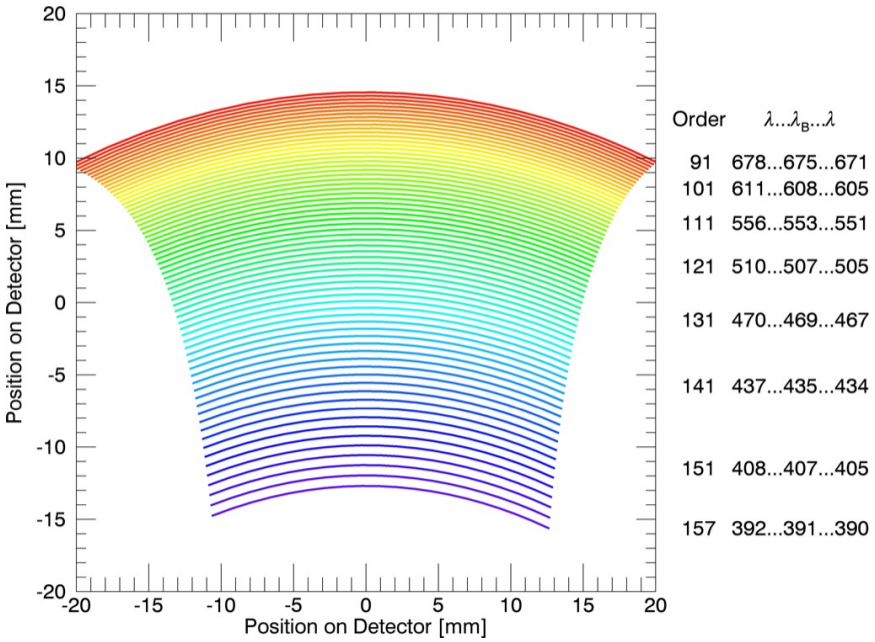

Figure 2.23: The KiwiSpec spectral format with a three prism train for cross-dispersion (generated by the Zemax model of the layout in Figure 2.21).

2.15.2 Grating Cross-Dispersion

Diffraction gratings are an attractive alternative to prisms for échelle cross-dispersion, as they can give a higher amount of dispersive power in a smaller mechanical package. They are typically also less expensive. Furthermore, the availability of different groove spacings (as opposed to the small subset of glass types that work for prisms) means that the focal length of the camera system can be partially relieved of setting the amount of cross-dispersion. This in turn can mean smaller camera focal lengths and detector sizes than are possible with prism cross-dispersion.

Disadvantages include a grating's peaked efficiency response with wavelength, as opposed to the more constant (and on average, higher) efficiency response of prism cross-dispersers. Also, as mentioned above, a prism gives a more uniform order separation across the detector.

Although traditional, surface relief gratings can be used for cross-dispersion, volume phase holographic (VPH) gratings are now being regularly employed as cross-dispersers within échelle spectrographs (i.e. STELES (Castilho et al., 2004), SALT (Barnes et al., 2008), PEPSI (Strassmeier et al., 2008)). Advantages of VPH gratings over traditional surface relief gratings include higher throughput (improvements of 5-10 per cent were reported by Barden et al. (2000)), and simplified spectrograph layouts, as VPH gratings are typically used in transmission. Also, with VPH gratings the grating line density is largely a free parameter, as each grating is created individually (and is not a replica from a finite set of existing master gratings). Given that VPH cross-dispersion is easily employed within the KiwiSpec design, VPH gratings will be considered in more detail here.

VPH gratings are composed of a thin layer of dichromated gelatin (DCG) sandwiched between two glass cover plates for protection (as shown in Figure 2.24a). During manufacture, the light-sensitive DCG layer is exposed to a repeating interference pattern of straight fringes, which generates a periodic variation in density (and hence refractive index) within the gelatin across the grating. The gelatin is then exposed to chemicals which remove its light-sensitivity and fix the repeating pattern in place. This repeating pattern of fringes (the 'grooves' of the grating), can be orthogonal or tilted with respect to the cover plates (a grating with orthogonal fringes was chosen for the KiwiSpec prototype). As described in Barden et al. (1998) and Barden et al. (2000), tilted fringes can be used to introduce anamorphic magnification to the beam, which can be used to stretch or compress the resolution elements in the cross-dispersion direction.

As with surface relief gratings, the traditional grating equation governs the angle of diffraction given the angle of incidence and grating parameters. Operating as cross-dispersers within échelle spectrographs, VPH gratings are typically used in the first order, with the grating frequency adjusted to set the required amount of dispersion.

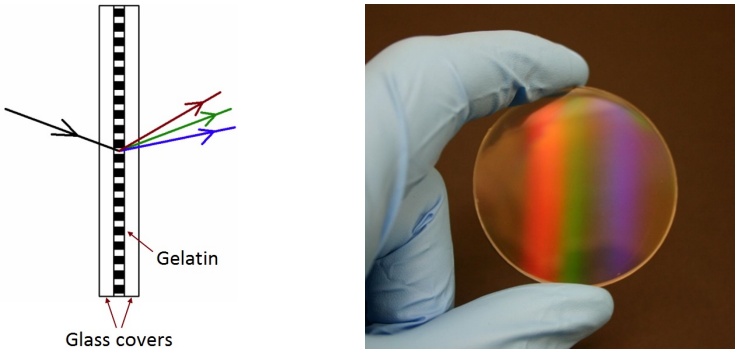

(a) (b)

Figure 2.24: Left: Schematic diagram of a VPH grating. Right: The VPH grating used within the KiwiSpec prototype, which is a 50 mm diameter, 725 line/mm grating.

A VPH grating is typically designed for a central wavelength, for which maximum efficiency is attained when the Bragg condition (from X-ray diffraction) is satisfied (Barden et al., 2000). This scenario is met at the Littrow condition, where the angle of incidence is equal to the angle of diffraction.

For the case of orthogonal fringes, the angle of incidence, α, on the grating which satisfies the Bragg condition can be calculated using:

$$\alpha = \sin^{-1}\left[\frac{m\lambda G}{2}\right], \tag{2.57}$$

and the angle of incidence on the grating gelatin layer is given by (again, for the case of orthogonal fringes):

$$\alpha_{\mathrm{DCG}} = \sin^{-1}\left[\frac{m\lambda G n_{\mathrm{air}}}{2n_{\mathrm{glass}}}\right], \tag{2.58}$$

where n_{air} and n_{glass} represent the refractive indices of air and the glass cover plates, respectively.

An example layout of the KiwiSpec design with a VPH grating as a cross-disperser is shown in Figure 2.25. An example echellogram created with the Zemax model of Figure 2.25 is shown in Figure 2.26. This figure should be compared against the corresponding spectral formats for prism and grism cross-dispersion (Figures 2.23 and 2.29). Of note is the change in order separation for red and blue orders, which is opposite with respect to prism cross-dispersion.

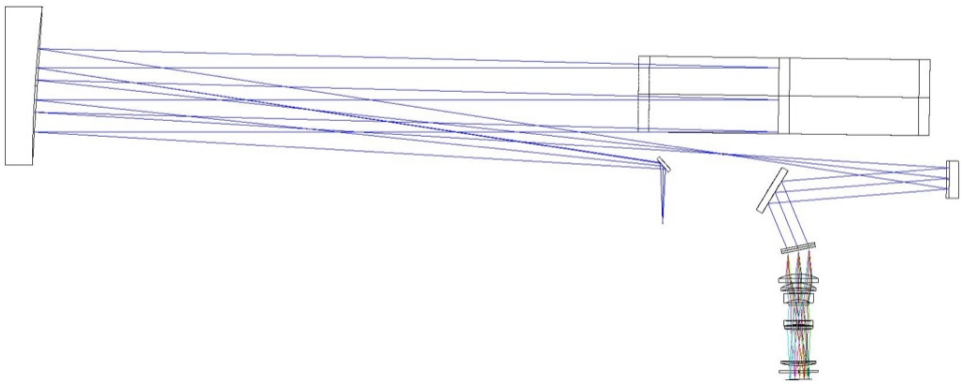

Figure 2.25: Optical layout of the KiwiSpec prototype with a VPH grating employed as a cross-disperser.

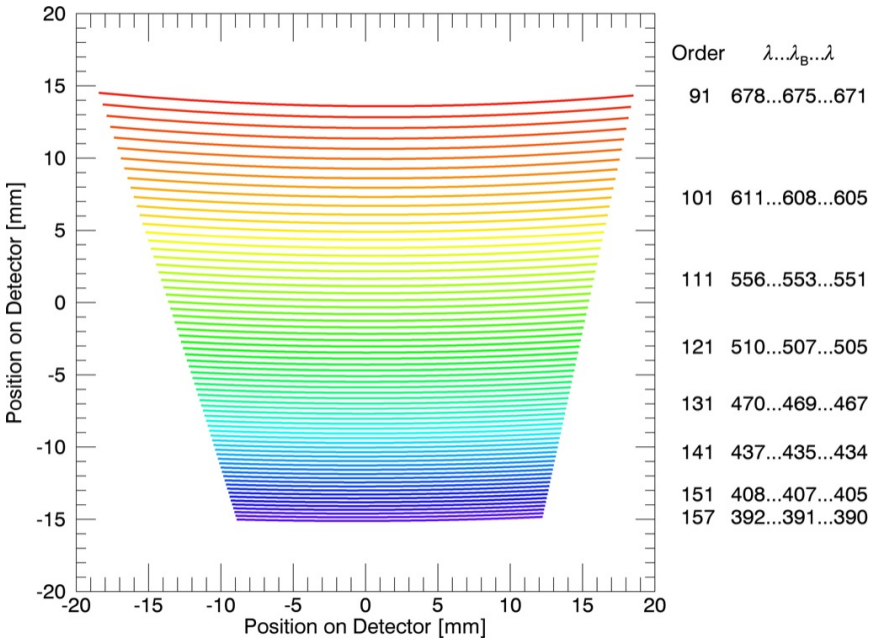

Figure 2.26: The KiwiSpec spectral format with a VPH grating for cross-dispersion.

2.15.3 Grism Cross-Dispersion

The advantages of gratings and prisms, given in the two previous sections, can be combined through the use of a grism for cross-dispersion. This is the cross-dispersion method employed for the KiwiSpec prototype, and the grism was constructed by optically cementing a VPH grating between a pair of symmetric prisms.

Within a typical grism, the grating provides most of the dispersive power. One contribution of the grism prism(s) is to provide a more uniform order spacing across the spectral format than the grating alone would provide. Another advantage is that, through appropriate setting of the prism angles, one wavelength can travel undeviated through the grism. This offers several advantages: the ability to interchange different grisms; mechanical simplification of the opto-mechanical components; and simplification of the alignment of the spectrograph.

As shown in Figure 2.27, for a spectrograph with a VPH grating as a cross-disperser, the grating, camera and detector would need to be set to accommodate the beam deviation caused by the grating. If at some future time a grating with a different line density was required (Figure 2.27b), not only would the grating angle have to change, but the camera and detector would need to pivot about the grating centre. Such a scenario would require complex mechanical mounts for the grating, camera and detector.

(a) 600 lines/mm (b) 900 lines/mm

Figure 2.27: When employing a VPH grating, changing to a different grating requires the grating to rotate, and also the camera and detector system to rotate about the centre point of the grating.

A mechanically simpler approach is to design the spectrograph and mounts for a zero-deviation situation, where the grism, camera and detector all lie on the same line. To achieve this, each grating is mated with a unique set of prisms, which have been designed to allow the central wavelength to pass straight through the prism. With this approach, a change in grating line density is matched by a change in prism angle. This leads to a different amount of dispersion, but the central wavelength remains undeviated (as shown in Figure 2.28).

The nominal KiwiSpec optical layout, employing a VPH grism for cross-dispersion, is shown in Figure 1.1. Figure 2.29 shows the nominal prototype spectral format.

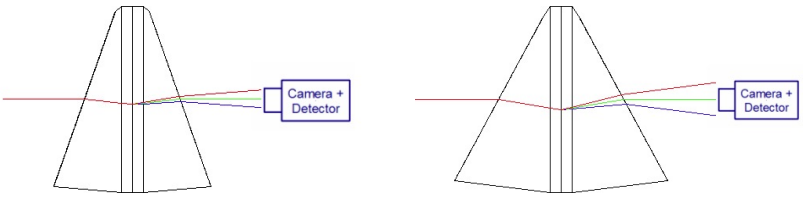

(a) 600 lines/mm (b) 900 lines/mm

Figure 2.28: With the VPH grism approach, each VPH grating has a unique set of symmetrical prisms cemented to the grating. With this arrangement, one VPH grism can be changed for another, and the mechanical mountings of the camera and detector do not need to change. Note that dispersion is also occurring within the grism prisms. However, the prismatic dispersion is much less than the dispersion of the VPH grating, and hence is not visible at the scale of this figure.

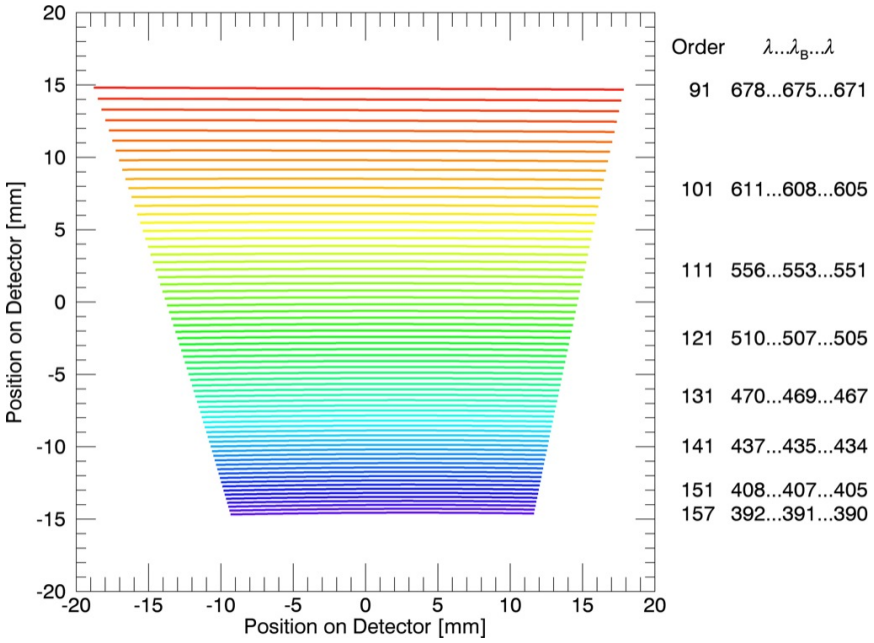

Figure 2.29: The KiwiSpec spectral format with a VPH grism for cross-dispersion.

2.16 Efficiency

The intensity profile of light diffracted from a grating can be approximated by the combination of an interference function (due to the contributions of all illuminated grooves) and a blaze function (equivalent to the diffraction pattern of a single groove). The combined effect is that the blaze function modulates the intensity of the interference function, and as such sets the efficiency profile within a given diffraction order. Intensity profiles of this modulating effect are typically given in introductory optics texts, such as Pedrotti and Pedrotti (1993).

For a collimated beam incident on a grating of equally spaced grooves, the normalized intensity can be expressed in terms of the interference function (IF) and the blaze function (BF):

$$I = \mathrm{IF} \cdot \mathrm{BF} = \left(\frac{\sin N\nu'}{N \sin \nu'}\right)^2 \cdot \left(\frac{\sin \nu}{\nu}\right)^2, \tag{2.59}$$

where ν' is half of the phase difference between the centres of adjacent grooves:

$$\nu' = \frac{\pi}{\lambda G}(\sin \alpha + \sin \beta), \tag{2.60}$$

and ν is the phase difference between the centre and edge of an individual groove:

$$\nu = \frac{\pi f}{\lambda}(\sin \alpha + \sin \beta). \tag{2.61}$$

Given that the interference function is modulated by the blaze function, when investigating the intensity profile within an order one can focus on the blaze function only, and ignore the contribution of the interference function.

For a blazed grating, the parameter ν is modified to include the tilt of the grooves, θ_B:

$$\nu = \frac{\pi f'}{\lambda}(\sin(\alpha - \theta_B) + \sin(\beta - \theta_B)), \tag{2.62}$$

where the parameter f' is the effective facet size and is given by:

$$f' = \frac{f \cos \alpha}{\cos \theta}. \tag{2.63}$$

This parameter accounts for the shadowing effect caused by adjacent grooves, which results in the effective facet size becoming smaller than the actual facet size (as shown in Figure 2.30). Through Equation 2.62, this decrease in facet size leads to a broadening of the blaze function profile with increasing θ values (Schroeder and Hilliard, 1980).

The above equations were investigated to calculate the blaze functions of gratings employing various values of R, G, θ and γ. The results, shown in

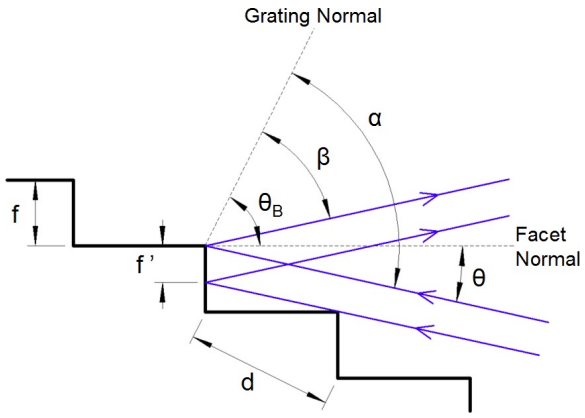

Figure 2.30: The shadowing effect of adjacent grooves results in an effective facet size (f') that is smaller than the actual facet size (f). Adapted from Schroeder (2000)

Figure 2.31, illustrate how the efficiency of an échelle grating changes with different R and θ values (the parameters G and γ do not affect the peak intensities). Within the figure, the individual blaze functions with non-zero θ values have been normalized (by area) against the blaze function of same order with the grating in the Littrow configuration.

This figure shows that as θ increases away from the Littrow configuration the efficiency profile changes, and the intensity profile becomes less concentrated within the free spectral range of the blaze wavelength. Therefore, the average intensity of a given order is lowered as more of the light is transferred from the centre to the wings of the blaze function, which are located in neighbouring orders (an effect also noted by Walker and Diego (1985) and Schroeder (2000)). As a measure of this change, shown on each sub-plot for the central order is the percentage of the area under the curve that lies within one blaze wavelength free spectral range.

Note that some of the light in neighbouring orders can be recovered by co-adding orders when the continuous spectrum is generated during reduction. However, this is not an ideal situation as: the light is then collected by more pixels than necessary (with each pixel contributing readout noise); each co-added section of the different orders will have differing dispersions (complicating the reduction procedure); and co-adding relies on there being considerable overlap in wavelength coverage on the detector (which necessitates a larger, more expensive detector than would otherwise be required).

Horizontal dotted lines on the sub-plots of Figure 2.31 provide a reference for the cross-over points of the blaze functions for the Littrow configuration. Of note is that for the R2, $\theta = 6°$ case, the intensity at the FSR boundary is higher than for the Littrow configuration. Walker and Diego (1985) investigated this further and found that for an R2 grating this effect was greatest at $\theta = 4°$. However, although this $\theta > 0$ effect has the benefit of producing a smaller intensity change across a FSR, it comes at the undesirable cost of lower average efficiency for the entire order (compared to the Littrow case). The R4 grating, for the same $\theta = 6°$ value, does not display an equivalent

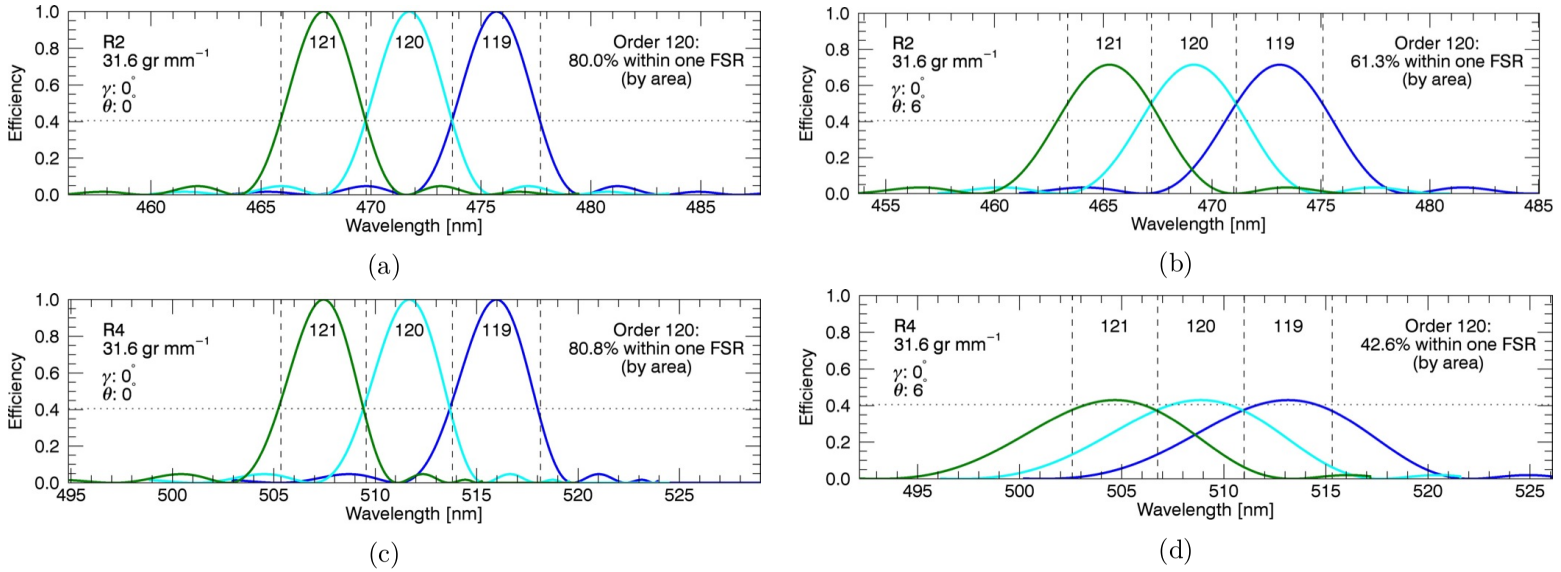

Figure 2.31: How the efficiency within an échelle diffraction order is affected by R-number and θ value. Dashed vertical lines indicate the free spectral range (FSR) for the blaze wavelengths of the indicated orders, and the horizontal dotted line provides a reference for the blaze function crossover points in the Littrow configuration. The orders within the plots on the right ($\theta = 6°$) have been normalized by area against the same orders within the plots on the left ($\theta = 0°$). The (further) reduction of efficiency owing to the grating's aluminium coating is not accounted for here.

intensity increase at the FSR boundary.

Also evident from Figure 2.31 is that R4 gratings are twice as sensitive to this θ-based efficiency loss than R2 gratings (also noted by Hearnshaw (2009)). Therefore, while R2 gratings can tolerate θ values of several degrees, (for example: UCLES, 6° (Walker and Diego, 1985); HERCULES, 3° (Hearnshaw et al., 2002)), R4 gratings require a much smaller Littrow angle (i.e. for KiwiSpec, $\theta = 0.1°$).

The above has assumed that $\theta > 0$ (i.e. $\alpha > \beta$), however, it is also possible for the échelle to be positioned so that $\theta < 0$ (i.e. $\alpha < \beta$). The two cases are described in detail in Schroeder and Hilliard (1980). As shown schematically in Figure 2.32, when $\theta < 0$, part of the incoming light beam strikes the step before the facet. It then undergoes reflection from the aluminized step surface, reflects again from the facet, and is then lost to the system. For this reason, the $\theta > 0$ situation is the preferred case as it offers the higher efficiency of the two scenarios.

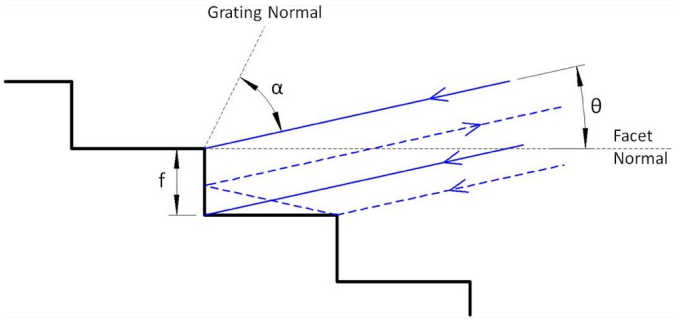

Figure 2.32: When $\theta < 0$, a percentage of the incoming light is lost by reflection from the step and facet, as represented by the dashed raypath. Adapted from Schroeder and Hilliard (1980)

2.17 Comparison between R2 and R4 échelles, and échelles with different groove densities

As the majority of échelle-based astronomical spectrographs are built around R2 or R4 gratings, a comparison between the two grating types is warranted.

A convenient comparison between the properties of R2 and R4 échelle gratings is provided by Figure 2.33. The spectral formats within the figure were produced by changing only the échelle properties within the nominal KiwiSpec Zemax model. Therefore, all are displayed with the same cross-dispersion parameters (725 line/mm VPH grism), camera focal length (150 mm) and detector size. The wavelength range is also the same for each subfigure.

Moving vertically between subfigures, that is, from an R2 grating to an R4 grating with the same line density, the spectral formats show that the dispersion of the grating is doubled. This comes directly from the equation for the angular dispersion of a diffraction grating (Equation 2.14). Note that between Subfigures 2.33a and 2.33c, (and also between Subfigures 2.33b

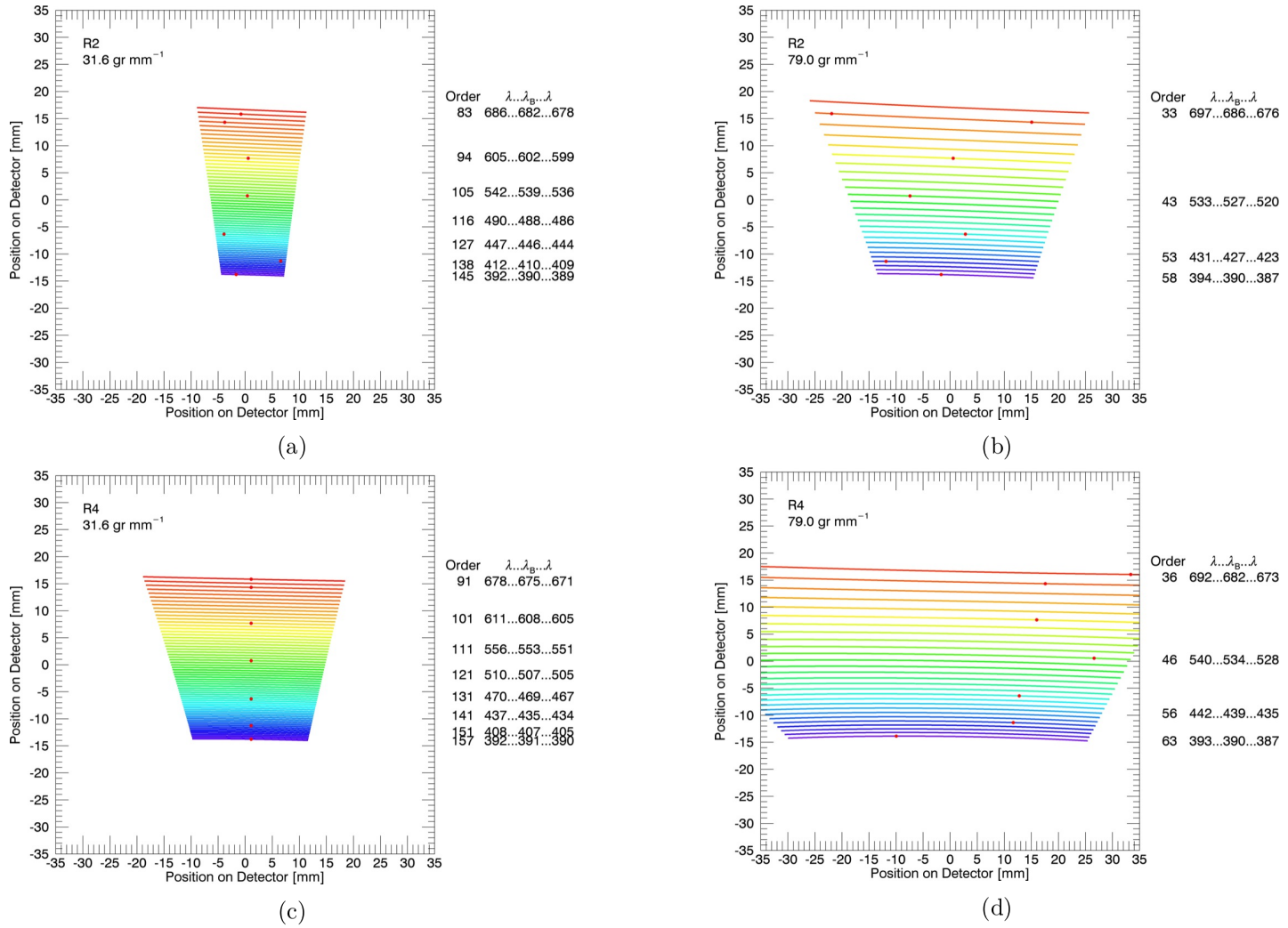

Figure 2.33: Zemax-generated spectral formats of the KiwiSpec prototype with different échelle grating parameters (indicated in the top left corner of each subfigure). Each of the subfigures was generated using the same cross-dispersion parameters (725 line/mm VPH grism), camera focal length (150 mm) and detector size to facilitate direct comparison. The wavelength range is also the same for each subfigure. The red dots within the subfigures indicate the positions of several blaze wavelengths of the nominal KiwiSpec design.

and 2.33d), the free spectral ranges have remained approximately the same (although the wavelengths have been placed in slightly different diffraction orders).

While the increase in angular dispersion increases the resolving power of the instrument, it also impacts the optical design of the spectrograph. The doubling of angular dispersion (when going from an R2 to an R4 grating) may mean that simpler camera designs are no longer acceptable options, as they cannot achieve adequate performance with respect to aberrations or distortion given the larger input field angles. Therefore simpler camera designs such as an achromatic doublet or a Schmidt camera would need to be replaced by complex, multi-element dioptric camera designs.

Another factor to consider with respect to the angular dispersion difference is the camera focal length. Given that an R4 grating has twice the angular dispersion of an R2 grating, the grating has done more of the dispersive 'work'. Therefore, to achieve the same linear dispersion on the detector, the camera in an R4 spectrograph would require half the focal length of the camera in an R2 instrument. This is shown mathematically by Equation 2.18.

Given the resolving power equation, (Equation 2.40), with other factors being equal, the collimated beam diameter in an R4 instrument is half the diameter of the beam in an R2 instrument of the same resolving power. Also, given Equation 2.47, all other factors being equal, an R4 grating will require a smaller focal length camera than an R2 grating to meet the Nyquist requirement. These two points indicate that R4 instruments are typically smaller than R2 instruments, which can have important implications in terms of instrument size, stability, mass and cost.

As was shown in Section 2.16, an R4 grating is more sensitive to efficiency losses caused by facet shadowing when $\theta \neq 0$. For a given non-zero θ value, the efficiency curve of an R4 order will be twice as broad as an R2 grating. Therefore R4 gratings must be used at small θ values, which generally means that out-of-plane angles ($\gamma > 0$) must be employed to separate the incoming and outgoing beams from the échelle grating.

The implication, however, of using non-zero γ angles is that the line tilt increases. As given by Equation 2.52, an R4 grating has twice the line tilt of an R2 grating, which may make the reduction of an R4 échelle spectrum more difficult.

Figure 2.33 also shows how the spectral formats of R2 and R4 gratings change with different groove densities. The subfigures on the left of the figure have groove densities of 31.6 grooves/mm, whereas those on the right have groove densities of 79 grooves/mm.

While at first glance it appears that the linear dispersion for the 79 grooves/mm gratings are about twice that of the 31.6 groove/mm gratings, what has actually occurred is a change in the length of the free spectral range of the échelle orders. This is expressed by Equation 2.25, and is also

evident by the wavelength list to the right of the spectral formats within the figure. Between the two groove densities, for each grating type the dispersion remains approximately the same through the mG factor of Equation 2.11, as the order numbers and grating groove density have changed in step.

A benefit due to the increase in the FSR is that the inter-order spacing is larger (Equation 2.55). This could be advantageous for spectrographs with prism cross-dispersers as some of the cross-dispersive 'work' is removed from the prisms. However, the longer free spectral range of a 79 groove/mm grating would require a larger (and therefore more expensive) camera and/or detector than a 31.6 groove/mm grating.

Chapter 3

Optical Design Aspects

3.1 Introduction

Within this chapter, several miscellaneous aspects of the KiwiSpec optical system will be discussed.

3.2 Asymmetry Factor

As introduced in Chapter 1, the KiwiSpec optical design is based on the asymmetric white pupil concept. This section will explore the implications of the amount of asymmetry between the focal lengths of the primary and secondary collimator mirrors.

Combining Equations 2.18 and 2.19, the (quasi-Littrow) linear dispersion of the KiwiSpec design is given by:

$$\frac{1}{P} \simeq \frac{2 \tan \theta_{\mathrm{B}} f_{\mathrm{KiwiSpec.cam}}}{\lambda_{\mathrm{blaze}}} \frac{f_{\mathrm{p.coll}}}{f_{\mathrm{s.coll}}}. \tag{3.1}$$

Within this equation the left-hand side represents the linear dispersion of a traditional spectrograph, whereas the right-hand side includes the asymmetry factor, or the ratio between the focal lengths of the two collimator mirrors ($\frac{f_{\mathrm{p.coll}}}{f_{\mathrm{s.coll}}}$). Arranging the equation in this way clearly shows how the asymmetry factor influences the amount of linear dispersion at the detector. The KiwiSpec design has an asymmetry factor of 3, and therefore the linear dispersion is three times that of an equivalent symmetric design.

Figure 3.1 shows layouts and spectral formats for three variations on the KiwiSpec design. All of the optical layouts and spectral formats are shown at the same scale for direct comparison. Figure 3.1a shows the nominal, asymmetric prototype design, Figure 3.1b shows a symmetric variation employing the same cross-disperser and camera focal length as the nominal design, and Figure 3.1c is a symmetric design with the cross-disperser power and camera focal length adjusted to generate a spectral format equivalent to the nominal design.

Immediately obvious in the figure is the larger mechanical footprint of the symmetric design. Another disadvantage of that design is the larger beam diameter following the secondary collimator mirror (requiring larger aperture optics for the cross-disperser and camera).

An analysis of Equation 3.1 shows that in order for an equivalent sym-

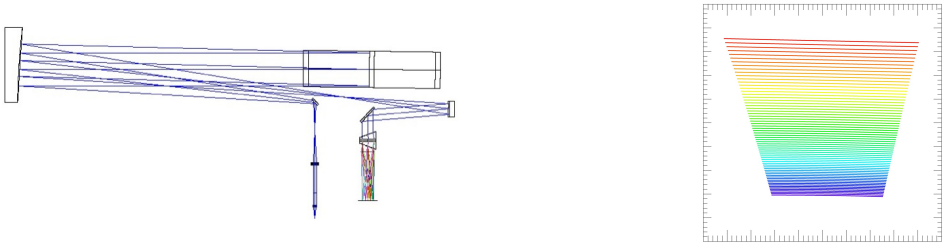

(a) The nominal KiwiSpec design, with 3:1 asymmetry, a 150 mm FL camera and a 725 line/mm grating within a grism for cross-dispersion.

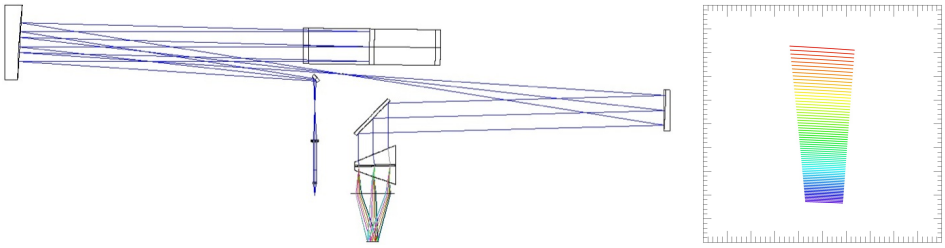

(b) A symmetric KiwiSpec variation, with a 150 mm FL camera and a 725 line/mm grating within a grism for cross-dispersion.

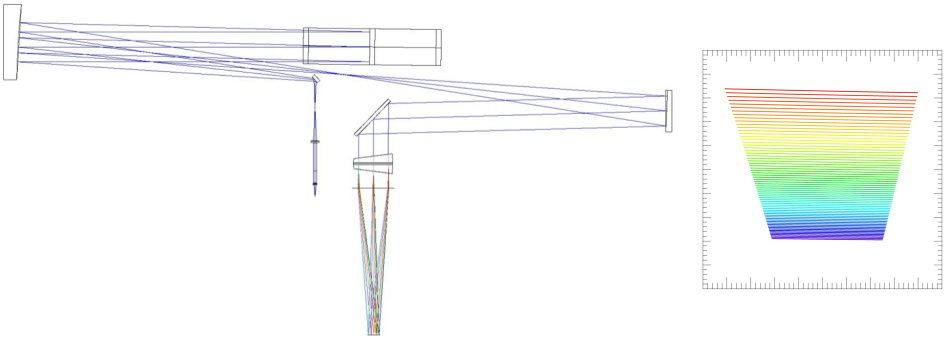

(c) Another symmetric KiwiSpec variation, but modified to have the same spectral format as the nominal KiwiSpec design in Figure 3.1a. The instrument then requires a 450 mm FL camera and a 241.7 line/mm grating within the grism for cross-dispersion.

Figure 3.1: Three variations of the KiwiSpec design, with different asymmetry factors, camera focal lengths, and cross-disperser powers. All three optical layouts are shown at the same scale for direct comparison. As well, all three spectral format figures are plotted the same scale, and show the same wavelength ranges for direct comparison.

metric design to achieve the same linear dispersion as the nominal asymmetric design, the camera would need to have a focal length three times longer. However, given Equation 2.55, this would also increase the cross-dispersion linear dispersion by a factor of three. Therefore, to achieve the same spectral format of the asymmetric KiwiSpec design, within a symmetric instrument the camera would require three times the focal length and the cross-disperser would need to have three times less dispersive power. A KiwiSpec variation with these parameters is shown in Figure 3.1c.

However, the increase in linear dispersion of the asymmetric design comes at the cost of increased divergent field angles for the monochromatic beams incident on the spectrograph camera (see Figure 1.2). The increase goes in step with the asymmetry factor, so that a 3:1 design has three times the field angle values at the camera than an equivalent symmetric design. For the nominal KiwiSpec design, this means maximum divergent half-field angles at the camera of approximately 9°. Such field angle values have implications in that the camera design probably needs to be a more complex all-refractive system in order to minimize aberrations and deliver acceptable image quality.

3.3 Input Relay

The input relay converts the approximately f/4 beam leaving the fibre to an f/10 focus at the entrance slit through a telecentric relay. A schematic of the optical layout is shown in Figure 3.2.

The relay also contains the vacuum chamber window, which is a plane-parallel optical window made of fused silica. The window is tilted at an angle to direct light towards the exposure meter (which will be described more in Section 5.6.3 and Chapter 8). Although the window has no optical power, as shown in Figure 3.2, its 20° tilt causes a slight lateral offset in the beam from the optical axis.

The relay was designed assuming 5 per cent fibre FRD, or a conversion from f/4.5 at the fibre input to f/4.29 at the fibre exit. A 10-mm diameter collimated beam was decided on, which then set the focal lengths of the two lenses at approximately 40 mm and 100 mm. As a performance compromise in favour of expediency and cost, for the prototype this relay was designed to utilize a pair of off-the-shelf doublets. A survey of lenses avail-

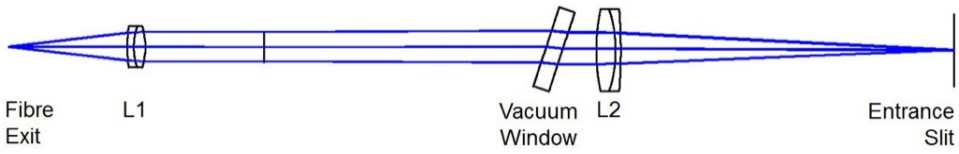

Figure 3.2: The KiwiSpec prototype input relay.

able from major manufacturers was undertaken, with the goal of finding a pair of stock lenses that, when combined, produced minimal aberrations. The most difficult design aspects were: finding a pair of doublets that minimized chromatic aberration (and spherochromaticism); and maintaining reasonable throughput below 400 nm. Although wavelengths below 420 nm are outside of the prototype's nominal wavelength range, they were investigated with a thought to the future (where a second channel might extend the prototype's wavelength range further into the blue/UV). The 40 mm lens proved to be most difficult in this regard, where the short focal length apparently attracted the stock lens' designers to choose 'flinty' glasses with poor blue transmission.

In the end a pair of stock lenses were found to give adequate performance for testing the prototype. As seen in the spot diagram in Figure 3.3a, best focus is a compromise with respect to wavelength. Given a future redesign, this is certainly a system that could benefit from custom lenses, which might each require three elements to help control the chromatic aberration.

Shown in Figure 3.3b is the Zemax (synthetic) image produced by the relay with a 100-μm, evenly illuminated fibre at the input. Given the relay magnification equation (Equation 1.2), the size of the image is magnified 2.5 times, as verified by the scale of the figure. Therefore, the relay generates a source image for the spectrograph which is 2.5 times larger than the fibre end, which causes a corresponding decrease in wavelength resolution. In a future version of KiwiSpec, a custom-designed and optimized relay system could give improved image quality and hence lead to a higher resolving power (assuming no slit) or higher throughput (for a given slit or pinhole).

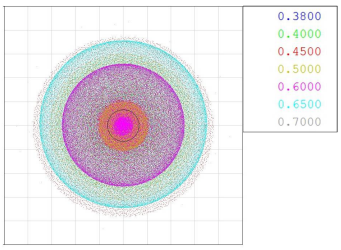

(a) The on-axis polychromatic spot diagram for the input relay. The square represents 100 μm on each side.

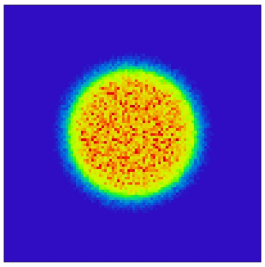

(b) A synthetic image of a uniformly illuminated 100 μm fibre end as formed by the input relay. The square represents 0.5×0.5 mm.

Figure 3.3: Image quality-related diagrams for the KiwiSpec prototype input relay.

3.4 Optical Fibres

This section investigates the choice of optical fibre length and diameter, which have implications with respect to efficiency and resolving power.

For the prototype instrument, 100-μm Polymicro FBP fibres were chosen. The fibres used were 30 m long, which was the length required for the telescope-spectrograph distance at Mt John University Observatory during the on-sky testing period.

3.4.1 Effect of Fibre Length on Efficiency

In any fibre-fed spectrograph, fibre length should be kept as short as possible, as the UV and blue wavelength throughput rapidly decreases with increased fibre length. Red wavelengths are also affected, but not to the same degree. These effects are shown in Figure 3.4.

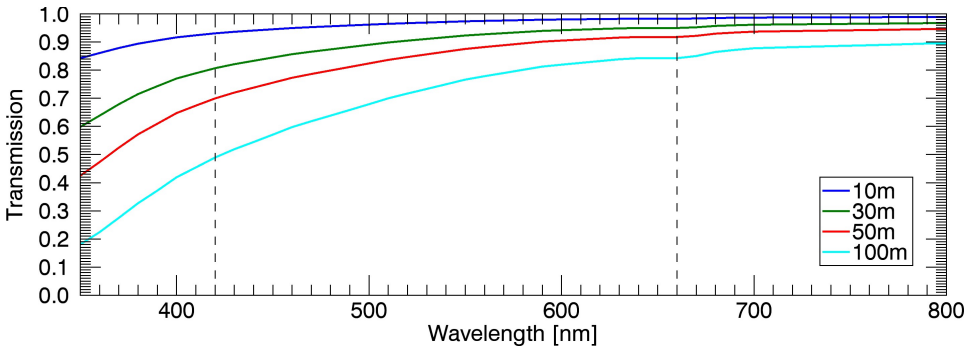

Figure 3.4: Spectral transmission of Polymicro FBP fibres for several fibre lengths (based on Polymicro transmission data). The dashed vertical lines represent the wavelength range of the KiwiSpec prototype.

3.4.2 Effect of Fibre Diameter on Efficiency

Ideally all of the light that a telescope collects from an object will make its way into the fibre at the telescope focal plane. For this to occur, the telescope focal length, telescope auxiliary optics, atmospheric seeing and the diameter of the fibre all need to be taken into consideration.

The native telescope focal length (and hence the image scale at the focal plane) can be modified through the use of auxiliary optical systems. These might include focal extenders/reducers, atmospheric dispersion correctors, fibre feed relays or microlenses. In general, the diameter of the fibre is chosen to match the image scale at the telescope system focal plane for a median seeing value, while the f/ratio of the system is chosen to match the FRD characteristics of the fibre and the expected f/ratio at the output end of the fibre. A constraint on the design is that (non-custom) optical fibres are only available in certain diameters (usually 50 μm, 100 μm, 200 μm, 300 μm etc.).

Figure 3.5 shows the effect of not optimizing the fibre diameter to the telescope system. The figure shows the result of using a 100-μm fibre on telescopes of various apertures and focal lengths, and the large efficiency losses that can result.

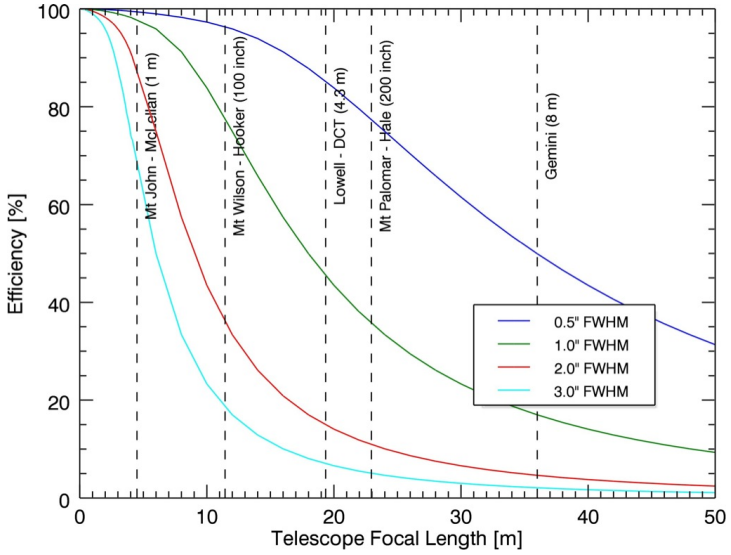

Figure 3.5: How the percentage of light entering a 100-μm fibre changes with telescope focal length. Curves for 4 different seeing conditions are shown, which are based on a modified Moffat function (as will be described in Section 7.3.3). The f/4.5 focal lengths of several well-known telescopes are included for reference (which assumes that auxiliary optics convert the telescope focal ratio to f/4.5 before light enters the fibre).

3.4.3 Effect of Fibre Diameter on Resolving Power

At the spectrograph, if the end of the fibre represents the entrance slit of the spectrograph, the choice of fibre diameter affects the resolving power of the instrument. As the spectrograph creates monochromatic images of the fibre exit at its focal plane, changing the size of the fibre changes the size of this resolution element. As such, larger fibres lead to larger resolution elements and lower resolving powers. The change in average resolution element size (measured by the FWHM, or full width half maximum) and resolving power for four common fibre diameters used with the KiwiSpec prototype is shown in Figure 3.6.

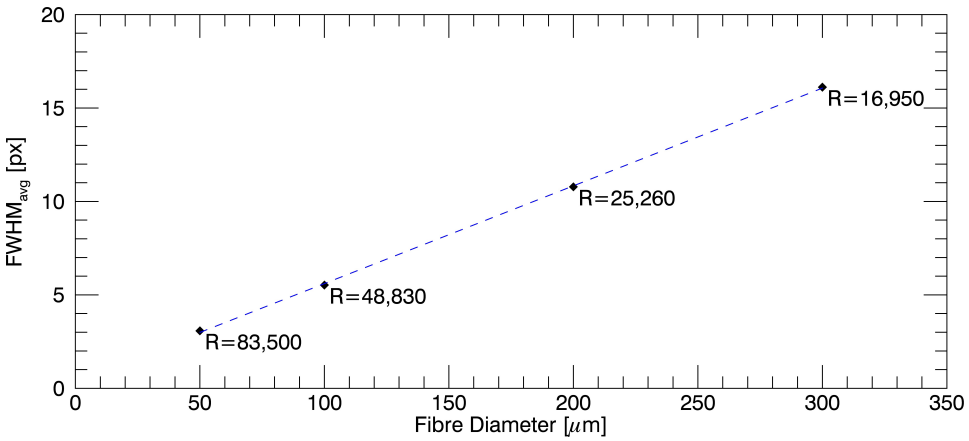

Figure 3.6: How the FWHM_{avg} (and also resolving power, R) are affected by a change in fibre diameter in the KiwiSpec prototype design. This plot is based on measurements of synthetic resolution elements generated within Zemax. Thirty-five resolution elements located across the spectral format were measured to determine their average FWHM value (this method will be described in more detail in Section 4.2.2). For the corresponding resolving powers displayed on the plot, only the central resolution element in the spectral format was used (and the element was only measured in the échelle dispersion direction).

3.5 VPH Order Contamination

To investigate the potential for stray light contamination by VPH orders adjacent to the VPH blaze order, a Zemax script was written to step through many wavelengths within a range of VPH and échelle orders, and to plot the resulting raypaths. VPH orders −2 to +3 were investigated, and for each VPH order the échelle orders 60–182 were analyzed (corresponding to wavelengths from 1 μm–336 nm). Eleven separate wavelengths were included per échelle order, which were evenly spaced across twice the free spectral range of each order. At the blue end, 336 nm became the lower boundary wavelength as dispersion data were not available below that for the glass types used. For each VPH order, the script generated 122 output diagrams of the camera arm (i.e. one diagram per échelle order). These plots were then manually inspected to see which wavelengths were able to enter the Hasselblad, make it through the Hasselblad, or make it through the CCD window. Also monitored were potential areas for stray light propagation, such as light reflecting or scattering from lens edges.

Note that this technique does not represent a rigorous stray light analysis, but rather a first-order look at which wavelengths can get through the camera optics via refraction (i.e. scattering effects are not included as they cannot be modelled in sequential Zemax).

Although the Hasselblad lens used within the prototype cannot be modified, employing this approach on a future custom camera lens would guide the opto-mechanical design of the lens barrel. Within the camera, stray light strikes many places (i.e. spacers, internal walls, lens edges) that could reflect diffusely and lead to an overall 'fogging' of the detector. Therefore, proper baffling within the camera barrel is very important to constrain this stray light, and this analysis can indicate areas requiring baffles, light traps, edge blackening, etc.

The results are shown in Figures 3.7 to 3.12 and summarized in Table 3.1. Note that the central band of rays in the figures is an artefact of the ray distribution employed to generate the layouts.

The results indicate that for the prototype design, no light of great intensity directly reaches the CCD from adjacent VPH orders – a result that was confirmed in practice with the prototype instrument.

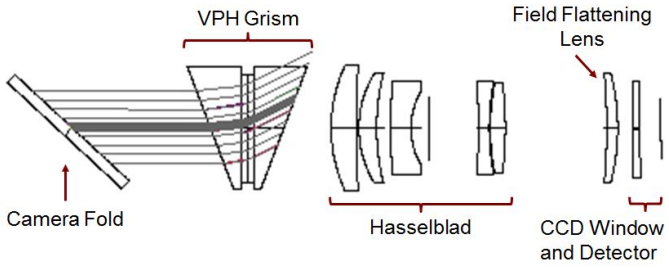

Figure 3.7: VPH Order -2: No concern; light does not enter Hasselblad.

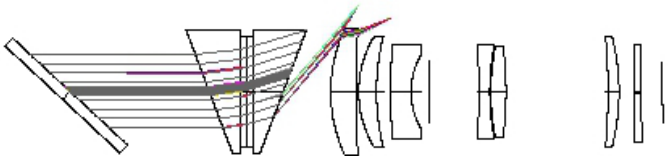

Figure 3.8: VPH Order -1: Light from échelle orders $m > 182$ ($\lambda_B < 337\,\text{nm}$) enters the Hasselblad. However, this is of little concern as the VPH grating is blazed for first order, and all coatings within the system have low efficiencies at such wavelengths.

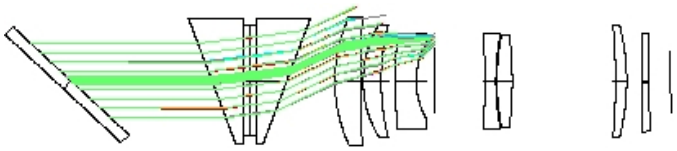

Figure 3.9: VPH Order 0: All échelle orders make it through to the Hasselblad's internal stop, but not past.

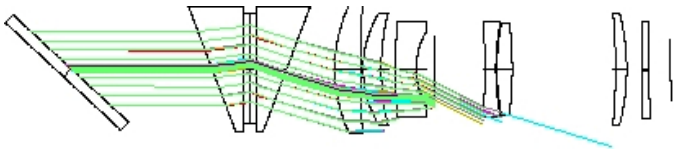

(a) VPH Order 1: light from échelle orders $m > 69$ ($\lambda_B < 890\,\text{nm}$) gets through the Hasselblad. Situations such as this call for proper baffling within the camera barrel, as well as painting all lens edges black to minimize reflected light from the finely ground edges of lenses.

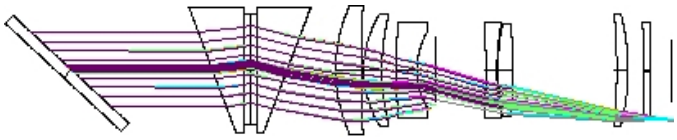

(b) VPH Order 1: Light from échelle orders $83 < m < 182$ ($740\,\text{nm} > \lambda_B > 337\,\text{nm}$) gets through the CCD window.

Figure 3.10: VPH Order 1: Two scenarios of concern for stray light. Being the blaze order, stray light from light within this order is of the highest concern.

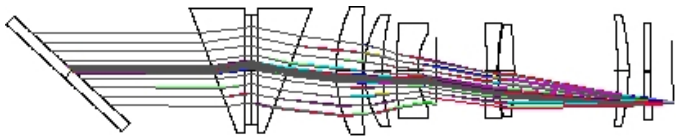

Figure 3.11: VPH Order 2: Échelle orders $m > 177$ ($\lambda_B < 347\,\text{nm}$) reach the edge of the detector. This would be hard to control with stray light baffles because of the short free spectral range of these orders. However, all of the coatings used have very low efficiency at 350 nm. Additionally, the VPH grating is blazed for the first order, meaning greatly decreased throughput within the second order. The end result is that any light that does get through to the detector will be of very low intensity.

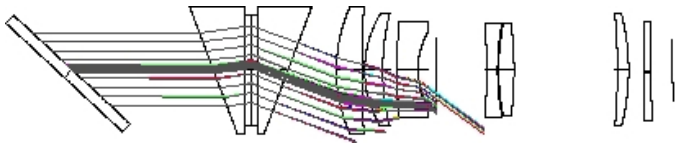

Figure 3.12: VPH Order 3: By échelle order 171 ($\lambda_B = 359\,\text{nm}$) light is getting through the Hasselblad stop. However, none of the light from this VPH order makes it into the rear lens group of the Hasselblad. Nonetheless, this situation calls for baffles or a grooved surface between the stop and rear group to prevent light from reflecting and propagating through the system.

Table 3.1: Summary of the investigations into stray light contamination by VPH orders adjacent to the blaze order.

Order	**Comments**
-2	No effect; light does not enter Hasselblad.
-1	Light just makes it into the Hasselblad.
0	Light gets to the Hasselblad stop, but not beyond.
1	The blazed VPH order: wavelengths from 337 nm to 738 nm get through the CCD window.
2	$\lambda < 388\,\text{nm}$ gets through the CCD window; $\lambda < 346\,\text{nm}$ gets to the detector. However, this light should be of very low intensity as the efficiency curve of every surface 'conspires' against it.
3	$\lambda < 359\,\text{nm}$ gets through the Hasselblad stop, but does not enter the rear lens group.

3.6 Calibration Lamp System

In order to provide calibration light from white light and thorium-argon lamps, the calibration system shown in Figure 3.13 was developed. Optically it consists of a telecentric relay with an input 'arm' for each lamp. For the thorium-argon arm, a 100-mm FL lens collimates the light from the lamp, which then passes straight through a beamsplitter before being focused on the fibre input by a 50-mm FL lens. For the white light arm, a parabolic torch reflector collimates the light from the lamp, which then passes through a 'top-hat' diffuser to generate a beam of uniform intensity. The diffused, collimated beam then reflects through 90° via the beamsplitter, and is then focused onto the fibre input by the same lens used by the thorium-argon arm.

Also included is a shutter within the thorium-argon arm, which allows the lamp to remain on while not in use (for lamp stability reasons). As well, a colour-balancing filter wheel is shared by both arms and contains filters of BG34, BG38 and BG39 glass. As their name suggests, these filters are used to balance the intensity of wavelengths output by the calibration lamps (by reducing the intensity towards the red wavelengths). Both the filter wheel and the shutter (as well as the on/off states of each lamp) are controlled via the KiwiSpec control software.

The system focuses the calibration light onto a 300-μm fibre, which in practice would travel from the calibration lamp system to the fibre feed on the telescope. In this way the calibration light would be injected into the science fibre at the telescope focal plane. From a stability perspective, this is the preferred situation, as then the starlight and calibration light traverse the same path through the science fibre and the spectrograph.

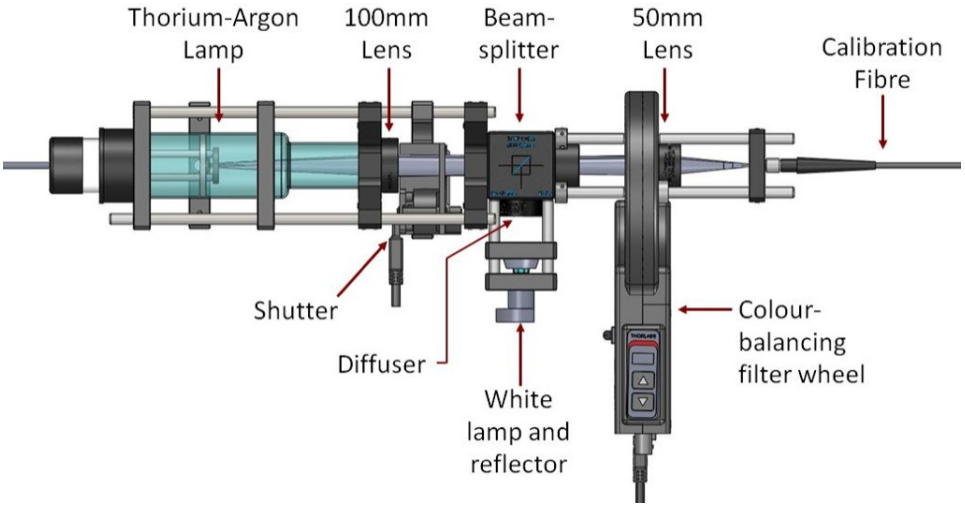

Figure 3.13: Schematic diagram of the calibration lamp system.

Chapter 4

Tolerancing

4.1 Introduction

Tolerancing is an essential step in the design of any optical system. The goal of a tolerancing study is to determine how sensitive a nominal design is to typical fabrication and alignment practices, for both optical and mechanical components.

Specifying reasonable and achievable tolerances on fabricated optical and mechanical components has the advantages of lower costs, shorter lead times and less risk of cost or time overruns. As well, the tolerancing results directly feed into the opto-mechanical design, as they give the required specifications for the number of degrees of freedom, amount of movement and adjustment accuracy required for each optical mount.

Two different tolerancing studies are described in this chapter. The first considers the fabrication, assembly and alignment of the entire spectrograph. The second study considers the construction parameters of the iodine cell.

The material presented in this chapter has been influenced by the work of Smith (2005), Smith (2007), Fischer et al. (2008), Lee et al. (2010) and the online Zemax 'Knowledge Base' [1].

4.2 Tolerancing of the KiwiSpec Prototype

The single-channel prototype configuration was toleranced, including the input relay and vacuum windows. Also included was a dichroic beamsplitter, which could be placed just before the camera fold mirror to direct light towards a second channel (which is a potential future upgrade for the prototype instrument).

The internal parameters of the Hasselblad lens were not toleranced as part of this study. As the actual internal optical and mechanical construction of the lens is not known, tolerancing the lens would not result in meaningful or applicable results. However, the positional tolerance of the entire Hasselblad lens was considered.

[1] `http://kb-en.radiantzemax.com/Knowledgebase/27`

4.2.1 Wavelength Sampling

During the tolerancing process, 35 wavelengths were used to monitor the effects of the tolerance perturbations on image quality and the position of the spectrum on the detector. The wavelengths were chosen to ensure good sampling across (and just outside of) the prototype detector in its nominal position. Seven different orders were selected, with five wavelengths equally spaced across one free spectral range within each, as is shown in Figure 4.1. Although there are gaps in the prototype's continuous spectrum redward of approximately 515 nm (as will be described in Section 5.6.12), for the purposes of tolerancing an oversized detector was used in the Zemax model to allow a complete spectrum (out to one free spectral range) to be analysed.

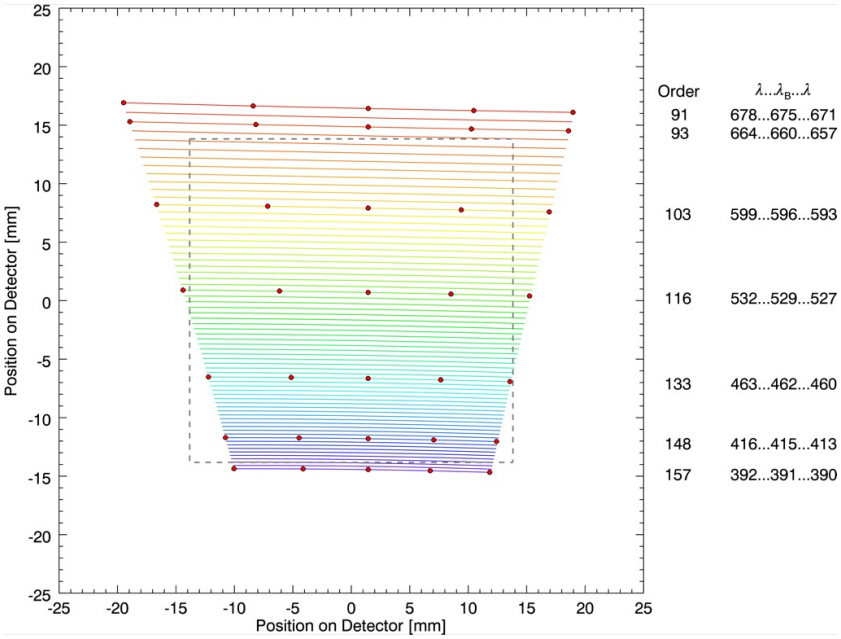

Figure 4.1: The KiwiSpec spectral format showing the wavelengths monitored during the tolerancing study (indicated by filled circles). One free spectral range is plotted for each of the orders 91 to 157, covering 390 to 678 nm. The dashed boundary shows the relative size of the actual detector, whereas the plot is correctly sized for the oversized detector used in the tolerancing study.

4.2.2 Image Quality Assessment

For each wavelength, a spectrograph creates an image of the entrance slit at the focal plane. This image, known as a resolution element, determines the resolution of the instrument as one cannot discern details in a spectrum that are smaller than the resolution element. Therefore, the size of the resolution element is an excellent parameter to monitor during a tolerancing study.

Synthetic resolution element images were created within Zemax using the 'Geometric Image Analysis' feature, which allows one to generate a pixellated image at the focal plane of an extended source. In this case the extended source used was an evenly-illuminated 100 μm circle (representing the full exit face of the fibre in the actual instrument). The nominal Zemax-generated resolution elements for the 35 wavelengths considered are shown in Figure 4.2.

The size of a resolution element is typically described by its full-width-half-maximum, (FWHM). This is measured by fitting a Gaussian curve to the intensity distribution across a resolution element. The standard deviation, σ, of the Gaussian distribution is then used to determine the FWHM through:

$$\mathrm{FWHM} = 2\sqrt{2\ln 2}\,\sigma. \tag{4.1}$$

However, as Zemax does not allow direct computation of the FWHM of a resolution element during a tolerancing analysis, the approach taken was to 'calibrate' a spot size-based merit function for a given FWHM increase. This was accomplished by monitoring the increase in the size of the 35 synthetic resolution elements as the Zemax model was stepped through several defocus positions. For this procedure, 700,000 rays were traced during the generation of each resolution element, as this value was found to give repeatable FWHM values to 0.001 pixels.

For each of the 35 wavelengths monitored, a FWHM value was calculated for each of the spatial and dispersion directions, as shown in Figure 4.3. This method was chosen as it accounts for the asymmetry present in many of the resolution elements owing to anamorphic magnification.

To measure the amount of FWHM increase across the spectrum, a single value, $\mathrm{FWHM_{avg}}$, was calculated for each focus position by taking the average of the dispersion and spatial FWHM for each resolution element, and then an average of all 35 such averages. This calculation is summarized by:

$$\mathrm{FWHM_{avg}} = \sum_{\mathrm{i}=1}^{35} \frac{1}{35}\left[\frac{\mathrm{FWHM(dispersion)_i} + \mathrm{FWHM(spatial)_i}}{2}\right]. \tag{4.2}$$

The results of this calibration process are shown graphically in Figure 4.4, while Table 4.1 lists the actual $\mathrm{FWHM_{avg}}$ values (and percentage increases) within the region surrounding nominal focus.

A best-fit line in the form of an 8^{th}-order polynomial was then fit to these data to allow the calculation of defocus positions based on a given percentage increase in $\mathrm{FWHM_{avg}}$ (lower order polynomials did not accurately match the asymmetric shape of the defocus curve). The results – a correlation between defocus position, $\mathrm{FWHM_{avg}}$, percentage change (from nominal)

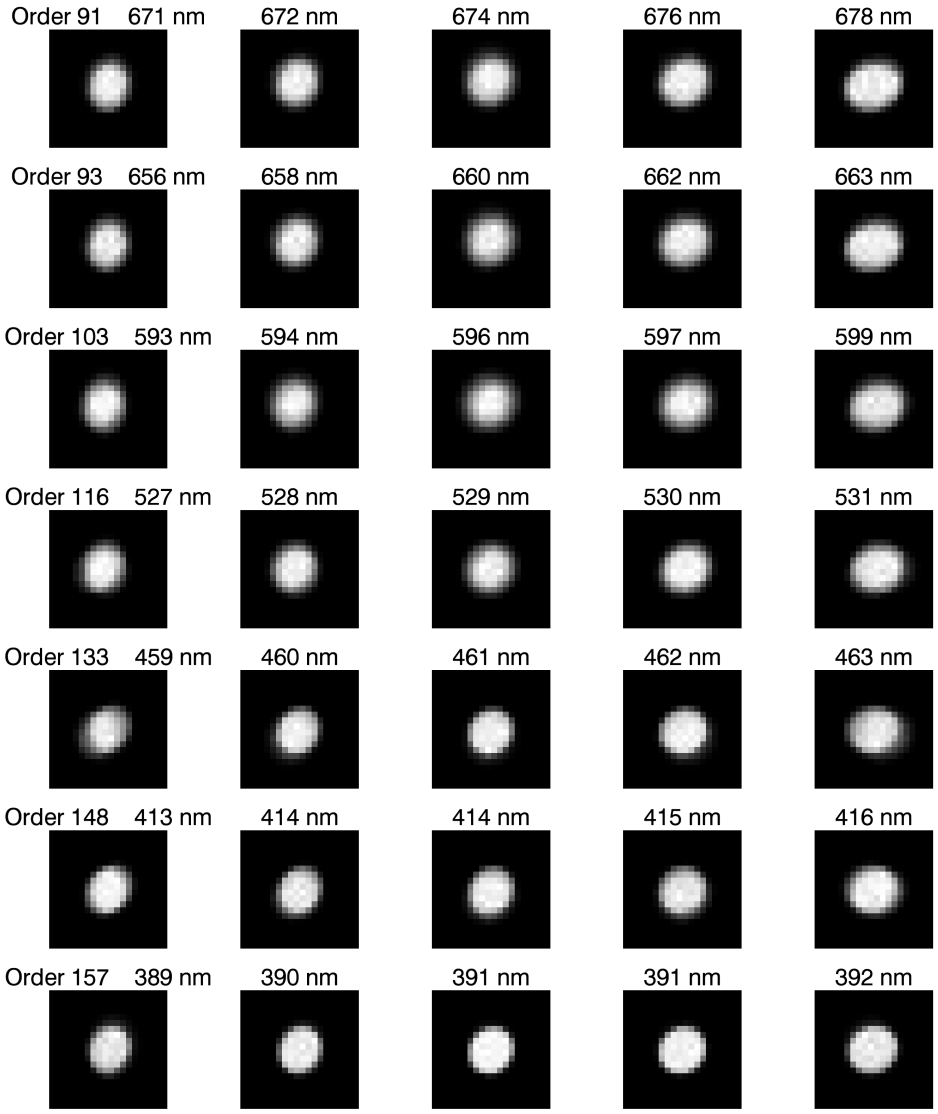

Figure 4.2: The Zemax-generated nominal resolution elements for 35 wavelengths across 7 échelle orders (which are horizontal in the diagram). The pixels in the above images have been sized to match the 13.5 μm square pixels of the KiwiSpec prototype detector.

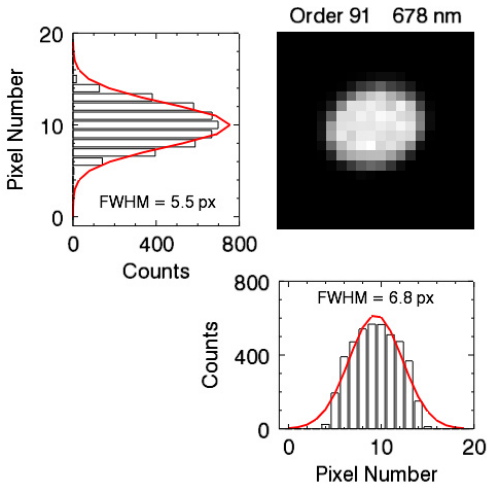

Figure 4.3: Full-width-half-max values were calculated for both the dispersion (horizontal) and spatial (vertical) directions. This particular resolution element, (located at the red end of an échelle order), demonstrates the asymmetry possible in the resolution elements owing to échelle anamorphic magnification and line tilt.

and the increase in the spot size-based merit function – are given in Table 4.2. This table provided the basis for the error budget used during the tolerancing study (to be described in Section 4.2.4).

As an aside, Table 4.2 can also be used to guide the opto-mechanical design of the instrument's focus system. The data presented shows that to change the $\mathrm{FWHM_{avg}}$ value by less than 0.5 per cent during a focus adjustment, the focus motor will need to move the camera along the optical axis in increments smaller than 80 μm per movement. Such a value is easily achievable with off-the-shelf motors and controllers.

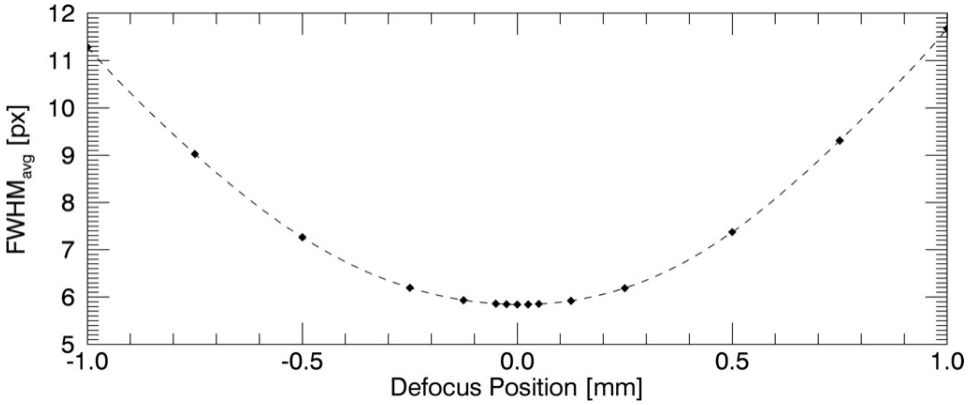

Figure 4.4: Change in the $\mathrm{FWHM_{avg}}$ values (average of the dispersion and spatial direction FWHM values) of 35 resolution elements for several defocus positions on either side of best focus. The dashed line follows the 8^{th}-order polynomial fit to the data.

Table 4.1: $FWHM_{avg}$ values and percentage change from nominal for the region surrounding the nominal focus position. This table contains the same data presented in Figure 4.4.

Defocus Position [mm]	**$FWHM_{avg}$ [px]**	**Change [per cent]**
-0.25	6.195	6.07
-0.125	5.931	1.54
-0.05	5.858	0.28
-0.025	5.847	0.09
0	5.841	0.00
0.025	5.844	0.05
0.05	5.852	0.19
0.125	5.919	1.33
0.25	6.187	5.93

Table 4.2: Increase in $FWHM_{avg}$ for several defocus positions, determined using an 8^{th}-order polynomial fit to the data in Figure 4.4 and Table 4.1. For each defocus position, the final column gives the equivalent Zemax spot size-based merit function increase from that of the nominal focused instrument.

Defocus Position [mm]	**$FWHM_{avg}$ [px]**	**Change [per cent]**	**Merit Function Increase [μm]**
+0.080	5.871	0.5	3.25
+0.110	5.901	1.0	4.43
+0.150	5.957	2.0	6.04
+0.180	6.013	3.0	7.31

4.2.3 Tolerancing Procedure

The first step in tolerancing the system within Zemax was to apply appropriate coordinate breaks for each optical surface, allowing the surface to be perturbed from its nominal state in some manner. Care was taken to avoid duplicate perturbations, and also to ensure that the applied coordinate breaks did not influence the position of other optical elements unexpectedly.

After the coordinate breaks were in place, a table of tolerance operands was constructed. This table contained all parameters that could deviate from their nominal values during either fabrication or alignment of the instrument. Such parameters include element translations and rotations, lens thicknesses and wedge, optical surface irregularities and glass inhomogeneities. For each tolerance operand there is a user-set minimum and a maximum value, representing the tolerance range for that particular parameter.

During the tolerancing process, the minimum/maximum ranges of the individual perturbations were adjusted so that tight tolerances (which would be expensive or difficult to achieve) were relaxed slightly, while easily achievable tolerances were tightened somewhat to maintain a balance at the desired amount of change in the system.

The effect of each tolerance perturbation on the system was determined by monitoring a spot size-based merit function value. To determine the cumulative effect of all tolerance perturbations, the Root-Sum-Squared (RSS) method was employed (Smith (2000) and Schwertz and Burge (2012)), given by:

$$T = \sqrt{t_1^2 + t_2^2 + t_3^2 + \ldots t_n^2}\,, \tag{4.3}$$

where:

T = resulting tolerance;
t = individual tolerance value;
n = number of individual tolerances.

The RSS combination of the separate merit function values (one per toleranced parameter) was calculated and then compared against the $\mathrm{FWHM}_{\mathrm{avg}}$ values shown in Table 4.2. The end result of the tolerancing procedure is a table of values giving the range of allowable variation for each parameter.

During tolerancing of the KiwiSpec design, both Zemax Programming Language (ZPL) and Zemax tolerance scripts were employed. These were preferred over the automated Zemax tolerancing routines as the scripts gave more control and allowed access to a greater number of calculated parameters.

An example of a script used is as follows:

1. For the nominal (unperturbed) case:
   (a) calculate spot sizes for each wavelength;
   (b) calculate centroid positions (x and y) for each wavelength;
   (c) write nominal results to an output file.
2. Then for each tolerance operand in turn:
   (a) perturb parameter to minus value;
   (b) calculate perturbed spot sizes for each wavelength;
   (c) calculate perturbed centroid positions (x and y) for each wavelength;
   (d) perturb parameter to plus value;
   (e) calculate perturbed spot sizes for each wavelength;
   (f) calculate perturbed centroid positions (x and y) for each wavelength;
   (g) write all perturbation results to an output file;
   (h) move to next tolerance operand.

This type of tolerance analysis (where tolerance operands are separately perturbed to minimum and then maximum values) is known as 'sensitivity analysis' within Zemax.

An IDL script was also written to arrange the Zemax output into a more meaningful format. An example output from this script for one tolerance operand (the input fold mirror tilt) is shown in Figure 4.5.

A second type of tolerance analysis was also undertaken within Zemax, known as 'Monte Carlo analysis'. During a Monte Carlo analysis, each tolerance operand is assigned a (statistically constrained) random value which lies between the pre-determined minimum and maximum tolerance values for the operand. Although this approach is most often used with high production number instruments, it has merit as well with one-off designs. The major advantage is that instrument performance can be determined with all variables perturbed simultaneously – as opposed to a sensitivity analysis where only one variable is perturbed at a time. This has obvious benefits given that in reality the detector sees the combination of all errors and perturbations at once.

4.2.4 Error Budget

Given the large number of possible degrees of freedom to tolerance in the KiwiSpec system, during this analysis the individual tolerances were split

```
*************************************************************************************************************
Input Fold   ty (tilt about mirror sfc vertex)   TUTY   sfc#: 38    min: -0.50   nominal: 0.00   max: 0.50

1)  spot sizes after tolerance perturbations:

      Hasselblad position [min]:      0.000000        Hasselblad position [max]:      0.000000
      Detector turn [min]:            0.000000        Detector turn [max]:            0.000000
      Detector tilt [min]:            0.000000        Detector tilt [max]:            0.000000
      Full MF [min]:                0.00154461        Full MF [max]:                0.00132647

                Min [% change]                                  Max [% change]
      107      88     103     120     117             102     114      96      94     101
      107      88     103     121     119             103     114      95      91      99
       92      88     102     119     122             108     114      94      82      91
       96      83      98     115     109              96     116      90      85      92
       96     105      97      84      95              84      85      99     101      95
       94      92      91      96     105              98      97      93      89      98
      123     122     117      99      89              86     103     123     127     118
                                      Max: 123                                        Max: 127

2)  centroid change after tolerance perturbations:

      Hasselblad position [min]:      0.000000        Hasselblad position [max]:      0.000000
      Detector turn [min]:            0.000000        Detector turn [max]:            0.000000
      Detector tilt [min]:            0.000000        Detector tilt [max]:            0.000000
      Full MF [min]:                  0.280794        Full MF [max]:                  0.278175

             Min [pixels]                                    Max [pixels]
      (-37,0)                 (-25,0)                 (36,0)                  (25,0)
                (-29,0)                                         (29,0)
      (-32,0)                 (-26,0)                 (32,0)                  (26,0)

*************************************************************************************************************
```

Figure 4.5: Example output of the IDL script used to analyze the tolerancing run output. The left and right columns are for the minimum and maximum perturbation values, respectively. Spot size changes are given in per cent from the nominal values, and are arranged to mimic the spectral format of the instrument.

into three groups: 'alignment' tolerances, 'optical fabrication' tolerances and 'optical surface quality' tolerances. Each of these groups will be described in detail in Section 4.2.5.

A 10 per cent increase in the $\mathrm{FWHM_{avg}}$ of the 35 monitored resolution elements was accepted as a reasonable total allowable error. Each of the three groups of tolerancing parameters was then ascribed a subset of this amount, as summarized in Table 4.3. Also included in the budget was a 2 per cent margin for unforeseen component fabrication or instrument assembly issues.

Table 4.3: The image quality error budget for the KiwiSpec tolerancing study.

Error/Perturbation Type	**Allowed $\mathrm{FWHM_{avg}}$ Increase**
Alignment	3%
Optical Fabrication	3%
Optical Surface Quality	2%
Unforeseen Issues	2%
Total:	10%

Although not included in the image quality error budget above, the location of the spectrum on the detector was also monitored during the tolerancing study. In general, wedge in lenses, decentered elements, alignment turns and tilts of mirrors and lenses, variations in prism angles and the clocking of the VPH grating cause movements of the spectrum on the detector. Monitoring the spectral position during tolerancing is important as it prevents large excursions in alignment for perturbations that do not strongly affect the FWHM of the resolution elements. For example, a 0.5° change of a grism prism face angle has a very small effect on image quality; however, it moves the spectrum on the detector by 50 pixels. For many of the parameters the tolerances were determined by their effect on location of the spectrum, and not by image quality concerns.

Each of the groups was allowed a 50 pixel total shift in each of the échelle and spatial dispersion directions. This value equates to a movement of the spectrum on the detector of 2.4 per cent of the detector width (or height).

4.2.5 Results

Each of the tolerance groups will be described in this section, as well as the results of the tolerancing study. It should be emphasized that the results shown here apply only to the prototype instrument with the Hasselblad lens. A future version of KiwiSpec with a custom camera lens (and hence improved image quality) will certainly require tighter tolerances than the prototype instrument.

4.2.5.1 Alignment Tolerances

The alignment tolerance group monitors the effects of the position of each optical element given the three translational and three rotational degrees of freedom. The translational coordinate system employed for the tolerancing study is shown in Figure 4.6, which was chosen for its convenience during integration and alignment of the instrument (as it coincides with the bolt pattern on the optical table).

The rotational degrees of freedom are shown in Figure 4.7. For each optical element, these degrees of freedom were chosen to match the movements of the optical mounts. In this way, the results of the tolerancing study could be directly applied to the opto-mechanical design (to be described in detail in Chapter 5). This approach is also convenient during the alignment phase, as the specified tolerances directly relate to the adjustable mount movements.

The list of tolerances determined for the alignment group are given in Table 4.4. Also indicated within the table is how the tolerance range for each degree of freedom was achieved within the opto-mechanical design of the instrument. Figure 4.8 shows graphically the relative contributions of the various perturbations (for both image quality and centroid movements).

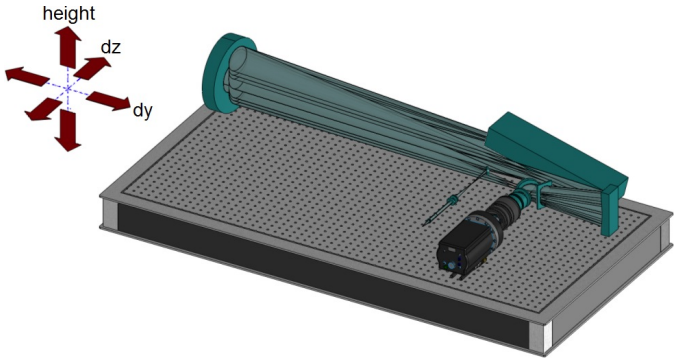

Figure 4.6: The translational degrees of freedom employed during the tolerance analysis. This coordinate system was chosen as it aligns with the threaded hole pattern in the optical table top.

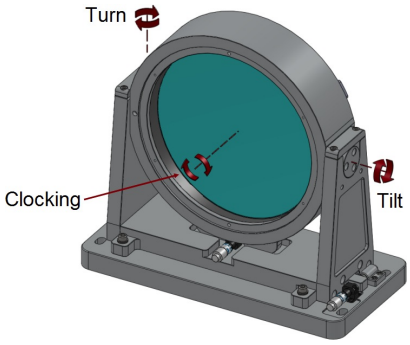

Figure 4.7: The rotational degrees of freedom employed during the tolerancing study. Shown is the primary collimator mirror mount.

Overall the alignment group tolerance values are quite reasonable, meaning that alignment of the instrument is relatively straightforward in theory, and this was found to be true during assembly of the prototype. Several of the tighter tolerance values are described here in more detail:

- The input relay collimator lens and focus lens 'dz' position tolerances ($\pm$ 0.01 mm and $\pm$ 0.25 mm, respectively), would be difficult to achieve with typical optical and mechanical fabrication practices. Therefore, in practice these parameters are compensated for during the assembly of the input relay, and each lens is independently focused via adjustments built into the mounts: the relay collimator lens can be separately focused with respect to the fibre exit, and the relay focus lens is separately focused with respect to the entrance slit.

- The focus requirement for the primary collimator mirror ($\pm$ 0.1 mm) would be very difficult to achieve without adjustment. Therefore, the input relay mount was designed to include a focus adjustment that allows the entrance slit to be set directly at the focus of the primary collimator.

Table 4.4: The alignment tolerance group, consisting of the translational and rotational degrees of freedom. Parameters with no effect on image quality or centroid movements are indicated by '-' (these parameters could generally be ascribed a tolerance of ± 1° or ± 1 mm). Also included beside each value in the table is how each tolerance value is achieved in the opto-mechanical design of the vacuum chamber prototype ('m' = degree of freedom set by machining; 'a' = adjustable degree of freedom; 'f' = focus adjustment). The detector translational degrees of freedom are indicated by a '*': detector height and dy movements have a 1:1 response (i.e. moving the detector upwards by 100 μm moves the spectrum by 100 μm); the dz adjustment is set by machining and is compensated for by focusing the Hasselbad/field flattening lens combination.

Component	**Turn** [°]		**Tilt** [°]		**Clocking** [°]		**Height** [mm]		**dy** [mm]		**dz** [mm]	
Relay Collimator Lens	± 1.0	m	± 1.0	m	-		± 0.1	m	± 0.1	m	± 0.01	f
External Input Relay	± 0.1	a	± 0.25	a	-		± 0.75	a	± 0.75	a	-	
Input Vacuum Window	± 1.0	m	± 1.0	m	-		-		-		-	
Relay Focus Lens	± 1.0	m	± 1.0	m	-		± 0.25	m	± 0.25	m	± 0.25	f
Input Fold	± 0.1	a	± 0.1	a	-		-		± 0.2	m	± 0.2	m
Primary Collimator	± 0.005	a	± 0.005	a	± 0.05	a	± 0.1	m	± 0.1	f	± 0.1	m
Échelle	± 0.005	a	± 0.005	a	± 0.015	a	-		-		-	
Secondary Collimator	± 0.01	a	± 0.01	a	-		± 0.1	m	± 0.1	f	± 0.1	m
Dichroic	± 1.0	a	± 1.0	a	-		-		-		-	
Camera Fold	± 0.01	a	± 0.05	a	-		-		± 1.0	m	± 1.0	m
Output Vacuum Window	± 1.0	m	± 1.0	m	-		-		-		-	
Entire Grism	± 1.0	a	± 1.0	m	± 0.25	a	-		± 1.0	m	± 1.0	m
Hasselblad	± 0.1	m	± 0.1	m	-		± 0.1	m	± 0.1	m	± 0.05	f
Field Flattening Lens	± 0.5	m	± 0.5	m	-		± 0.25	m	± 0.25	m	± 0.25	m
Hasselblad and Ff-Lens	± 0.1	m	± 0.1	m	-		± 0.1	m	± 0.1	m	± 0.05	f
Detector and Window	± 0.2	a	± 0.25	a	-		*	a	*	a	*	m

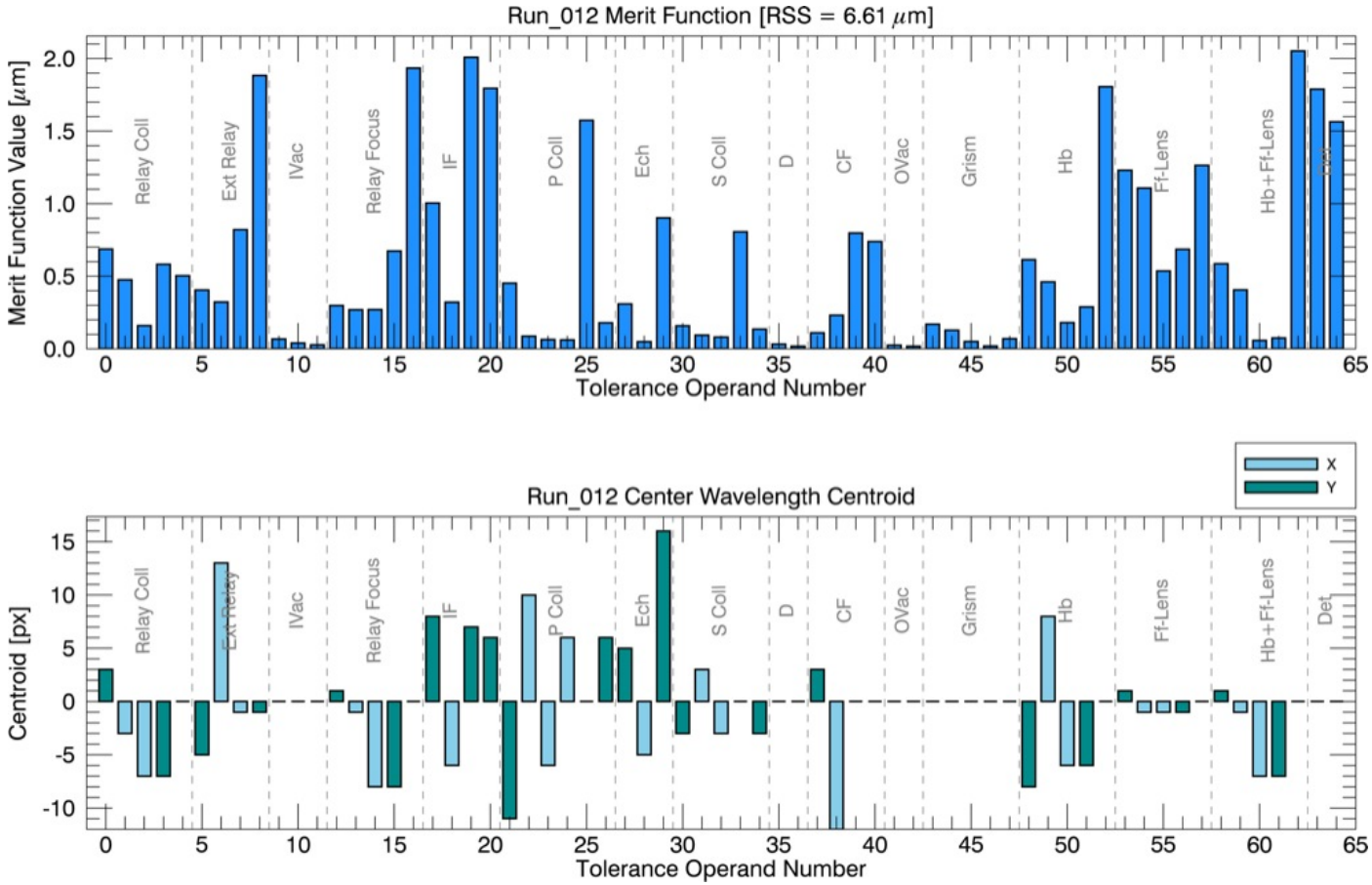

Figure 4.8: Contributions of the various degrees of freedom to the alignment group error budget value during the sensitivity analysis. The top plot shows the spot size-based merit function values for each parameter. The bottom plot shows the centroid movements in the x (échelle dispersion) and y (cross dispersion) directions for each perturbation. Each component is labelled with the degrees of freedom across each group (left to right) corresponding to the same columns in Table 4.4. Note that degrees of freedom indicated with a '-' in the table are not included within these plots.

- The small turn and tilt tolerance values for the primary collimator and échelle grating (all are at $\pm$ 0.005°) are driven by centroid movements. The primary collimator and échelle are the most sensitive components with respect to turn and tilt, owing to optical leverage and the fact that the primary collimator is used in double pass. These tolerance values, while small, are achievable as appropriately-sensitive adjustments were designed into the mounts supporting these optical elements.

- The échelle clocking parameter (rotating the grating within its cell) is equivalent to a turn adjustment (i.e. the échelle γ adjustment). The tolerance value, ($\pm$ 0.015°), corresponds to setting the échelle grating parallel to the edge of its cell within $\pm$ 0.110 mm (which is easily achievable with a precision depth gauge).

- Similarly the turn and tilt requirements on the secondary collimator and camera fold mirror are achievable with the mount designs and the actuators employed.

- The grism clocking could be set to $\pm$ 1°, but is constrained here to avoid large centroid changes owing to the 'shearing' effect that this rotation has on the spectrum.

4.2.5.2 Optical Fabrication Tolerances

The optical fabrication tolerance group contains individual optical fabrication parameters, including: wedge, centre thickness, glass index homogeneity, radius of curvature (or surface flatness) and conic constant. As well, it includes the fabrication of the grism: turn, tilt, clocking and decentre tolerances for both prisms and the VPH grating.

The lists of tolerances determined for the optical fabrication group are given in Table 4.5 (refractive elements), Table 4.6 (reflective elements) and Table 4.7 (grism assembly).

The results show that the KiwiSpec prototype is quite forgiving to optical fabrication errors. Several design parameters support this conclusion. First, the input relay system (which is not optimized and employs a pair of off-the-shelf doublets), produces a magnified and aberrated image of the fibre exit at the spectrograph entrance slit location. This results in a large resolution element at the detector that overwhelms and hides the various small errors. Secondly, the primary collimator operates at f/10, and such slow f/ratios are more forgiving to optical quality errors than faster systems. Thirdly, the Hasselblad is being used in an application it was not optimized for, and therefore will be introducing some aberrations that would not be present in a custom lens optimized for KiwiSpec. And finally, the Hasselblad and field flattening lens combination operates at f/5, which is also a reasonably slow f/ratio and hence more forgiving to the tolerance perturbations.

Table 4.5: The optical fabrication tolerances for the refractive optical components.

Component	**Wedge** [°]	**Centre Thickness** [mm]	**Index Homo-geneity**	**Surface Flatness** [fringes at 632.8 nm]	**Radius of Curvature** [fringes at 632.8 nm]
Relay Collimator Lens (E1/E2)[a]	± 0.1/± 0.1	± 0.2/± 0.1[b]	- ± 2E-5/± 2E-5	-	±0.5 (all sfcs)
Input Vacuum Window	± 0.1	± 0.2	± 2E-5	± 0.5/± 0.5	-
Relay Focus Lens (E1/E2)	± 0.1/± 0.1	± 0.2/± 0.2	± 2E-5/± 2E-5	-	±0.5 (all sfcs)
Dichroic	± 0.1	± 0.2	± 2E-5	± 0.5/± 0.5	-
Output Vacuum Window	± 0.1	± 0.2	± 2E-5	± 0.5/± 0.5	-
Grism Prisms (Angled/Flat Face)	± 0.1	± 0.2	± 2E-5	± 0.5/± 0.5	-
VPH Cover Plates	± 0.1	± 0.2	± 2E-5	± 0.5/± 0.5	-
Field Flattening Lens	± 0.1	± 0.1[b]	± 2E-5	-	± 1.0/± 1.0
CCD Window	± 0.1	± 0.2	± 2E-5	± 1.0/± 1.0	-

[a] 'E1/E2' refers to 'Element 1' and 'Element 2' of an achromatic doublet.

[b] Uncompensated values. These two centre thicknesses can be relaxed to the more typical value of ± 0.2 mm when focusing is allowed (as it is in the actual instrument).

Table 4.6: The optical fabrication tolerances for the reflective optical components.

Component	Surface Flatness [fringes at 632.8 nm]	Radius of Curvature [mm]	Conic Constant
Input Fold	± 0.5	-	-
Primary Collimator	-	± 0.25[a]	± 0.05
Secondary Collimator	-	± 0.5[a]	-
Camera Fold	± 0.5	-	-

[a] Uncompensated values. See text for details.

Table 4.7: The optical fabrication tolerances required for assembly of the grism.

Component	Turn [°]	Tilt [°]	Clocking [°]	Height [mm]	dy [mm]	dz [mm]
Prism 1	± 0.5	± 0.5	± 0.1	± 1.0	± 1.0	duplicate[a]
VPH	duplicate[b]	duplicate[c]	± 0.05	± 1.0	± 1.0	duplicate[a]
Prism 2	± 0.5	± 0.5	± 0.1	± 1.0	± 1.0	duplicate[a]

[a] Equivalent to a centre thickness increase of either a prism or a VPH grating cover plate.
[b] Equivalent to turning prisms.
[c] Equivalent to tilting prisms.

The various findings from the tolerancing of the optical fabrication group are discussed here:

Wedge: Wedge was one of only two parameters within this group that caused centroid movements (the other was clocking). Even so, the easily-achieved value of $\pm 0.1^\circ$ (6 arcmin) was able to be applied to all refractive elements.

Centre Thickness: The centre thicknesses of the second element of the input relay collimator lens, the field flattening lens and CCD window are critical parameters if focus is not allowed. However, all can be set to the typical value of ± 0.2 mm when focusing is allowed (as it is in the actual instrument).

Index Homogeneity: The value determined for all lenses equates to Schott homogeneity class 'H1' (the lowest homogeneity class). This is justified in that none of the lenses within the KiwiSpec prototype have centre thicknesses greater than 14 mm (i.e. not thick enough for inhomogeneity to have a significant effect).

Surface Flatness/Radius of Curvature: Aside from the primary and secondary collimator mirrors, for variations in flatness or radius of curvature (ROC), all surfaces can be set to the reasonable value of ± 0.5 fringe ($\pm 0.25\lambda$). The specifications on the field flattening lens and the CCD window can be relaxed to ± 1 fringe, as at that point within the system the footprint of each wavelength is small compared to the diameter of the optical elements.

Collimator ROCs: The values given in Table 4.6 for the radii of curvature of the primary and secondary collimators would be difficult to achieve given typical optical and mechanical fabrication methods. Therefore, the instrument was designed so that these values can be compensated for during alignment via a focus adjustment. Based on the mechanical design, up to ± 4 mm on both of these radii of curvature values is allowable (i.e. $\pm$ 2 mm on focal length).

Grism Assembly: The grism is largely insensitive to decentres of the components during assembly, but care must be taken with clocking the components. The VPH grating is the most sensitive component, which has a tolerance on clocking of $\pm 0.05^\circ$. However, this value is driven by centroid movements and could be relaxed in practice. Of importance though is the clocking of the prisms with respect to the grating. During assembly, the clocking of the grism components should be monitored optically: a laser beam, (directed through the grism and projected onto a distant wall), could be used to ensure that the two prisms are

correctly clocked with respect to the grating before the prisms are bonded with optical cement.

4.2.5.3 Optical Surface Quality Tolerances

The optical surface quality group is concerned with tolerancing defects which are polished into optical surfaces during manufacture. These defects are commonly described by opticians as 'holes' (depressions) or 'hills' (raised areas). They are typically measured by their diameter in mm and their peak-to-valley (P-V) depth or height in wavelengths of light.

Figure 4.9 shows the effect of three types of defects on a flat mirror. Large, smooth, full-aperture deviations from the perfect mirror figure (as shown in Figure 4.9b) generally have a small effect on overall image quality.

Comparing a full aperture defect and a sub-aperture defect with the same P-V, the sub-aperture defect will be much more damaging to image quality owing to the greater rate of change of the surface slope. Figures 4.9c and 4.9d show the effect of a hole and hill, respectively.

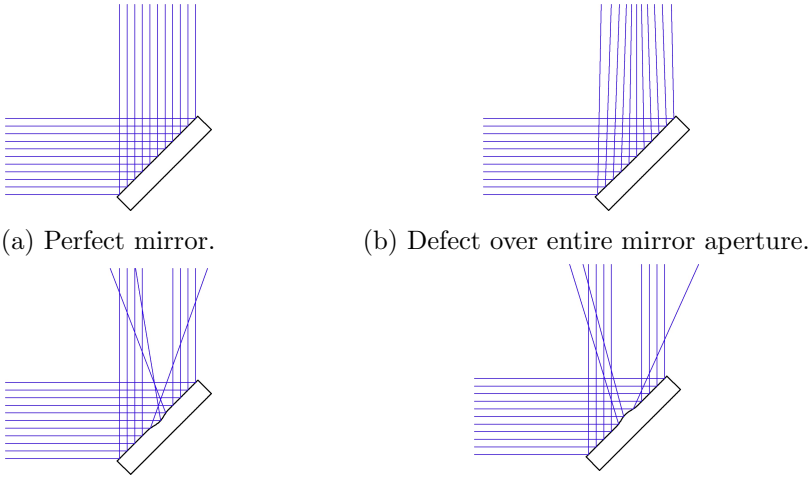

(a) Perfect mirror.

(b) Defect over entire mirror aperture.

(c) Sub-aperture 'hole' defect.

(d) Sub-aperture 'hill' defect.

Figure 4.9: The effect of full- and sub-aperture surface defects on a flat mirror. All defects are of the same P-V. For clarity, the magnitudes of the defects have been greatly exaggerated from what would be encountered in practice.

To model the effects of sub-aperture defects within the KiwiSpec system, the Zemax 'Grid Sag' surface type was employed to add a defect to an underlying optical surface (which could be flat, spherical, or aspherical in shape). The defect shape employed was a rotationally symmetric half period of a cosine curve[2]. A cross-sectional view of a defect is shown in Figure 4.10. As shown in that figure, the cosine-curve method results in smooth boundary between the defect and the nominal optical surface.

[2]Based on discussions with Damien Jones (Prime Optics, Australia)

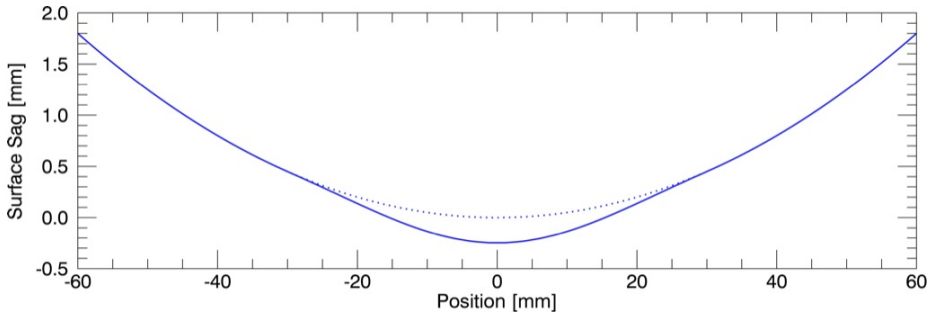

Figure 4.10: Cross-section of the sag of a spherical mirror with an exaggerated defect applied to the centre. The dotted line indicates the nominal surface of the mirror without a defect. Note the smooth transition between the defect and the nominal spherical surface.

While in reality surface defects polished into glass can occur in all shapes and sizes, in an attempt to model the effects of sub-aperture defects a circular defect was added to each lens and mirror surface in the Zemax model. Each defect was sized to be about one-quarter the diameter of the optical element it was placed on, with the diameter and the depth of the defect being adjustable parameters. The position of the defect was also moved around each optic, as shown in Figure 4.11, while the effect of each position on a spot size-based merit function was noted. Through the spot size to $\mathrm{FWHM}_{\mathrm{avg}}$ calibration presented in Table 4.2, the goal was to ensure that the worst-case combined effect of all errors did not amount to more than a 2 per cent increase in the $\mathrm{FWHM}_{\mathrm{avg}}$ value (to meet the error budget requirements of Table 4.3).

The results are given in Table 4.8. As shown in the table, the KiwiSpec prototype is very insensitive to errors of this type. This is attributed to the reasons given in Section 4.2.5.2; namely the oversampled resolution element, the non-optimized input relay and camera lens, as well as the relatively slow f/ratios employed within the system.

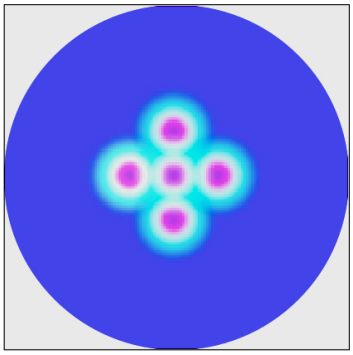

Figure 4.11: An example of how the surface defects were moved around an optical surface (shown is the input fold mirror). Five defect positions (one on-axis and four off-axis) are combined in this figure to show the coverage on the optical surface. However, in practice they were applied separately to note their effects.

Table 4.8: The optical surface quality tolerances.

Component	**Allowable Defect P-V**[a] **(λ=632.8 nm)**
Relay Collimator Lens	0.5λ over 3.5 mm circle[b]
Input Vacuum Window	0.5λ over 6.5 mm circle[b]
Relay Focus Lens	0.5λ over 6.5 mm circle[b]
Input Fold	0.5λ over 6.5 mm circle[b]
Primary Collimator	0.5λ over 60 mm circle
Secondary Collimator	0.5λ over 37.5 mm circle
Dichroic	0.5λ over 20.5 mm circle
Camera Fold	0.5λ over 18.5 mm circle
Output Vacuum Window	0.5λ over 16 mm circle
Prism 1	0.5λ over 15.5 mm circle
VPH Cover Plates	0.5λ over 13 mm circle
Prism 2	0.5λ over 15.5 mm circle
Field Flattening Lens	0.5λ over 13 mm circle
CCD Window	0.5λ over 14.5 mm circle

[a] 'P-V' = 'peak-to-valley'

[b] Optical elements of such a (small) size are typically blocked together during manufacture, making this a very large defect for lenses or mirrors of this size.

4.2.5.4 Monte Carlo Results

Monte Carlo analyses were performed on the alignment and the optical fabrication groups. It was not possible to perform a Monte Carlo analysis on the surface quality group owing to the way the 'Grid Sag' surface type is implemented within Zemax.

Image quality and centroid movements were monitored during the Monte Carlo analyses. Two types of centroid movements were monitored: the movement of the entire spectrum on the detector, and also the movement of centroids within the spectrum (as a measure of distortion).

The results are shown in Tables 4.9 and 4.10, and indicate that if 1000 KiwiSpec prototypes were manufactured with the alignment and optical fabrication tolerance sets, 100 per cent of the instruments would meet the error budget requirements.

Table 4.9: Statistics for the alignment group Monte Carlo analysis. 1000 randomly-perturbed KiwiSpec systems were generated. Re-focusing was not included as a compensator. Note that the centroid 'pairs' of ($X_{\max}$, $Y_{\max}$) are not necessarily from the same run, but rather maximum values of each across all of the runs.

Image Quality	
Percentage of runs	**ΔFWHM$_{\text{avg}}$**
100.0%	$< 3\%$ increase
99.6%	$< 2\%$ increase
94.7%	$< 1\%$ increase
81.9%	$< 0.5\%$ increase

Centroid Movements		
	$\boldsymbol{X}_{\max}$	$\boldsymbol{Y}_{\max}$
Entire spectrum:	-46.5 px	-43.8 px
Distortion:	-12.6 px	9.6 px

Table 4.10: Statistics for the optical fabrication group Monte Carlo analysis. 1000 randomly-perturbed KiwiSpec systems were generated. Re-focusing was included as a compensator; the maximum amount of refocusing required across all of the runs was 0.21 mm. Note that the centroid 'pairs' of ($X_{\max}$, $Y_{\max}$) are not necessarily from the same run, but rather maximum values of each across all of the runs.

Image Quality	
Percentage of runs	**ΔFWHM$_{\text{avg}}$**
100.0%	$< 3\%$ increase
100.0%	$< 2\%$ increase
100.0%	$< 1\%$ increase
100.0%	$< 0.5\%$ increase

Centroid Movements		
	$\boldsymbol{X}_{\max}$	$\boldsymbol{Y}_{\max}$
Entire spectrum:	-30.0 px	29.4 px
Distortion:	4.6 px	7.0 px

4.3 Tolerancing of the Iodine Cell

This section describes the tolerancing of the iodine reference cell, to ensure it does not negatively affect the performance of the KiwiSpec prototype when the cell is placed within the light path.

4.3.1 Cell Construction

Iodine cells are typically made of a hollow glass tube with optical windows cemented on either end. A small mass of iodine vapour is injected into the tube through a filling stem, which is then permanently closed off[3]. Typically the windows are made of fused silica, are slightly wedged, and are coated with anti-reflection coatings to minimize throughput losses.

The window wedge is required to remove the possibility of interference effects, which are common when plane-parallel windows or filters are placed within collimated beams (as all rays within a collimated beam strike the window at the same angle). The absolute value of the wedge angle is not critical.

For this study a cell with windows perpendicular to the long axis of the central tube was toleranced (i.e. arranged like |=|). The tube is 45 mm long, 25 mm in diameter, and has 1.5 mm thick windows. A second type of cell was briefly investigated, in which the cell is constructed with the windows set at a deliberate angle (i.e. such as /=\). However, this type of cell was discounted because the angled, wedged windows operate as an anamorphic prism pair and introduce astigmatism into the beam.

4.3.2 Motivation

For observing programs not requiring measurement of precision radial velocities, the presence of the iodine absorption lines within the spectrum and the associated loss of throughput between 500 and 630 nm can be undesirable. Therefore it is a useful feature for a spectrograph to be able to switch between observing with and without an iodine cell in place. In the KiwiSpec instrument, the iodine cell is moved into and out of the light path within the collimated space of the input relay system (to be described in detail in Chapter 5), and the reason for tolerancing the design of the cell is to ensure a minimal change in the light path in either position. The positioning requirements of the entire cell were also toleranced to determine the degrees of freedom required by the iodine cell mount.

Although the wedged windows are required to prevent interference effects, they act as weak prisms and cause two undesirable effects: beam deviation and dispersion. Beam deviation causes the f/10 beam focused on the (potential) entrance slit to wander off the slit location when the cell is

[3] See `http://exoplanets.astro.yale.edu/instrumentation/iodine_cells.php`.

moved into the beam. Dispersion causes each wavelength to leave the iodine cell at a slightly different angle, leading to an elongated spread of fibre images at the entrance slit (there is one fibre image for each wavelength). The angular orientation of this extended image depends on the clocking angles of the cell windows. As blue and red wavelengths are at opposite ends of this elongated image, throughput at these wavelengths will be reduced if the length of the image is longer than the physical length of the slit. This effect is minimal over the narrow wavelength region of interest of the iodine cell – but can play a role in efficiency losses over the entire wavelength range of the instrument.

4.3.3 Method

The input relay and iodine cell system were modelled in non-sequential Zemax to determine the required tolerances on both the manufacture and positioning of the iodine cell. Parameters such as window coating efficiencies and the absorption of the iodine gas itself were not accounted for. The goal was to limit the throughput losses of placing the cell into the beam to less than 2 per cent. Transmission through the windows, coatings, and the iodine gas itself would lead to additional losses which are not accounted for here.

Within the Zemax model, a 100-μm pinhole was used as an entrance slit. A pinhole was chosen as it limits the amount of allowable beam deviation or dispersion in all directions (as opposed to a rectangular slit which would be more forgiving along the long axis of the slit).

Two wavelength bandpass sets were used for the tolerance analysis; a reduced set for the iodine region only (480 nm, 500 nm, 550 nm, 600 nm, 630 nm and 650 nm), and a larger set to monitor the effect on an extended spectrum (350 nm to 800 nm in 50 nm steps). The number of rays traced for each tolerancing run was 1,000,000.

To measure the efficiency of the various perturbations, the number of rays was counted just before and just after the pinhole, with the ratio between the two measurements giving the efficiency of the system. By using this approach the losses of the relay system itself are excluded. The centroid of the light rays on the final detector surface was also calculated to ensure there were no large movements of the beam centroid because of the introduction of the iodine cell into the relay.

The nominal values of throughput and centroid position were determined with the iodine cell out of the beam. With the cell in place, the system was then toleranced both in sensitivity (to see the effect of individual parameter perturbations) and using Monte Carlo analysis (to monitor the effect of all tolerance perturbations applied simultaneously).

4.3.4 Results

The most significant result is that the two wedged windows must be clocked 180° apart in order to minimize the effects of beam deviation and dispersion (as shown in Figures 4.12 and 4.13).

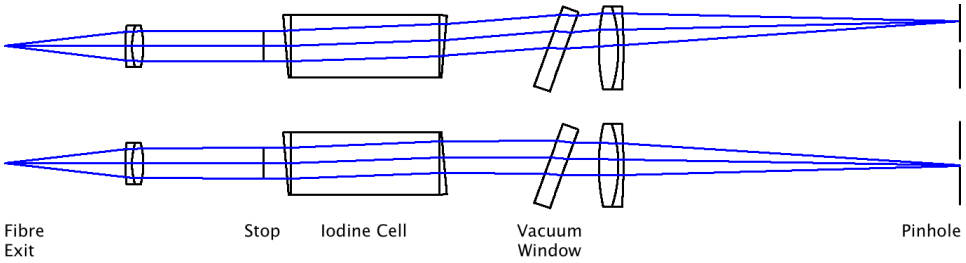

Figure 4.12: The beam deviation effect of iodine cell window clocking. For clarity, each window is drawn with a large wedge angle to exaggerate the effect (in practice wedge angles are 0.4°). Top: Wedged windows with the same clocking lead to a deviated beam. Bottom: Clocking the two windows 180° apart leads to a compensating effect and the beam stays within the pinhole.

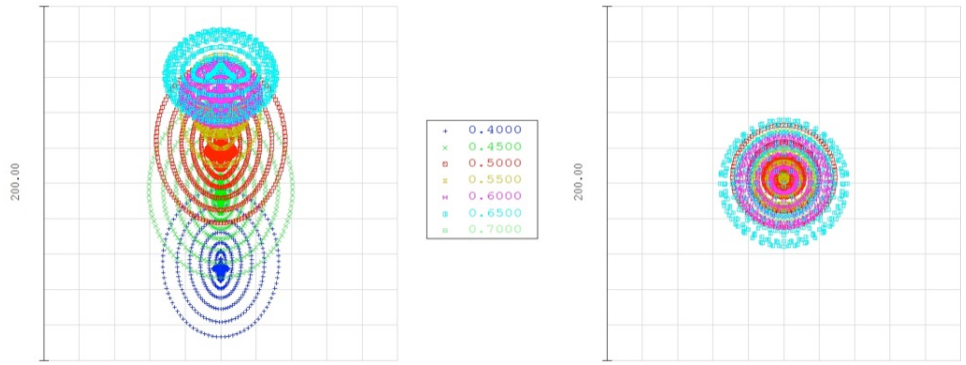

Figure 4.13: Spot diagrams illustrating the prismatic dispersion effects of the wedged iodine cell windows. Left: Both windows with the same clocking (prismatic effect amplified). Right: Windows clocked 180° apart (prismatic effect of first window compensated by second window). For these diagrams, a large wedge angle was chosen (2°) to emphasize the effect. Only the on-axis field spots are shown (i.e. not from an extended source such as a fibre end).

A second significant finding is that the window wedges require a tight tolerance to keep the two windows as similar as possible (so that the second window compensates for the first window as much as possible).

As mentioned above, the absolute value of wedge angle on the windows is not critical. However, the greater the wedge angle, the tighter the tolerance on the window clocking needs to be (this is because larger wedge angles cause more beam deviation).

It was also found that centroid movements were correlated with efficiency losses. This is to be expected, because as the centroid moves off-axis more light is occulted by the pinhole.

Overall the required tolerances are quite loose (the results are shown in Table 4.11). The wedge and clocking parameters are slightly tighter than those found in off-the-shelf iodine cells, but certainly easily achievable given standard fabrication practices. For example, the tightest tolerance required is for the wedge on the cell windows ($0.4 \pm 0.05^\circ$). However, optical shops can routinely measure wedge in an element to 5 μm of total indicator runout, which equates to 0.01° wedge over the 25 mm window diameter.

The Monte Carlo results, shown in Table 4.12, show that for the fifty runs generated, 100 per cent of the iodine cells constructed had less than a 2 per cent decrease in efficiency over the iodine wavelength bandwidth. Therefore when all of the parameters are perturbed simultaneously the design still meets the desired specification. The extended wavelength range analysis shows greater efficiency losses, which is to be expected as the greater wavelength range increases the amount of angular dispersion (leading to less light entering the pinhole).

Table 4.11: Nominal values and required tolerances for the individual iodine cell windows and overall cell position.

	Window 1	**Window 2**	**Entire Cell**
decentre x	0 ± 2 mm	0 ± 2 mm	0 ± 2 mm
decentre y	0 ± 2 mm	0 ± 2 mm	0 ± 2 mm
decentre z	0 ± 2 mm	0 ± 2 mm	0 ± 2 mm
tilt x	$0 \pm 2^\circ$	$0 \pm 2^\circ$	$0 \pm 2^\circ$
tilt y	$0 \pm 2^\circ$	$0 \pm 2^\circ$	$0 \pm 2^\circ$
clocking	$0 \pm 10^\circ$	$180 \pm 10^\circ$	$0 \pm 90^\circ$
window wedge	$0.4 \pm 0.05^\circ$	$0.4 \pm 0.05^\circ$	–
window centre thickness	1.5 ± 0.5 mm	1.5 ± 0.5 mm	–

Table 4.12: Statistics for the iodine cell Monte Carlo analysis. Fifty randomly-perturbed iodine cells were generated for each of the iodine bandwidth and extended wavelength range analyses.

Iodine Wavelength Range		Extended Wavelength Range	
Percentage of runs	**Efficiency**	**Percentage of runs**	**Efficiency**
96%	$< 1\%$ decrease	82%	$< 1\%$ decrease
100%	$< 2\%$ decrease	96%	$< 2\%$ decrease
100%	$< 3\%$ decrease	96%	$< 3\%$ decrease
100%	$< 4\%$ decrease	96%	$< 4\%$ decrease
100%	$< 5\%$ decrease	98%	$< 5\%$ decrease

Chapter 5

Opto-Mechanical Design

5.1 Introduction

The development of the KiwiSpec spectrograph proceeded in two stages. At first, a prototype consisting of the core components of the instrument was constructed with the goal of proving the design concept. This instrument, which operated in-air, was the version of KiwiSpec that was transported to Mt John University Observatory for on-sky testing.

Following the successful tests at Mt John, work began on the second stage of the project, which involved converting the in-air prototype to the vacuum chamber prototype. About half of the opto-mechanical mounts in the first prototype carried across to the second prototype with only minor changes and improvements. The other half of the mounts were completely redesigned. The redesigns were based on experience gained during the assembly and use of the first prototype, and also on the need to accommodate the addition of the vacuum chamber itself.

In this chapter, the opto-mechanical components of both versions of the prototype are described. An overview diagram of the first version, the 'in-air prototype', is shown in Figure 5.1. Similar diagrams of the second version, described as the 'vacuum chamber prototype', are shown in Figures 5.2 and 5.3 (note that a full description of the vacuum chamber system follows in Chapter 6). The in-air prototype will be described here in the past tense, as it was disassembled during the build of the vacuum chamber prototype.

5.2 Common Features Among Optical Mounts

The mechanical mountings for the various optical components were designed with several common features. These included:

Pivot Locations: To avoid cross-talk between adjustments, the vertical (turn) and horizontal (tilt) axes of the optical mounts were designed to intersect on the optical surfaces of the various components. For concave mirrors, the intersection point was placed at the vertex or

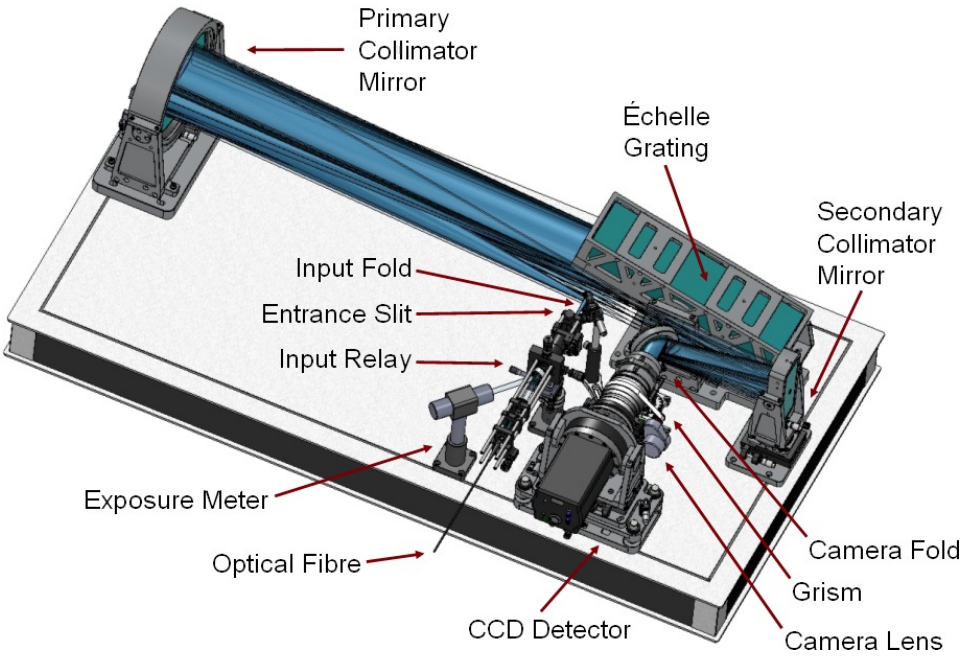

Figure 5.1: Schematic diagram of the KiwiSpec in-air prototype with key components labeled. Although not shown in the diagram, in practice the optical table was 'floated' on a vibration-isolation support.

pole of the mirrors. For flat surfaces, (the fold mirrors, the échelle grating, and the CCD detector), the intersection point of the mount axes was placed on the front surface.

Fine Adjustment: Care was taken to ensure that there was a suitable amount of adjustment for each degree of freedom. In general terms, fine alignment control is much better than not enough control when aligning optical elements.

Off-the-shelf (OTS) when possible: OTS mounts are more cost-effective than custom-designed and fabricated assemblies. Where possible, OTS components were used.

Locking mechanisms: Each mount (custom or OTS) has a locking mechanism for each adjustable degree of freedom. The design goal was that after alignment each mount can be rigidly locked into position.

Transportability: The optical mounts were designed to be easily disassembled for shipping. Each mount allows its optical element to be removed without disturbing the actuator/locator positions. The goal was to retain the pre-shipping alignment after transport, so that reassembly is straightforward.

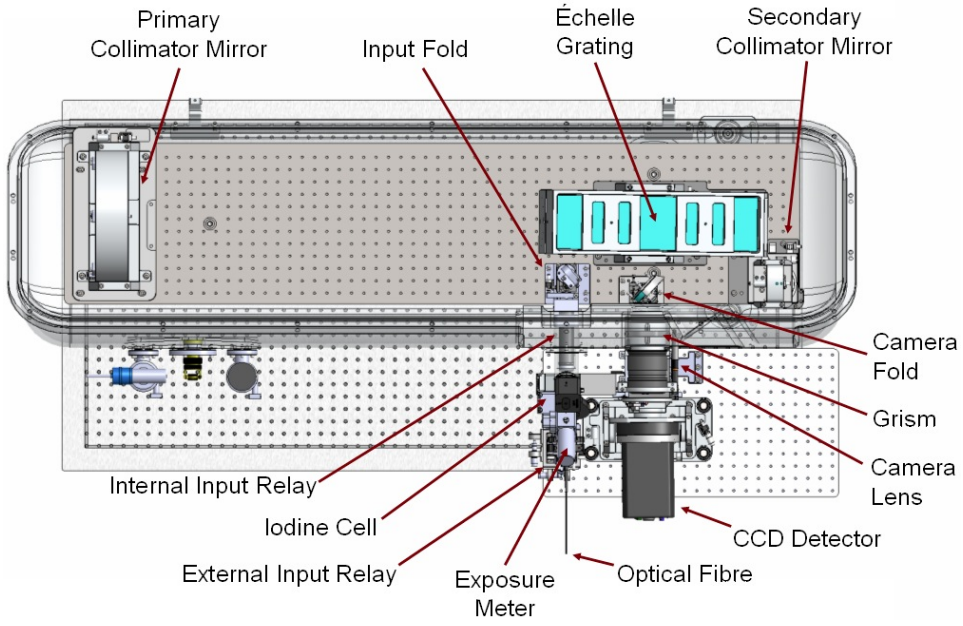

Figure 5.2: Schematic diagram of the KiwiSpec vacuum chamber prototype with key components labeled. Although not shown in the diagram, in practice the bottom optical table is 'floated' on a vibration-isolation support. For clarity, the vacuum chamber lid has been removed, and the chamber is shown as being transparent. Figure 5.3 provides a more detailed view of the external input relay system.

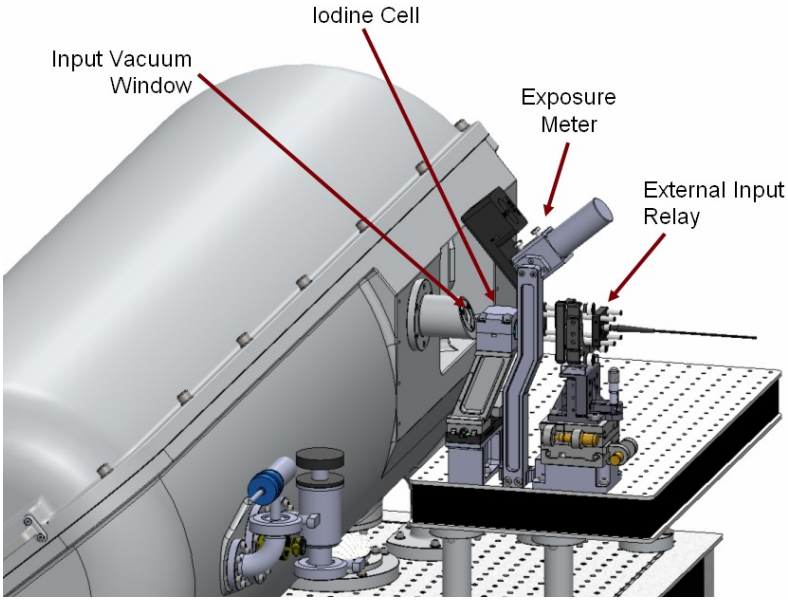

Figure 5.3: Close up of the external input relay system of the vacuum chamber prototype (the camera arm and detector have been removed for clarity).

Covers and stray light masks: Each mount was designed so that a protective cover can be easily bolted over the exposed optic (as shown in Figure 5.4). The same attachment method can be used to attach a stray light baffle, which is similar to the cover but features an appropriately-sized aperture to control which light rays reach the optic.

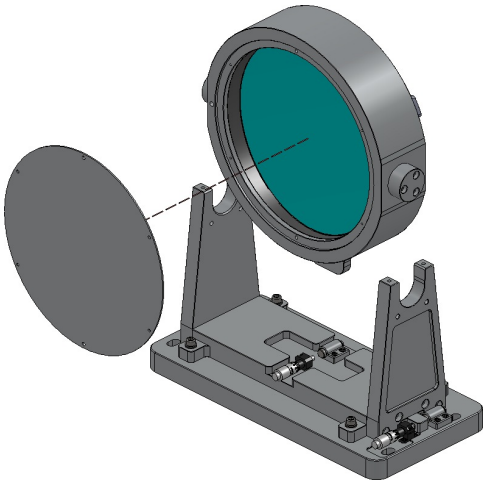

Figure 5.4: The optical mounts were designed so that the optics in their cells can be removed from the mount base for shipping/transport. Each mount also allows for a cover to be attached to protect the optic. Shown is the primary collimator mirror mount.

Adjustment Repeatability: For the in-air prototype – where it was expected that many adjustments would be made during the initial setup and testing – micrometers were used as actuators throughout the system. The numbered scales on the micrometers allowed a position to be noted and then returned to after adjustment if necessary. For the vacuum chamber prototype, the non-vacuum-compatible micrometers were replaced with fine-thread actuators, which, although lacking numbered dials, have a finer pitch thread (0.32 mm travel per rotation vs. 0.5 mm per rotation for the micrometers).

Fabrication: Custom components were manufactured exclusively out of 6061-T6 aluminium and anodized black. Aluminium was chosen over other metals because of its cost-effectiveness and ease of machining. The sub-components of each mount were designed to be fabricated using CNC (Computer Numerical Control) machining processes.

Stability: The vacuum chamber prototype mounts were designed to have improved stability over the in-air prototype mounts. To this end many of the non-essential degrees of freedom present in the original mounts were removed, resulting in simpler mounts with fewer adjustments.

Temperature stability: For the in-air prototype several of the mounts were supported by stainless steel posts, while other mounts were constructed entirely of aluminium. However, this led to a coefficient of

thermal expansion (CTE) mismatch, causing a differential change in height among the various mounts as the temperature changed. Therefore, care was taken for the vacuum chamber prototype to design the mounts entirely out of aluminium.

5.3 Room Temperature Vulcanizing Silicone (RTV)

RTV was used to pot three of the optical elements within their mounts: the primary collimator, the échelle grating, and the secondary collimator. RTV is a common method of mounting optical elements within mechanical cells. It results in a compliant mount that does not stress the optic, and it can also be used to create an athermal mounting arrangement that balances the expansion coefficients of the optic, RTV and cell.

Although RTV is used for support, each optic was also mechanically referenced by deliberately contacting a flat face on the optic against a machined face within the mount. The mounts also contain tapped holes surrounding the optic, which were used for adjustment screws to centre the optical element within its cell before potting (Figure 5.5).

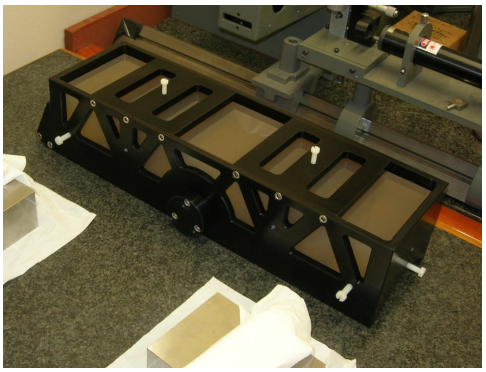

Figure 5.5: The échelle grating shown just before RTV potting. The grating was centered within its cell by adjusting eight nylon bolts around its periphery (coloured white in the picture).

The thickness of the discrete RTV pads in each case was chosen to create an athermal response to temperature changes between the mirror, RTV, and aluminium cell. Two equations typically used to calculate the RTV thickness required are the Bayar and Muench equations. The Bayar equation employed contains a correction factor applied to the RTV CTE value (as suggested by Herbert (2006)). This version of the Bayar equation applies to RTV pad shapes with high aspect ratios (i.e. diameter-to-thickness ratio greater than 10), as employed in the KiwiSpec instrument. The Muench equation is another widely used equation for determining an athermal bond thickness (Herbert, 2006). The Bayar equation is given by:

$$t_{\text{Bayar}} = \frac{d_{\text{lens}}}{2}\left[\frac{\alpha_{\text{cell}} - \alpha_{\text{lens}}}{\frac{1+\nu_{\text{RTV}}}{1-\nu_{\text{RTV}}}\alpha_{\text{RTV}} - \alpha_{\text{lens}}}\right], \tag{5.1}$$

and the Muench equation employed is:

$$t_{\text{Muench}} = \frac{d_{\text{lens}}}{2}\left[\frac{\alpha_{\text{cell}} - \alpha_{\text{lens}}}{\alpha_{\text{RTV}} - \alpha_{\text{cell}} + \left(\alpha_{\text{RTV}} - \frac{\alpha_{\text{cell}}+\alpha_{\text{lens}}}{2}\right)\frac{2}{1-\nu_{\text{RTV}}}\nu_{\text{RTV}}}\right], \quad (5.2)$$

where (for both Bayar and Muench equations):

t	=	RTV thickness	[m];
d_{lens}	=	lens or mirror diameter	[m];
α_{cell}	=	mount CTE	[m/°C];
α_{lens}	=	lens or mirror CTE	[m/°C];
α_{RTV}	=	RTV CTE	[m/°C];
ν_{RTV}	=	RTV Poisson's ratio	[unitless].

Values for athermal bond thicknesses for the three mounts utilizing RTV were calculated using both the Bayar and Muench equations, and the results are shown in Table 5.1. As shown in that table, for the KiwiSpec mounts the two equations agreed within 0.1 mm (an amount that lies within the typical mechanical fabrication tolerance range for the mount components). The values in Table 5.1 were used as guidelines during the mechanical design process.

Table 5.1: Calculated RTV pad thicknesses for an athermal response.

Mount	Bayar	Muench	Difference
Primary Collimator	2.03	2.08	0.05 mm
Échelle - Long Axis	4.45	4.54	0.09 mm
Échelle - Short Axis	1.17	1.19	0.02 mm
Secondary Collimator - Long Axis	1.32	1.36	0.04 mm
Secondary Collimator - Short Axis	0.48	0.49	0.01 mm

While mounting the optics with RTV is certainly advantageous from an induced stress standpoint, it is a semi-permanent mounting approach that makes the optic difficult to remove. Therefore, for future versions of KiwiSpec different mirror mounting techniques may be investigated.

5.4 Tolerances

Each mount was designed to meet the results of the optical tolerancing study of Chapter 4. Several of the mounts rely on non-adjustable machined components to set their height above the optical table. To determine how the mechanical tolerances 'stacked up' as these machined parts were assembled together, the Root-Sum-Square (RSS) rule was employed (described in Section 4.2.3).

5.5 Alignment Bars

In order to locate the various mounts on the optical table during assembly, a series of accurately-machined alignment bars was developed to span between the mount baseplates. The échelle grating mount is the 'anchor' for the system, with each of the alignment bars connected to and referenced off the échelle baseplate. Each alignment bar has two dowel pins in each end to interface with the baseplates, so that the alignment bars locate the baseplates both in angular position and separation. Once the alignment bars are in place, the baseplates will be bolted down to the optical table and the alignment bars removed.

As a modern CNC mill can achieve better than 25 μm accuracy over the length of a meter (and even better over shorter distances)[1], this approach leads to much higher positional accuracy for the mounts than simply measuring between the mounts with a long-reach micrometer. It is also much more accurate than relying on the tapped hole grid pattern on an optical table itself. Based on discussions with Newport Corporation regarding their optical tables, the standard tolerance on hole positions is $\pm$ 0.43 mm in each of the orthogonal directions across the table top. Therefore, for any given hole position both of these tolerances are summed in quadrature. This means that each tapped hole could be located anywhere within a 1.22 mm diameter circle centered on the 'true' or nominal position of the hole.

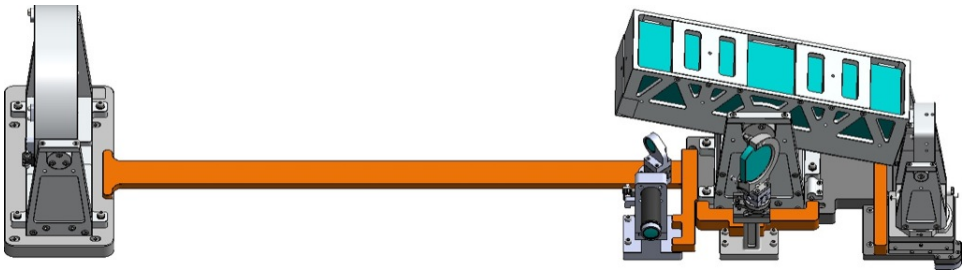

Figure 5.6: The various alignment bars (shown in orange) employed during assembly of the vacuum chamber prototype.

5.6 Mechanical Mounts

In this section the design of the mounts within each prototype will be described separately.

[1]Based on discussions with Robert Jakobsson and Hokmeng Ung (machinists at Callaghan Innovation).

5.6.1 Input Relay

Two very different versions of the input relay mount were designed: one for the in-air prototype, and one for the vacuum chamber prototype. This was necessitated by the introduction of the vacuum chamber (the wall of which passes through the centre of the input relay). Since a redesign was expected, the input relay system for the in-air prototype was not completely optimized, and was built using a majority of in-house OTS components. While this arrangement certainly worked for the in-air prototype, a goal of the redesign was to increase the stability of this mount.

The design of the input relay mount for the in-air prototype is shown in Figure 5.7. This mount allowed the fibre focus to be adjusted, accounted for the beam offset due to the tilted vacuum window, and allowed the entrance slit position to be set at the focus of the 100-mm focal length lens. As well, the entire relay could be adjusted in tilt, decentre and also be focused with respect to the collimator mirror. The height of the mount was set coarsely via a post within a holder (but could also be more accurately set via a grub screw within a collar on the post).

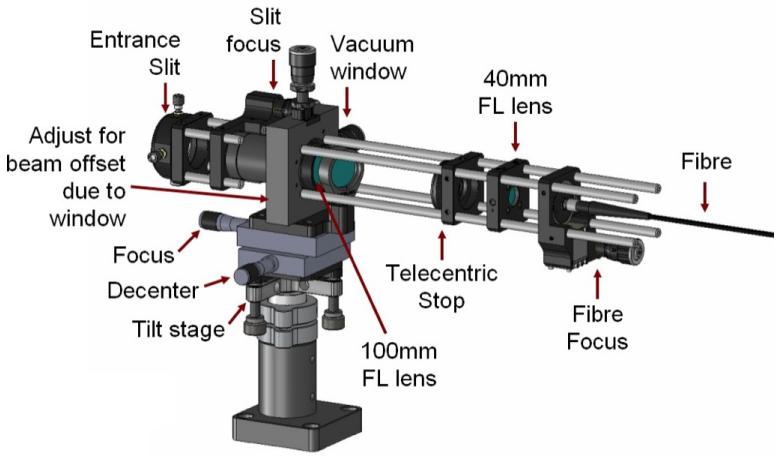

Figure 5.7: The input relay mount for the in-air prototype.

For the vacuum chamber prototype the relay was split into external and internal sections. This allowed for the vacuum chamber wall to be placed in the centre of the input relay (driven by the need to place the input vacuum window within a collimated light path).

The external section consists of the fibre exit, a 40-mm focal length collimating lens, and a telecentric stop. Figure 5.8 shows the major features of this mount and the adjustable degrees of freedom. To aid with the first assembly of the vacuum chamber prototype, many degrees of freedom were designed into this mount using OTS parts. It is envisaged that future versions of this mount could be simpler and less adjustable.

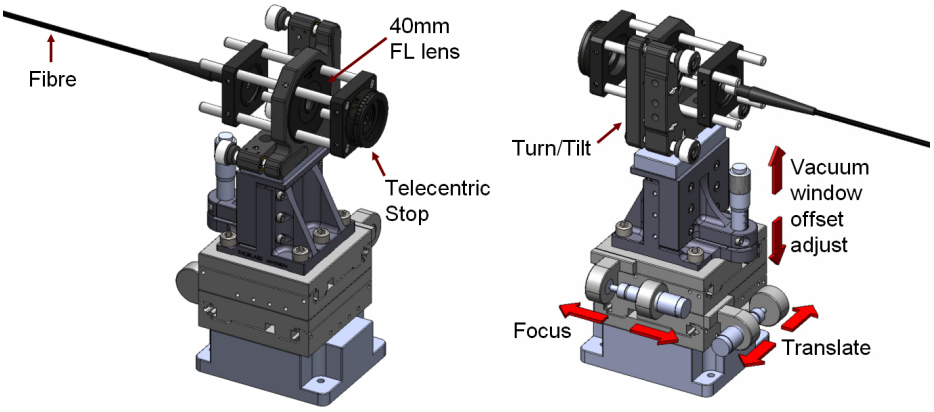

(a) Front view. (b) Rear view.

Figure 5.8: The external section of the input relay for the vacuum chamber prototype.

The internal section of the input relay consists of a 100-mm focal length lens and the entrance slit of the spectrograph. As is shown in Figure 5.9, the input relay mount is co-located on a pedestal with the input fold mirror mount (described in Section 5.6.4). The location of this pedestal is set using an alignment bar referenced off the échelle baseplate (as described in Section 5.5).

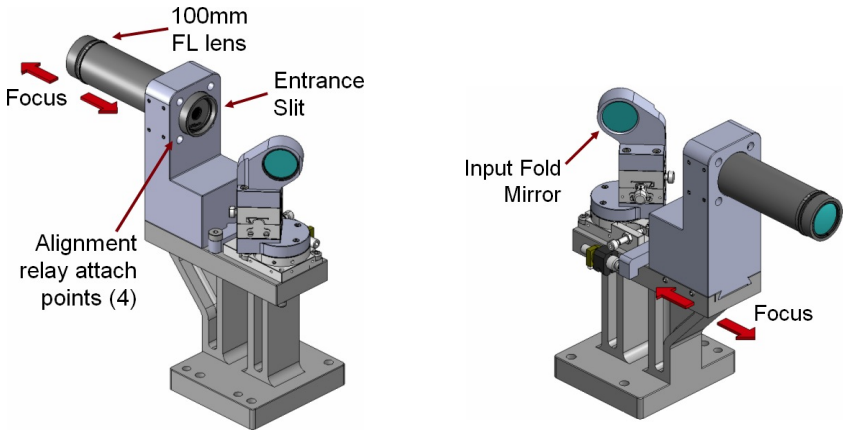

(a) (b)

Figure 5.9: The internal section of the input relay for the vacuum chamber prototype. The input fold mirror mount will be described in Section 5.6.4.

Within the internal input relay mount, the axial position of the 100-mm focal length lens can be adjusted to place the focus of the lens at the entrance slit position. Once the lens-slit spacing is set, the assembly of the lens and slit can be moved along a precision dovetail slide to set the entrance slit at

the focal point of the collimator mirror.

The input vacuum window lies between the external and internal input relays, as shown in Figure 5.10. The window is tilted at an angle of 20° to reflect a small percentage of the incoming light towards the exposure meter (which will be described in Section 5.6.3). The vacuum window is mounted at the end of a closed cylinder that attaches to the outside wall of the vacuum chamber. The interior of this cylinder is hollow to allow the 100-mm focal length lens to be positioned in the correct location behind the vacuum window. The internal input relay mount does not contact the vacuum chamber at any point.

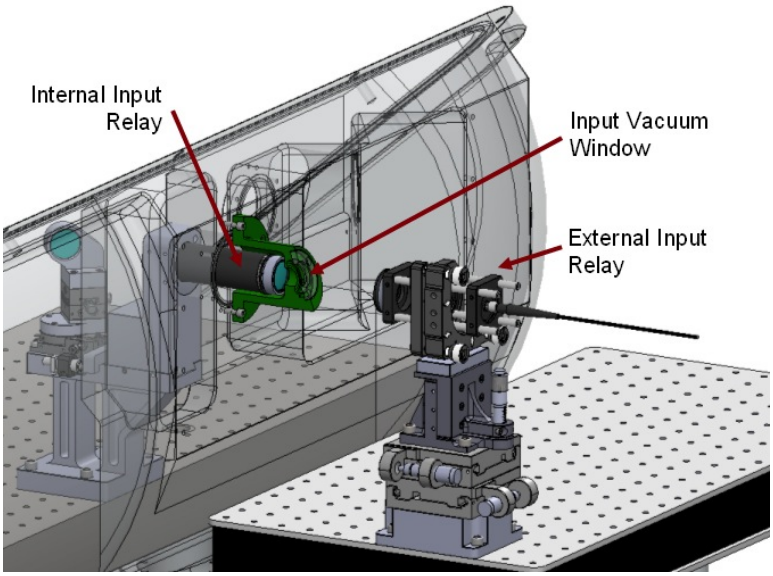

Figure 5.10: The input vacuum window is located between the internal and external sections of the input relay systems of the vacuum chamber prototype. For clarity, the vacuum chamber is shown as being transparent, and the vacuum window holder is coloured green and shown in cross-section.

The initial design of the vacuum chamber prototype allows a single entrance slit aperture to be mounted within the input relay mount. Future work will include the development of a mechanism to allow remote (computer-controlled) selection of the slit type (i.e. the choice between no slit, a pinhole, or a rectangular slit).

As an aid for initial alignment, the internal input relay mount accommodates the connection of a Thorlabs cage system assembly that contains the optical fibre, 40-mm focal length collimator lens and telecentric stop (shown in Figure 5.11). This method ensures that for initial assembly and alignment these components are located on the optical axis of the instrument. After initial assembly, the cage system is to be removed, and the vacuum window and the external input relay mount installed. Spectra taken before and after

the switch will be compared, and the external input relay mount adjusted until the two spectra match.

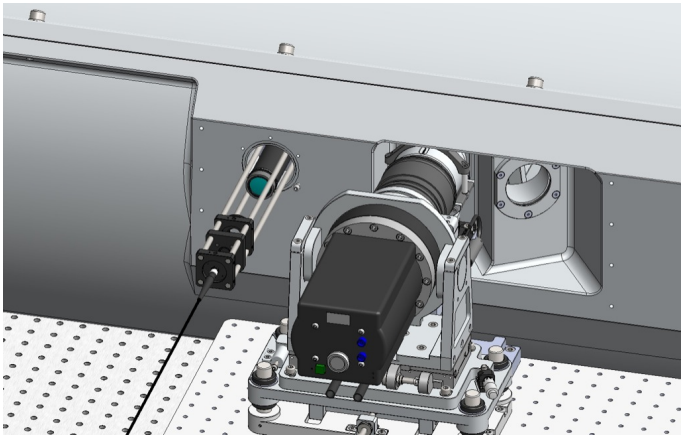

Figure 5.11: The KiwiSpec vacuum chamber prototype with the input relay alignment cage in place.

5.6.2 Iodine Cell Mount

The iodine cell mount is placed within the input relay system, and is located between the relay's telecentric stop and the input vacuum window. The mount is shown in Figure 5.12. This system was not included in the design of the in-air prototype.

During operation the cell is heated to 50°C to achieve the correct density of iodine gas within the cell. To minimize the amount of heat lost, the iodine cell is encased within an insulation block. This block is made from MultiPanel[2], a building insulation material which is easily machined. Further insulation will be provided within the MultiPanel block by surrounding the cell with an Aerogel-based thermal wrap.

The mount includes a motorized linear stage that allows the cell to move into and out of the light path (as some observing programs may not require the cell). The chosen Thorlabs stage offers the advantages of computer-controllable 50-mm linear travel, higher-than-required accuracy, and a minimal mechanical footprint.

5.6.3 Exposure Meter Mount

Described here is the exposure meter mount; the exposure meter device and location choice will be described in more detail in Chapter 8.

For the in-air prototype, the exposure meter was placed within a simple mount on the optical table as shown in Figure 5.1. Although it was not used as a pressure boundary, the vacuum window was included in the in-air

[2] `www.multipanel.com.au`

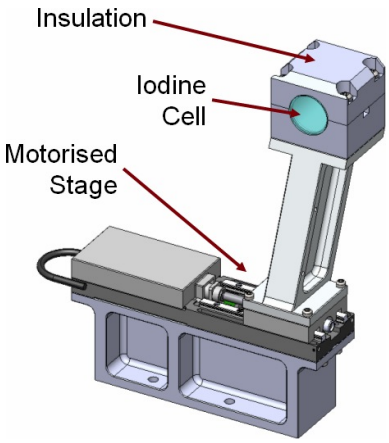

Figure 5.12: The iodine cell mount

prototype to reflect about 1 per cent of the light entering the spectrograph towards the exposure meter.

The design of the mount for the vacuum chamber prototype is shown in Figure 5.13. Compared to the in-air prototype, the orientation of the input vacuum window was changed to reflect light upwards towards the exposure meter. This was done mainly for mechanical convenience as it avoids interference with other mounts. Another advantage is that the exposure meter generates a subtle amount of heat, and placing it in an elevated position ensures that convection will not transfer the heat to other mounts. To further thermally isolate the exposure meter, an insulating G10 fibreglass spacer was designed into the mount.

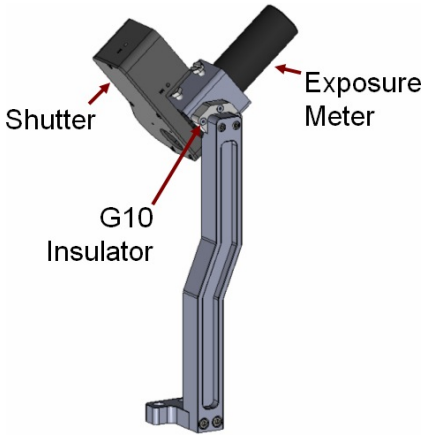

Figure 5.13: The exposure meter mount

The exposure meter itself is a photomultiplier tube (PMT), and is extremely sensitive to light (exposing it to room lighting while powered on can permanently damage the device). To protect the PMT, a normally-closed shutter is included in the mount design. This shutter is powered and controlled by a safety interlock circuit that monitors ambient light levels.

5.6.4 Input Fold Mount

For the in-air prototype, the mount for this 25-mm diameter mirror consisted of an OTS Thorlabs gimbal mount placed on a simple post as shown in Figure 5.14a. Fine adjustments included micrometer-driven turn and tilt movements that intersected on the face of the mirror. The other degrees of freedom were manually (and coarsely) set.

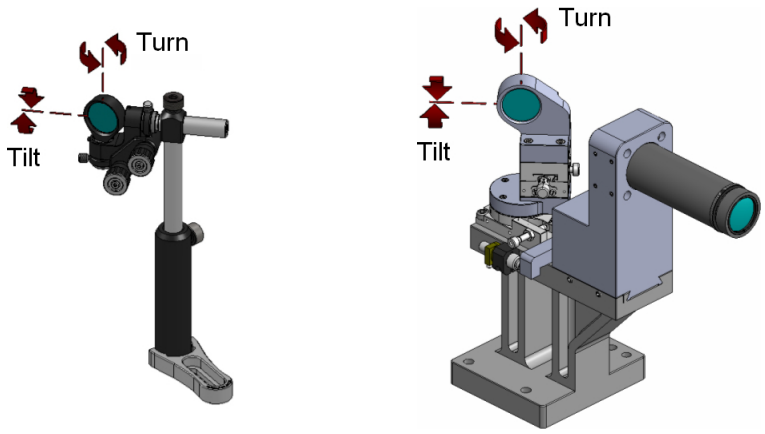

(a) In-air prototype version. (b) Vacuum chamber prototype version.

Figure 5.14: Input fold mirror mount with adjustable axes labelled.

However, this simple mount design did not prove adequate during the initial assembly of the in-air prototype, as the location of this mirror proved to be the most sensitive adjustment of the entire instrument. The translational position of this mirror determines the off-axis angle for the collimator mirror, and is also the first mirror in a complex light path that continues on to the primary collimator mirror, the échelle, the collimator mirror again, and then to the secondary collimator mirror. Owing to this long path length with multiple reflections, the location of the input fold mirror becomes critical for the light rays to strike each mirror in the appropriate places. This positional sensitivity was not fully appreciated until alignment was underway.

In order to simplify the input fold alignment and also to increase the stability of the mount, the mount was redesigned for the vacuum chamber prototype (Figure 5.14b). In this design, the mirror is co-located on a platform with the internal input relay. The platform is mechanically located using an alignment bar referenced to the échelle mount baseplate (see Section 5.5).

The mount allows the mirror to be adjusted in both turn and tilt through the combination of an OTS vacuum compatible rotation stage and goniometer. The two rotational axes intersect at the centre of the mirror, and the rotary stage is placed under the goniometer to ensure independent horizon-

tal and vertical rotations. The mirror height is set by machining, and the mirror is held within the cell with a retaining ring.

5.6.5 Primary Collimator Mirror Mount

The design of the in-air primary collimator mirror mount is shown in Figure 5.15. The mount design includes three adjustable degrees of freedom: tilt, turn, and off-axis clocking. Note that the tilt and turn adjustments intersect at the parent vertex, and not at the centre of the off-axis section. Each of the three adjustments is designed into the custom mount, and each has a locking mechanism.

The basic design of the mirror holder section of this mount is a 'cell within a cell' arrangement. The mirror is potted into an inner cell by six RTV pads symmetrically distributed around its periphery. A flat annulus was ground around the edge of the front surface of the mirror so as to act as a mechanical reference to accurately locate the mirror within its mount. This annulus was then carefully measured and the inner cell machined to suit. The inner cell slides into an outer cell that interfaces with the fork mount base, and is free to rotate within the outer cell to give the off-axis clocking adjustment.

The design of this mount proved satisfactory during testing of the in-air prototype and the only change for the vacuum chamber prototype was swapping the three micrometers to vacuum-compatible fine-thread actuators.

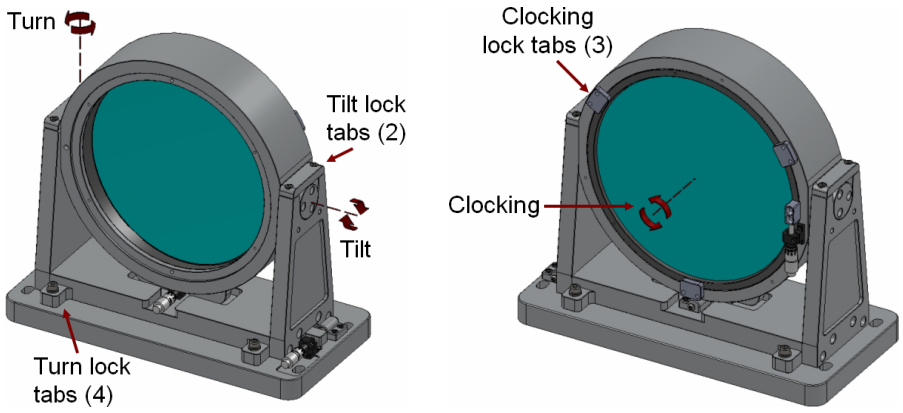

(a) Front view. (b) Rear view.

Figure 5.15: Primary collimator mount with fine adjustable axes labelled.

5.6.6 Échelle Mount

The design of the échelle grating mount is shown in Figure 5.16. The mount allows for fine adjustment of the échelle angle of incidence (α) and gamma (γ) angles, with the two axes intersecting on the surface of the grating at

the centre of the ruled area. The grating and its cell are largely balanced in the fork, with a slight weight bias towards the rear of the cell due to the α-adjustment 'tailpiece'. A pair of preload springs at the rear of the mount also ensure that the cell remains in contact with the α adjust actuator. Both of the α and γ movements can be locked in place after adjustment.

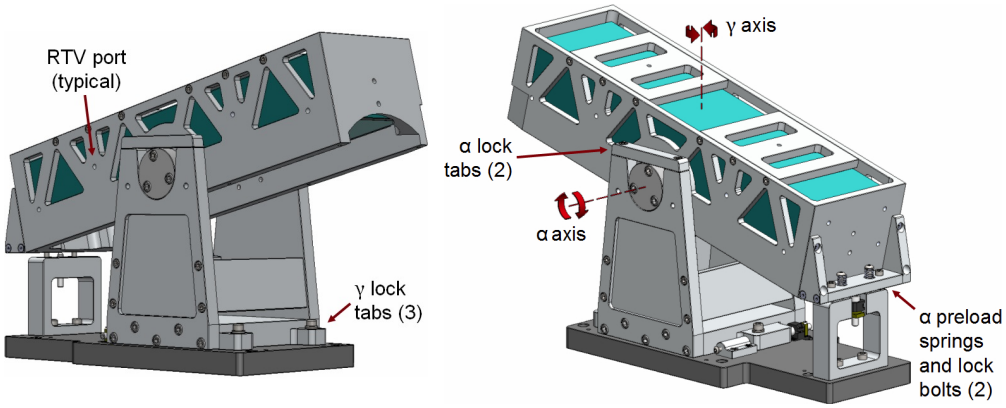

(a) Front view. (b) Rear view.

Figure 5.16: The échelle mount with fine adjustable axes labeled.

The échelle grating is mounted within a cell machined out of a single piece of aluminium, with two separate top plates employed to contain the grating. The grating faces downwards within its cell to protect it from dust accumulation and accidental contact or damage. As the ruled area of the échelle grating does not extend completely to the edges of the Zerodur substrate, there is a 4-mm gap available on each side of the ruled area that was used to support the grating. Twelve discrete pads (six per side) were machined into the échelle cell to support the grating, with a thin (0.1-mm) mylar sheet acting as a buffer between the aluminium cell and the grating substrate. These pads support the weight of the grating, while several discrete RTV pads around the sides and top of the grating keep it centered within the cell.

Finite element analysis (FEA) was employed to determine if the self-weight of the 7.7-kg grating would introduce distortions within the active area of the grating. Two situations were modeled for the current mounting arrangement (as shown in Figure 5.17): the best-case scenario with the grating in contact with all 12 support pads, and the worst-case scenario with only three widely-spaced pads in contact with the grating. Also included within the FEA model were five other support points that contact the lower end of the grating (i.e. the end of the grating facing towards the right in Figure 5.17). These were included to simulate the RTV pads located within the cell which prevent the échelle from 'sliding' downwards as a result of gravity.

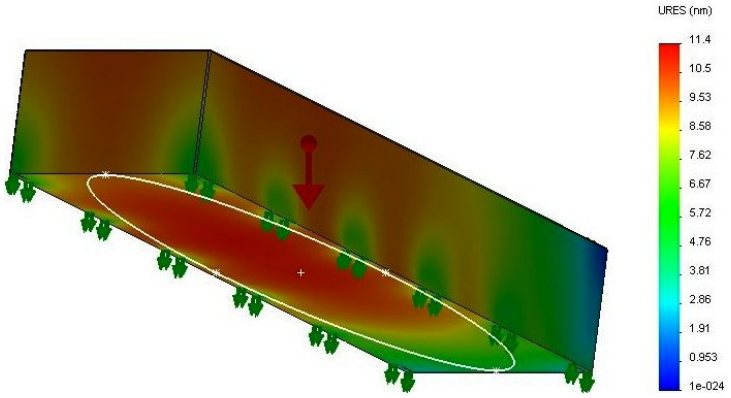

(a) Equally supported by 12 pads outside of the ruled area (best case).

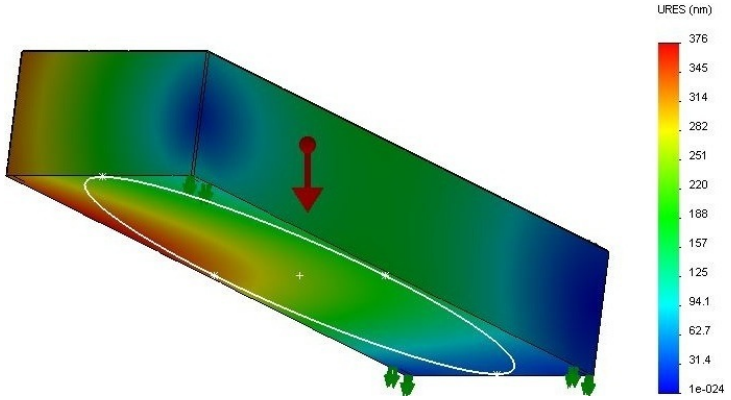

(b) Supported by three widely separated pads outside of the ruled area (worst case).

Figure 5.17: FEA results showing the self-weight deflection of the échelle grating for two mounting configurations. Note the scale difference between the two figures. The ellipse drawn on the face of the grating indicates the active area. The red arrows indicate the gravity vector and the green arrows indicate the fixed points used during the simulation run. Not visible in the views presented are fixed points contacting the right (lower) end of the grating.

Based on the FEA analysis, when the grating is supported by 12 pads along its sides the maximum deflection due to self-weight equals 11.4 nm. At the KiwiSpec prototype's central wavelength of $\lambda = 540$ nm, this equates to an insignificant $\lambda/47$. For the worst-case situation of the grating contacting 3 widely separated pads, the maximum deflection due to self-weight within the active area equals 356 nm (or 0.66λ). Because of the slight compliance of the mylar sheet between the grating and the aluminium cell, it is likely that the actual deflection lies somewhere between these two values.

The worst-case scenario value of 0.66λ is slightly more than the 0.56λ peak-to-valley (PV) surface deformation present (at $\lambda = 540$ nm) on the grating itself (as indicated by the Richardson Gratings interferometric test report shown in Figure 5.18). The actual deflection of the grating will be a combination of these two effects, and will remain constant during use as the échelle grating does not experience a changing gravity vector.

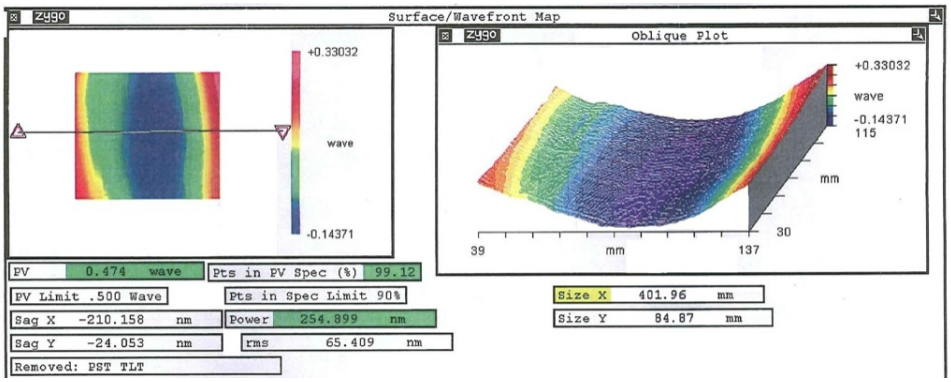

Figure 5.18: The interferometric test report of the KiwiSpec échelle grating (supplied by Richardson Gratings). Note that the values within this report are with respect to a wavelength of 632.8 nm.

If one assumes that the grating will rest only on three pads, then a possible future approach would be to redesign the grating cell to support the échelle at three locations based on the Airy points. The Airy points specify support points under a bar of material that cause the minimum deflection due to self-weight. For a bar of length L, they are located a distance of $\frac{L}{2\sqrt{3}}$ from the centre of the bar.

To adapt this approach to supporting the échelle face-down (using the area of the grating outside the ruled area), two supports could be placed at the Airy points on one side of the grating, with the third support at the centre of the opposite side. The FEA results for this mounting arrangement are shown in Figure 5.19. The maximum deflection within the ruled area is 120 nm (or 0.22λ at $\lambda = 540$ nm), a definite improvement over the the 0.66λ for the worst-case scenario of three widely spaced pads.

One final mounting arrangement explored with FEA analysis involves

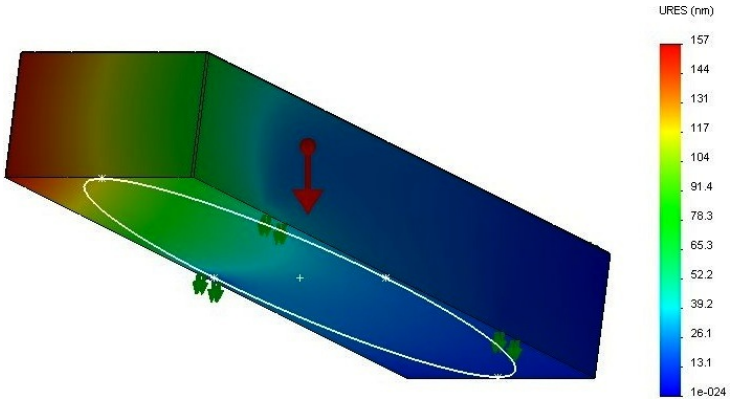

Figure 5.19: FEA results showing the self-weight deflection of the échelle grating when supported by three points on the front of the grating (outside of the ruled area), with locations based on the Airy point principle. The ellipse drawn on the face of the grating indicates the active area. The red arrows indicate the gravity vector and the green arrows indicate the fixed points used during the simulation run. Not visible in this view are fixed points contacting the right (lower) end of the grating.

mounting the échelle grating with three support points on its back (with the ruled area facing upwards). This arrangement has the advantage that the support points can be placed anywhere on the back surface as they do not interfere with the ruled area of the grating. The three support points employed for the analysis, with locations based on the Airy point principle, are shown in Figure 5.20. Results of the FEA analysis are shown in Figure 5.21, which indicate that this mounting approach shows the smallest deflection of all of the scenarios considered (30.3 nm or 0.06λ at $\lambda = 540$ nm). However, this arrangement has the major practical disadvantages of exposing the ruled surface of the échelle to contamination and dust, and also potential damage from accidental contact (from fingerprints or tools during assembly). For these reasons it was decided to mount the KiwiSpec échelle grating as described above, with the ruled area facing downwards.

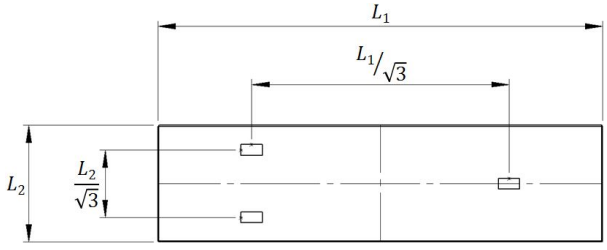

Figure 5.20: Location of three potential support points on the back of the échelle grating, with locations based on the Airy point principle.

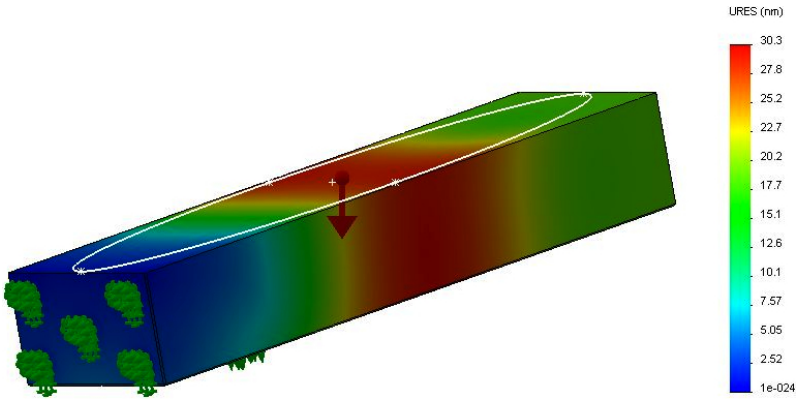

Figure 5.21: FEA results showing the self-weight deflection of the échelle grating when supported by three Airy points on the rear of the grating, with the ruled area facing upwards. The ellipse drawn on the face of the grating indicates the active area. The red arrows indicate the gravity vector and the green arrows indicate the fixed points used during the simulation run. Visible in this view are the fixed points contacting the left (lower) end of the grating.

A brief survey of other fibre-fed spectrographs indicates that a variety of échelle mounting positions are employed. The CHIRON instrument design (Schwab et al., 2010) orients the échelle grating facing upwards, whereas the HERMES (Raskin et al., 2011) and FEROS (Kaufer et al., 1997) instruments employ the échelle grating facing downwards. The HARPS (Mayor et al., 2003) and SOPHIE (Perruchot et al., 2008) instruments place the échelle grating on its side, with the stated intent (for HARPS) being to orient the grating grooves parallel to the direction of gravity for reasons of stability. This orientation, however, is not practical with the KiwiSpec design, as all of the optical elements after the échelle would need to rotate by 90 degrees. Such a rotation would greatly complicate the mechanical design, and would also introduce a large amount of vignetting caused by the mechanical mounts near the intermediate focus.

Overall, the KiwiSpec échelle mount described above proved satisfactory during testing of the in-air prototype, and the only change for the vacuum chamber prototype was swapping the two micrometers to vacuum-compatible fine-thread actuators.

5.6.7 Secondary Collimator Mount

The design of the secondary collimator mount is shown in Figure 5.22. The mount allows the mirror to be moved in turn with an OTS rotation stage, and moved in tilt via an actuator in the custom mount. A linear stage also provides a focus adjustment between the primary and secondary collimator mirrors to accommodate the as-built focal lengths of these two mirrors (which will differ from the nominal values due to manufacturing tolerances).

All of the adjustment movements are lockable.

The mirror is held within its cell via six RTV pads around its periphery. It is mechanically referenced within the cell via two flat faces ground into the top and bottom of the mirror face.

This mount worked well for the in-air prototype, and was only slightly redesigned for the vacuum chamber prototype as the OTS linear and rotational stages had to be exchanged for vacuum compatible versions. The tilt actuator was also changed from a micrometer to a vacuum-compatible adjustment screw.

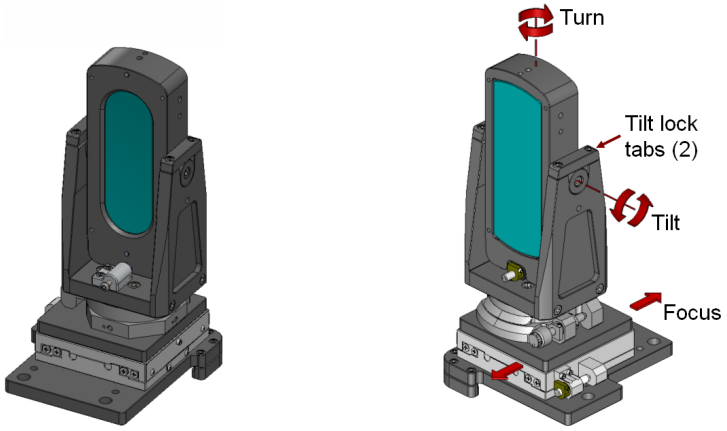

(a) Front view. (b) Rear view.

Figure 5.22: Secondary collimator mount with adjustable axes labeled.

5.6.8 Camera Fold Mount

The design of the camera fold mirror mount for the in-air prototype is shown in Figures 5.23a and 5.23b. A goniometer with a precision-thread actuator was used for tilt, and a manual rotation stage was employed for turn. Height was coarsely set with a vertical post within a holder but could also be more accurately set via a grub screw within a collar on the post.

The rotational sensitivity of this mirror was not fully appreciated until alignment of the in-air prototype. Small adjustments of the turn and tilt of this flat fold mirror do not affect image quality, but they have a very large effect on the position of the spectrum on the detector. Furthermore, the turn and tilt angles of this mirror are important, as they set the optical axis for the grism, camera lens and detector that follow it.

As described above, for the in-air prototype the mirror was placed on a manual rotational stage without a precision actuator for the turn adjustment. It was quickly realized during alignment that this was not sufficient, and also that the required sensitivity of turning the mirror was increased because rotating the mirror by θ° moves the reflected beam by $2\theta^\circ$.

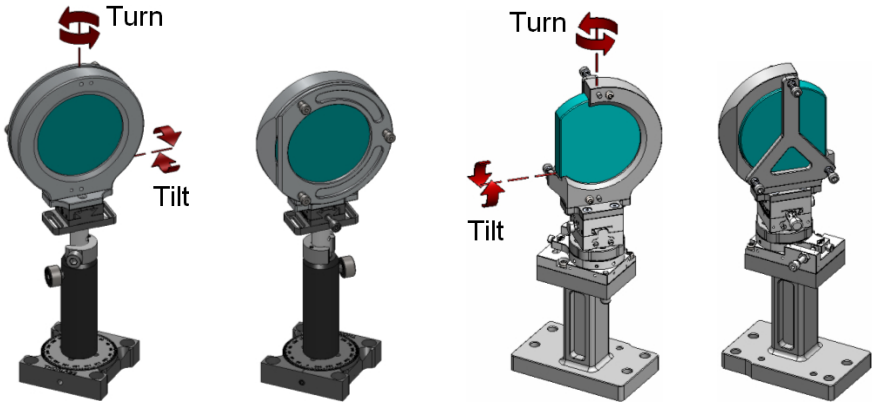

(a) Front view. (b) Rear view. (c) Front view. (d) Rear view.

Figure 5.23: The camera fold mirror mount for the in-air prototype ((a) and (b)) and the vacuum chamber prototype ((c) and (d)).

The camera fold mount was redesigned for the vacuum chamber prototype to address the above issues, and is shown in Figures 5.23c and 5.23d. The baseplate of the mount is now located on the optical table using an alignment bar referenced from the échelle mount baseplate (see Section 5.5), the turn axis is adjusted via a vacuum-compatible rotational stage with a fine-thread actuator for adjustment, and tilt is set with a vacuum-compatible fine-adjustable goniometer stage. The two rotational axes intersect on the face of the mirror, and the rotary stage is placed under the goniometer to ensure independent horizontal and vertical rotations. The height of the mount is fixed by machining.

The mirror shape was also changed from circular to a 'D' shape so that the mirror does not collide with the vacuum chamber wall. The mirror face is mechanically located against three raised pads within the mirror cell, and held in place by a spring-loaded plate that provides force in-line with the raised pads to avoid imparting stress into the mirror.

5.6.9 Grism Mount (in-air prototype)

The design of the grism mount for the in-air prototype is shown in Figure 5.24. The prisms within the grism used in the prototype instrument were designed to have cylindrical edges so that the entire grism could be mounted within a cylindrical tube. The location of the grism within the tube is set by two spacers held by a retaining ring. This assembly rests within a cradle, which allows it to be rotated with low precision to set the grism clocking (which is locked in place with the top clamp). The cradle features an indicator which points to fiducials on the grism holder marked in 1° increments. The height and turn of the mount were coarsely set by adjusting the bottom post within its holder.

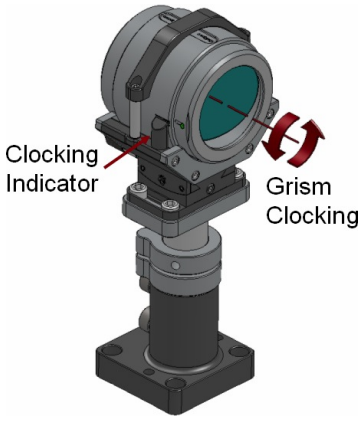

Figure 5.24: The grism mount for the in-air prototype.

The grism holder and cradle from the in-air prototype grism mount were retained for the vacuum chamber prototype. They were combined with the Hasselblad lens and field flattening lens mounts to form the camera arm mount, which is described in detail in Section 5.6.11.

5.6.10 Hasselblad and Field Flattening Lens Mount

The design of the Hasselblad and field flattening lens mount from the in-air prototype is shown in Figure 5.25. Tilt adjustment was accomplished with a tilt-plate system actuated by a micrometer. Turn was adjusted via an OTS rotation stage. The height was coarsely set with a post in a holder, but could also be more accurately set via a grub screw within a collar on the post.

Focus was achieved by simply rotating the existing focus ring on the Hasselblad lens, which translates the camera lens along the optical axis (the Hasselblad is a fixed focal length lens). Focus was motorized through a simple system that consisted of a stepper motor driving a belt stretched over the Hasselblad focus ring. For the in-air prototype, the field flattening lens was fixed and did not translate during a focus adjustment.

It was not possible to attach the shutter directly to the detector, as optically it is desirable to have the field flattening lens as close as possible to the detector. Therefore the shutter was placed between the Hasselblad lens and the field flattening lens. The shutter is controlled by the Spectral Instruments detector.

Experience with the in-air prototype showed this mount to have unnecessary degrees of freedom and adjustment. Therefore, this mount was redesigned and simplified for the vacuum chamber prototype, as described in Section 5.6.11.

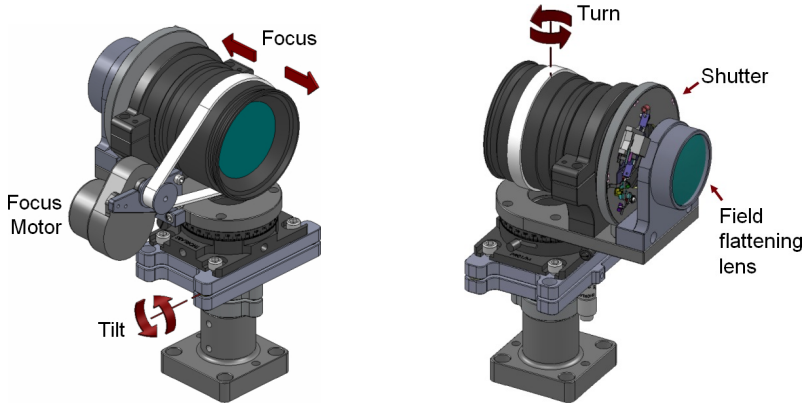

(a) Front view. (b) Rear view.

Figure 5.25: The Hasselblad and field flattening lens mount for the in-air prototype.

5.6.11 Camera Arm (vacuum chamber prototype)

During assembly of the in-air prototype, it was realized that alignment would be improved if the grism, Hasselblad lens, and field flattening lens were co-mounted on a single platform. The optical tolerancing results also showed that machining tolerances could be relied upon to accurately locate these mounts with respect to each other – and with higher accuracy than if the components were mounted separately. The camera arm mount is shown in Figure 5.26. Included in the design is a 'locator block' that allows the camera arm to be removed from the instrument and replaced at the same location. This option is useful during assembly for removing (or installing) the grism.

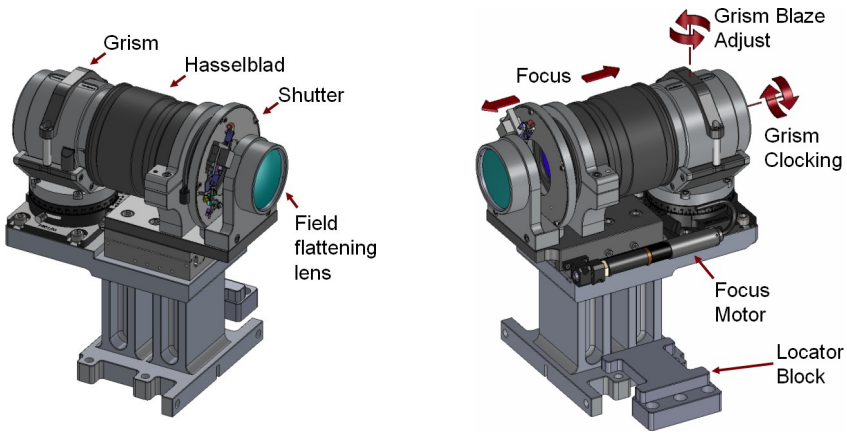

(a) Front view. (b) Rear view.

Figure 5.26: The camera arm mount for the vacuum chamber prototype.

The grism holder and cradle were carried over from the in-air prototype (see Section 5.6.9). In the camera arm design, these components are mounted on an OTS rotary stage to allow shifting of the grism blaze wavelength (a technique to be described more in Section 7.2.5.4). As well, the Hasselblad cradle, shutter holder, and field flattening lens cell were carried over from the in-air prototype designs.

Focusing the Hasselblad lens within the in-air prototype showed that when the focus ring reversed direction, the spectrum shifted noticeably on the detector. For this reason, and also because future, custom-designed lenses would not have such a focusing ring, the focus mechanism was changed. For the vacuum chamber prototype, the camera lens is mounted on a linear stage, and the focus position is actuated by a servo-motor driving a leadscrew.

5.6.12 Detector Mount

The design of the detector mount is shown in Figure 5.27. The mount allows the detector to turn and tilt, and also scan the image plane with up/down and left/right translations. The turn and tilt adjustments are designed into the mount and are actuated by micrometers. Horizontal scanning is executed via two Newport linear stages ganged together and actuated by a micrometer. Vertical scanning is accomplished with a set of moving wedges contacting a set of stationary wedges, with a linear bearing at each corner of the mount to constrain the movement. Vertical scanning is controlled by a coarsely threaded actuator.

To ensure independent adjustments, the turn and tilt rotation axes intersect on the surface of the CCD. The order of the adjustment 'stack' was set to allow for scanning of the image plane while maintaining the nominal detector turn and tilt. If this were not the case one would have to re-optimize the detector turn, tilt and focus after each translation across the focal plane.

The orientation of the detector within the mount was set by the location of the water chiller hose connectors and also the orientation of the CCD columns. Placing the water chiller hoses at the bottom of the detector was driven by failure concerns (i.e. if the water chiller hoses develop a leak, the water will drip harmlessly away from the detector itself).

The CCD columns were oriented perpendicular to the échelle dispersion direction. With this approach, a potentially bad column will cross several échelle orders but will only affect an insignificant one-pixel-wide section of each order. This is more desirable than the alternative orientation where a bad column would remove a one-pixel-wide strip along an entire échelle order. A further advantage of this orientation is that strong emission lines which saturate the detector will leak charge between the échelle orders and not along them.

The detector mount was designed to scan the image plane because the

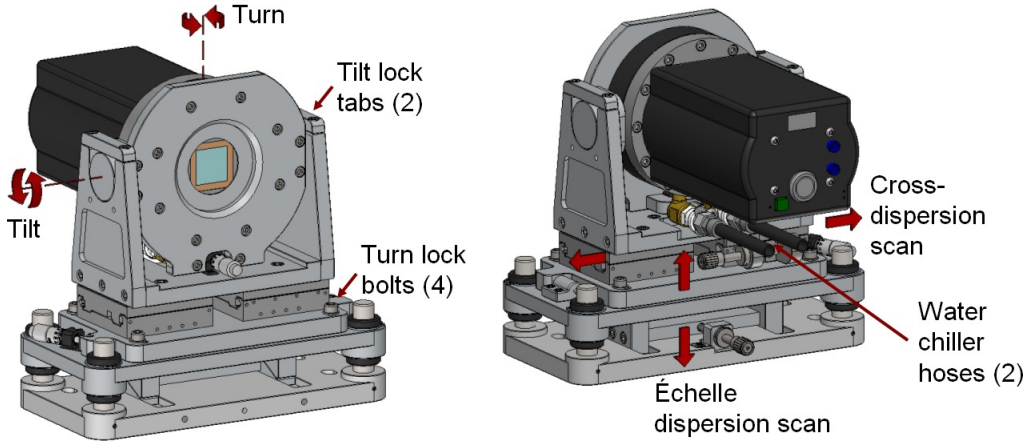

(a) Front view. (b) Rear view.

Figure 5.27: The detector mount.

size of the CCD used in the KiwiSpec prototype is slightly too small to cover the entire spectral format without gaps in the continuous spectrum. This was a deliberate compromise made for the prototype which allowed the use of a detector and camera lens that were both OTS and readily available. The mount movement provides a maximum of ± 5 mm of travel with respect to a nominal position in the cross-dispersion and échelle dispersion directions, and is shown diagrammatically in Figure 5.28. In the cross-dispersion direction, this allows a movement towards the blue of approximately 16 orders, or redward of approximately five orders (with a loss of order coverage in the direction opposite to the movement). In the échelle dispersion direction, there is enough travel to move to one side of each free spectral range out to order number 83 ($\lambda_B = 736$ nm), although with a corresponding loss at the opposite end of the orders (and a resulting shift in the locations of the gaps within the continuous spectrum).

The detector mount worked well for the in-air prototype, and no substantial changes were made for the vacuum chamber prototype. Future versions of KiwiSpec with a custom camera lens will have a camera focal length optimized for the pixel size and overall dimensions of the CCD employed. In such a situation the image plane scanning feature of the current mount could be discarded, with only the turn and tilt adjustments remaining.

5.7 Focus Method

For the in-air prototype, the camera focus was adjusted by moving only the Hasselblad lens (the field flattening lens was fixed and did not move during focusing). This approach was chosen out of convenience as the Hasselblad lens features a built-in focus ring mechanism.

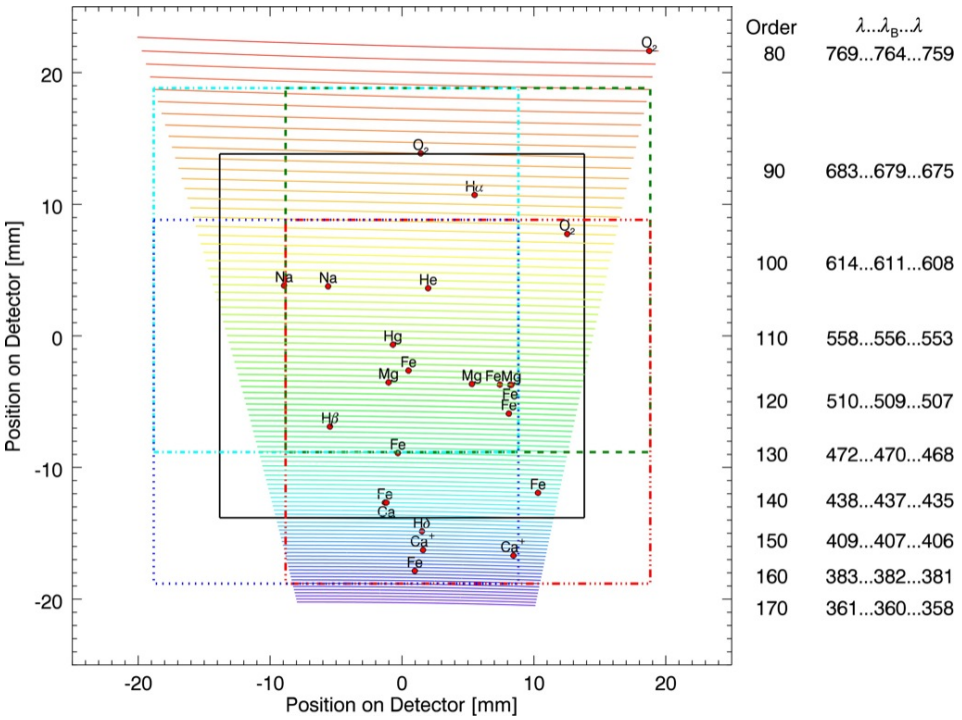

Figure 5.28: The detector mount allows the detector to scan around the image plane. Nominal detector position is shown by the central box with a solid line; other boxes with dashed and dotted lines indicate the maximum movements of the detector in the échelle- and cross-dispersion directions. One free spectral range is plotted for each échelle order, and major Fraunhofer lines are indicated.

As described in Section 5.6.11, for the vacuum chamber prototype the focus method was changed so that the Hasselblad was translated on a linear stage. During the redesign process it was realized that a mechanical simplification could occur if the field flattening lens was also translated by the same stage. Therefore, the two focus methods were investigated using Zemax to determine the effect of each.

This analysis determined that focusing with both the Hasselblad and the field flattening lens together is clearly the superior solution, as the focal length of the camera lens does not change during focus adjustments. The results are shown in Figure 5.29.

Also investigated was how the optimized detector turn and tilt are affected by defocus. This analysis was motivated by effects noticed while aligning and focusing the in-air prototype. As Figures 5.30 and 5.31 show, the optimal detector turn and tilt values (based on smallest spot sizes) are a function of defocus position. Therefore, in practice the focus should always be set before finalizing the detector turn or tilt angles. Figures 5.30 and 5.31 also indicate that neither focusing method is superior with respect to the optimal detector turn or tilt for a given defocus position.

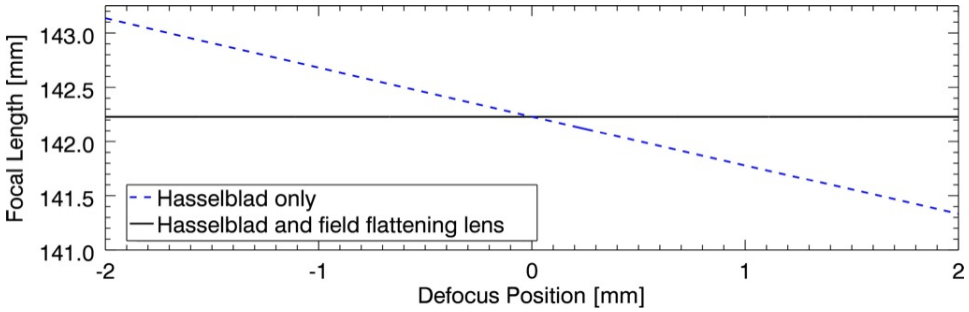

Figure 5.29: Change in focal length of the camera system (the Hasselblad plus field flattening lens) for two possible focus methods. The camera system focal length changes when the Hasselblad is moved with respect to a stationary field flattening lens, but does not change when the two lenses are moved together. Plot values determined using Zemax.

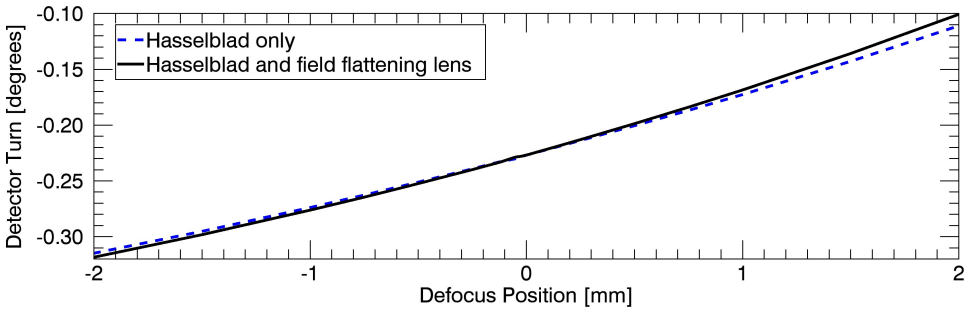

Figure 5.30: How the optimal detector turn setting (based on smallest spot sizes) changes with defocus for the two focus methods. Plot values determined using Zemax.

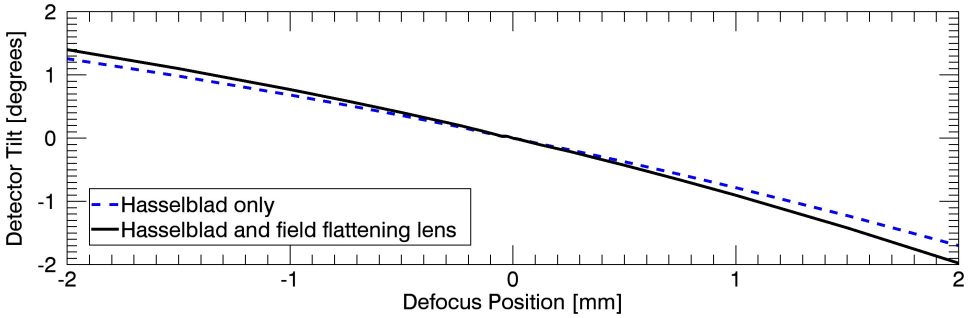

Figure 5.31: How the optimal detector tilt setting (based on smallest spot sizes) changes with defocus for the two focus methods. Plot values determined using Zemax.

Chapter 6

Vacuum Chamber System

6.1 Motivation

Decoupling a spectrograph from its environment to improve stability is the primary reason for placing the instrument within a vacuum chamber. Specifically, the role of the vacuum chamber is to prevent changes in the refractive index of air in the vicinity of the échelle grating.

When a light wave crosses a boundary between two media with different refractive indices, the frequency of the light remains constant but the wavelength and the velocity of the wave change. With regard to spectrograph stability, the change in wavelength is of particular concern. As shown in Figure 6.1a, when light of a given wavelength λ_0 is incident on a diffraction grating, it is diffracted at an angle β_0 as governed by the grating equation. However, if at some later time (Figure 6.1b) the échelle is surrounded by a cell of air with a different refractive index (caused by an environmental change in pressure, temperature or relative humidity), the light will change wavelength at the boundary. This changed wavelength, λ_1, will then strike the échelle and diffract at a different angle, β_1. This situation occurs for all wavelengths, and the net effect is that the change in the angle of diffraction causes the spectrum to move on the detector, mimicking a radial velocity shift of the science object.

6.1.1 Effect of Refractive Index of Air Instability

The refractive index of air is a function of temperature, pressure, and relative humidity. The effect of a change in the refractive index of air on radial velocity stability was investigated using the National Institute of Standards and Technology (NIST) 'Engineering Metrology Toolbox Refractive Index of Air Calculator'[1]. This tool is based on a modified[2] version of the Edlén equation (Edlén, 1966), which calculates the refractive index of air for a set

[1] Online tool: `http://emtoolbox.nist.gov/Wavelength/Edlen.asp`

[2] See documentation at:
`http://emtoolbox.nist.gov/Wavelength/Documentation.asp#References`

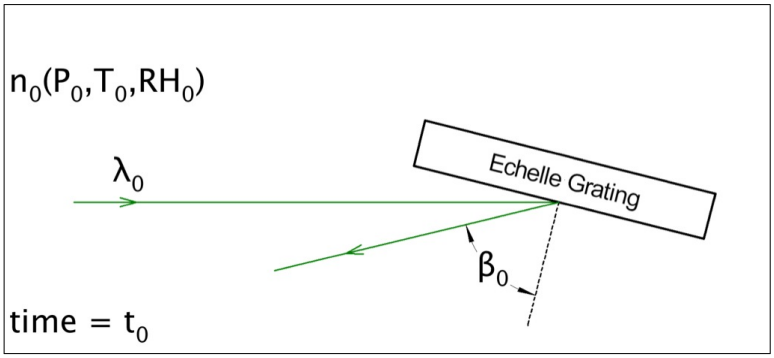

(a)

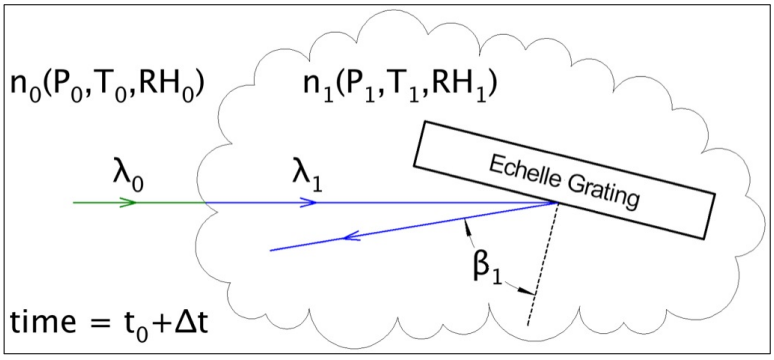

(b)

Figure 6.1: When light of wavelength λ_0 crosses a boundary of refractive index, the frequency of the wave is conserved but both the wavelength and the speed of the wave change. If the light then strikes a diffraction grating, this leads to changes in the angle of diffraction for a given wavelength λ_0.

of temperature, pressure and humidity values. An IDL-based version of the online calculator was also developed by the author using equations provided on the NIST website. The IDL program listing is included in Appendix A.

The general methodology of using the NIST modified Edlén equation involves determining a baseline wavelength in air for a given vacuum wavelength, air temperature, pressure and relative humidity. One or more environmental parameters are then changed and a new wavelength in air calculated for the changed environment (but using the same vacuum wavelength). The difference between the two wavelengths in air is then converted to a velocity shift using the Doppler equation:

$$\Delta v = \frac{\Delta\lambda \cdot c}{\lambda_{\text{vacuum}}}, \tag{6.1}$$

where:

Δv	=	velocity change;	[m/s];
c	=	speed of light;	[m/s];
$\Delta\lambda$	=	wavelength change;	[nm];
λ_{vacuum}	=	vacuum wavelength	[nm].

Changes in the refractive index of air can have a very large effect on the radial velocity stability of a spectrograph, as shown in Figure 6.2. For a spectrograph sitting in-air without environmental control, the values used in Figure 6.2 are indicative of changes that could be experienced over the course of an hour.

6.1.2 Stability Goal

The goal of the addition of the vacuum chamber is to increase the absolute radial velocity stability of the instrument. Of importance is to maintain the desired level of stability over the course of the longest practical exposure time (plus the exposure times of the before and after calibration spectra). For the KiwiSpec design process, this time was assumed to be one hour.

The working goal is to attain better than 10 m/s in absolute stability over the course of one hour, with an ideal goal of attaining closer to 1 m/s in absolute stability over the course of one hour. With the instrument in a vacuum chamber and with the use of an iodine cell (one method of contemporaneous calibration), it is expected that precisions close to (and ideally better than) 1 m/s will be achieved.

In the sections below several different parameters are analysed to determine their individual effects on the stability of the instrument. It should be noted, however, that the stability of the entire instrument will be the sum of the interaction of all such parameters.

6.2 Description of KiwiSpec Vacuum Chamber System

This section will discuss various aspects of the KiwiSpec vacuum chamber system.

6.2.1 System Overview

The KiwiSpec vacuum chamber does not enclose the entire instrument, but rather has components at atmospheric pressure and components under vacuum. Vacuum windows in the chamber wall allow light to pass into and out of the chamber. Components outside of the chamber include half of the input relay, and the camera arm (grism, camera lens, shutter, and detector). Components within the vacuum chamber include the second lens of the input relay, the entrance slit, the primary collimator, the échelle, the secondary

Temperature:	ΔT = +1 C			
Baseline:				
Vacuum Wavelength:	500 nm		Wavelength in air (baseline):	499.863146 nm
Temperature:	20 C			
Pressure:	101.325 kPa			
Relative Humidity:	50% percent			
Temperature changed to:	21 C		Wavelength in air (after change):	499.863626 nm
			delta lambda:	0.00048 nm
			corresponds to RV of:	287.8 m/s
Pressure:	ΔP = +0.1 kPa	(1 mbar)		
Baseline:				
Vacuum Wavelength:	500 nm		Wavelength in air (baseline):	499.863146 nm
Temperature:	20 C			
Pressure:	101.325 kPa			
Relative Humidity:	50% percent			
Pressure changed to:	101.425 kPa		Wavelength in air (after change):	499.863011 nm
			delta lambda:	-0.000135 nm
			corresponds to RV of:	-80.9 m/s
Relative Humidity:	ΔRH = +10%			
Baseline:				
Vacuum Wavelength:	500 nm		Wavelength in air (baseline):	499.863146 nm
Temperature:	20 C			
Pressure:	101.325 kPa			
Relative Humidity:	50% percent			
Humidity changed to:	60 %		Wavelength in air (after change):	499.863188 nm
			delta lambda:	4.2E-05 nm
			corresponds to RV of:	25.2 m/s

Figure 6.2: Effects on radial velocity due to independent changes in temperature, pressure and relative humidity. For a given change of one parameter (temperature, pressure or relative humidity), the corresponding change in wavelength is calculated, which is then converted to an equivalent change in radial velocity with the Doppler equation (Equation 6.1). Calculations were made using the NIST modified Edlén equation as explained in the text.

collimator, and the camera fold mirror. Although the KiwiSpec prototype is a single-channel instrument, the vacuum chamber was designed to accommodate two channels (each comprised of a grism, camera, and detector), and in such a configuration would have two output vacuum windows.

This design was chosen as being preferable to placing more components (or the entire instrument) within the vacuum chamber. Reasons for this approach include:

Future upgrade path: One of the advantages of the KiwiSpec design is that it is configurable and can accommodate multiple camera arms. Leaving the camera arm entirely outside of the vacuum chamber means that the size of the chamber is not dependent on the number of camera arms present. With the current prototype vacuum chamber design, it is envisioned that a second channel could be added at any point without any changes required of the vacuum chamber itself.

Detector cost: The cost of a vacuum compatible version of the Spectral Instruments 850S camera would be approximately $1.5-2\times$ the price of the standard version. In a multi-channel instrument, this cost increase would apply to each detector employed.

Chamber size and cost: A vacuum chamber that enclosed the entire instrument would need to be much larger than the current design. It would also need to be stronger to resist the increased atmospheric force acting on its greater surface area. This would increase the mass, footprint and probably the complexity of the chamber. As well, a larger chamber would certainly be more expensive to manufacture and to transport.

Vacuum compatibility of components: Locating the camera arm outside of the vacuum chamber means that the grism, camera and detector mounts, the shutter, the detector and the focus motor do not need to be vacuum compatible.

Detector electrical and cooling lines: The detector requires electrical power and data lines, as well as some form of coolant system (water chiller hoses in the case of the KiwiSpec prototype detector). It is therefore much simpler to place it outside the chamber and not have to use feedthroughs to pass cables and hoses through the chamber wall. In the case of a multi-channel instrument, each detector would require its own feedthroughs, complicating the mechanical design of the chamber.

6.2.2 Vacuum Window Locations

The location of the vacuum windows was driven by the need to place the windows at mechanically convenient locations, and also within collimated spaces in the optical design (see Section 6.3.1). The input window is located in the collimated space of the input relay, whereas the output windows are located in the collimated space between the camera fold mirror and the grism, as shown in Figure 6.3. The vacuum windows are nominally plane-parallel, but have a slight wedge present to avoid interference effects. Section 6.3 describes the vacuum windows in detail.

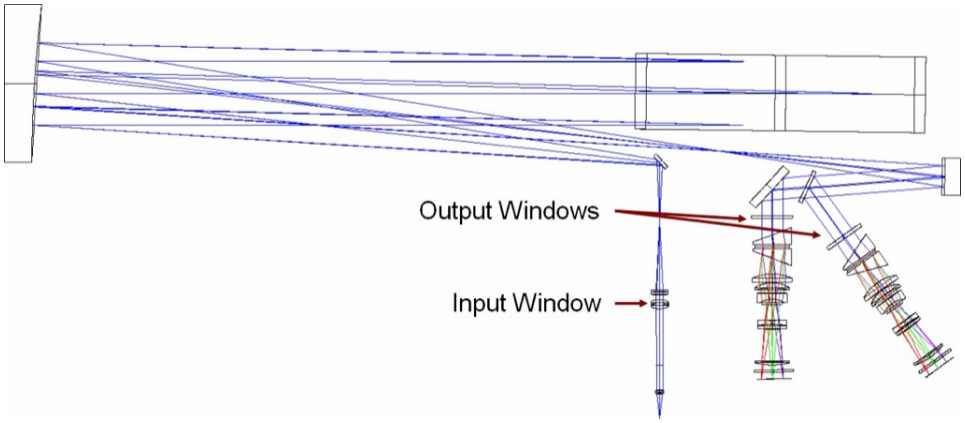

Figure 6.3: The KiwiSpec dual-channel optical layout with the vacuum window locations indicated.

6.2.3 Mechanical Design Overview

Various aspects of the KiwiSpec vacuum chamber system are highlighted in Figure 6.4.

Mechanically, the main design driver is to prevent flexure in the chamber (due to changing atmospheric pressure) from transferring into the optical tables and moving the optical components. Care was therefore taken with the KiwiSpec design to isolate the chamber from direct contact with the internal and external optical tables. The internal table is connected directly to the parent table through three support legs (two under the échelle end of the table and one at the collimator end). The internal table legs pass through flanges in the the base of the chamber (without contacting the chamber wall at any point), and vacuum bellows are employed to provide a flexible interface between the feet and the chamber. The bellows also provide the seal against atmospheric pressure. Figure 6.5 shows details of the design. The chamber itself rests on three 'canoe spheres', which are employed to constrain the chamber from moving, while at the same time not rigidly connect it to the parent table. A canoe sphere is composed of two large-radii spherical surfaces ($R = 0.5\,\mathrm{m}$), with their centres of curvature offset. The canoe spheres rest in V-grooves (Figure 6.6), and are vertically constrained by gravity as well as atmospheric pressure forces on the three bellows. The three canoe spheres on the bottom of the chamber are aligned as shown in Figure 6.7. The reasoning behind this approach is that if the chamber does flex during initial pump-down, the input vacuum window should remain stationary as it is located directly in-line with the canoe sphere intersection point.

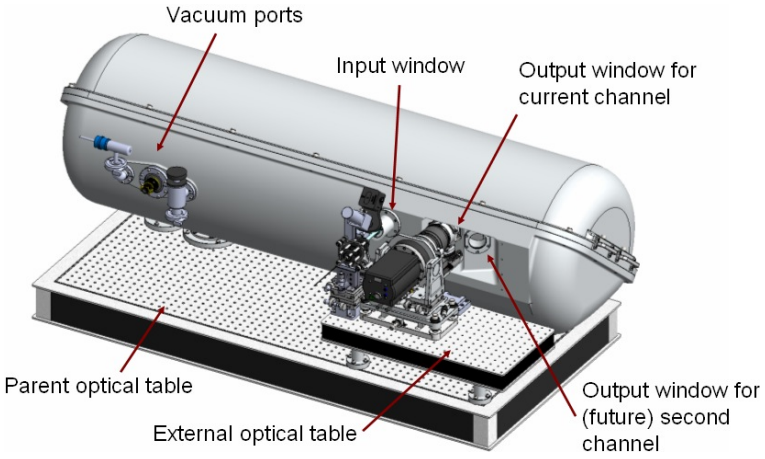

(a) Front view.

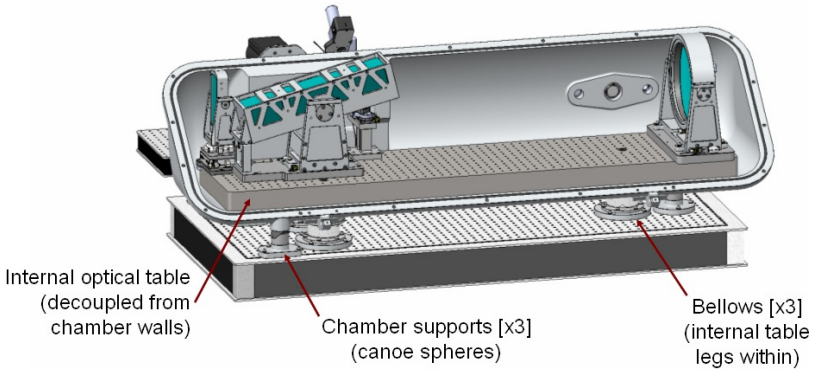

(b) Rear view (with lid removed).

Figure 6.4: The KiwiSpec vacuum chamber system with major components labelled. Although not shown in the diagram, in practice the parent optical table is 'floated' on a vibration-isolation support.

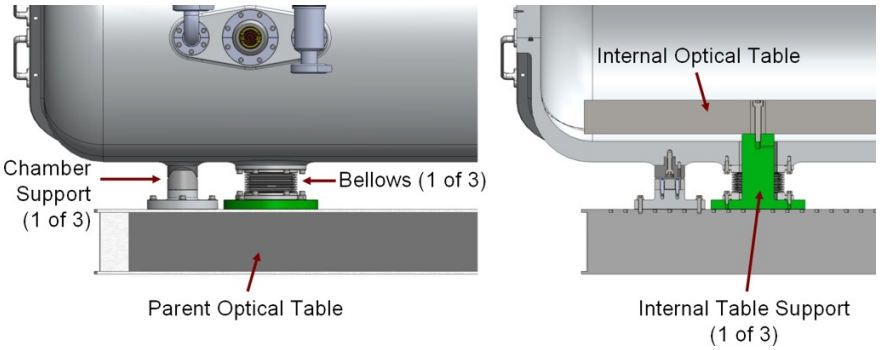

Figure 6.5: Two views of the chamber and internal table support system. Left: Exterior view. Right: Cross-section view. The internal table support is shown in green to better differentiate it from the bellows.

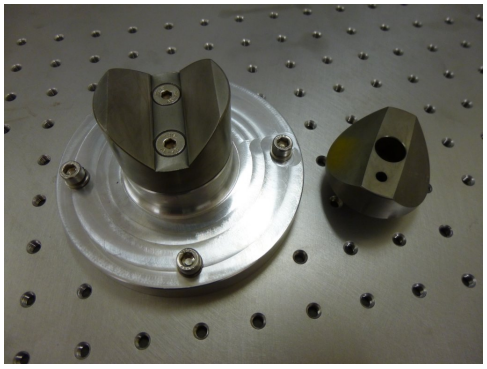

Figure 6.6: One of the KiwiSpec canoe spheres with its mating V-groove.

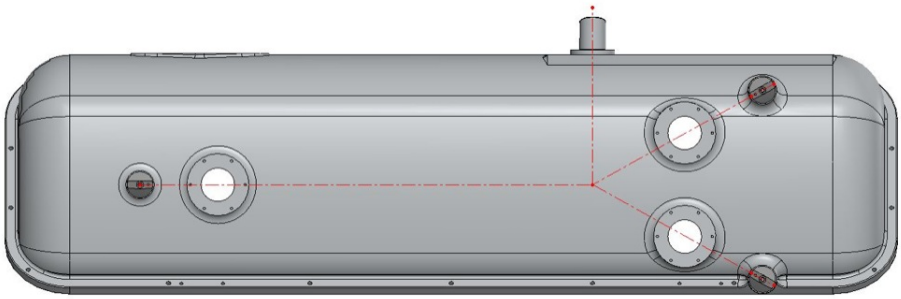

Figure 6.7: The canoe spheres are aligned to point towards the centreline of the long axis of the chamber, and in line with the input vacuum window.

6.2.4 Interior Access

The chamber was designed with a removable lid on an angled flange to allow complete access to the interior optical table and the components inside the chamber. Figure 6.8 shows the chamber lid in the open position. Hinges allow the lid to be tipped backwards and outwards in a controlled manner, without any threat of damaging the O-ring seal on the flange or the optical components within the chamber. After the lid has been tipped to a near-vertical position it can be lifted out of the open hinges and placed to the side. The 41 kg lid has handles attached to each end, allowing it to be lifted and maneuvered by two people.

6.2.5 Optical Tables

As shown in Figure 6.4, the vacuum chamber design employs three optical tables – an interior table inside the vacuum chamber, an external table to support the external input relay, exposure meter, iodine cell and camera arm(s), and a parent table to support the entire system. The internal table is a custom, vacuum-compatible breadboard from Newport. The external table is also a custom Newport optical table with tapped holes on the underside

for mounting the support feet. The parent table is a standard, off-the-shelf Thorlabs optical table.

When assembled into the complete instrument, the co-planearity of the interior and exterior table tops is important to maintain the optical axis height inside and outside of the chamber. While these optical breadboards have a tight flatness tolerance on their top surfaces, they have a much larger tolerance on their overall thickness ($\pm$ 0.5 mm in the case of the Newport tables). This is presumably because these tables are typically supported in a way that does not depend on the absolute thickness of the table (i.e. on vibration isolation pedestals). Measurements of the actual KiwiSpec tables showed that the overall thickness can vary by up to 0.5 mm.

To ensure the co-planearity of the tables in the final instrument, each table with its feet attached will be placed inverted on a milling machine. The bottoms of the feet will then be machined parallel to the table tops to ensure a uniform height for both tables.

Also important from a stability standpoint is maintaining the co-planearity of the two tables during temperature changes. Therefore, it was ensured that the two tables were of the same thickness and internal construction to avoid a coefficient of thermal expansion (CTE) mismatch between the two tables.

6.2.6 Mechanical Envelope

The mechanical envelope for the vacuum chamber system (not including the parent optical table, electrical cables, water chiller hoses, or optical fibre) is shown in Figure 6.9. The interior volume of the chamber is approximately 0.275 m^3 or 275 litres.

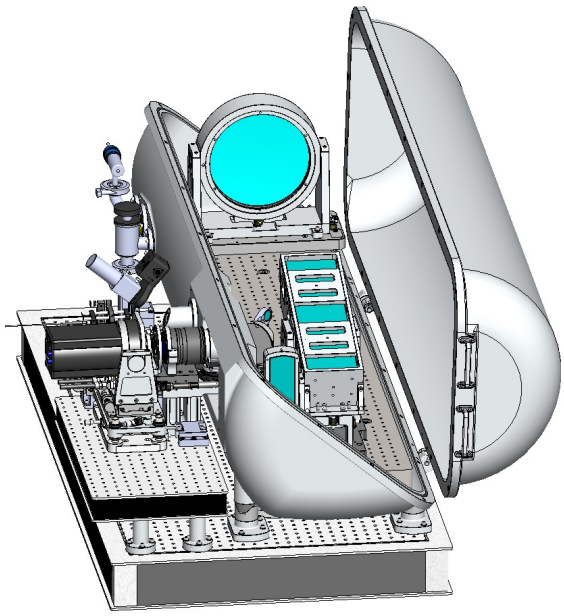

Figure 6.8: The vacuum chamber lid pivots outwards on hinges to allow access to the interior of the chamber. Open hinges are employed so that the lid can be removed entirely from the chamber base, allowing easy access to the interior of the chamber.

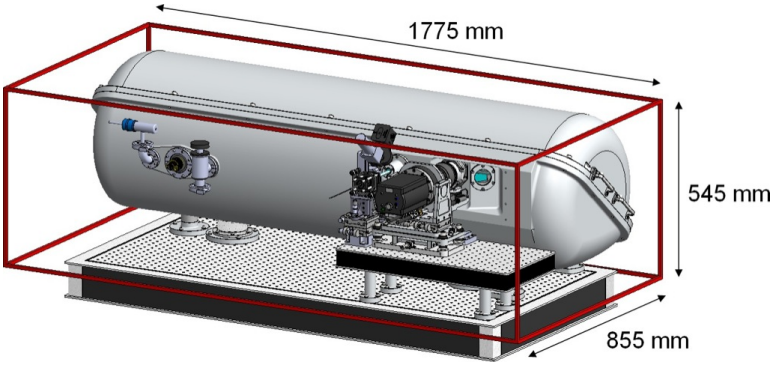

Figure 6.9: The mechanical envelope of the vacuum chamber prototype (not including parent optical table).

6.3 Vacuum Windows

This section discusses various aspects surrounding the vacuum chamber optical windows.

6.3.1 Effect of Vacuum Window Tilt

An important consideration with respect to stability is ensuring that flexure in the chamber itself does not move or tilt the vacuum windows from their nominal positions. This section gives an overview of the effect of window tilt as well as justification for placing the windows within collimated spaces. Section 6.3.2 describes the tolerancing analysis undertaken to determine the amount of allowable movement to meet the radial velocity stability goals.

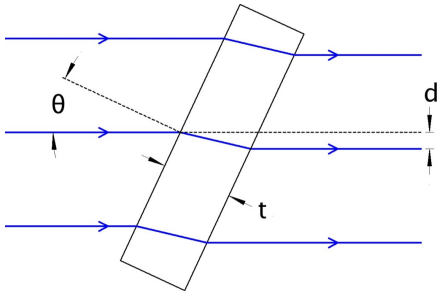

Figure 6.10: The displacement of a collimated beam due to a tilted window. Adapted from Smith (2000).

As shown in Figure 6.10, placing a tilted window into a collimated light beam results in a beam displacement. Smith (2000) gives the following equation for estimating the amount of beam displacement caused by a tilted window:

$$d = \frac{t \cdot \theta \cdot (n-1)}{n}, \tag{6.2}$$

where:

d	=	beam displacement	[mm];
t	=	window thickness	[mm];
θ	=	window tilt	[radians];
n	=	index of refraction (wavelength dependent)	[unitless].

This equation is valid for small tilt angles. The amount of displacement is a function of window thickness, window tilt, and the index of refraction of the window glass type.

For the KiwiSpec design, the vacuum window thickness was determined by fabrication practices (see Section 6.3.3), and the amount of window tilt will be very small. This leaves the index of refraction (i.e. glass type) as an open design variable to minimize beam displacement due to window tilt. Choosing a lower-index glass for the window is advantageous as the beam displacement due to a fused silica window is approximately 7.7 per cent less than a N-BK7 window of the same thickness (ratio calculated using Equation 6.2 at $n = n_d = 587.6\,\text{nm}$).

When a tilted window is placed within a converging or diverging beam, the situation becomes more complex. As shown in Figure 6.10, for the collimated beam scenario all rays within the beam strike the tilted window at the same angle of incidence. Figure 6.11 shows the effects of placing a tilted window within a converging beam, where the change of angle of incidence on the window is immediately apparent. The beam displacement for the chief ray is the same as for the collimated case. However, the other rays in the beam undergo different displacements. This introduces aberrations which cause the centroid to shift more than the chief ray displacement amount.

Therefore, from a stability standpoint it is preferable to place the vacuum windows within collimated beams to minimize the effect of window tilt.

6.3.2 Window Movement Tolerances

A constraint on the vacuum chamber design is that during changes in atmospheric pressure the vacuum windows cannot move enough to deviate the light rays and mimic a radial velocity shift. This section outlines the results of the Zemax tolerancing study undertaken to determine the amount that the windows can move and still meet the stability goals.

Six degrees of freedom of window movement were investigated as shown in Figure 6.12. Each of the degrees of freedom were perturbed in turn while monitoring the shift of the centroid positions of 35 wavelengths along the échelle dispersion direction. The wavelengths employed are the same as those used for the tolerancing study of Chapter 4 (7 échelle orders containing 5 wavelengths each). The criterion employed was that the maximum centroid movement could not exceed an amount equivalent to a 1 m/s shift,

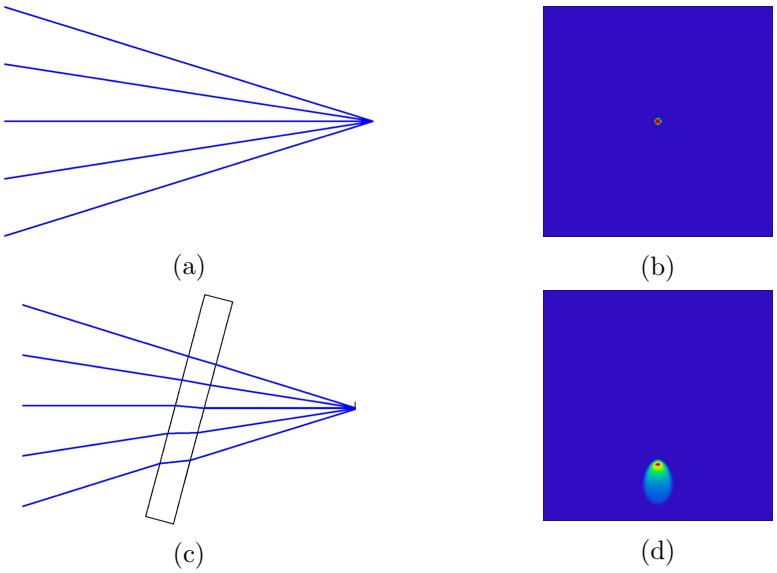

Figure 6.11: Effect of placing a tilted window into a converging beam (a large window tilt value of 20° is shown to emphasize the effect). a) ray paths for case with no window; b) synthetic image for case with no window; c) ray paths with a tilted window in a converging beam; d) synthetic image for the tilted window case. For direct comparison, the synthetic image fields are both 2 mm × 2 mm and are both centered on the optical axis.

which was determined by converting centroid movement to a radial velocity through the relationship that 1 m/s equals approximately 1/1000 pixels for the KiwiSpec instrument (as shown in Section 2.5.2). In actual use of the instrument, the centroids of (possibly) hundreds of spectral lines will be monitored and measured. However, doing so within Zemax would be prohibitively expensive from a computational viewpoint. Therefore the worst-case maximum movement of one line (out of the 35 monitored) is used here as a stability metric.

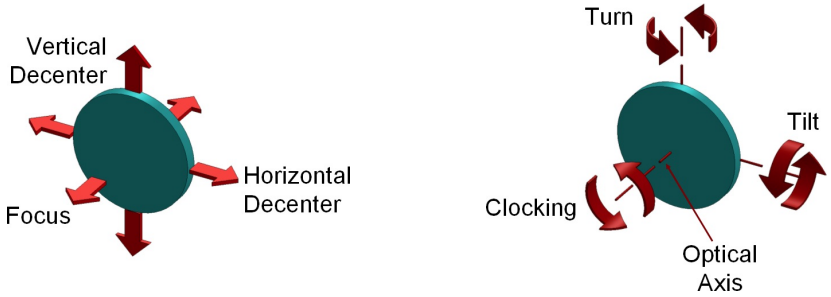

(a) Translational degrees of freedom. (b) Rotational degrees of freedom.

Figure 6.12: The degrees of freedom investigated during the vacuum window movement tolerancing.

Of the six degrees of freedom, only turn and tilt were found to influence the centroid positions. The amounts of allowable movement of these two degrees of freedom to meet the 1 m/s limit are summarized in Table 6.1.

Table 6.1: Maximum vacuum window tilts that meet the 1 m/s limit. Also included are conversions from angular tilts to linear movements at the edge of the window.

	Input Window		**Output Window**	
	Angular	**Linear**	**Angular**	**Linear**
Turn	± 0.0075°	± 1.6 μm	± 0.05°	± 26 μm
Tilt	± 0.0075°	± 1.6 μm	± 0.05°	± 26 μm

6.3.3 Window Thickness Determination

The minimum window thickness required to prevent rupture (given the pressure differential and mounting arrangement) was determined for both fused silica and BK-7 using the following equation (from Yoder (2008)):

$$t_{\mathrm{W}} = 0.5 A_{\mathrm{W}} \sqrt{\frac{K_{\mathrm{W}} f_{\mathrm{s}} \Delta P}{S_{\mathrm{F}}}}, \tag{6.3}$$

where:

t_{W}	=	window thickness	[mm];
A_{W}	=	window support aperture	[mm];
K_{W}	=	a support condition constant,	
		1.25 (if unclamped) or 0.75 (if clamped)	[unitless];
f_{s}	=	factor of safety;	[unitless];
ΔP	=	pressure differential;	[Pa];
S_{F}	=	fracture strength of material	[Pa].

For the KiwiSpec case:

K_W	=	1.25 (unclamped)
A_{W}	=	Input Window: 14.5 mm; Output Windows: 50 mm
f_{s}	=	5 (Yoder (2008) suggests 4 or higher)
ΔP	=	108,480 Pa - 13.3 Pa = 108,466.7 Pa (worst case)
S_{F}	=	Fused silica: 60 MPa; BK-7: 16.5 MPa.

Minimum thicknesses required to survive the worst-case pressure differential are given in Table 6.2. Fused silica is clearly a stronger material for this application as it allows the windows to be approximately 0.53 times thinner than BK-7 given the same pressure differential and mounting conditions. Therefore, the KiwiSpec vacuum windows are made from fused silica.

Table 6.2: Calculated required window thicknesses based on survivability.

Window	**Thickness**	
	Fused Silica	BK-7
Input	0.8 mm	1.5 mm
Output	2.7 mm	5.1 mm

However, fused silica windows of the thicknesses listed in Table 6.2 would be more difficult to manufacture than a thicker window. Therefore, a nominal thickness of 5 mm was chosen for both vacuum windows.

6.3.4 Window Deflection Due to Pressure Differential

The distance that the centre of each (5 mm thick) vacuum window will bow inward due to the pressure differential was predicted using the following equation (from Yoder (2008)):

$$\Delta x = 0.0117(1-\nu^2)\frac{\Delta P_{\mathrm{W}} A_{\mathrm{W}}^4}{E_G t_{\mathrm{W}}^3}, \tag{6.4}$$

where:

Δx	=	deflection	[mm];
ν	=	Poisson's ratio	[unitless];
ΔP_{W}	=	pressure differential	[Pa];
A_{W}	=	window support aperture	[mm];
E_{G}	=	Young's modulus for the glass	[Pa];
t_{W}	=	window thickness	[mm].

For the KiwiSpec case:

ν	=	0.17 (fused silica)
ΔP_{W}	=	108,480 Pa - 13.3 Pa = 108,466.7 Pa (worst case)
A_{W}	=	Input window: 14.5 mm; Output window: 50 mm
E_{G}	=	7.3 x 10^4 MPa
t_{W}	=	Both windows: 5 mm.

This deflection effectively changes the plane-parallel windows into (very) weak meniscus lenses. The amount of deflection was also converted to a radius of curvature (ROC) value with the spherometer equation:

$$R = \frac{(\frac{D}{2})^2}{2h} + \frac{h}{2}, \tag{6.5}$$

where:

D = diameter of spherometer,
(the edge of the clear aperture in this case);

h = measured sag,
(the deflection of the window, result of Equation 6.4).

The results are given in Table 6.3. As both ROC values are extremely large considering the size of the windows, the deflection of the vacuum windows due to the pressure differential will introduce negligible optical power and/or aberrations. This was verified by including these ROC values in the KiwiSpec Zemax model.

Table 6.3: The calculated defection and radius of curvature (ROC) values for the two vacuum windows.

Window	**Deflection**	**ROC**
Input	0.01 μm	4402 m
Output	0.84 μm	370 m

6.3.5 Coatings and Wedge

The windows for the vacuum chamber prototype were coated with single-layer MgF_2 coatings on both sides. Although MgF_2 coatings are sufficient for testing the prototype, an improvement in throughput could be achieved by coating the windows with a high-efficiency coating. The output window, which was manufactured by KiwiStar Optics, was fabricated with a wedge angle of 0.03° to avoid interference effects (which can be a problem when plane-parallel windows are placed in a collimated beam). This wedge angle was chosen as it is easily fabricated, and was found to cause minimal dispersion and beam deviation during a Zemax analysis of the effects of window wedge.

6.4 Pressure and Temperature Stability

In order to determine the effect of refractive index changes on the KiwiSpec vacuum chamber system, calculations were undertaken using both the NIST modified Edlén equation (described in Section 6.1.1), and Zemax raytracing.

The NIST website-based modified Edlén calculator does not allow use of pressures below 100 mbar owing to reduced accuracy of the equation at such pressure levels. However, documentation on the website discusses reduced accuracy at the $n = 10^{-8}$ level, whereas changes in refractive index that lead to 1 m/s radial velocity changes occur at the $n = 10^{-6}$ level. Therefore, use of the equation was cautiously extended below 100 mbar for the calculations that follow.

A KiwiSpec model was constructed within Zemax that allows both the external and internal pressures and temperatures to be changed. The only parameters affected by temperature changes in this model are the refractive indices of glass and air (the expansion and contraction of glass or mounts are not considered here). Also, as the Zemax manual states that Zemax is capable of working at all pressures down to a perfect vacuum (0 mbar), the use of this model allows confirmation of the NIST-modified Edlén calculations made outside of that equation's recommended range of use.

The methodology involved changing the pressure or temperature, then determining the resulting radial velocity movement. For the NIST modified Edlén equation approach, the radial velocity shift was calculated using the Doppler equation (Equation 6.1). Within Zemax, the radial velocity shift was measured by monitoring the centroid movements of 35 wavelengths in the échelle dispersion direction. Actual movements were converted to radial velocity space by assuming 1 m/s corresponds to a movement of 1/1000 of a pixel (see Section 6.3.2 for more details).

Four situations were investigated to determine the allowable changes in internal and external pressure and temperature. Also investigated was the wavelength shift during evacuation of the chamber, and what vacuum pressure level should be employed within the vacuum chamber.

6.4.1 Allowable Pressure Change - Internal

Once the vacuum valve is closed on the chamber, the vacuum pressure level will slowly increase due to outgassing of components within the chamber, or possible small leaks around the O-ring seals. Of interest then is to determine what rate of pressure increase is allowable given the goal of 10 m/s stability over the course of an hour.

Figure 6.13 shows the results of increasing the internal vacuum level for various starting pressures. Results are given for both the NIST modified Edlén calculations and Zemax raytracing, and the plot shows the strong correlation between the two methods (for the 10 m/s level, the NIST modi-

fied Edlén value differed from the Zemax raytraced value by an insignificant 0.009 mbar). The plot also shows that regardless of the vacuum chamber base pressure, an increase of 0.012 mbar leads to a 1 m/s radial velocity shift. Similarly, regardless of the vacuum chamber base pressure, an increase of approximately 0.12 mbar leads to a 10 m/s shift. Therefore, from a pressure increase standpoint, a deeper vacuum level offers no benefit for instrument stability. However, as will be shown in Section 6.4.3, a harder vacuum level offers the benefit of decreased sensitivity to temperature changes.

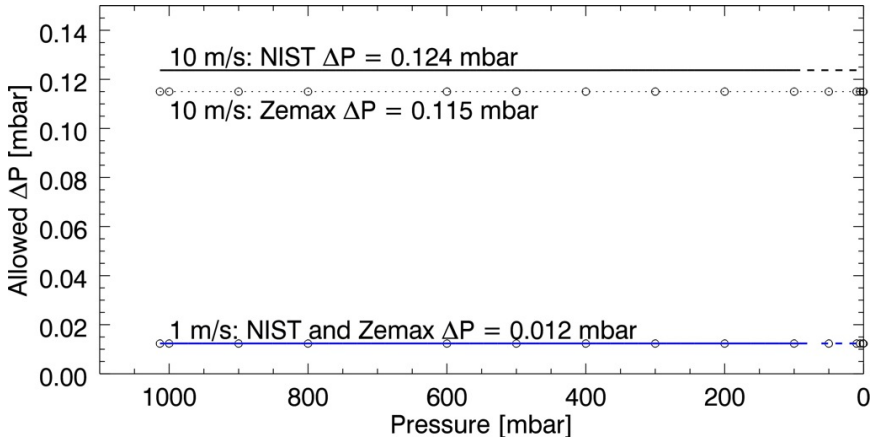

Figure 6.13: Allowable increase in vacuum chamber pressure at a given pressure to achieve 1 m/s and 10 m/s stability in refractive index of air. Calculations were made using the NIST-modified Edlén equation as explained in the text, for λ=540 nm, and with a constant temperature of 20°C, and a constant relative humidity value of 0%. The dashed section of each line indicates values that fall outside of the recommended accuracy range of the equation. Zemax results are also shown by open circles for the pressure values investigated.

6.4.2 Allowable Pressure Change - External

While the vacuum chamber will maintain constant pressure within it, the components outside of the chamber will be subjected to changing atmospheric pressure. The Zemax model was used to determine how refractive index changes due to changing external pressure affect radial velocity stability. For this analysis the temperature of the entire instrument was constant at 20°C and the vacuum pressure within the chamber was constant at 0.01 mbar.

External pressure changes cause a shift of the spectral features within the spectral format. Figure 6.14 shows the relative movements due to a pressure increase for the 35 spectral lines monitored. Because spectral features are moving in both directions along the échelle orders, for this analysis the 1 m/s and 10 m/s shifts were determined from the difference between the maximum positive shift and the maximum negative shifts. However, this is a worst-case

scenario as in practice the movements of all wavelengths will be averaged in some manner to obtain the resulting radial velocity shift. Therefore, three other values were calculated as well for the échelle dispersion direction: the average of the minimum and maximum shifts; the average of all 35 centroid shifts; and the standard deviation of all 35 centroid shifts. The results are shown in Figure 6.15. Immediately obvious from the figure is the marked improvement in stability when the centroid movements are averaged.

For the worst-case scenario of considering only the maximum positive and negative shifts, Figure 6.15 indicates that an increase in external atmospheric pressure of 3.8 mbar causes a 1 m/s radial velocity shift. To put this into perspective, Figure 6.16 shows that the maximum hourly pressure change over an (arbitrary) 12 hr period over North America was approximately 2.3 mbar. As an indication of pressure changes at a mountaintop observatory, Table 6.4 gives barometric pressure data for one year at the European Southern Observatory (ESO) Paranal observatory site (historical atmospheric pressure data were not available for Mt John University Observatory). The website source for this table also states that over the course of the year-long measurement period, the site experienced an absolute pressure gradient of $<$0.6 mbar hr^{-1} (95 per cent of the time), and a 'dark time' average pressure gradient of -0.2 mbar hr^{-1}. Therefore, it is very likely that atmospheric pressure changes will be less than 3.8 mbar hr^{-1} and fall under the worst-case 1 m/s stability level.

Figure 6.15 also indicates that an external atmospheric pressure increase of 35.6 mbar causes a worst-case 10 m/s radial velocity shift. Because such an atmospheric pressure change cannot physically occur during the one hour stability window of interest, external pressure changes should not prohibit the instrument from measuring to 10 m/s precision.

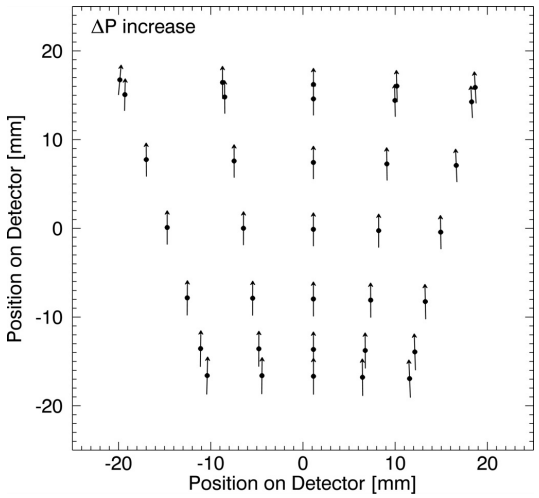

Figure 6.14: Exaggerated movements of spectral lines due to an increase in external (atmospheric) pressure. The lengths of the vectors are proportional to each other, but the lengths do not match the scale of the plot in an absolute sense.

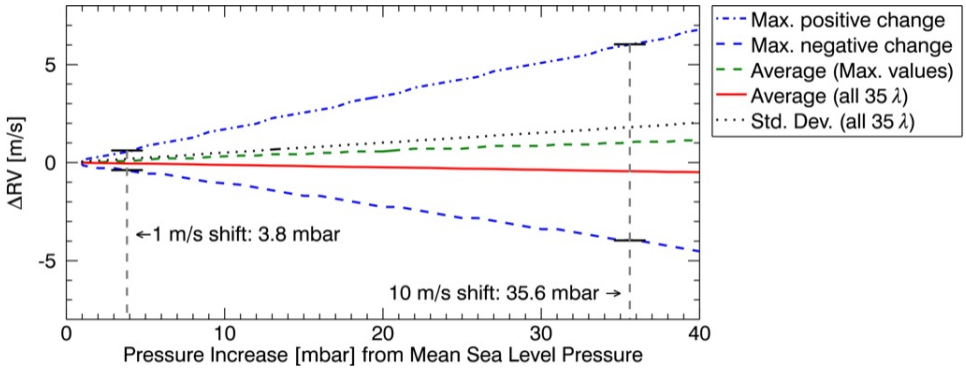

Figure 6.15: Allowable increase in atmospheric pressure surrounding the vacuum chamber given a constant (20°C) temperature. Results are based on raytracing through a Zemax model of the spectrograph with increasing atmospheric pressure outside of the vacuum chamber and constant vacuum pressure within. Shown are various statistics for the centroid movements in the échelle dispersion direction only. As a worst-case scenario, the difference between the maximum positive and maximum negative centroid shifts was used to determine the indicated stability levels.

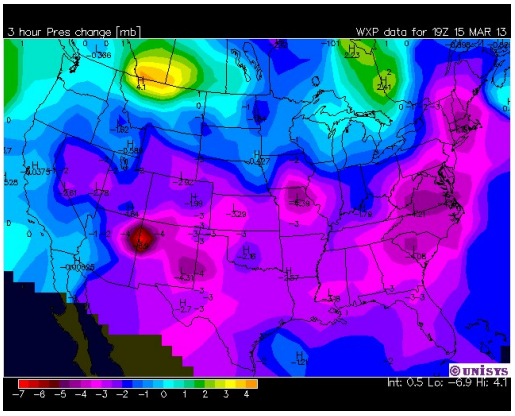

Figure 6.16: Change in surface pressure during the previous 3 hr period over North America for 19Z 15 March 2013 (from `http://weather.unisys.com`). This chart shows the greatest 3 hr pressure change that occurred over a 12 hr period. Assuming a constant change, the maximum hourly change rate would be -2.3 mbar/hr.

Table 6.4: Air pressure data at the European Southern Observatory (ESO) Paranal observatory site. Data is based on hourly averages recorded between September 1989 and September 1990. Table adapted from `http://www.eso.org/gen-fac/pubs/astclim/paranal/pressure/`.

	Pressure [mbar]			
	Min.	**Average**	**Max.**	**# Samples**
Day and Night	731	743	749	5576
Dark Time	731	743	748	2553
24h Change	0	10	63	4800

6.4.3 Allowable Temperature Change - Internal

The temperature stability required for various vacuum pressure levels was also investigated with the NIST-modified Edlén equation and the Zemax model of the KiwiSpec system. For a given pressure, the temperature was increased from 20°C until a 1 m/s radial velocity shift was induced. The results are shown in Figure 6.17. This figure shows that the NIST-modified Edlén and Zemax-based calculations correlate very well - even within the NIST equation's 'reduced accuracy' region below 100 mbar. The required temperature range for various pressures are also summarized within Table 6.5. These results show that based on refractive index of air considerations, as the vacuum chamber pressure decreases, the allowable temperature range increases. This intuitively makes sense as at lower pressures there are fewer air molecules present to be affected by temperature changes. The results also show that even with a relatively soft vacuum pressure of 1 mbar, the temperature can increase by 3.7°C before a 1 m/s shift is induced because of refractive index of air changes. Since that temperature change is much larger than the change that can be tolerated by other aspects of the spectrograph's design, there is no need to go to a lower pressure within the chamber. Furthermore, an advantage of a higher vacuum pressure is that there are more air molecules present, which can lead to better thermal equalisation between the components within the chamber.

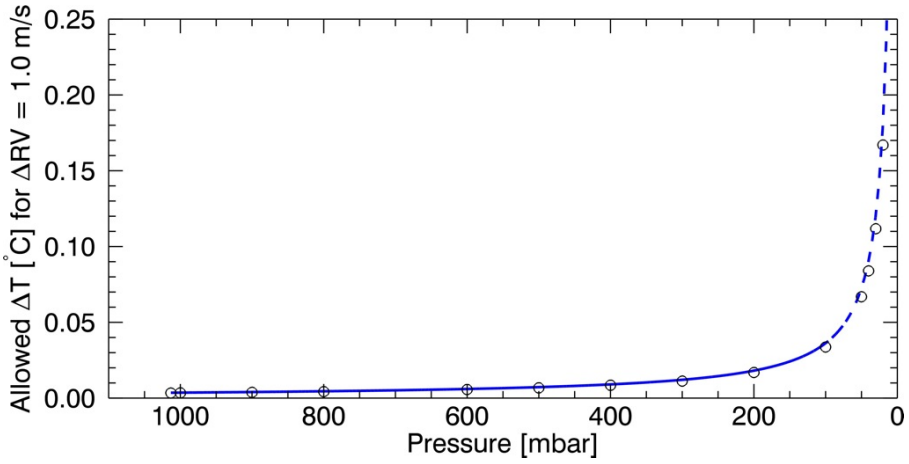

Figure 6.17: Allowable increase in temperature from 20°C for a given pressure to achieve 1 m/s stability in refractive index of air. Only the temperature within the chamber was adjusted during this theoretical analysis, which was undertaken for λ=540 nm at a constant relative humidity of 0 per cent. NIST modified Edlén equation values are shown by the blue line, with the dashed section indicating values that fall outside of the recommended accuracy range of the equation. Zemax-based results are shown by open circles.

Table 6.5: Allowed temperature increases for a given vacuum level to achieve 1 m/s stability in refractive index of air.

Chamber Pressure [mbar]	**Allowed ΔT [°C]**
1013.25	0.004
500	0.007
100	0.036
10	0.363
1	3.672
<0.1	>10.000

6.4.4 Allowable Temperature Change - External

The allowable external temperature change was also investigated using the Zemax model. The temperature within the chamber was maintained at 20°C, while the external temperature was increased. The chamber was at a constant vacuum pressure while the external pressure was mean sea level pressure (1013.25 mbar). The model changes the temperature of both air and lenses (i.e. dn/dT is included), however, it does not account for expansion or CTE effects.

The movement of spectral features due to an increase in temperature is shown in Figure 6.18. The movements show an increase in the size of the spectrum, mimicking a focal length change in the camera. As expected, (based on the change in density of air), the direction of motion to a temperature increase is opposite to that of an increase in pressure. This implies that if a decrease in pressure is due to the arrival of a cold front, the associated decrease in temperature could help counteract the pressure-induced radial velocity shift.

As with the analysis of external pressure changes (Section 6.4.2), the centroid changes were monitored within Zemax and the worst-case 1 m/s level determined by the difference between the maximum positive shift and the maximum negative shift. The results are shown in Figure 6.19. An increase in external temperature of 0.1°C causes a 1 m/s radial velocity shift, whereas an increase in external temperature of approximately 1°C causes a 10 m/s radial velocity shift. Both of these temperature increases are reasonable values, as probably smaller variations could be achieved with a thermal enclosure surrounding the instrument.

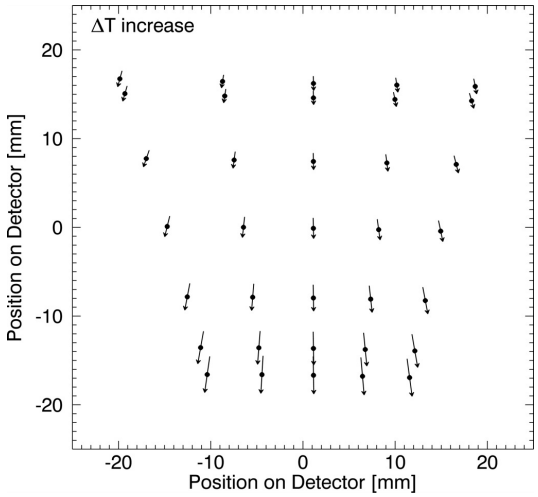

Figure 6.18: Exaggerated movements of spectral lines due to an increase in external temperature. The lengths of the vectors are proportional to each other, but the lengths do not match the scale of the plot in an absolute sense.

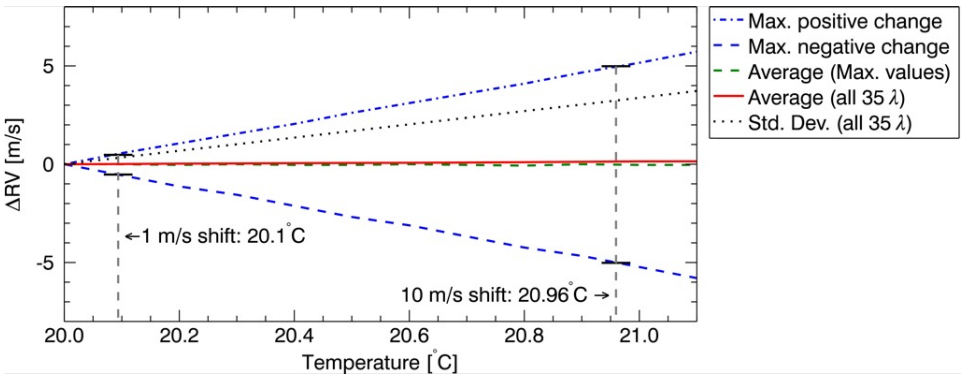

Figure 6.19: Allowable increase in the temperature surrounding the vacuum chamber. Results are based on raytracing through a Zemax model with constant atmospheric pressure (mean sea level) outside of the vacuum chamber and constant vacuum pressure and temperature within. Shown are various statistics for the centroid movements in the échelle dispersion direction only. As a worst-case scenario, the difference between the maximum positive and negative centroid shifts was used to determine the indicated stability levels.

6.4.5 Summary of Allowable Changes

The various parameters discussed in the above sections are summarized in Table 6.6; they are reasonable values that can be achieved without extreme measures taken for environmental control. However, as mentioned above, the stability of the entire instrument will be determined by the combination of these parameters simultaneously.

Table 6.6: Summary of changes that result in 1 m/s and 10 m/s radial velocity shifts. In order to meet the stability goal, these changes would need to be sustained over the course of one hour.

Parameter	1 m/s	10 m/s
Internal Pressure	0.012 mbar	0.12 mbar
External Pressure	3.8 mbar	35.6 mbar
Internal Temperature	>3°C	>3°C
External Temperature	0.1°C	1°C

6.4.6 Wavelength Shift while Evacuating Chamber

The movement of the spectral format on the detector due to evacuating the chamber from atmospheric pressure to 0.01 mbar was also investigated using the Zemax model. Results are shown in Figure 6.20.

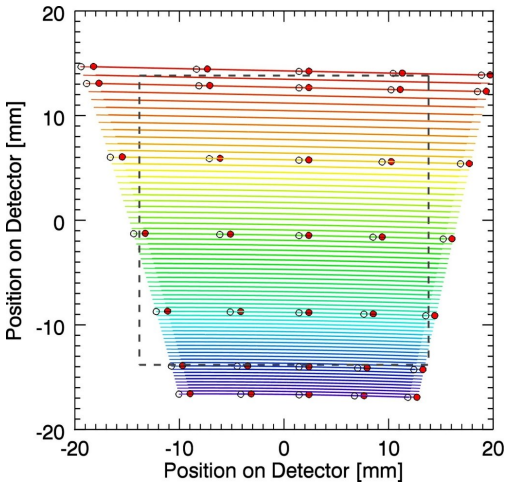

Figure 6.20: The movement of the spectral format due to evacuating the vacuum chamber from atmosphere to 0.01 mbar. Filled circles are the positions of 35 example wavelengths with the chamber at atmospheric pressure; open circles are the positions of the same wavelengths with the chamber interior at 0.01 mbar. The wavelengths move redward along the échelle orders as the pressure decreases. Orders 91 to 157 are shown (λ_B = 391 nm to 674 nm). The dashed boundary indicates the dimensions of the KiwiSpec prototype detector.

6.4.7 Vacuum Chamber Pressure Level

It is important that the vacuum pressure within the chamber must not increase by more than the stability requirements. However, with regard to the absolute value of the vacuum pressure level, this section has demonstrated that:

- the absolute vacuum pressure level within the chamber is not critical;
- little is gained by going to an ultra-low vacuum pressure; even at 1 mbar pressure the temperature stability requirements are more than adequate.

Therefore, the vacuum chamber prototype will be initially tested with a vacuum chamber pressure of 1 mbar. As opposed to an ultra-low vacuum pressure, a benefit of such a 'soft' vacuum level is that there are more air molecules present, which can lead to better thermal equalisation between the components within the chamber.

6.5 Vacuum Chamber Mechanical Design and Manufacture

The detailed design of the vacuum chamber was a collaboration between Deon Grobler, Dave Cochrane (both of KiwiStar Optics), kanDO Innovation (Auckland, NZ), Stuart Barnes (Stuart Barnes Optical Design), and the author. kanDO Innovation was responsible for the computer-aided drafting (CAD) work. Both the author and kanDO Innovation performed the finite element analysis (FEA) simulations required during the design process. This section describes the development and mechanical design of the vacuum chamber itself.

6.5.1 Material and Manufacture

The vacuum chamber was manufactured out of 6061-T651 aluminium, with the chamber and base each machined out of a solid piece of billet using a large computer numerical control (CNC) mill. Figure 6.21 shows pictures of the two halves on the mill part-way through the multi-stage machining process. Aluminium was chosen over other metals because of its ease of machining, light weight, and cost-effectiveness. CNC-based manufacture was chosen as it allows the vacuum chamber walls to form the complex shapes required by the geometry surrounding the output vacuum windows. Since it is envisaged that several KiwiSpec vacuum chambers will be manufactured, CNC machining also offers a method to easily replicate the prototype chamber.

Casting was briefly explored as an alternative to machining the chamber out of solid pieces of aluminium. However, Harris (2005) suggests avoiding air castings for vacuum chambers as the resulting material tends to be porous. Harris (2005) does recommend vacuum castings, and this option might be explored for future versions of the vacuum chamber. However, for the prototype, CNC machining of solid billets was chosen over casting as the lower-risk option.

Figure 6.21: The vacuum chamber being machined on the CNC mill at Allied Industrial Engineering (Kawerau, New Zealand). Each half was machined from a single piece of billet. Left: Chamber base. Right: Chamber lid.

Another approach investigated was to manufacture the chamber out of sections of stainless steel plate. This design would have required complex cuts and bends, with various welds required to join the sections together and attach the flanges and ports. As well, the heat generated during the welding process can distort flanges and thin-walled sections (requiring post-weld machining to square them up). Furthermore the welds would need to be leak-tested to ensure they do not contain pinholes that would degrade the vacuum. This approach was discounted as being very labour-intensive, expensive, and not easily repeatable.

6.5.2 FEA - Atmospheric Pressure Criteria and Modeling

When a vacuum chamber is evacuated, the chamber must be able mechanically to withstand the pressure differential that exists between the interior and exterior of the chamber. As well, atmospheric pressure changes caused by the passage of weather systems result in a changing force being applied to the external surface area of a vacuum chamber. Care must be taken during the design of a spectrograph vacuum chamber to ensure that changing atmospheric pressure does not impact the stability of the instrument through mechanical flexure. This section describes the pressure values used during the design phase of the KiwiSpec vacuum chamber, and also the results of the FEA analysis of the vacuum chamber design.

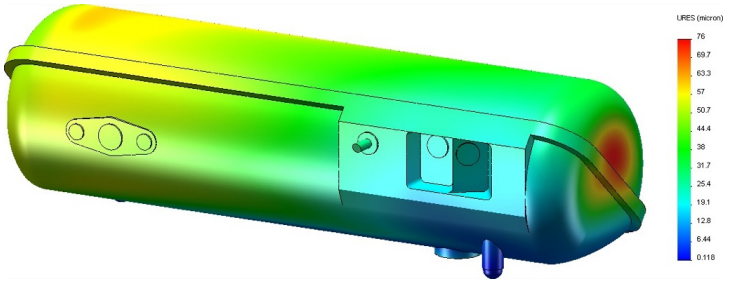

(a) Front view.

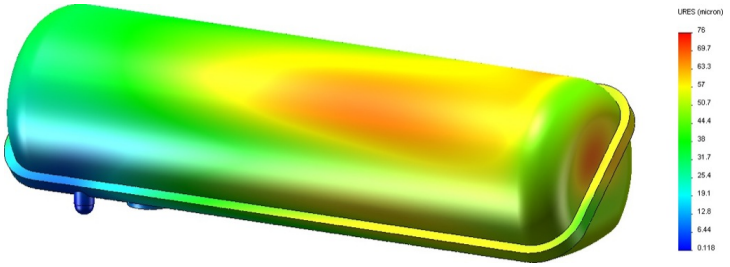

(b) Rear view.

Figure 6.22: FEA results showing deflection due to highest atmospheric pressure recorded on Earth. Maximum deflection is 76 μm.

The highest (adjusted to sea level) atmospheric pressure ever recorded on Earth is 1084.8 mbar, measured at Tosontengel, Mongolia in 2001[1]. This atmospheric pressure value was used to ensure that the chamber will survive (and minimally flex/distort) as a result of the pressure differential between atmospheric and vacuum pressure levels. It gives a worst-case scenario for the pressure differential, as most observatories are located on hills or mountains and hence experience lower maximum pressures.

To achieve a high strength-to-weight ratio, the overall shape of the chamber was designed to be cylindrical (with departures from a cylinder only where required by the vacuum windows). Results of the FEA modelling to determine maximum flexure at the highest sea-level pressure recorded are shown in Figure 6.22. Note that the foot bellows were not included in the FEA model owing to the complexity required to simulate their movements.

Survivability of the chamber design was also tested with FEA analysis, to ensure that the tank will not buckle or catastrophically fail due to the expected pressure differential. The analysis showed that the chamber design will survive a pressure differential approximately 30 times that of the maximum pressure recorded on Earth.

After pump-down deflection and survivability, an important design consideration is to ensure that the chamber does not excessively flex while adjusting to changes in atmospheric pressure. As a conservative estimate of

[1] `http://wmo.asu.edu/highestsealvlairpressureabove700m`

atmospheric pressure change, a decrease of 4 per cent from the maximum pressure over the course of an hour was chosen during the design phase. In retrospect this is a very high value, as a 4 per cent hr^{-1} decrease from the highest recorded pressure equates to a drop of approximately 45 mbar hr^{-1}. To put this into perspective, the WMO reports that the the fastest intensification recorded for a tropical cyclone is 100 mbar in under 24 hr (which assuming a constant change equates to 4.1 mbar hr^{-1})[2]. Certainly astronomical observations would not be taking place if such an hourly pressure change was occurring.

The amount of movement in the vacuum windows during a 4 per cent pressure decrease from 1084.8 mbar was monitored during the FEA analysis to ensure the values were less than those determined during tolerancing of the window movements (Section 6.3.2). The results are given in Table 6.7.

Table 6.7: Results of the FEA analysis showing the calculated vacuum chamber window deflection during a pressure decrease of approximately 45 mbar.

	Deflection [μm]		
Window	**Required**	**Horizontal**	**Vertical**
Input	< 1.6	0.06	0.02
Output (90° to chamber wall)	< 26	0.30	0.16
Output (35° to chamber wall)	< 26	-0.52	-0.53

In summary, the mechanical design of the chamber was based on two very conservative values; the highest atmospheric sea level pressure recorded and a very high hourly pressure change.

6.5.3 O-Ring Seals

Several O-rings are employed to provide seals at the openings in the chamber walls and at the main flange. A summary of the O-rings used is given in Table 6.8.

Within the system, each O-ring sits in a groove machined into metal. The sizes of the O-rings grooves were carefully chosen so that when the chamber is under vacuum, the O-rings will deform and the vacuum windows will be pulled tight against the metal chamber wall. This is to avoid the windows 'floating' on the O-rings during atmospheric pressure changes.

Based on suggestions in the *Parker O-Ring Handbook* (Parker Hannifin Corporation, 2007), the groove dimensions were set to give a 40 per cent deformation of the O-ring and an 80 per cent fill-factor in the groove when the windows are pressed against the chamber wall. Care was also taken to

[2] `http://wmo.asu.edu/tropical-cyclone-fastest-intensification-tropical-cyclone`

Table 6.8: The O-ring seals used in the vacuum chamber system. The material used for all O-rings is Nitrile 70.

Description	Qty	Size
Foot Bellows	6	90 x 2 mm
Input Window Flange	1	56 x 2 mm
Input Window	1	19 x 1.5 mm
Output Window	2	54 x 2 mm
Main Flange	1	1324 x 6 mm
Vacuum Gauge	1	KF 25 Centering Ring
Electrical Feedthru	1	KF 50 Centering Ring
Vacuum Valve	1	KF 25 Centering Ring

specify appropriate surface finishes for machining on the sealing surfaces to avoid leaks to atmospheric pressure.

All of the grooves are rectangular in cross section except for the main seal groove. The concern with the main seal was that a rectangular cross-section groove would not retain the O-ring when the lid was opened – allowing the O-ring to fall inside the chamber and possibly contact an optical surface. Therefore a dovetail-style groove was designed (using data in Paykel Engineering (1980) and Parker Hannifin Corporation (2007)). This groove retains the O-ring after the lid is lifted, and is shown in cross-section in Figure 6.23.

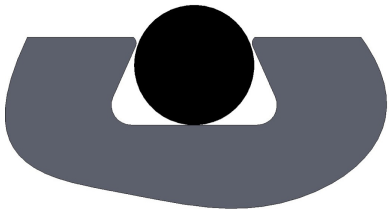

Figure 6.23: The main flange O-ring groove is a dovetail groove designed to retain the O-ring when the lid is opened. Shown is the O-ring and a part of the main flange in cross-section.

6.5.4 Ports

Three ports through the chamber wall are located on the front of the chamber at the collimator end. The ports are required for a vacuum gauge, electrical feedthrough and vacuum valve (as shown in Figure 6.24).

The vacuum gauge monitors the vacuum pressure level within the tank and is connected to a readout display as well as the KiwiSpec computer. The 90° elbow between the chamber wall and the gauge head is needed to position the gauge head in the required orientation.

A 41-pin electrical feedthrough allows temperature sensor cables to pass through the vacuum chamber wall. A number of pins will be available for future use since the temperature sensor cables will not use all of the 41 pins.

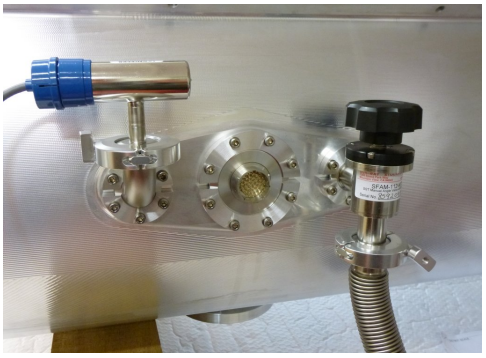

Figure 6.24: The ports through the vacuum chamber wall include a vacuum gauge (left), an electrical feedthrough (centre) and a vacuum valve (right).

The third port is provided for a manual, right-angle vacuum valve which allows for sealing and venting the chamber. During pump-down the vacuum pump is attached to the bottom of this valve via a flexible stainless steel hose; once the desired vacuum pressure level is reached the valve is closed and the pump disconnected.

6.5.5 Interior Paint

The interior of the chamber requires coating in a flat black paint to minimize scattered light within the chamber. The paint must be vacuum compatible and not out-gas volatiles which would degrade the vacuum pressure or contaminate the optical surfaces.

After a lengthy search for a paint that would meet the above requirements, 'MLS-85-SB Silicone Black' from AZ Technology, Inc. was chosen. Unlike the other companies contacted, AZ Technology was able to provide spectral reflectivity data, outgassing characteristics and application advice for their product to ensure that it would work for our application.

The total hemispherical spectral reflectance of MLS-85-SB is shown in Figure 6.25. For comparison, the values for two other paints investigated (Lord Aeroglaze Z-306 and Nextel velvet black) are also included. As the plot shows, MLS-85-SB compares very well with Nextel velvet black, which is commonly used in optical systems for stray light control. However, the Nextel paint is not proven to be vacuum compatible (based on discussions with the manufacturer).

Two parameters used to measure the outgassing of materials in a vacuum environment are the per cent total mass lost (TML) and per cent collected volatile condensable material (CVCM). Both of these parameters are typically determined for a given material through the American Society for Testing and Materials method for measurement of outgassing in a vacuum environment (ASTM E 595, 1993). This test procedure involves subjecting the materials to 125°C at less than $7\text{x}10^{-5}$ mbar for 24 hr. TML is the percentage of mass lost during the test period (the sample is weighed before and after). CVCM is determined by the amount of outgassed material

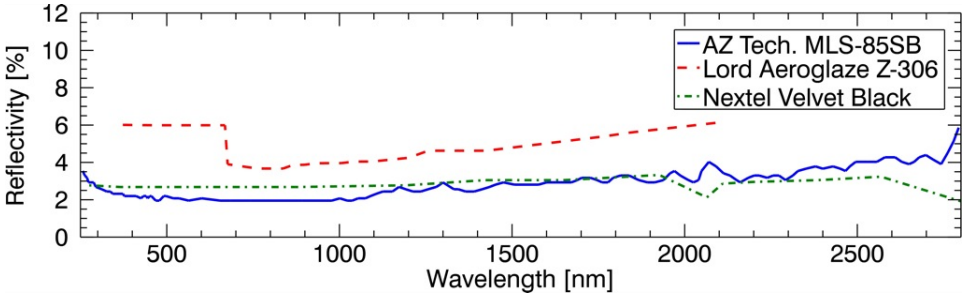

Figure 6.25: Total hemispherical spectral reflectance of three types of black paint investigated for stray light control within the KiwiSpec vacuum chamber. Data for MLS-85-SB from AZ Technology, Inc.; data for Lord Aeroglaze Z-306 and Nextel Velvet Black from Pompea and Beault (1995).

that condenses on a colder (25°C) plate within the test chamber. The National Aeronautics and Space Administration (NASA) recommends values of < 1 per cent TML and < 0.1 per cent CVCM for use in space applications[3], which was taken as a suitable guide for the outgassing requirements of the KiwiSpec vacuum chamber. Table 6.9 summarizes the outgassing specifications for MLS-85-SB (supplied by AZ Technology, and based on measurements made at NASA/George C. Marshall Space Flight Center).

Table 6.9: Outgassing specifications for MLS-85-SB black paint.

	TML	**CVCM**
NASA specification	$< 1\%$	$< 0.01\%$
MLS-85-SB	0.049%	0.001%

6.6 Vacuum Pump and Pump-down Methodology

The vacuum pump chosen for the KiwiSpec vacuum chamber system is the Varian (now Agilent Technologies) 'TriScroll 300 Dry Vacuum Pump'. This pump is an excellent choice for an optical system as it does not contain oil in the vacuum creation mechanism, thereby removing the risk of contamination backstreaming into the chamber.

The pump is specified to have an ultimate pressure of 0.013 mbar, which is more than adequate given the conclusions of Section 6.4.7. The pump can achieve this pressure level when pumping down from atmospheric pressure without the need for a roughing or backing pump.

The components of the vacuum pump system are shown in Figure 6.26. The pump connects temporarily to the vacuum chamber via a flexible stain-

[3] `http://www.nasa.gov/offices/oce/llis/0778.html`

less steel vacuum hose, which attaches to the vacuum valve on the side of the chamber. Once the desired vacuum pressure level is reached, the valve is closed and the pump powered off (after which the hose could be disconnected).

Owing to the initial outgassing of spectrograph components it is expected that the complete chamber will take some time to 'settle down' to a consistent pressure increase rate. During this initial period the vacuum will need to be refreshed on a more consistent basis than will be required in a few weeks' time. To accelerate this process (and remove the risk of possible contamination of optical components), during assembly each mechanical component will be exposed to vacuum pressures in a secondary vacuum chamber before being installed within the main KiwiSpec vacuum chamber.

Figure 6.26: The KiwiSpec vacuum pump system, shown while the (empty) vacuum chamber was undergoing initial pump-down tests. For this test, the windows and ports were closed with blank flanges.

6.7 Vacuum Chamber Testing

The KiwiSpec vacuum chamber was put through some initial pressure tests to determine the pump-down time and leak/outgassing rate of the empty chamber. Both of these parameters will change once the chamber interior is painted and the spectrograph components installed; nonetheless they are useful as a baseline of what the chamber alone can achieve.

After two initial (and longer) pump-down periods, the KiwiSpec chamber was evacuated from atmosphere to 0.007 mbar in 6.6 hr; details are shown in Figure 6.27. For this test, the chamber was unpainted, empty, and the O-ring seals were installed without vacuum grease applied.

Figure 6.28 shows the results of one of the early tests of vacuum pressure stability for the KiwiSpec vacuum chamber. This initial test demonstrates that the chamber itself will hold vacuum and not increase in pressure at a substantial rate.

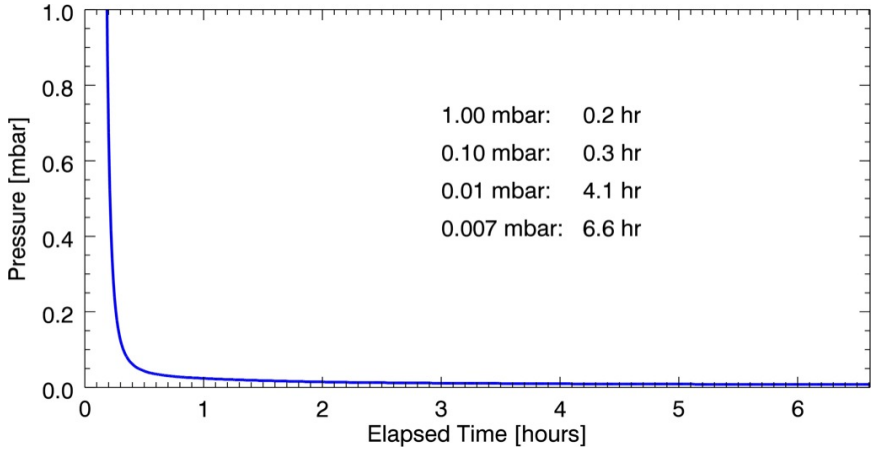

Figure 6.27: The third pump-down test of the empty (and unpainted) KiwiSpec vacuum chamber. The chamber was evacuated from atmospheric pressure to 0.007 mbar.

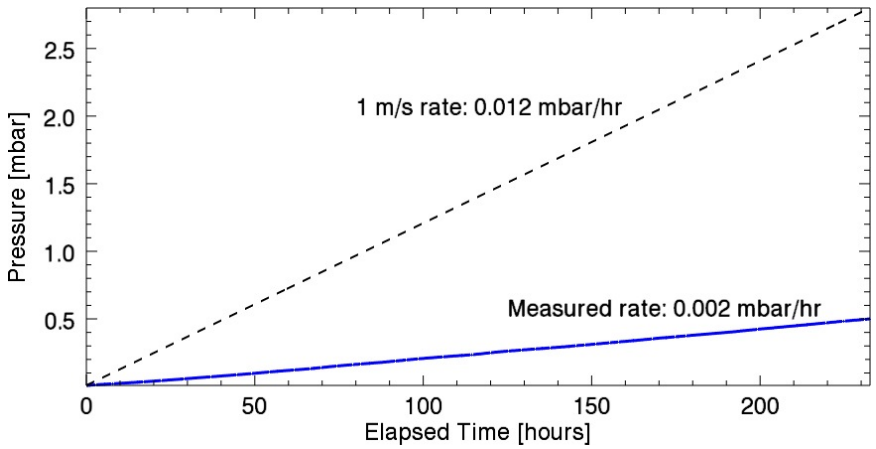

Figure 6.28: The measured increase in the vacuum pressure level of the empty (and unpainted) chamber over 9.7 days. The chamber was pumped down to 0.007 mbar when the valve was closed. For comparison, the dashed line shows the calculated pressure increase required to cause a 1 m/s shift due to a change in the refractive index of air inside the chamber.

Chapter 7

Efficiency

7.1 Introduction

In this chapter, the various aspects of the efficiency or light throughput of the KiwiSpec instrument will be discussed.

7.2 Efficiency Measurements of KiwiSpec Components

Several of the optical components within the KiwiSpec prototype required measurement to determine their spectral reflectivity or transmissivity. This was due to measured data not being available from the manufacturer (i.e. the input fold mirror, VPH gratings, and the Hasselblad lens); the optics being coated in-house at KiwiStar Optics (i.e. the primary collimator mirror, secondary collimator mirror, and the camera fold mirror); or the components being assembled at KiwiStar Optics (i.e. the grism).

7.2.1 Input Fold Mirror

The KiwiSpec input fold mirror is an ultra-broadband 'MaxMirror' manufactured by Semrock. This flat mirror with a multilayer coating was tested for reflectivity by the author using the spectrophotometer of the photometry and radiometry group of the Measurement Standards Laboratory of New Zealand (MSL). The reflectivity was measured at an angle of incidence of 48° to compare directly with the mirror's orientation within the instrument. The results of the measurements (compared against the Semrock-calculated theoretical reflectivity) are shown in Figure 7.1. The variation of each curve from a smooth line is likely due to interference effects between the multiple layers of the mirror's coating.

Shortly after the reflectivity measurements were made by the author, a polarization bias within the spectrophotometer was detected by MSL. Given that mirrors with high angles of incidence would be most affected by such a bias, the reflectivity of the input fold mirror was remeasured by MSL for both the vertical and horizontal polarization planes to ensure that the

spectrophotometer polarization was not biasing the measurement. As shown in Figure 7.1, there was a difference in reflectivity between the non-polarized and polarized measurements, which amounted to a 0.6 per cent difference in average reflectivity across 350 nm to 800 nm.

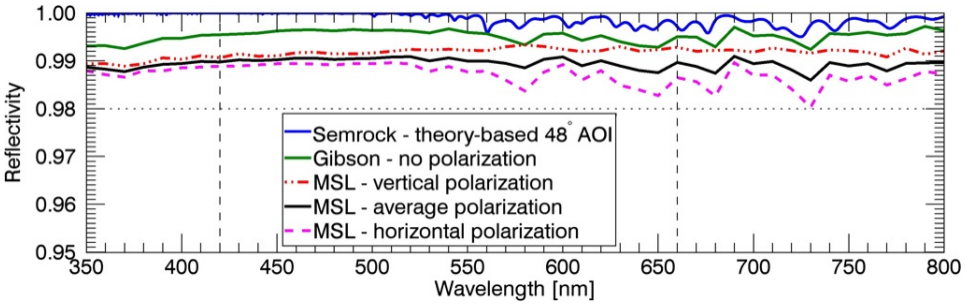

Figure 7.1: Theoretical and measured values of the spectral reflectivity of the KiwiSpec input fold mirror. Measurements were made at 10 nm intervals, at angle of incidence of 48°, with a 6.5 mm diameter measurement beam of 2 nm bandwidth. The horizontal dotted line shows the Semrock average reflectivity specification for wide-angle reflectance ($R_{avg} > 98\%$), which the KiwiSpec mirror clearly meets. The vertical dashed lines indicate the wavelength range of the KiwiSpec prototype (420–660 nm).

7.2.2 Collimator Mirrors

The secondary collimator mirror was coated in-house at KiwiStar Optics with bare aluminium, and the coating reflectivity was measured by MSL. The mirror was tested at an angle of incidence of 5.5° to mimic the mirror's use in KiwiSpec. The results are shown in Figure 7.2.

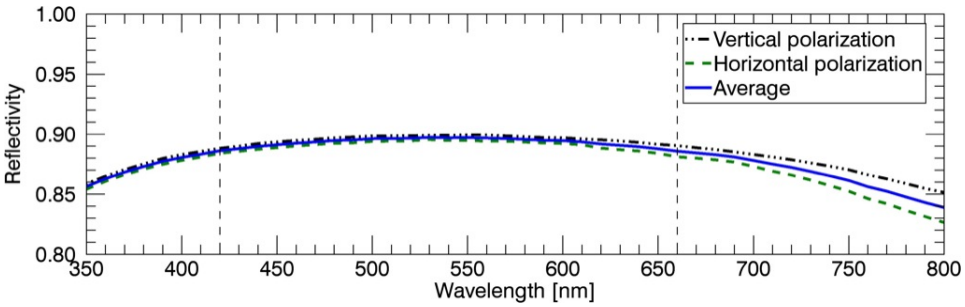

Figure 7.2: The measured spectral reflectivity of the KiwiSpec secondary collimator mirror (coated with bare aluminium). Measurements were made at 10 nm intervals, with a 10 mm diameter measurement beam of 2 nm bandwidth, and at angle of incidence of 5.5°. The vertical dashed lines indicate the wavelength range of the KiwiSpec prototype (420–660 nm).

The primary collimator was also coated in-house with bare aluminium. However, due to the complexity of measuring the coating reflectivity of the

primary collimator mirror (owing to its long focal length and off-axis nature), it was not tested using a spectrophotometer. This mirror was coated at the same time as the secondary collimator mirror, and therefore the results of the secondary collimator mirror coating tests were taken to be representative of this mirror's reflectivity. A further justification for this approach is that the angles of incidence for the two beams striking the collimator mirror within KiwiSpec are within a few degrees of the angle used to test the secondary collimator mirror. Therefore there should be a minimal difference between the reflectivities of the two mirrors.

7.2.3 Camera Fold Mirror

The KiwiSpec camera fold mirror was coated with bare aluminium in-house at KiwiStar Optics. The spectral reflectivity of the mirror was measured by MSL, with the results shown in Figure 7.3. Of note is the difference between this figure and the equivalent figure for the secondary collimator mirror reflectivity (Figure 7.2). Although both mirrors were coated with bare aluminium, the increased angle of incidence for the camera fold mirror (47.4° vs. 5.5°) causes a significant difference between the reflectivities of the two polarization states.

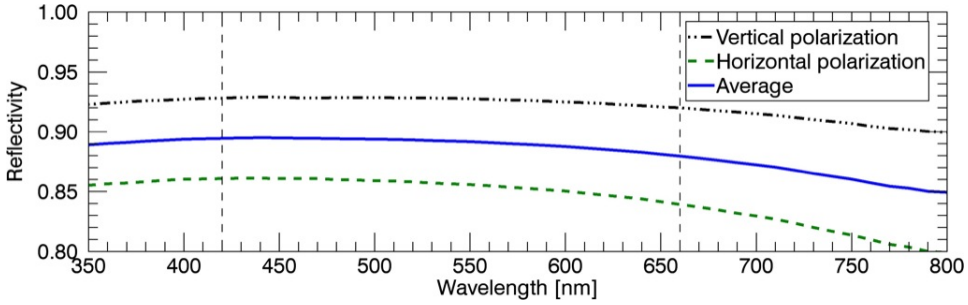

Figure 7.3: The measured spectral reflectivity of the KiwiSpec camera fold mirror (coated with bare aluminium). Measurements were made at 10 nm intervals, with a 10 mm diameter measurement beam of 2 nm bandwidth, and at angle of incidence of 47.4°. The vertical dashed lines indicate the wavelength range of the KiwiSpec prototype (420–660 nm).

7.2.4 Hasselblad Lens

The spectral throughput of the Hasselblad lens was measured by MSL, and the results are shown in Figure 7.4. The lens has a surprisingly high throughput, with a peak efficiency of just over 97 per cent at 610 nm.

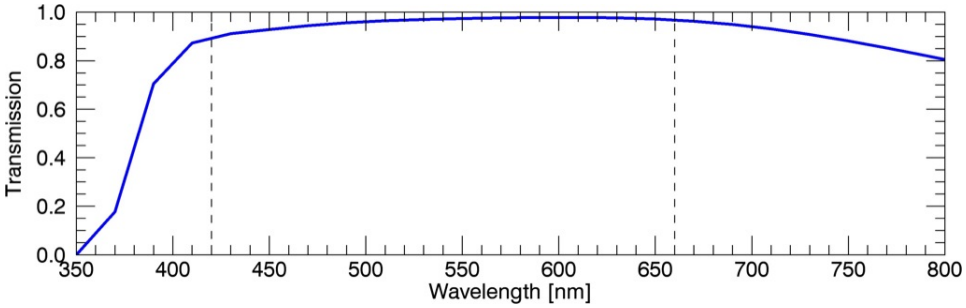

Figure 7.4: The on-axis measured spectral throughput of the Hasselblad lens. Measurements were made at 20 nm intervals, with a 10 mm diameter measurement beam of 2 nm bandwidth. The vertical dashed lines indicate the wavelength range of the KiwiSpec prototype (420–660 nm).

7.2.5 VPH Grating Efficiency Tests

Two VPH gratings were purchased for the KiwiSpec prototype, with the intent to test both and use the better of the two gratings within the instrument. The gratings were tested by the author in order to measure their efficiency as a function of grating angle and wavelength. The test was based on the methods described by Barden et al. (2000) and Adams et al. (2008), which in turn are based on the 'tunable spectrograph' concept of Barden et al. (1998).

For testing the gratings, a collimated light source of selectable wavelength was generated with the fore-optics of the MSL spectrophotometer system. This system includes a dual-grating monochromator (employing a 2 nm-wide slit illuminated by a xenon lamp), a computer-controlled stepper driver system, the facility to amplify and read voltages from the detector (a silicon photodiode), and LabView-based software routines to control all of the above.

A schematic of the test parameters is shown in Figure 7.5. During the test, the VPH grating was placed at a known angle of incidence within a collimated beam of monochromatic light, and the grating equation was used to predict the angle of diffraction for the given wavelength of light. A detector, mounted on an arm rotating about the centre of the grating, was then rotated to the predicted angle, and five intensity measurements taken over one degree of arc centered on the predicted diffraction angle. This approach of scanning around the predicted angle ensured that the maximum value was recorded (and accounts for grating manufacturing tolerances, slight misalignments, etc.).

Three grating angles were tested for each grating - the design angle of incidence (AOI) of the gratings (11.29°) and $\pm$ 2° around that value.

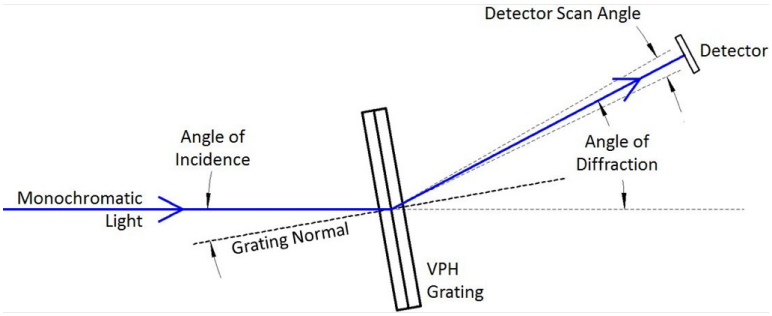

Figure 7.5: Schematic layout of the VPH diffraction efficiency test, showing relevant angles. The detector employed was a silicon photodiode.

7.2.5.1 Optical

The optical layout for the test is shown in Figure 7.6. Collimated light from the monochromator (within the spectrophotometer system) passes through a 40-mm diameter entrance aperture, and then strikes the grating. A large diameter collimated beam was chosen as it averages out spatial efficiency non-uniformities across the grating (Chonis et al., 2012), and replicates its use within the spectrograph. The light is diffracted by the grating and then focused onto the detector by a plano-convex lens. The detector is placed inside of the focal point of the lens, resulting in a defocused spot of light falling on the detector. The defocused spot size was chosen so as to nearly fill the detector, which minimized the effects of possible response non-uniformities across the detector's surface.

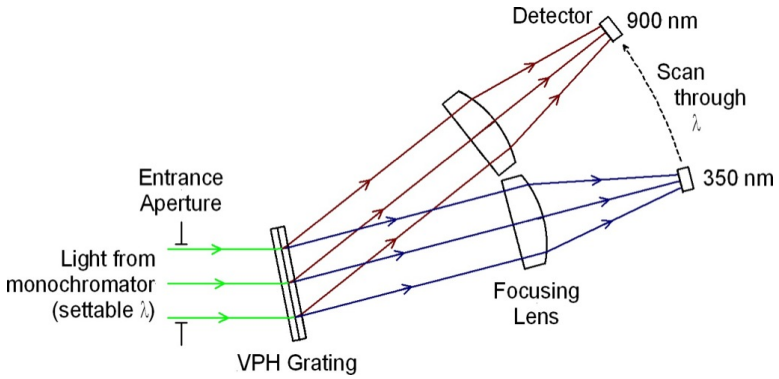

Figure 7.6: Schematic diagram showing the optical layout and operation of the VPH diffraction efficiency test jig. The detector arm, consisting of a focusing lens and detector, is shown in two positions in the diagram (at the measurement points for 350 nm and 900 nm).

7.2.5.2 Mechanical

An existing rotary stage was employed as the base of the test jig for this test, which featured two platforms rotating about a common axis. Each platform was driven by a 1.8 degree/step stepper motor reduced through a 180-tooth worm gear, giving a rotation resolution of 0.01 degrees per motor step. The motors used were compatible with the existing spectrophotometer stepper control system, and each of the motors features an integral encoder which provides positional feedback to the control system.

Modifications to the rotation stage required the design and fabrication of an arm to hold the detector and focusing lens, as well as a support for the grating. A picture of the test setup is shown in Figure 7.7. The top platform has the detector arm attached, and the bottom platform rotates the VPH grating. This arrangement was chosen so that a high-resolution encoder could be located on the shaft driving the top (detector) platform.

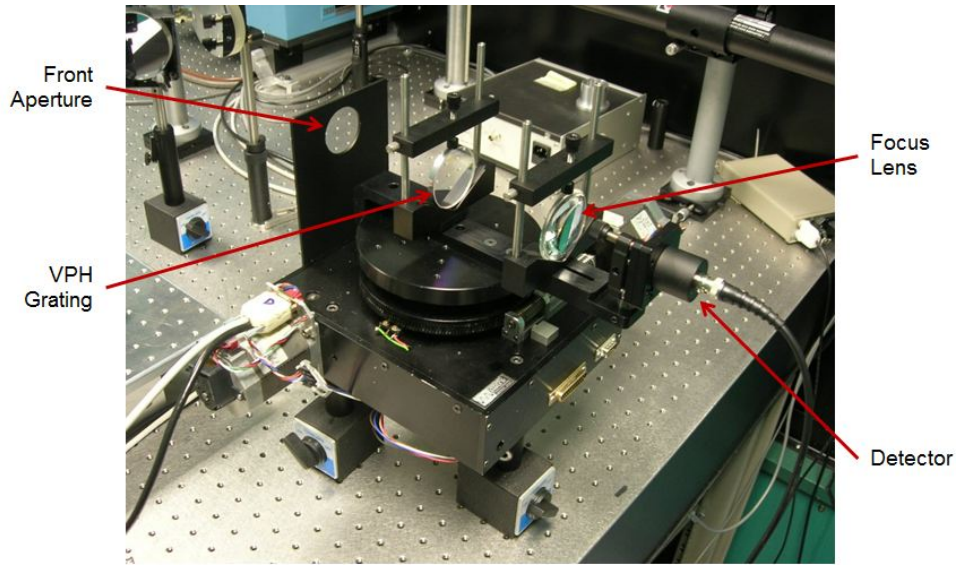

Figure 7.7: The VPH test jig with both the grating and detector arms aligned in the 'home' position.

7.2.5.3 Software

Software was written in LabView to control the test (i.e. setting the monochromator wavelength, calculating the diffraction angle, controlling the grating and detector rotations, taking detector readings and logging the data). The main graphical user interface (GUI) for the software (shown in Figure 7.8) contains the desired settings for the test, including: the VPH parameters, wavelength range and step size, grating angle of incidence range and step size, the detector scan angle, the number of readings to take through the

detector scan angle and the integration time for the detector. The test procedure followed by the software is shown in Algorithm 1. Included within the algorithm are two $I_0(\lambda)$ measurements which measure the intensity of light incident on the test jig (to be compared against the diffracted intensity). The pair of before and after $I_0(\lambda)$ measurements provided a check to ensure that that lamp's spectral intensity did not change appreciably during the test.

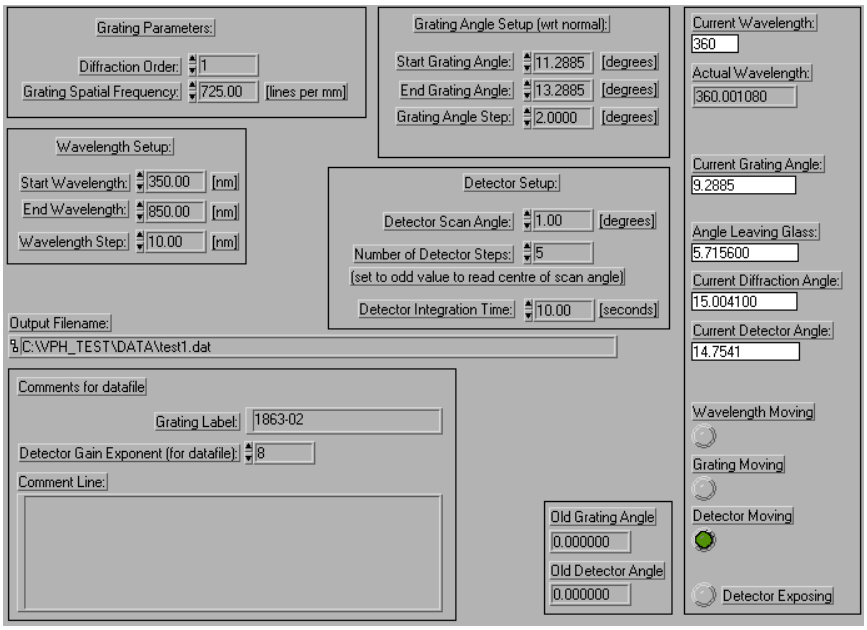

Figure 7.8: The user interface for the LabView-based program that drives the test jig.

Algorithm 1: The measurement procedure followed by the VPH test software.

```
· remove grating from test jig;
· move detector arm to home position;
/* measure the lamp response                                    */
for wavelength = 350 nm to 850 nm step 10 nm do
    · move monochromator to current wavelength;
    · take measurement I_0(λ);
end
· place grating within test jig;
for grating_angle = 9.29° to 13.29° step 2° do
    · move grating to current grating_angle;
    for wavelength = 350 nm to 850 nm step 10 nm do
        · move monochromator to current wavelength;
        · calculate diffracted beam angle (β) using grating equation;
        /* scan through β to make sure peak measured            */
        for detector_angle = (β − 0.5°) to (β + 0.5°) step 0.25° do
            · move detector to current detector_angle;
            · take measurement I(λ);
        end
    end
end
· remove grating from test jig;
· move detector arm to home position;
/* re-measure the lamp response                                 */
for wavelength = 350 nm to 850 nm step 10 nm do
    · move monochromator to current wavelength;
    · take measurement I_0(λ);
end
```

7.2.5.4 Results

The transmitted efficiency of each wavelength was calculated using:

$$T(\lambda) = \frac{I(\lambda)}{I_0(\lambda)_{\text{avg}}}, \tag{7.1}$$

with the measurements $I(\lambda)$ and $I_0(\lambda)$ as noted within Algorithm 1. $I_0(\lambda)_{\text{avg}}$ indicates the average of the before and after $I_0(\lambda)$ values.

The results of the measurements for the two gratings are shown in Figures 7.9a and 7.9b. Also shown in each figure is the theoretical predicted efficiency of the gratings, calculated by the manufacturer, Wasatch Photonics. For each grating, Table 7.1 summarizes the peak efficiency values and the wavelengths at which they occur. Although the peak efficiency of each

grating is a few per cent below the theoretical value, the two gratings do meet the requested specifications. The grating with the higher throughput, 1863-02, was selected for use in the KiwiSpec prototype.

The difference in peak wavelength between the measured gratings (510 nm) and the design wavelength (546 nm) cannot be accounted for. An incorrect setting of the angle of incidence could in theory have caused such a shift; however, each grating was initially aligned in the test jig to better than 0.1° by monitoring a reflected laser beam over a long path length. Furthermore, an incorrect AOI would also have resulted in shifted diffracted beam positions, which was not found in practice.

Direct comparisons between these results and VPH efficiency measurements given in the literature (i.e. Barden et al. (1998), Barden et al. (2000), Adams et al. (2008), Chonis et al. (2012)) are difficult owing to the different design parameters of the various gratings (i.e. line densities, peak design wavelengths, angles of incidence, presence or absence of anti-reflection (AR) coatings). However, of interest is that in spite of the differences in design parameters, the gratings tested within the listed papers and the measurements here show peak efficiencies in the vicinity of 80 per cent. Given that all of the gratings were likely optimized in efficiency for their given parameters, 80 per cent (or possibly even 85 per cent) might represent the typical achievable efficiency peak for current manufacturing processes of VPH gratings.

The results also show the benefits of the tunable aspect of VPH gratings, in that changing the grating angle of the KiwiSpec gratings by only 2° can lead to a 60-nm shift in the peak wavelength. This can lead to a marked increase in the efficiency at blue wavelengths. For example, if the AOI for grating 1863-02 is changed from 11.29° to 9.29° the grating efficiency at 420 nm increases by approximately 12 per cent (albeit with an efficiency loss at the red end of the wavelength range). Given such a possible increase, there is good reason to allow the ability to tune the spectrograph efficiency for wavelengths of interest. Therefore the KiwiSpec opto-mechanical design includes this adjustment, as described in Section 5.6.11.

7.2.6 Complete Grism

The spectral throughput of the assembled VPH grism was measured by MSL, and the results are shown in Figure 7.10. Included for comparison in the figure are the theoretical efficiency curve (provided by Wasatch Photonics) for the VPH grating, as well as the measured diffraction efficiency for the grating 1863-02 used within the grism (the same results shown in Figure 7.9a for the 11.29° AOI).

Of note is the slight increase in efficiency of the grism over the VPH grating alone. Although the grism adds approximately 34 mm of BK7 glass to the system, it also adds two MgF_2 anti-reflection coatings (on the grism entrance and exit prism faces). The net effect is a slight increase in efficiency

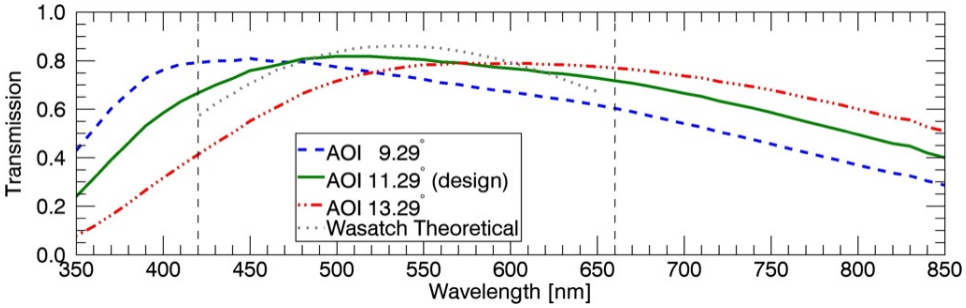

(a) Grating number 1863-02, which has a measured peak of 81.8% at 510 nm.

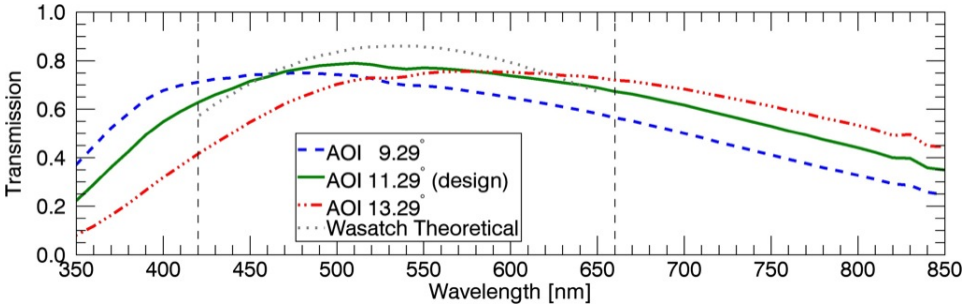

(b) Grating number 1863-04, which has a measured peak of 79.0% at 510 nm.

Figure 7.9: Measured efficiencies of the two purchased VPH gratings. Each grating was tested at three angles of incidence (AOI). The vertical dashed lines indicate the wavelength range of the KiwiSpec prototype (420–660 nm). Note that the gratings were not anti-reflection coated for this test. Also included is the Wasatch Photonics predicted peak throughput for the 11.29° AOI. Fresnel reflection has been added to the Wasatch theoretical values to allow for better comparisons against the measured values.

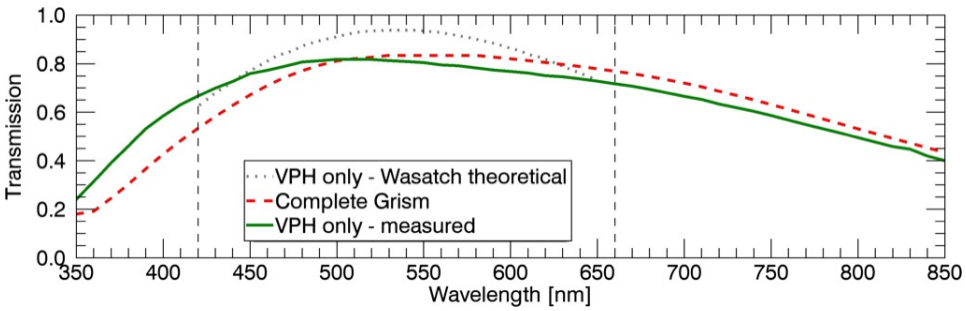

Figure 7.10: Measured transmission of the complete grism used within the KiwiSpec prototype. The prism faces were coated with MgF_2. Also included is the measured diffracted efficiency curve for the VPH grating used within the grism (1863-02), and the Wasatch Photonics predicted peak throughput for the design AOI (11.29°). Fresnel reflections were not added to the Wasatch theoretical values for this plot as the grating cover plates are bonded to the grism prisms.

Table 7.1: Summary of the measured peak throughputs for three angles of incidence for the two VPH gratings. Also included is the Wasatch Photonics predicted peak throughput for the design AOI (11.29°). Fresnel reflection has been added to the Wasatch theoretical values to allow for better comparison between it and the measured values.

	1863 − 02		1863 − 04	
AOI	**Peak Throughput** [%]	**Peak** λ **[nm]**	**Peak Throughput** [%]	**Peak** λ **[nm]**
9.29°	80.9	450	75.0	480
11.29°	81.8	510	79.0	510
13.29°	79.1	570	75.6	570
Wasatch	86.0	547	86.0	547

compared to the grating without AR coatings (which would be further increased if high efficiency coatings were employed instead of MgF_2).

Also evident in the figure is a shift in the peak wavelength between the grism and the VPH grating alone, which is likely due to assembly errors of the grism. Unfortunately, mechanical references (as opposed to optical references) were used during assembly, and as such the relative clockings of the VPH grating and prisms were not controlled accurately enough to achieve the tolerance specification of ± 0.1° (see Table 4.7). Post-assembly, the grism was tested using a laser beam in reflection (from the prism faces), and also in transmission through the grism to determine to first-order the clockings of the two prisms and the VPH grating. Analysis of the results in Zemax showed that with respect to the first prism, the VPH grating is incorrectly clocked by 3° and the second prism is off by 2°. Such errors will result in a change in the angle of incidence of the light rays on the VPH grating, leading to a wavelength shift in the efficiency peak. As described in Section 4.2.5.2, future grisms should be assembled and aligned via an optical method that monitors the deviation of a laser beam in two planes as each component of the grism is added to the assembly.

7.3 Instrument Efficiency Model

In order to calculate the expected throughput of the KiwiSpec prototype, an efficiency model was constructed using IDL (Interactive Data Language). This model contains spectral efficiency data for each optical component encountered by the light as it passes through the instrument. The model includes parameters such as the effects of coatings (both reflection and anti-reflection), Fresnel reflection losses, and the internal transmission of glasses. These parameters are based on vendor data, theoretical calculations, and actual spectrophotometric measurements of system components.

7.3.1 Efficiency Model Description

Table 7.2 shows a simplified version of the efficiency model containing only three 'surfaces' (such as a mirror coating, anti-reflection coating, or glass internal transmission). For a given wavelength, the efficiency values for each surface are multiplied together to give the total efficiency for the entire system at that wavelength.

Table 7.2: A simple efficiency model for a three-surface system. Each 'surface' is an element that the light strikes on its path through the system (such as a mirror coating, anti-reflection coating, or glass internal transmission). Each 'T' value is a ratio between 0 and 1 indicating how much of the incident light is transmitted by that surface at that wavelength.

λ [nm]	**Sfc A**	**Sfc B**	**Sfc C**	**Total Throughput**
420	$\mathrm{T}_{A(420)}$	$\mathrm{T}_{B(420)}$	$\mathrm{T}_{C(420)}$	$= \mathrm{T}_{A(420)} \cdot \mathrm{T}_{B(420)} \cdot \mathrm{T}_{C(420)}$
430	$\mathrm{T}_{A(430)}$	$\mathrm{T}_{B(430)}$	$\mathrm{T}_{C(430)}$	$= \mathrm{T}_{A(430)} \cdot \mathrm{T}_{B(430)} \cdot \mathrm{T}_{C(430)}$
⋮	⋮	⋮	⋮	⋮
660	$\mathrm{T}_{A(660)}$	$\mathrm{T}_{B(660)}$	$\mathrm{T}_{C(660)}$	$= \mathrm{T}_{A(660)} \cdot \mathrm{T}_{B(660)} \cdot \mathrm{T}_{C(660)}$

The KiwiSpec efficiency model contains fifty surfaces when all components from the telescope to the spectrograph CCD detector are included. The model allows individual surfaces (or groups of surfaces) to be included or excluded from the total efficiency calculations. This is useful for examining component groups within the model (i.e. for calculating the efficiency of the spectrograph only). A listing of the full set of possible surfaces that could be included within the model is given in Table 7.3.

Table 7.3: Parameters available within the full KiwiSpec efficiency model.

Sfc	Description	Data Source
1	Primary mirror reflectivity	Aluminium coating reflectivity (measured by MSL)
2	Dust on primary mirror	Dust on primary mirror (6.00% loss)
3	Secondary mirror reflectivity	Aluminium coating reflectivity (measured by MSL)
4	Dust on secondary mirror	Dust on secondary mirror (2.75% loss)
5	50mm EFL PRS[1] relay lens - front sfc coating	JML coating '101' (data from JML website)
6	50mm EFL PRS relay lens - first element transmission	S-TIM25 internal transmission (scaled for thickness)[2]
7	50mm EFL PRS relay lens - second element transmission	BK-7 internal transmission (scaled for thickness)[2]
8	50mm EFL PRS relay lens - back sfc coating	JML coating '101' (data from JML website)
9	50mm EFL PRS relay lens - front sfc coating	JML coating '101' (data from JML website)
10	50mm EFL PRS relay lens - first element transmission	BK-7 internal transmission (scaled for thickness)[2]
11	50mm EFL PRS relay lens - second element transmission	S-TIM25 internal transmission (scaled for thickness)[2]
12	50mm EFL PRS relay lens - back sfc coating	JML coating '101' (data from JML website)
13	Micro lens coating	Theoretical MgF_2 coating on BK-7
14	Micro lens transmission	BK-7 internal transmission (scaled for thickness)[2]
15	Guiding errors	Guiding errors (5.00% loss)
16	Seeing disk and fibre diameter calculations	Seeing ratio (calculated using Moffat function)
17	Fibre pointing losses	Fibre pointing losses (5.00% loss)
18	Fibre internal transmission (with 30m length correction)	Data from Polymicro website
19	Fibre exit Fresnel losses	Fresnel losses calculated using Zemax glass catalog
20	Prototype fibre FRD losses	Design-based fibre FRD (10.00% loss)
21	Alignment losses	Alignment-based fibre FRD (5.00% loss)

Continued on Next Page...

Table 7.3: (continued)

Sfc	Description	Data Source
22	40mm EFL relay lens - front sfc coating	Edmund UV-VIS coating (data from Edmund website)
23	40mm EFL relay lens - first element transmission	F2 internal transmission (scaled for thickness)^2
24	40mm EFL relay lens - second element transmission	N-FK5 internal transmission (scaled for thickness)^2
25	40mm EFL relay lens - back sfc coating	Edmund UV-VIS coating (data from Edmund website)
26	Input vacuum window - first surface coating	Theoretical MgF_2 coating shifted for 20° AOI
27	Input vacuum window - transmission	Data from Thorlabs website (Fresnel reflections removed)
28	Input vacuum window - second surface coating	Theoretical MgF_2 coating shifted for 20° AOI
29	100mm EFL relay lens - front sfc coating	Thorlabs '-A' coating (data from Thorlabs website)
30	100mm EFL relay lens - first element transmission	BK-7 internal transmission (scaled for thickness)^2
31	100mm EFL relay lens - second element transmission	F4 internal transmission (scaled for thickness)^2
32	100mm EFL relay lens - back sfc coating	Thorlabs '-A' coating (data from Thorlabs website)
33	Input fold mirror	Measured input fold mirror reflectivity
34	Primary collimator mirror - first reflection	Secondary collimator mirror reflectivity (measured by MSL)
35	Échelle grating - diffraction and coating (scaled)	Scaled to measured data, includes aluminium coating
36	Échelle overfill losses	Échelle overfill (0.15% loss)
37	Primary collimator mirror - second reflection	Secondary collimator mirror reflectivity (measured by MSL)
38	Secondary collimator mirror	Secondary collimator mirror reflectivity (measured by MSL)
39	Camera fold mirror	Camera fold mirror reflectivity (measured by MSL)
40	Output vacuum window - first surface coating	Theoretical MgF_2 coating on fused silica
41	Output vacuum window - transmission	Data from Thorlabs website (Fresnel reflections removed)
42	Output vacuum window - second surface coating	Theoretical MgF_2 coating

Continued on Next Page...

Table 7.3: (continued)

Sfc	Description	Data Source
43	Grism assembly	Grism assembly transmission (measured by MSL)
44	Hasselblad lens throughput	Hasselblad lens transmission (measured by MSL)
45	Hasselblad lens vignetting	Hasselblad lens vignetting profile (determined with Zemax)
46	Field-flattening lens coating	Thorlabs '-A' coating (data from Thorlabs website)
47	Field-flattening lens transmission	N-BK7 internal transmission (scaled for thickness)[2]
48	Field-flattening lens coating	Thorlabs '-A' coating (data from Thorlabs website)
49	Detector window and coating transmission	Data from Spectral Instruments
50	CCD response	e2v report for KiwiSpec CCD

[1]Pinhole Relay System, which was installed on the McLellan telescope during the testing period.
[2]The internal transmission data for optical glasses was sourced from the Zemax glass catalog.

The efficiency model is an approximation of a complex optical system, and by necessity it makes some compromises and assumptions. Some comments on the various data sources it contains are listed below:

Coatings: The model includes both reflectance coatings for mirrors and anti-reflection coatings for lenses. Coating data came from in-house spectrophotometer measurements, from theory-based calculations for single layer MgF_2 coatings, or from plots or data listed on the vendor websites. The in-house spectrophotometer measurements were described in Section 7.2. The theoretical MgF_2 coating calculations followed the procedure described in the Melles-Griot Technical Guide (Melles Griot, 1997). For coating data for which only a plot was available, a digitization routine was written in IDL that allowed one to trace a curve on a plot to generate a correctly-scaled datafile of wavelength vs. efficiency information.

Polarization: The S and P polarization states were not separately accounted for in the model as the majority of data sources did not contain separated polarization data. In cases where polarization data was available, the average of the two polarization states was used.

Telescope Alignment Losses: Mis-alignments of the telescope and fibre feed optical system (and the resulting aberrations or vignetting) lead to a decrease in the amount of light entering the fibre. Such issues include telescope collimation, telescope focus and fibre-feed misalignments. To account for these possible losses within the model (which were not characterized during the testing period at Mt John University Observatory (MJUO)), the model allows for a percentage loss of white light (i.e. all wavelengths are reduced equally).

Atmospheric Dispersion: This effect causes the stellar image to become dispersed in the direction normal to the horizon, resulting in some wavelengths not entering the fibre. Stars at lower elevation are affected more than stars near the zenith.

The theoretical losses can be calculated with the approach of Filippenko (1982). However, in practice which wavelengths enter the fibre is dependent on the the seeing and the telescope guiding (both of which can change during a single exposure). Guiding and seeing effects will move the dispersed stellar image with respect to the fibre entrance, and hence vary which wavelengths are entering the fibre (note that if these movements happen to be along the dispersion direction, they will partially mitigate the effect of atmospheric dispersion). The spectral sensitivity of the guide camera system also plays a role, as it determines which wavelengths the telescope is guiding on (and hence which

wavelengths are nominally centered over the fibre entrance). Therefore, because of the difficulty in accurately accounting for these guiding and seeing effects during the on-sky testing period, atmospheric dispersion is not included in this efficiency model.

Vacuum Window Efficiency: The input vacuum window in the KiwiSpec prototype is placed at an angle of 20° to reflect a small percentage of the incoming light towards an exposure meter (see Section 5.6.3 and Chapter 8). This tilt angle was not accounted for during the design of the MgF_2 coating thickness for either side of the vacuum window. The tilt of the input vacuum window causes the coating to present a longer path length to the incoming beam, and has the effect to shift the efficiency curve of the coating towards bluer wavelengths. Smith (2000) indicates that the wavelength shift can be approximated by:

$$\lambda_\theta = \frac{\lambda_0}{n}\sqrt{n^2 - \sin^2\theta}, \tag{7.2}$$

where:

λ_θ	=	shifted wavelength	[nm];
λ_0	=	wavelength	[nm];
n	=	index of refraction (wavelength dependent)	[unitless];
θ	=	window tilt	[degrees].

The effect on the efficiency curve is shown in Figure 7.11. Initially this incorrect coating thickness was thought to be an oversight; however, as shown in the figure it actually has the benefit of slightly increasing blue transmission with a negligible decrease in red transmission.

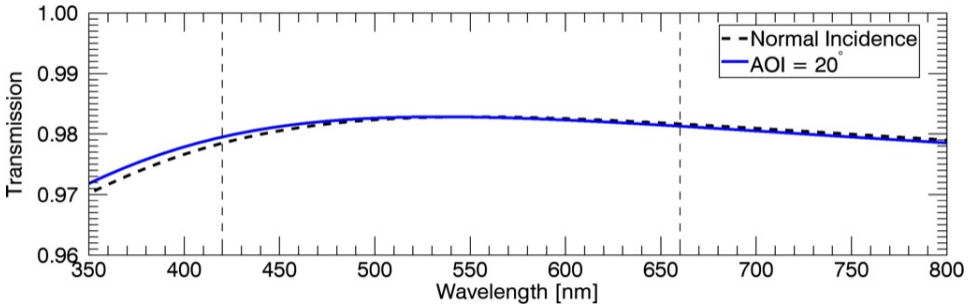

Figure 7.11: The calculated effect of changing the angle of incidence on the KiwiSpec vacuum window MgF_2 coating (which was designed for normal incidence). Shown is the efficiency curve for one of the two coated surfaces on the vacuum window.

Guiding Losses: The model contains a parameter that can be set to a percentage loss of white light due to telescope guiding errors.

Dust on Telescope Optics: Two parameters within the model allow for a percentage of white light to be lost due to dust on each of the primary and secondary telescope mirrors. Giordano (1997) reported on the results of dust contamination of a pair of exposed mirrors at the Very Large Telescope (VLT) site at Paranal, Chile. One mirror in the test was pointing upwards and one downwards, in order to mimic the arrangement of the primary and secondary mirrors of a telescope. Giordano found that the 'primary' test mirror reflectivity decreased by 8 per cent per year, and the 'secondary' test mirror reflectivity decreased by 3.65 per cent per year during what is described as the 'normal dusty period'. Unfortunately, reflectivity data during the study were measured at only one wavelength (670 nm), and therefore the spectral response of the dust was not determined.

Accounting for dust on the telescope optics is warranted within the model as only five weeks after the KiwiSpec on-sky testing period, the primary and secondary mirrors of the 1-m McLellan telescope were due for their yearly cleaning and re-coating of aluminium. Based on a conservative 75 per cent scaling of the Giordano results, the reflectivity losses in the efficiency model were set at 6 per cent and 2.75 per cent for the 1-m McLellan primary and secondary mirrors (respectively).

Fibre FRD Losses: The issue of focal ratio degradation (FRD) was not explicitly solved for in this prototype instrument, because the design goal was to use off-the-shelf optics whenever possible in order to expedite assembly of the instrument. Future versions of KiwiSpec will feature a custom input relay that accounts for (and minimizes) this loss of light. The prototype FRD losses were calculated to be approximately 10 per cent and are included in the model.

Fresnel Reflections: Fresnel reflections were calculated when required. The simplified normal incidence Fresnel equation was employed, as the small angles of incidence on the refractive components did not warrant the need to calculate the two polarization states separately.

The Fresnel equation employed, adapted from Yoder (2006), is:

$$r = \frac{(n_2 - n_1)^2}{(n_2 + n_1)^2}, \tag{7.3}$$

where:

r	=	ratio reflected from the surface	[unitless];
n_1	=	refractive index of material before surface	[unitless];
n_2	=	refractive index of material after surface	[unitless].

Fibre Pointing Losses: The model allows for an overall loss due to the fibres not being located perfectly on-axis. Decentered or incorrectly-pointed fibres at either the telescope or spectrograph end of the fibre link could introduce efficiency losses.

Echelle Overfill: The model accounts for the 0.15 per cent loss of white light due to the 100-mm collimated beam slightly overfilling the ruled area of the échelle grating (102 mm x 408 mm).

Hasselblad Vignetting: The Hasselbad camera lens introduces some vignetting, which affects the intensity within the spectrum radially outward from the centre. Zemax was employed to determine the vignetting profile for the blaze wavelengths, which is included in the model.

Internal Transmission: Internal transmission accounts for absorption losses when light is transmitted through glass; it does not include Fresnel (surface reflection) losses. Data for the internal transmission of the glass types used were taken from the Zemax glass catalogue, which is tabulated for 25-mm thick glasses. These data were scaled to the actual thicknesses of the various lenses using the following equation (from Hoya Optics Division (2010)):

$$\tau = \tau_0^{\frac{d}{d_0}}, \tag{7.4}$$

where:

τ	=	internal transmission of glass for thickness d	[unitless];
τ_0	=	data source internal transmission of glass for thickness d_0	[unitless];
d	=	actual glass thickness	[mm];
d_0	=	glass thickness from data source	[mm].

The average thickness of each lens was determined in Zemax by measuring the length of the ray passing through the lens at 70 per cent of the diameter of the beam footprint on the lens. The 70 per cent zone was chosen for the average thickness, as half of the rays lie inside this zone, and half outside (with respect to surface area). The model makes the assumption that all wavelengths pass through the same thickness of glass.

7.3.2 Theoretical Échelle Efficiency

A theoretical efficiency profile for the échelle grating was calculated using the equations within Section 2.16, which use various échelle parameters (R-value, grooves per mm, γ, θ and θ_B values) to calculate the blaze function for each échelle diffraction order over one free spectral range. Each blaze function was then multiplied by the reflectivity of aluminium to account for the coating on the actual KiwiSpec échelle. The overall efficiency profile was also scaled to absolute efficiency measurements of the KiwiSpec échelle, which were supplied for three diffraction orders by Richardson Gratings, the grating manufacturer. The result is shown in Figure 7.12.

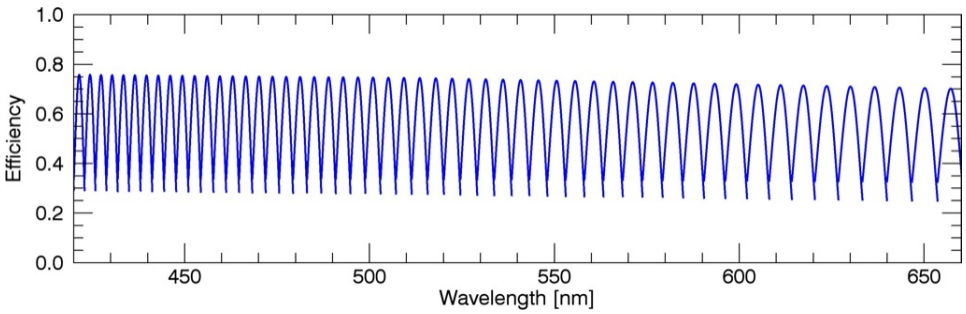

Figure 7.12: The calculated efficiency profile of the KiwiSpec échelle grating over the wavelength range of the prototype. The plotted data include the theoretical blaze function, an aluminium coating, and here has also been scaled to match the absolute efficiency data for the KiwiSpec grating (provided by Richardson Gratings). Each échelle diffraction order is plotted over one free spectral range.

7.3.3 Theoretical Seeing Calculations

Atmospheric seeing affects instrument efficiency by changing the size of the stellar image formed by the telescope. As the seeing worsens, the flux within the image of the star becomes less centrally concentrated and is redistributed over a larger surface area at the telescope focal plane. In the case of a fibre-fed spectrograph with a fixed fibre diameter at the telescope focal plane, this means that as the seeing worsens, less light enters the fibre (and therefore the spectrograph receives less light at the fibre exit).

The common metric for measuring seeing is the FWHM (Full Width Half Maximum) of the stellar image intensity profile. This is defined as the width of the intensity curve measured at half of the maximum intensity. It is typically reported in arcseconds, with excellent seeing implying sub-arcsecond FWHM values.

King (1971) combined empirical data from several sources and described the observed radial intensity profile of a stellar image as being composed of three parts: a central section comprised of a uniform disk surrounded by

falling intensity that can be approximated by a gaussian curve; a transition region that King indicated is exponential in shape; and an extended aureole, which decreases in intensity following an inverse-square law. Stetson et al. (1990) mentions that the intensity of the extended aureole "... appears to be dominated by scattering from dust and aerosols in the atmosphere, and from dirt and scratches in the optical system".

Moffat (1969) investigated the profiles of stellar images and found that the intensity profile *shape* did not depend on the brightness of the star (although of course the *height* of the profile is dependent on the brightness). From curve fitting densitometer traces of stellar images on photographic plates, he found that a stellar image profile can be described by an equation of the general form given by (adapted from Moffat (1969) and Stetson et al. (1990)):

$$I(\theta) = \frac{F}{(1 + (\frac{\theta}{HW})^2)^\beta}. \tag{7.5}$$

Here F is the stellar flux, which scales the height of the intensity profile depending on the magnitude of the star, and θ is the radial distance away from the centre of the intensity profile in arcsec. HW is the half width at half peak intensity in arcsec (i.e. 0.5 * FWHM), and β is a shape parameter controlling the strength of the profile 'wings' (Racine, 1996).

A more complex form of this 'Moffat' function, as used by the DAOPHOT photometry software (and described by Racine (1996)) is given by:

$$I(\theta) = \frac{1}{\pi HW^2} \left[\frac{(2^{\frac{1}{\beta}} - 1)(\beta - 1)F}{(1 + (2^{\frac{1}{\beta}} - 1)(\frac{\theta}{HW})^2)^\beta} \right]. \tag{7.6}$$

Racine (1996) noted that a good fit to stellar profiles over a range of 15 magnitudes of surface brightness can be achieved by summing two of the above Moffat functions, one with $\beta = 7$ (containing 80 per cent of the total flux), and one with $\beta = 2$ (containing the remaining 20 per cent of the flux). This two-part Moffat function provides a better fit to the outer 'wings' of the stellar profile and is the equation used in this work to calculate theoretical stellar intensity profiles:

$$I(\theta) = \frac{F}{\pi HW^2} \left[\frac{(2^{\frac{1}{7}} - 1)(7 - 1)(0.8F)}{(1 + (2^{\frac{1}{7}} - 1)(\frac{\theta}{HW})^2)^7} + \frac{(2^{\frac{1}{2}} - 1)(2 - 1)(0.2F)}{(1 + (2^{\frac{1}{2}} - 1)(\frac{\theta}{HW})^2)^2} \right]. \tag{7.7}$$

Moffat functions are normalized, meaning that in three dimensions the volume under the image profile surface is equal to one (for the case of $F = 1$). Therefore, setting $F = 1$ and integrating from the centre of the profile out to the radius of the fibre gives the ratio of the total flux entering the fibre. Note that the calculated ratio is for white light (i.e. the flux of each wavelength

is affected equally as the effects of atmospheric dispersion are not included). By employing Equation 7.7, the ratio of light entering the fibre can be calculated for any seeing condition (characterized by the value of HW). Figure 7.13 shows how the calculated Moffat stellar profile changes with the seeing conditions, and Figure 7.14 shows how the percentage of light entering the fibre is affected by seeing.

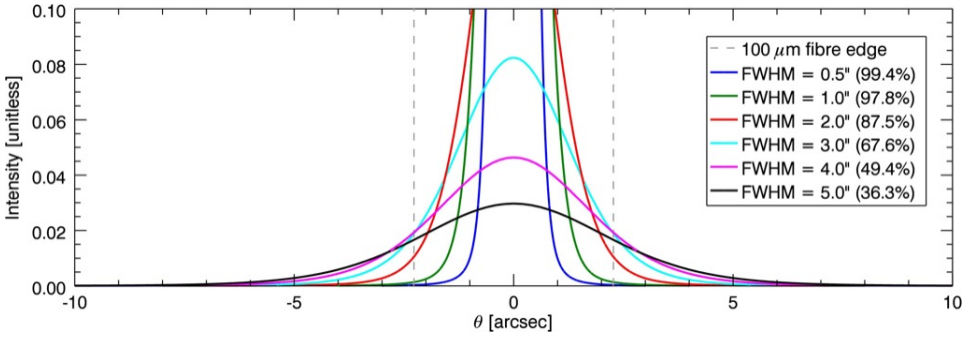

Figure 7.13: Calculated intensity profiles for a star observed under various seeing conditions, generated with the two-part Moffat function of Equation 7.7. Values in parentheses in the legend give the percentage of light entering the fibre (as described in the text) for each plotted FWHM value. The dashed vertical lines mark the edges of a 100-μm fibre when used with a microlens on the 1-m McLellan telescope (resulting in a focal length of 4.54 m).

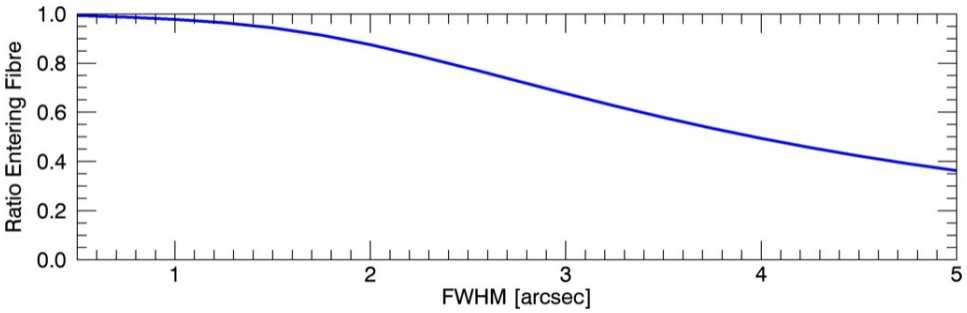

Figure 7.14: Calculated percentage of light entering a fibre as a function of seeing conditions. This plot was generated using the two-part Moffat function of Equation 7.7 and assumes a 100-μm fibre used with a microlens on the 1-m McLellan telescope (resulting in a focal length of 4.54 m).

7.3.4 Results

Figure 7.15 gives the results of the instrument efficiency model for the KiwiSpec vacuum chamber prototype, including surfaces from the fibre exit to the CCD. As shown in the figure, the peak efficiency of the prototype instrument (with non-optimized coatings) is 30.2 per cent. The efficiency is lower at the blue end of the prototype wavelength range, which although typical for optical instruments, is also due to the fact that the mirror coatings within KiwiSpec are for the most part bare aluminium, and the anti-reflection coatings are either MgF_2 or off-the-shelf broadband coatings.

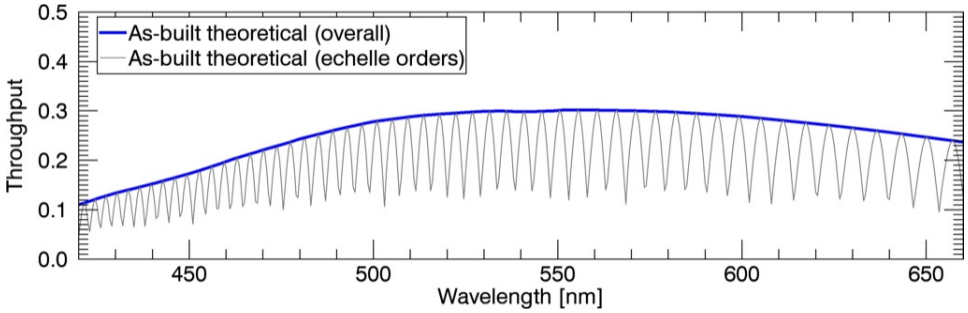

Figure 7.15: KiwiSpec theoretical efficiency from the fibre exit to the CCD. The subpeaks shown in grey are the intensity profiles of the individual échelle diffraction orders.

It is expected that the theoretical efficiency will be slightly higher than the actual, measured efficiency (due to inevitable manufacturing and assembly-induced losses). Given that assumption, instrument efficiencies reported for other fibre-fed échelle spectrographs show that the predicted maximum efficiency is a reasonable value. The HERMES instrument on the 1.2-m Mercator telescope at Roque de los Muchachos Observatory (Raskin et al., 2011) indicates a maximum efficiency of 20 per cent for the spectrograph alone in low resolution mode (i.e. directly fed by a fibre without an image slicer in place). The HARPS spectrograph on the European Southern Observatory (ESO) 3.6-m telescope at the La Silla Observatory achieves a measured efficiency of 28 per cent for the spectrograph alone (Pepe et al., 2003). Finally, the HERCULES spectrograph on the 1-m McLellan telescope at MJUO achieves a peak efficiency of 15 per cent for the spectrograph and fibre (Hearnshaw et al., 2002).

Figure 7.16 shows the efficiency losses contributed by each surface that the light encounters between the entrance of the fibre at the telescope and the spectrograph CCD. Three wavelengths are shown (indicating the centre, and blue and red extremes of the prototype wavelength coverage).

This figure indicates the major efficiency losses within the spectrograph (and therefore denotes areas for possible future efficiency improvements within the instrument). Starting at the left of the plot, the first group

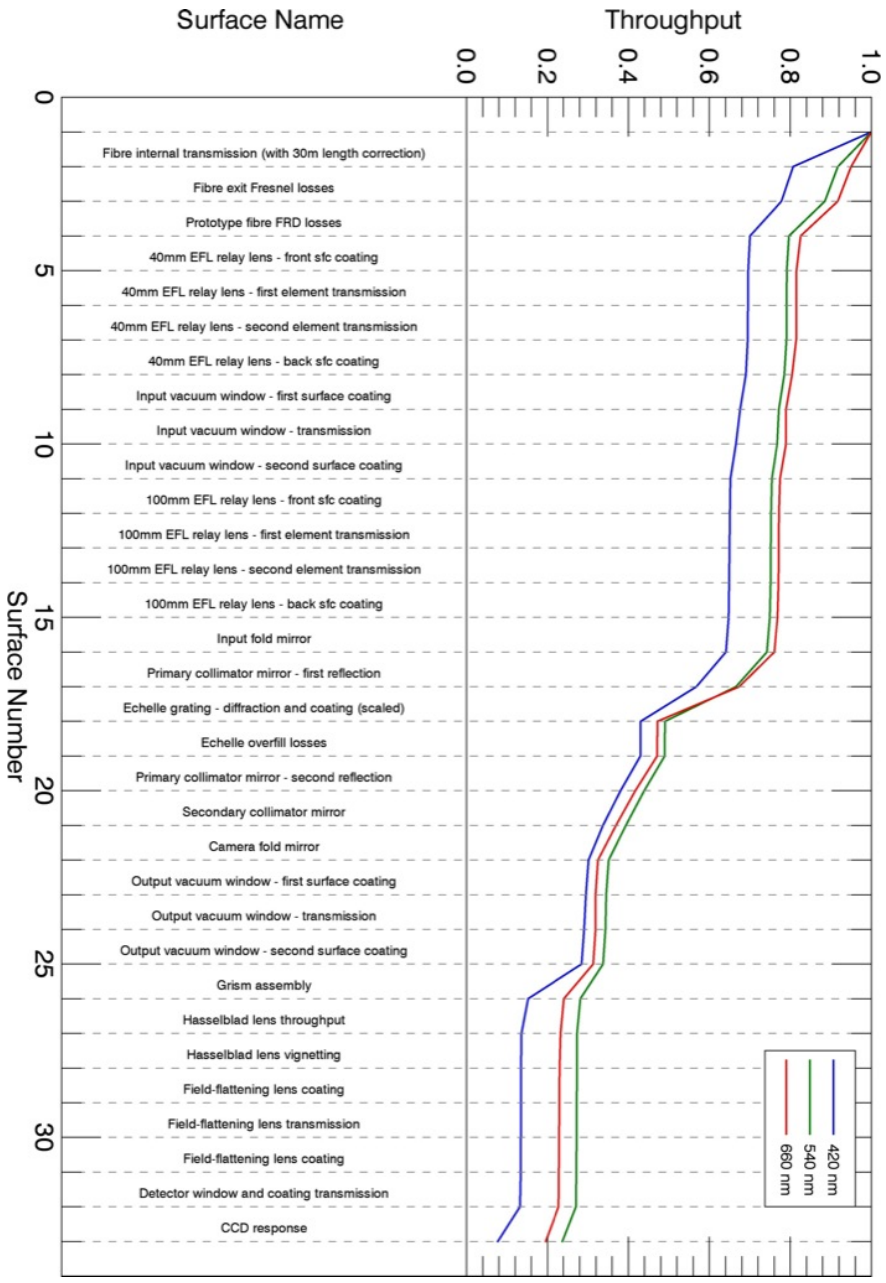

Figure 7.16: Effect of each surface on the overall efficiency. Three wavelengths are shown (indicating the centre, and blue and red extremes of the prototype wavelength coverage).

of major losses are caused by fibre-related issues. Transmission through the fibre has a significant effect on the blue wavelengths, amounting to a 20 per cent loss at 420 nm. Therefore, fibres should be kept as short as possible to minimize this loss. Fresnel losses at the fibre exit could be minimized by redesigning the input relay system to allow for a microlens to be cemented to the end of the fibre (with a high-efficiency anti-reflection (AR) coating applied). Fibre focal-ratio degradation (FRD) losses are also significant in the prototype, as the input relay is composed of off-the-shelf optics and was not optimized for the actual focal ratio of the light leaving the fibre. A future, optimized version of the input relay system would certainly better account for FRD and minimize this loss from the system.

Surfaces 4 through 15 (the lenses of the input relay, the vacuum window, and the input fold mirror) introduce negligible losses to the system. Nonetheless, the AR coatings on the relay lenses could be improved by moving to high-efficiency coatings. A MgF_2 coating is required on the exterior surface of the input vacuum window in order to reflect sufficient light to the exposure meter; however, the interior surface coating could be changed from MgF_2 to a high-efficiency AR coating to improve throughput.

In order to expedite assembly of the prototype instrument, the primary collimator within the prototype was coated in-house at KiwiStar Optics with bare aluminium. Changing this coating to a high reflectivity coating (such as an enhanced silver or a dielectric coating) would significantly improve the throughput of the instrument, especially since this mirror is used in double-pass.

The next surface, the échelle grating, causes a significant efficiency loss, This loss must be accepted as there are no techniques available to offer improved efficiency. Following the grating in Figure 7.16 is the negligible loss incurred by slightly overfilling the ruled surface of the échelle grating.

After the second reflection from the primary collimator mirror are the reflections from the secondary collimator mirror and the camera fold mirror. As with the primary collimator, these mirrors were coated in-house with bare aluminium for the prototype instrument, and a change to high reflectivity coatings for these surfaces would have a significant impact on the overall efficiency.

The output vacuum window, which was coated in-house with MgF_2 coatings, could give improved throughput with a high-efficiency AR coating on both surfaces.

The next item in the system is the grism assembly. The major loss within the assembly is due to the efficiency of the VPH grating (Section 7.2.5), which (when aligned on-axis) is responsible for the loss of approximately 15 per cent of the light at 420 nm. Although the grating efficiency response cannot be changed, an improvement in the grism throughput could be achieved by changing the MgF_2 coatings on the prism faces to high-throughput AR coatings.

The next system encountered in the instrument is the camera, which includes the Hasselblad and field flattening lenses. These elements have quite high efficiencies, as shown by the near-horizontal lines for these components in the figure.

The final loss in the system is due to the CCD detector. Although the KiwiSpec CCD is backside illuminated and AR-coated, the efficiency could be further improved by employing a 'graded' coating to the CCD surface (Kelt et al., 2006). Such a coating has a varying thickness along the cross-dispersion direction of the CCD, with the thickness of the coating tailored to match the dispersion across the spectrum (i.e. gradually increasing in thickness from blue to red wavelengths in the cross-dispersion direction). Further advantages of such a coating include fringe suppression at red wavelengths, as the optimized coating reduces Fresnel reflections at the front surface of the silicon wafer (Kelt et al., 2006).

Applying these suggested changes can lead to significant improvements in efficiency, as seen in the 'ideal' KiwiSpec prototype efficiency plots in Figures 7.17 and 7.18. Figure 7.17 shows the improvement possible for the overall spectral efficiency response of the spectrograph only (from fibre exit to CCD): the peak efficiency has improved from 30.2 per cent to 44.3 per cent (a factor of 1.47). These figures assume the prototype configuration with ideal mirror and AR coatings, as well as minimal FRD losses. As discussed above, a graded CCD coating could be employed to further increase the throughput, but was not included here as the details required to model such a coating are not available owing to proprietary reasons (Kelt et al., 2006).

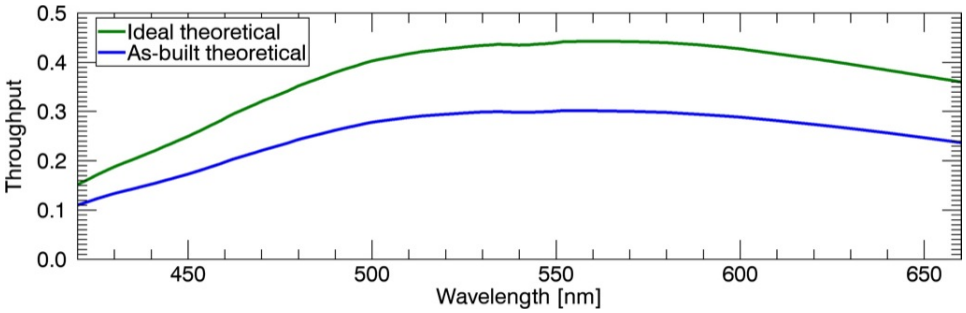

Figure 7.17: KiwiSpec theoretical efficiency from the fibre exit to the CCD for the as-built case and the ideal case with high efficiency reflective and anti-reflective coatings.

Figure 7.18: Effect of each surface on the overall efficiency of a KiwiSpec prototype with ideal mirror and AR coatings. Three wavelengths are shown (indicating the centre, and blue and red extremes of the prototype wavelength coverage).

7.4 On-Telescope Measurements

In April 2011, the in-air prototype was transported to Mt John University Observatory (MJUO) for a two week period of on-sky testing using the 1-m McLellan telescope. A primary goal of this testing period was to obtain spectra of spectrophotometric standard stars in order to determine the efficiency of the KiwiSpec instrument while in use on a telescope.

Spectrophotometric standards are stars which have had their fluxes measured very carefully. The primary standard, Vega (α Lyrae), has been measured in an absolute sense by several observers (for example, Tüg et al. (1977) compared the flux from Vega against blackbody sources maintained at the melting point of copper or platinum).

At Mt John, however, Vega transits the meridian at an altitude of approximately 7°, which is far too low for spectrophotometric measurements. As other observatories in the southern hemisphere experience the same issue, a set of secondary standards has been developed. These secondary standard stars are located near the celestial equator to be accessible to telescopes in both hemispheres, and have their fluxes tied in a relative sense to Vega. In general, early-type stars (i.e. spectral classes O, B, and A) are best-suited for this work, as the spectra of these stars contain a minimum of absorption features which can skew the spectrophotometric measurements (Oke, 1964).

Hamuy et al. (1992) provide fluxes for several secondary spectrophotometric stars, from which five stars were selected for measuring the efficiency of KiwiSpec under normal observing conditions. Hamuy et al. (1994) later provided updated fluxes covering a wider wavelength range for the same stars, and it was data from the later paper that were used here. The spectral types and V-magnitudes of the five stars observed are listed in Table 7.4.

Table 7.4: Summary table of the spectrophotometric stars observed during the on-sky testing period at Mt John University Observatory. Spectral types and magnitude values are from Hamuy et al. (1992). Note that SIMBAD indicates that HR 3454 is a β Cep variable, and that it can vary in brightness by $0.01-0.3$ magnitudes (`http://simbad.u-strasbg.fr/simbad/sim-basic?Ident=hr+3454&submit=SIMBAD+search`).

Star Name	**Spectral Type**	$\mathbf{m_V}$
HR 3454 (η Hydrae)	B3 V	4.3
HR 4468 (θ Crateris)	B9.5 V	4.7
HR 4963 (θ Virginis)	A1 IV	4.4
HR 5501 (108 Virginis)	B9.5 V	5.7
HR 7596 (58 Aquilae)	A0 III	5.6

7.4.1 Spectrophotometric Spectra Analysis

This section outlines the method employed to analyze the raw spectra recorded at MJUO. After each spectrum was wavelength calibrated and reduced[1], the following procedure was undertaken:

1. The analogue to digital unit (ADU) counts in the reduced spectrum datafile were converted to electrons (or equivalently, detected photons) using the CCD gain (1.3037 [e^- ADU^{-1}] for the CCD mode that was used exclusively during the observations). It was assumed that the conversion between detected photons and electrons was lossless (i.e. 1 e^- = 1 photon).

2. The image header was read from the original spectrum FITS file. Parameters read from the header include exposure length, exposure start time, CCD readout rate, CCD gain and the date of the observation.

3. A secondary datafile for the star was read containing the observatory's latitude and longitude, as well as the star's Right Ascension (RA) and Declination (DEC).

4. Local sidereal time (LST) for the mid-point of the spectrum exposure was calculated using the image header and location data and the IDL Astronomy Library routine CT2LST.

5. The hour angle, h, of the star was calculated and converted to angular measure (using 1 hour $\equiv 15^\circ$) with:

$$h = (LST - RA)\frac{15^\circ}{\text{hr}}. \tag{7.8}$$

6. The stellar flux data presented in Hamuy et al. (1994) represent flux incident on the top of the Earth's atmosphere. Therefore, the losses introduced by scattering and absorption during transmission through the atmosphere need to be removed from the reduced spectra.

   The 'air mass' is the path length that the starlight traverses from the top of the atmosphere to the telescope mirror. The shortest possible path for starlight through the atmosphere is vertically downwards from the zenith; whereas the longest path traverses the atmosphere horizontally from the horizon. Therefore, air mass is a function of the angle that the light rays make with the vertical, known as the zenith angle, z. Relative air mass is the air mass at a zenith angle of z, expressed as a ratio of the zenith air mass.

[1] Wavelength calibration and reduction of spectra were performed by Stuart Barnes.

For small zenith angles, the relative air mass for a given object can be determined via Equation 7.9a (adapted from Walker (1987)) . However, at greater zenith angles, the simplistic $\sec z$ approach begins to deviate from the true air mass value. Equation 7.9b is described by Allen and Cox (2000) to be valid for $X < 5$ with an error less than 6×10^{-4}. Although all spectrophotometric standard stars were observed at relative air masses less than 1.7, for this work the more complete Equation 7.9b was used to calculate relative air mass. The two air mass equations are:

$$\sec z = \frac{1}{\sin\psi \sin\delta + \cos\psi \cos\delta \cos h}; \tag{7.9a}$$

$$\begin{aligned} X = &-0.0045 + 1.00672 \sec z \\ &- 0.002234 \sec^2 z - 0.0006247 \sec^3 z; \end{aligned} \tag{7.9b}$$

where:

X	=	relative air mass (with respect to zenith value)	[unitless];
z	=	star's zenith angle	[degrees];
ψ	=	latitude of telescope's location	[degrees];
δ	=	observed star's declination	[degrees];
h	=	star's hour angle	[degrees].

7. The relative air mass was then used to calculate the transmission of the atmosphere, and the photon values for each pixel were increased to remove the effect of extinction from the observations. The transmission of the atmosphere is given by:

$$T_{\text{atm}} = e^{\frac{-k(\lambda)}{1.086}X}, \tag{7.10}$$

where:

$k(\lambda)$	=	the extinction coefficient	[unitless];
X	=	relative air mass of object at time of observation	[unitless].

The extinction data employed for this work were based on measurements made by Alan Gilmore at MJUO (and reported by Barnes (2004)).

Therefore, to remove the atmospheric extinction from the reduced spectrum data, for each pixel the photon flux was increased by the factor:

$$F_0(\lambda) = \frac{F_{\rm obs}(\lambda)}{T_{\rm atm}(\lambda)}, \tag{7.11}$$

where:

$F_0(\lambda)$	=	flux incident on the Earth's atmosphere	[photons cm^{-2} s^{-1} Å^{-1}];
$F_{\rm obs}(\lambda)$	=	observed flux	[photons cm^{-2} s^{-1} Å^{-1}];
$T_{\rm atm}(\lambda)$	=	transmission of the Earth's atmosphere	[unitless].

8. With the above calculations and values in hand, the counts in each reduced spectrum were adjusted as follows. For each échelle diffraction order:

   (a) The pixel containing the maximum number of photons in the order was determined.

   (b) In order to remove cosmic ray hits within the spectrum from skewing the analysis, the wavelength of the peak pixel found in Part 8a was checked to ensure that it was located within 1 nm of the calculated blaze wavelength for the order. If it did not, the pixel was rejected and Part 8a was repeated.

   (c) The average number of photons within 41 pixels (arbitrary number) centered on the peak photon value was calculated. This value has units of photons pixel^{-1}.

   (d) The average nm per pixel value over this range was calculated (for KiwiSpec this value ranges from 0.0027 nm pixel^{-1} at 660 nm to 0.0018 nm pixel^{-1} at 420 nm).

   (e) The result of 8c was divided by the result of 8d, which has units of photons nm^{-1}.

   (f) The result of 8e was divided by the exposure length (in seconds). This value has units of photons nm^{-1} s^{-1}.

9. Item 8 was repeated for each order in the reduced spectrum.

In summary, the observed spectra were reduced and the losses due to the atmosphere removed. The peak values within each order were then determined, and then were compared against the expected flux values from Hamuy et al. (1994) (after accounting for the area of the telescope mirror) to obtain the measured efficiency of the telescope-spectrograph system.

7.4.2 Theoretical Model

The theoretical efficiency model described in Section 7.3 was employed to obtain an expected efficiency for each spectrophotometric star under various seeing conditions. The approach used was as follows:

1. The fluxes listed within Hamuy et al. (1994) are given in terms of monochromatic magnitudes. In order to compare against the acquired spectra, the flux data were converted to stellar flux per unit wavelength and then divided by the energy of a photon at each given wavelength. This conversion is summarized by:

$$F(\lambda) = \frac{10^{(-\frac{m(\lambda)+48.590}{2.5})}}{h\lambda}, \tag{7.12}$$

where:

$F(\lambda)$	=	stellar flux	[photons cm^{-2} s^{-1} Å^{-1}];
$m(\lambda)$	=	monochromatic magnitude	[unitless];
h	=	Planck constant	[erg s];
λ	=	wavelength	[Å].

2. To determine the amount of flux entering the telescope, the result of Part 1 was multiplied by the area of the telescope primary mirror minus the area of the secondary mirror obstruction (in cm^{-2}). The result has units of photons s^{-1} Å^{-1}.

3. The result of Part 2 was then multiplied by the instrumental efficiency model described in Section 7.3. The model employed contained the combined spectral efficiency of all optical surfaces, coatings and components from the telescope primary mirror to the spectrograph CCD. These data were generated for several different seeing profiles, using the Moffat function approach described in Section 5. The units after this step remain unchanged from Part 2 (i.e. photons s^{-1} Å^{-1}).

7.4.3 Results

The observed and theoretical efficiency results for each of the five spectrophotometric standards are shown in Figures 7.19 to 7.23. These figures show the observed efficiencies for the best nights during the on-sky testing period. For clarity additional spectra captured on nights of poor seeing (and hence low efficiency) were not included.

The figures also indicate expected efficiencies for several seeing conditions, and as seen in the figures the profiles of the observed and theoretical efficiencies with respect to wavelength are closely matched.

Unfortunately, however, the actual seeing conditions at the 1-m McLellan telescope were not monitored during the on-sky testing period. The software for the HERCULES spectrograph at Mt John can record the guide star images as a measure of seeing, however, the KiwiSpec software could not access this feature during the on-sky testing period.

To provide some measure of the conditions, seeing logs from the observing period were obtained from the MOA (Microlensing Observations in

Astrophysics) telescope, which is located adjacent to the 1-m McLellan telescope on Mt John. However, these data were used with caution, as the seeing at the McLellan telescope would most certainly be different owing to a variety of conditions, such as: local seeing within the dome (due to heat sources or the aiming of the dome shutter with respect to the wind direction), air turbulence surrounding the dome exterior, or heat rising from the observer's quarters attached to the dome. In general, the MOA seeing FWHM values for the observations shown in Figures 7.19 to 7.23 ranged between 1.7 and 2 arcseconds.

However, the figures show that the efficiencies recorded would correspond to seeing at the 5 arcsecond level, and not the 2 arcsecond values recorded by the MOA telescope. Therefore, losses not accounted for within the theoretical model must have been occurring, which is reasonable to expect as many of the parameters of the telescope-fibre system were not monitored or rigorously optimized during the testing period. Such parameters include the telescope collimation, telescope focus, fibre alignment, dome seeing, guiding errors, and the effects of atmospheric dispersion.

Although the 1-m McLellan telescope fibre feed does not have the capability, ideally images of the fibre entrance at the telescope focal plane would have been recorded to monitor the amount of light entering the fibre. Such images would have provided information on the losses due to seeing conditions, atmospheric dispersion, and telescope guiding accuracy. These measurements, coupled with the spectrograph's exposure meter counts (which is located near the fibre exit, but was not fully operational during the on-sky testing period), would have provided a more complete picture of the efficiency losses incurred before light reached the spectrograph itself.

The maximum efficiencies recorded for each star are summarized in Table 7.5. The maximum efficiency achieved was 5.59 per cent. Of note is the consistency of the peak values, which are all close to 5 per cent. A brief survey of the reported on-sky efficiencies for other fibre-fed échelle spectrographs serves to put this into perspective, and is shown in Table 7.6.

Table 7.5: The maximum efficiency measured for each of the observed spectrophotometric standard stars.

Star Name	**Efficiency** [%]
HR3454	4.75
HR4468	5.59
HR4963	4.83
HR5501	4.95
HR7596	4.81

Table 7.6: Reported maximum efficiencies of the spectrograph-telescope system for several fibre-fed spectrographs.

Instrument	Peak Efficiency	Source
HARPS	5%	(Pepe et al., 2003)
HERMES	12%	(Raskin et al., 2011)
FEROS	17%	(Kaufer et al., 1999)
ELODIE	1.3%	(Baranne et al., 1996)

However, as described above in Section 7.3.4, there were several choices made for the prototype design that were known to compromise throughput, but were selected nonetheless in the interest of cost and time. These include: the mirror coatings (bare aluminum as opposed to high efficiency coatings); the lens and prism AR coatings (single layer MgF_2 as opposed to multi-layer coatings); the design of the input relay (off-the-shelf optics and not perfectly matched to the fibre FRD characteristics); and the Hasselblad camera lens (known to introduce vignetting). These prototype-based losses, combined with the possibly significant losses due to the 1-m McLellan telescope system, indicate that the data shown in Figures 7.19 to 7.23 and Table 7.5 should be taken as a low-end measurement of the potential efficiency capabilities of the KiwiSpec design.

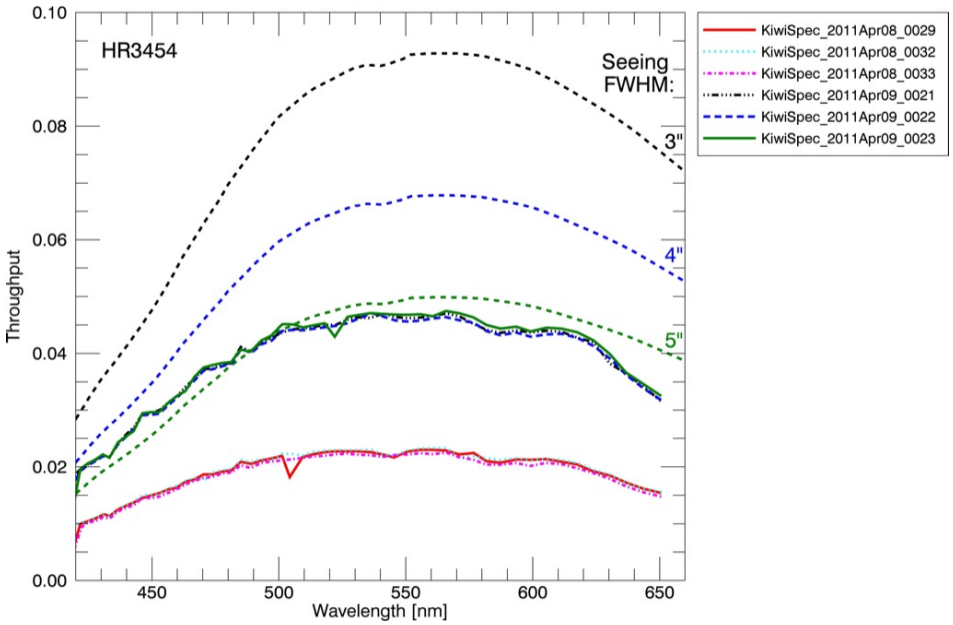

Figure 7.19: Measured on-sky KiwiSpec efficiencies with the 1-m McLellan telescope at Mt John University Observatory for the spectrophotometric standard star HR3454. Also shown are theoretical efficiency curves for three seeing conditions.

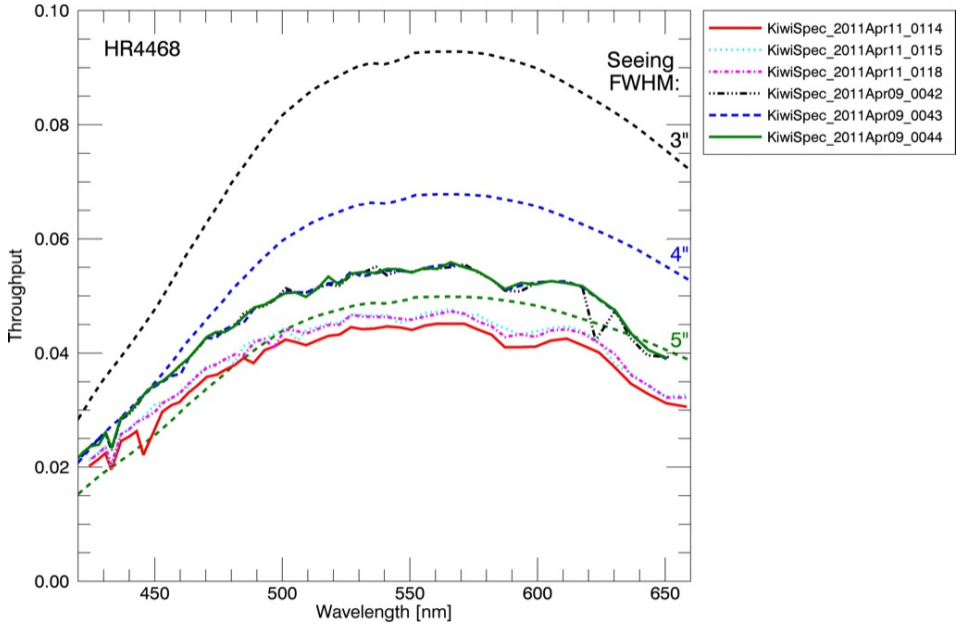

Figure 7.20: Measured on-sky KiwiSpec efficiencies with the 1-m McLellan telescope at Mt John University Observatory for the spectrophotometric standard star HR4468. Also shown are theoretical efficiency curves for three seeing conditions.

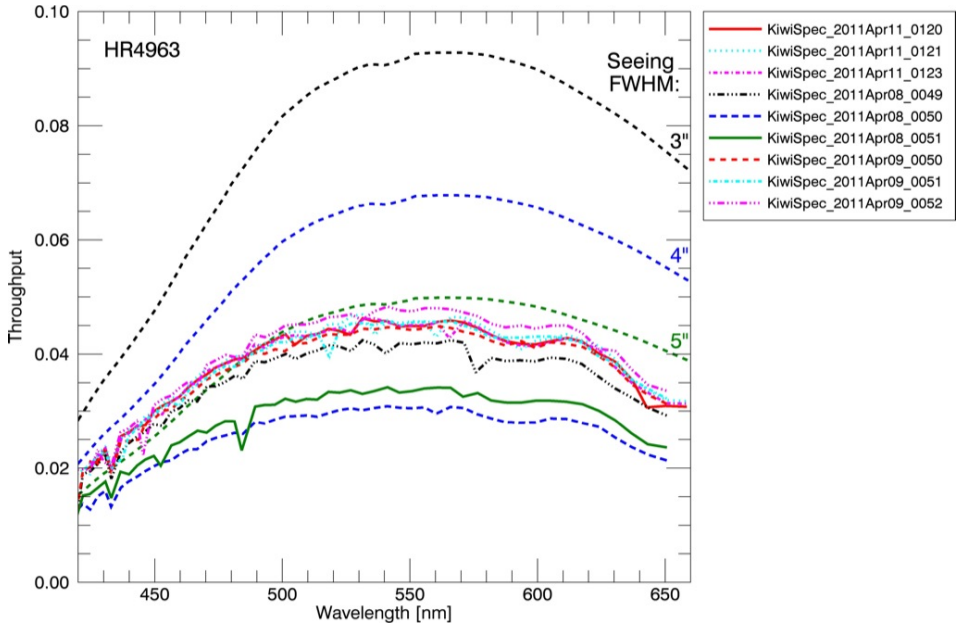

Figure 7.21: Measured on-sky KiwiSpec efficiencies with the 1-m McLellan telescope at Mt John University Observatory for the spectrophotometric standard star HR4963. Also shown are theoretical efficiency curves for three seeing conditions.

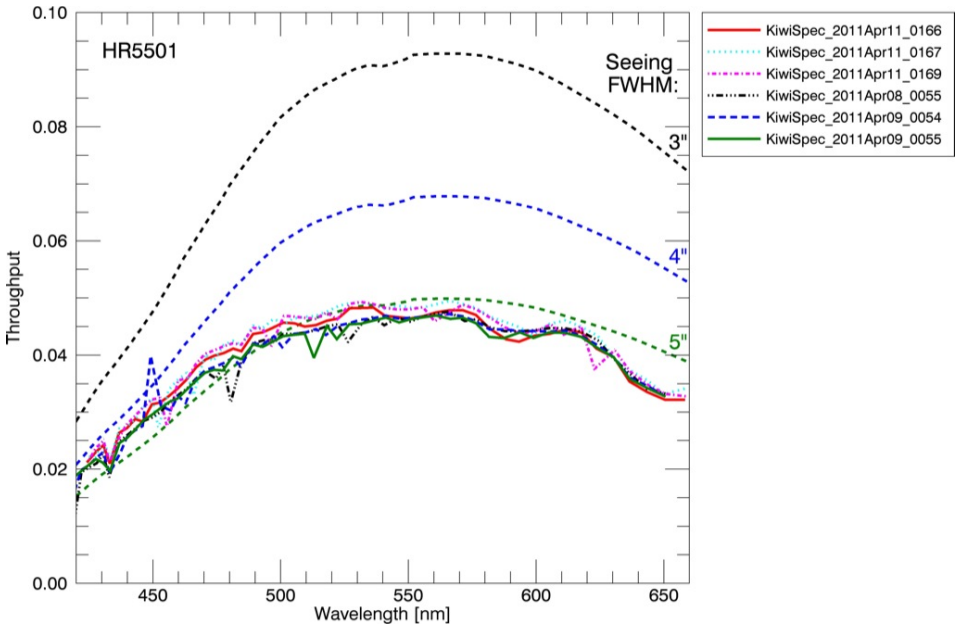

Figure 7.22: Measured on-sky KiwiSpec efficiencies with the 1-m McLellan telescope at Mt John University Observatory for the spectrophotometric standard star HR5501. Also shown are theoretical efficiency curves for three seeing conditions.

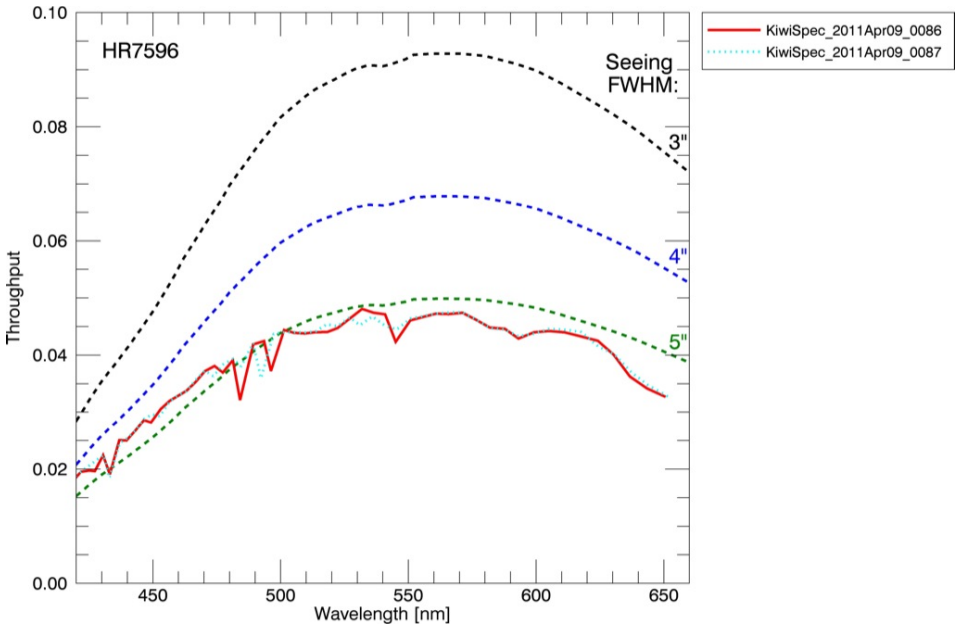

Figure 7.23: Measured on-sky KiwiSpec efficiencies with the 1-m McLellan telescope at Mt John University Observatory for the spectrophotometric standard star HR7596. Also shown are theoretical efficiency curves for three seeing conditions.

Chapter 8

Exposure Meter

8.1 Introduction

An exposure meter is an essential component of an astronomical spectrograph, as it allows for continuous monitoring of the amount of light entering the instrument. Owing to the low light levels involved, a photomultiplier tube (PMT) is typically used as the exposure meter detector.

Monitoring the number of photon counts s^{-1} measured by the exposure meter during an observation has several benefits:

Monitoring guiding: The number of counts will decrease if the star moves off the fibre.

Monitoring transparency: Counts will decrease if a cloud passes in front of the star.

Monitoring seeing: Counts will decrease in poor seeing, as the size of the star image at the telescope focal plane has increased with respect to the fixed size of the fibre.

Setting telescope focus: Best focus can be determined by maximum counts.

Alignment of pre-fibre optics: Optimal alignment is indicated by maximum counts.

Determination of the flux-weighted middle of the exposure: Whereas the CCD only provides the number of photons collected per exposure (which could be 30 min or more), the exposure meter provides a much finer time resolution, on the order of photons collected per 100 ms. These data can be used to determine the flux-weighted midpoint of the exposure (which could be offset from the exposure time midpoint owing to clouds, guiding errors, or other losses occurring during an exposure). The flux-weighted midpoint is required during radial-velocity analysis of spectra to correct for the movement of the Earth during the observation (i.e. to calculate the barycentric correction).

Error catching: Monitoring counts immediately reveals errors such as closed shutters, incorrect light source selections (science light vs. calibration light), incorrect filter selections, etc.

Detector control: With software monitoring the total number of exposure meter counts accumulated, exposure lengths can be determined by the total number of photons collected. This scenario would lead to spectra with consistent signal-to-noise ratios (although each spectrum could have a different exposure length). This approach has been employed on other spectrographs as well (e.g. Baranne et al. (1996)).

Furthermore, graphical output of the exposure meter counts is ideal for monitoring the amount of light entering the spectrograph during an exposure. Figure 8.1 shows a typical case, where the exposure meter counts varied during the recording of a spectrum owing to telescope guiding errors, seeing changes, or intermittent cloud cover.

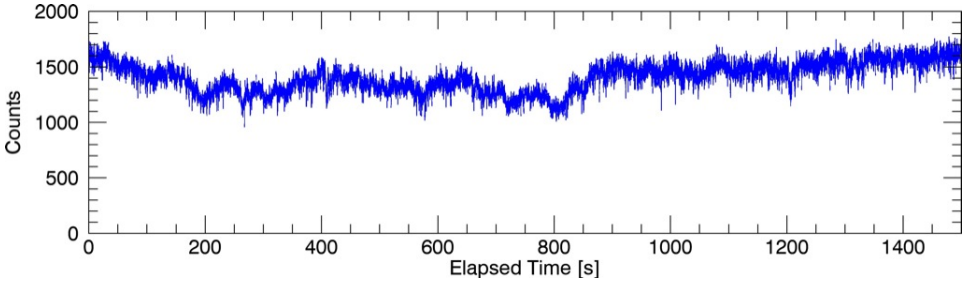

Figure 8.1: KiwiSpec exposure meter data recorded while exposing a spectrum of the star HD752896 during the on-sky testing at Mount John University Observatory. The variation of counts is due to telescope guiding errors, seeing changes, or intermittent cloud cover during the exposure.

8.2 Device Choice

The exposure meter chosen for the KiwiSpec prototype was a Sens-Tech P25USB PMT, shown in Figure 8.2. This device provides the benefits of small size (a 34-mm diameter, 120-mm long cylinder) with an all-in-one form factor that contains the high-voltage power supply and photon-counting circuitry. Power requirements are minimal (5 V, 125 mA) and it connects directly to a computer via USB. The 'bialkali' photocathode version of the device was chosen over the 'S20' photocathode version, as it provides significantly lower maximum dark counts (200 s^{-1} vs. 5000 s^{-1})

8.3 Location Options

Two locations for the exposure meter were investigated through the use of the efficiency-based model described in Section 7.3. These included a

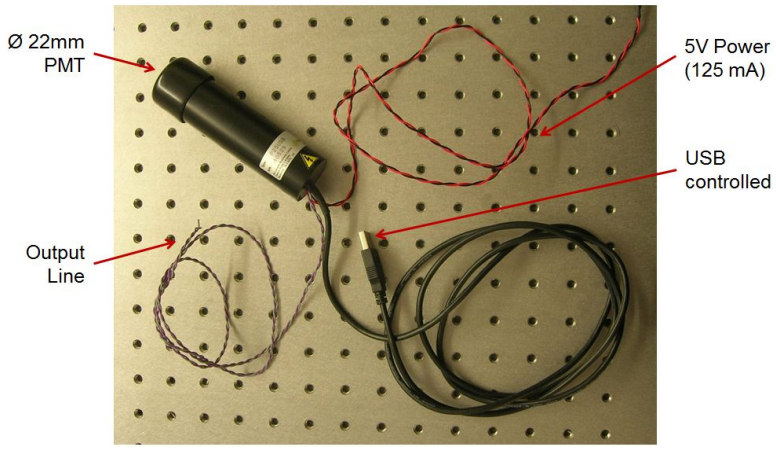

Figure 8.2: The Sens-Tech P25USB device which is employed as the KiwiSpec exposure meter. The output line allows control of an external device (such as a shutter) directly from the device.

location after the échelle grating (monitoring the zero-order reflection from the grating), and a position within the input relay (monitoring the reflection from the input vacuum window). Each location will be described in more detail in the following sections. The input relay location prevailed as the preferred choice, as it receives higher light levels and is also the mechanically simpler location to implement.

These two potential locations were chosen as the exposure meter would be utilizing light that would otherwise be lost to the instrument. This approach was considered more favourable than other scenarios which would require the addition of another optical element to the system (such as a dichroic beamsplitter to divert light to the exposure meter).

A few examples of exposure meter systems in other instruments showcases the variety of techniques used in monitoring the light entering a spectrograph. The exposure meter in the Hamilton Spectrometer is based on a rotating, reflective beam chopper located behind the slit (Kibrick et al., 2006). This chopper reflects approximately 8 per cent of the light entering the spectrograph to the exposure meter (a PMT). The exposure meter for the HIRES spectrograph, which is based on the design of the Hamilton Spectrometer exposure meter, operates in a similar fashion (Kibrick et al., 2006). The HERCULES spectrograph utilises a folded Schmidt telescope as a camera system with the detector located behind a central hole in the camera's fold mirror. A diagonal pickoff mirror located before the Schmidt corrector plate reflects light towards an exposure meter that would otherwise be lost through the perforation in the fold mirror (Hearnshaw et al., 2002). The HERMES spectrograph employs an annular mirror, centered on the optical axis within the input relay system, but tilted at a 15° angle to reflect light towards the exposure meter. The light collected by this

annular mirror would otherwise be lost to the system owing to focal ratio degradation (Raskin et al., 2011). Finally, the (now decommissioned) bHROS instrument exposure meter system collected light reflected from the cross-dispersion prism, which was then focused onto a PMT by a Fresnel lens[1]. The bHROS system also featured a series of filters which enabled the monitoring of wavelength bandpasses of interest.

8.3.1 Post-Échelle Location

Due to the blaze angle of the échelle grating, the majority of light incident on the grating is diffracted back in the direction of the incident light. However, a small amount of light is diffracted into other directions. The 'zero-order' light is equivalent to a plane reflection from the grating surface, with the angle of incidence equal to the angle of reflection about the grating normal.

In order to utilize this light for an exposure meter, a Fresnel lens could be used to focus the 100 mm diameter beam onto the exposure meter, as shown in Figure 8.3. A Fresnel lens is ideal for this purpose as image quality is not important, and it has a smaller physical footprint and cost than an equivalent 100 mm diameter glass lens.

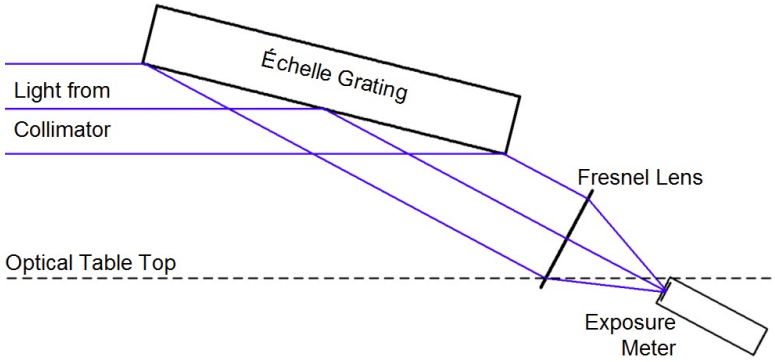

Figure 8.3: Schematic diagram showing the proposed placement of the exposure meter after the échelle. The position of the optical table top is shown to indicate the mechanical interference that would need to be addressed with this arrangement. Not shown is the échelle mount, which would also interfere with the reflected beam.

As shown in Figure 8.3, a disadvantage of this location is the orientation of the reflected beam, which is directed downwards towards the optical table top. Not shown in the figure is the mechanical mount for the échelle, which also lies in the path of the beam following the grating. Therefore, use of this location would probably require a mirror to redirect the beam, and also a redesign of the échelle mount. The vacuum chamber would also require the added complexity of an extra window for the light to leave the chamber to avoid the issues surrounding placing the exposure meter within

[1] `http://www.gemini.edu/sciops/instruments/hros/hrosExpMeter.html`

the vacuum chamber (vacuum compatibility, electrical feedthroughs, cooling system, etc.).

Despite these complexities, however, this location was further investigated as an option for the location of the exposure meter.

8.3.1.1 Échelle Zero-Order Reflectivity Measurements

In order to determine if the post-échelle location would provide enough flux for the exposure meter to make useful readings, the zero-order reflectivity of the échelle grating was tested by the author. The MSL spectrophotometer fore-optics were employed to provide a collimated beam of selectable wavelength (the same system described in Section 7.2.5).

A schematic diagram of the test setup is shown in Figure 8.4. An adjustable cam was used to set the grating angle, and was oriented with an accurate digital protractor. The wedge in the échelle substrate was also measured accurately to ensure it was not affecting the angle of the échelle ruled surface within the test jig. Figure 8.5 shows an image of the échelle positioned on the test jig and installed within the MSL spectrophotometer system.

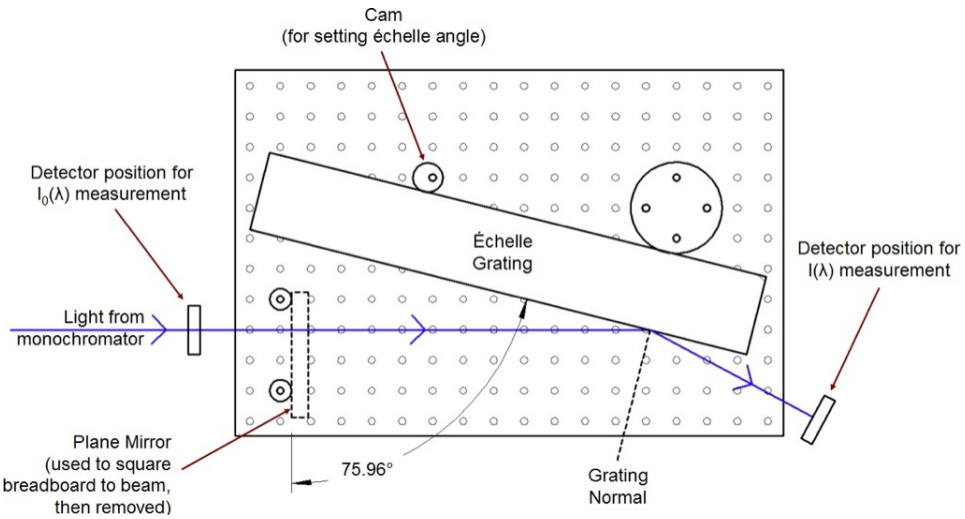

Figure 8.4: A schematic diagram showing the test setup for testing the zero-order reflectivity of the échelle grating

The test procedure followed is given in Algorithm 2. The before and after $I_0(\lambda)$ measurements were taken so as to account for possible intensity changes in the lamp over the time required to complete the test. The two $I_0(\lambda)$ values were then averaged when calculating the reflectance.

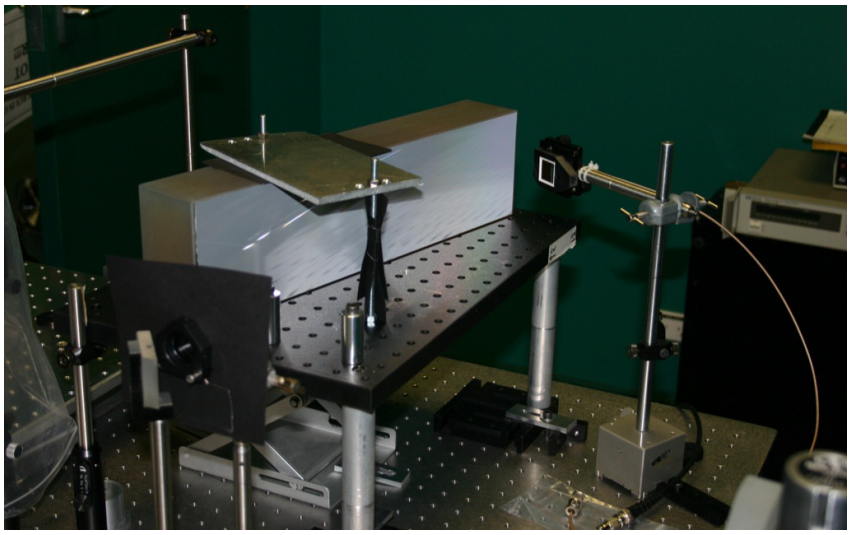

Figure 8.5: The échelle zero-order reflectivity test jig with the échelle in place. The detector (an 18-mm square silicon photodiode) is shown in the reflected light measurement position. An aperture (in the left foreground of the picture surrounded by a black card light shield) was used to limit the diameter of the collimated beam falling on the échelle to 7 mm in diameter. An aluminium plate was placed over the échelle to secure it to the breadboard as a safety measure.

Algorithm 2: The measurement procedure followed for the échelle zero-order reflectivity test.

```
/* measure the lamp response                                    */
· place detector in position before grating;
for wavelength = 350 nm to 1000 nm step 10 nm do
    · move monochromator to current wavelength;
    · take measurement I_0(λ);
end

/* measure the grating reflectivity                             */
· place detector in position after grating;
for wavelength = 350 nm to 1000 nm step 10 nm do
    · move monochromator to current wavelength;
    · take measurement I(λ);
end

/* re-measure the lamp response                                 */
· place detector in position before grating;
for wavelength = 350 nm to 1000 nm step 10 nm do
    · move monochromator to current wavelength;
    · take measurement I_0(λ);
end
```

The reflected efficiency of each wavelength was calculated using:

$$R(\lambda) = \frac{I(\lambda)}{I_0(\lambda)_{\text{avg}}}, \tag{8.1}$$

with the measurements $I(\lambda)$ and $I_0(\lambda)$ as noted within Algorithm 2. $I_0(\lambda)_{\text{avg}}$ indicates the average of the before and after $I_0(\lambda)$ values.

The test was repeated three times, and the results averaged for the plot shown in Figure 8.6. Overall the reflectivity is very low, with the average across all wavelengths being only 0.21 per cent. Considerable structure is evident within the plot, probably owing to the contributions of the reflectivity of aluminium, contamination from orders out to ± 9 (determined by Zemax raytracing for the beam diameter and detector size employed), and the blaze functions of these orders. While order contamination is typically not desirable, in this case it is beneficial as it increases the amount of flux detected by the exposure meter. In retrospect, a better test scenario would have been to use a 100-mm diameter collimated beam with a correctly sized and located Fresnel lens positioned after the grating. This would have mimicked the proposed setup within the spectrograph, and would have allowed for accurate measurement of the total contribution of adjacent orders to the exposure meter efficiency.

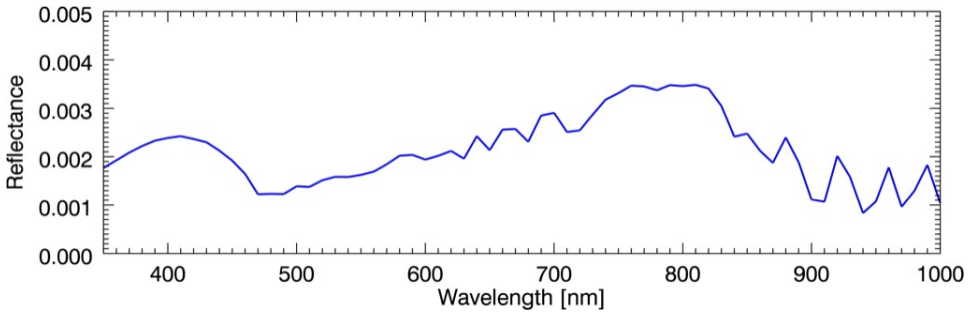

Figure 8.6: The measured spectral response of the zero and low-order light reflected from the KiwiSpec échelle grating.

Baranne et al. (1996), in a paper describing the ELODIE spectrograph, mentions an attempt to use light for an exposure meter from 'low and grazing orders' (presumably from the échelle), but only 0.3 per cent of the light entering the instrument was collected at that position. That result compares well against the 0.21 per cent efficiency measured here. The final location for the ELODIE exposure meter was before the échelle grating, in a position that receives ten times more flux.

The zero-order reflectivity from this test will be used within an efficiency-based model (described in Section 8.4) to predict exposure meter counts from the post-échelle location.

8.3.2 Input Relay Location

Alternatively, the exposure meter could be positioned to monitor a reflection from an appropriately-tilted input vacuum window, as shown in Figure 8.7.

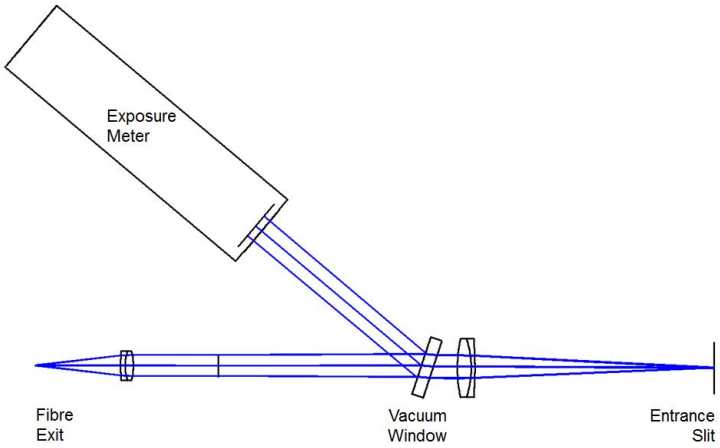

Figure 8.7: Schematic diagram showing the placement of the exposure meter within the input relay system. In practice, the exposure meter would be located further away from the vacuum window to allow more mechanical clearance between the various mounts.

This location has the advantages of high light levels, mechanical simplicity, and no complications due to the vacuum chamber. Higher light levels offer the major advantage of allowing use of the exposure meter on fainter stars.

A slight disadvantage of this position is that the exposure meter is measuring the light before the entrance slit of the spectrograph. However, one could calibrate the exposure meter output to account for throughput losses at the slit.

8.4 Exposure Meter Flux Model

In order to determine the best location (with respect to efficiency) for the exposure meter, a slightly modified version of the efficiency model described in Section 7.3 was employed. This model generates expected exposure meter counts s^{-1} for stars of six different spectral types and various V-magnitudes. Seeing effects are also accounted for, based on the Moffat function described in Section 7.3.3.

The procedure employed within the model was as follows. Note that items described as being 'spectral' have a wavelength dependence.

1. Spectral flux data for six spectral types at $V = 0$ were employed as the source of the model (from Allen (1973)). Fluxes for various other V-magnitudes were scaled from these values via:

$$F_x(\lambda) = F_0(\lambda)\, 10^{\frac{m_x(\lambda) - m_0(\lambda)}{-2.5}}, \tag{8.2}$$

where:

$F_x(\lambda)$	=	m_x equivalent flux	[erg cm^{-2} s^{-1} Å^{-1}];
$F_0(\lambda)$	=	$V = 0$ flux	[erg cm^{-2} s^{-1} Å^{-1}];
$m_x(\lambda)$	=	desired V magnitude	[unitless];
$m_0(\lambda)$	=	$V = 0$ magnitude	[unitless].

2. The stellar flux values given in Allen (1973) are for above the Earth's atmosphere. In order to account for losses due to the atmosphere, the spectral flux from Part 1 was multiplied by spectral transmission data from a theoretical atmospheric absorption model in Allen (1973). The result has units of erg cm^{-2} s^{-1} Å^{-1}.

3. To determine the amount of flux entering the telescope, the result of Part 2 was multiplied by the area of the telescope primary mirror (in cm^{-2}), minus the area of the secondary mirror obstruction. The result has units of erg s^{-1} Å^{-1}.

4. The result of Part 3 was multiplied by the appropriate conversion factors to change the units from erg s^{-1} Å^{-1} to W nm^{-1}.

5. The result of Part 4 was then multiplied by the percentage of light entering the fibre for various seeing conditions. This was calculated with the Moffat function based method described in Section 7.3.3. The result has units of W nm^{-1}.

6. The result of Part 5 was then multiplied by the spectral efficiency of each optical surface or component between the telescope primary mirror (included) and the exposure meter (excluded). The result has units of W nm^{-1}.

7. The quantum efficiency of the exposure meter was converted to spectral responsivity via the following equation from the Sens-Tech P25USB manual (Sens-Tech Limited, 2010):

$$R(\lambda) = QE(\lambda)\, f\left[\frac{\lambda}{hc}\right], \tag{8.3}$$

where:

$R(\lambda)$	=	responsivity of exposure meter	[counts s^{-1} W^{-1}];
$QE(\lambda)$	=	quantum efficiency of exposure meter	[unitless];
f	=	dynode efficiency constant (0.95)	[unitless];
λ	=	wavelength	[nm];
h	=	Planck constant	[J s];
c	=	speed of light	[nm s^{-1}].

8. The result of Part 6 was then multiplied by the result of Part 7, resulting in units of counts s^{-1} nm^{-1}.

9. Integration under the spectral response curve of Part 8 sums the contributions of all wavelengths and produces the predicted exposure meter counts s^{-1} for the given seeing conditions and the given star's spectral type and magnitude.

8.5 Model Results

The predicted exposure meter counts for the post-échelle placement are shown in Table 8.1, and the predicted counts for the input relay location are shown in Table 8.2. Owing to the low numbers, predicted counts for the post-échelle case are only shown for one arsecond seeing. Although not included in this analysis, the use of an iodine cell within the input relay would further decrease these predicted counts (and would affect both cases equally).

Comparing the one arcsecond tables for the two location options shows that on average, 13.7 times more counts s^{-1} are detected at the input relay position than at the post-échelle location. These results, coupled with the mechanical complexity required to install an exposure meter in the post-échelle location, discount that location as a viable position for the exposure meter.

The results for the input relay location (Table 8.2), show that a MgF_2 coating on the front surface of the input relay reflects a sufficient amount of light for the exposure meter (with an average reflectance of 1.8 per cent over the prototype wavelength range of 420–660 nm). The rear surface of the vacuum window, however, could have a high-efficiency anti-reflection coating applied.

Table 8.1: Predicted exposure meter counts s^{-1} for the post-échelle placement, assuming the Mt John University Observatory 1-m McLellan telescope with a 100-μm fibre and microlens.

Seeing: FWHM = 1.0 arcsec

	Spectral Type					
$\mathbf{V}_{mag}$	**B0**	**A0**	**F0**	**G0**	**K0**	**M0**
1	7.2E+05	5.7E+05	4.4E+05	3.7E+05	2.9E+05	2.1E+05
3	1.1E+05	9.0E+04	6.9E+04	5.9E+04	4.6E+04	3.4E+04
5	1.8E+04	1.4E+04	1.1E+04	9311	7301	5316
7	2864	2258	1746	1476	1157	843
9	454	358	277	234	183	134

Table 8.2: Predicted exposure meter counts s^{-1} for the input relay relay location, assuming the Mt John University Observatory 1-m McLellan telescope with a 100-μm fibre and microlens. On average, 13.7× more counts s^{-1} are detected in this position than at the post-échelle location.

Seeing: FWHM = 1.0 arcsec

	Spectral Type					
$\mathbf{V}_{mag}$	**B0**	**A0**	**F0**	**G0**	**K0**	**M0**
1	1.0E+07	7.7E+06	6.0E+06	5.1E+06	3.9E+06	2.9E+06
3	1.6E+06	1.2E+06	9.5E+05	8.1E+05	6.2E+05	4.5E+05
5	2.5E+05	1.9E+05	1.5E+05	1.3E+05	9.9E+04	7.2E+04
7	4.0E+04	3.1E+04	2.4E+04	2.0E+04	1.6E+04	1.1E+04
9	6379	4869	3786	3215	2481	1803

Seeing: FWHM = 3.0 arcsec

	Spectral Type					
$\mathbf{V}_{mag}$	**B0**	**A0**	**F0**	**G0**	**K0**	**M0**
1	7.0E+06	5.3E+06	4.1E+06	3.5E+06	2.7E+06	2.0E+06
3	1.1E+06	8.5E+05	6.6E+05	5.6E+05	4.3E+05	3.1E+05
5	1.8E+05	1.3E+05	1.0E+05	8.8E+04	6.8E+04	5.0E+04
7	2.8E+04	2.1E+04	1.7E+04	1.4E+04	1.1E+04	7862
9	4408	3365	2616	2222	1715	1246

Seeing: FWHM = 5.0 arcsec

	Spectral Type					
$\mathbf{V}_{mag}$	**B0**	**A0**	**F0**	**G0**	**K0**	**M0**
1	3.8E+06	2.9E+06	2.2E+06	1.9E+06	1.5E+06	1.1E+06
3	5.9E+05	4.5E+05	3.5E+05	3.0E+05	2.3E+05	1.7E+05
5	9.4E+04	7.2E+04	5.6E+04	4.8E+04	3.7E+04	2.7E+04
7	1.5E+04	1.1E+04	8869	7531	5812	4224
9	2368	1808	1406	1194	921	669

8.6 On-Telescope Results

The exposure meter was installed within the KiwiSpec prototype during the on-sky testing period at MJUO. Unfortunately, however, it wasn't noticed until disassembly that the exposure meter had been seriously mis-aligned on the beam reflecting from the vacuum window. Analysis of pictures of the exposure meter installation showed that approximately only 15 per cent of the light was directly striking the PMT surface during the on-sky testing period. However, more light probably reached the exposure meter via indirect reflections off a mounting tube placed immediately in front of the device.

Table 8.3 shows the results of comparing the results from exposure meter logs from the on-sky testing period against predicted counts from the exposure meter flux model. Four stars were chosen for this comparison, with all four being spectrophotometric standards for which there were flux data available for input into the model (Hamuy et al., 1994). Seeing values from the time period of observation, recorded at the 1.8-m Microlensing Observations in Astrophysics (MOA) telescope (adjacent to the 1-m McLellan telescope at Mt John University Observatory), were also used within the exposure meter model to generate predicted counts. As mentioned in Section 7.4.3, the MOA seeing data are not completely representative of the seeing experienced by the 1-m McLellan telescope. Nonetheless they are used here with caution as they give some measure of the conditions during the observations.

Also included is a column listing 'Corrected Observed' counts, within which the observed counts have been artificially increased by a factor of 2.9 so as to better match the predicted counts. Such an increase correlates with only 35 per cent of the predicted light levels being detected by the exposure meter. Of interest is that a single correction factor was able to bring the observed counts of four stars, observed during different seeing conditions, into agreement with the values predicted by the model.

Unfortunately, however, within these data the exposure meter misalignment losses cannot be separated from other losses within the system. As such, it remains unknown how much light was lost by the telescope-fibre system during the on-sky testing period at Mt John University Observatory.

Table 8.3: Comparison between observed and predicted exposure meter counts s^{-1}. The 'Corrected Observed' column artificially corrects for the misalignment of the exposure meter (see text for details).

Star	**Seeing FWHM [arcsec]**	**Observed [counts s^{-1}]**	**Corrected Observed [counts s^{-1}]**	**Predicted [counts s^{-1}]**
HR3454	2.0	1.2E+05	3.5E+05	3.9E+05
HR4468	2.4	9.3E+04	2.7E+05	2.1E+05
HR4963	1.7	1.0E+05	2.9E+05	3.1E+05
HR5501	1.6	3.3E+04	9.4E+04	9.5E+04

Chapter 9

Stability

9.1 Introduction

This chapter investigates the required temperature stability of the KiwiSpec instrument and includes a summary of the various stability factors affecting the vacuum chamber prototype. This chapter also reports on stability tests undertaken with the in-air prototype, and describes the progress made to date towards testing the stability of the vacuum chamber prototype.

9.2 Stability Requirements of the Optical Mounts

This section investigates the stability requirements of the positions of the optical elements. In order to provide insight into the required temperature stability of the instrument, the results are then converted to allowable temperature changes based on the design parameters of the opto-mechanical mounts.

9.2.1 Stability Analysis

The goal of this Zemax-based study was to determine, for each optical element, the amount of movement necessary for each degree of freedom to mimic a 1 m/s radial velocity shift. The approach taken was basically that of a tolerancing sensitivity analysis, in which each movement or perturbation was investigated separately and the resulting shift of centroids within the spectrum noted.

The same 35 wavelengths employed for the tolerancing of the entire instrument were monitored. Centroid movements along the échelle dispersion direction were the primary concern (although centroid movements in the cross-dispersion direction were also monitored to prevent large excursions). To compare with actual on-sky radial velocity measurement techniques, the average of the centroid movements in the échelle dispersion direction were calculated and used as the primary measurement. Centroid positions from Zemax (given in mm) were converted to radial-velocity space using

the KiwiSpec relationship that a 1 m/s radial velocity shift equates to approximately 0.001 pixels of centroid movement on the detector (as shown in Section 2.5.2).

The results are given in Table 9.1. Values given in the table equate to a radial velocity shift of ± 1 m/s in the échelle dispersion direction. The same degrees of freedom were used as in the alignment tolerancing study, described in Section 4.2.5.1.

Although movements in the échelle dispersion direction were the primary focus of this analysis, movements in the cross-dispersion direction were monitored as well. While not reported in detail here, in the cross-dispersion direction the movements within Table 9.1 resulted in at most a 7-pixel movement. The majority (91 per cent) of degrees of freedom listed in the table caused less than a 0.5 pixel shift in the cross-dispersion direction.

The results in Table 9.1 show that for the rotational degrees of freedom, the tilt movements are the most sensitive, and for the translational degrees of freedom, the height movements are the most sensitive. This is owing to the fact that within the KiwiSpec instrument, the échelle orders are oriented vertically (i.e. perpendicular to the optical table top). Because of the importance of movements along the échelle dispersion direction, it follows that degrees of freedom that cause vertical movements at the focal plane will be the most sensitive parameters with respect to radial velocity precision (i.e. height changes and tilts about a horizontal axis). Clocking of the primary collimator and échelle grating are also sensitive parameters (both of which can move the spectrum along the échelle dispersion direction).

The tolerances on the vacuum windows given here are more relaxed than the values determined in Section 6.3.2. The goal of that analysis was to ensure that the maximum centroid movement was less than the 1 m/s level, whereas this analysis is concerned with the mean centroid movement causing less than a 1 m/s shift in the échelle dispersion direction only.

9.2.2 Allowable Temperature Changes

As the temperature of the spectrograph increases or decreases, every component within the instrument reacts by expanding or contracting. Such changes can cause optical elements to move, mimicking a radial velocity shift.

By combining the results of Table 9.1 with design parameters from the opto-mechanical mounts, one can gain insight into the required temperature stability of the instrument. This approach is followed in the next two sections for the rotational and translational degrees of freedom. It should be noted that this approach is intended to be a first-order analysis and is not a rigorous thermal or stability model.

Table 9.1: The tolerances that result in radial velocity shifts of ± 1 m/s in the échelle dispersion direction. Degrees of freedom indicated by '-' do not have an effect on radial velocity stability.

Component	**Turn** [°]	**Tilt** [°]	**Clocking** [°]	**Height** [mm]	**dy** [mm]	**dz** [mm]
Fibre	± 0.05	± 0.025	-	± 0.00001	± 0.0001	± 0.02
Relay Collimator Lens	± 0.0025	± 0.00025	-	± 0.00001	± 0.0001	± 0.02
External Input Relay	± 0.0001	± 0.00001	-	± 0.0005	± 0.0025	-
Input Vacuum Window	± 0.1	± 0.01	± 0.25	-	-	-
Relay Focus Lens	± 0.0025	± 0.0005	-	± 0.000025	± 0.00025	± 0.1
Input Fold	± 0.0001	± 0.00001	-	-	± 0.0002	± 0.0002
Primary Collimator	± 0.000005	± 0.00000025	± 0.000005	± 0.00001	± 0.002	± 0.00025
Échelle	± 0.00001	± 0.0000005	± 0.0000005	-	-	-
Secondary Collimator	± 0.005	± 0.000002	-	± 0.000025	± 0.025	± 0.075
Dichroic	-	± 0.2	± 0.2	-	-	-
Camera Fold	± 0.01	± 0.0000025	-	-	± 0.1	± 0.1
Output Vacuum Window	-	± 0.2	-	-	-	-
Entire Grism	± 0.25	± 0.001	± 0.01	-	-	-
Hasselblad	± 0.01	± 0.00001	-	± 0.00001	± 0.05	± 0.0025
Field Flattening Lens	± 0.025	± 0.0005	-	± 0.0001	± 0.1	± 0.005
Hasselblad and Fflens	± 0.01	± 0.00005	-	± 0.00001	± 0.1	± 0.0025
Detector and Window	± 0.025	± 0.001	± 0.01	± 0.00001	± 0.01	± 0.0025

9.2.2.1 Rotational Movements

Many of the optical mounts within the KiwiSpec prototype rely on a stainless steel actuator to adjust the rotational degrees of freedom (see Chapter 5), such as the échelle mount shown in Figure 9.1. Confronted with a temperature change, the stainless steel actuator will expand or contract by a different amount than the surrounding aluminium mount - resulting in the grating changing in tilt.

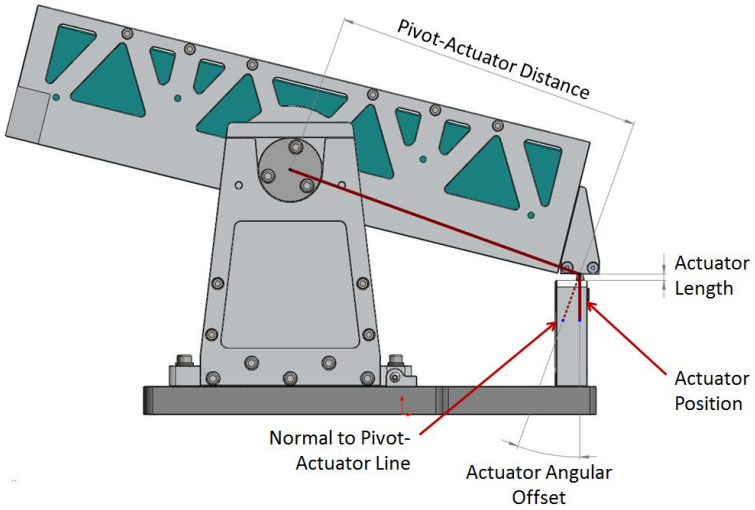

Figure 9.1: An expansion or contraction of an adjustment actuator can lead to a rotational change of an optical element. Shown is the échelle mount with the tilt axis geometry highlighted. Note that the actuator is not perpendicular to the line between the actuator and the pivot.

For a given temperature change, the amount that the actuator changes in length is governed by:

$$\Delta L_{\mathrm{a}} = L_{\mathrm{a}} \alpha \Delta T, \tag{9.1}$$

where:

ΔL_{a}	change in actuator length	[mm];
L_{a}	nominal actuator length	[mm];
α	coefficient of thermal expansion	[°C^{-1}];
ΔT	change in temperature	[°C].

Several of the mounts have actuators that are oriented at an angle to the pivot-actuator line, as shown in Figure 9.1. Employing the geometry shown in Figure 9.2, a change in actuator length can be converted to a change

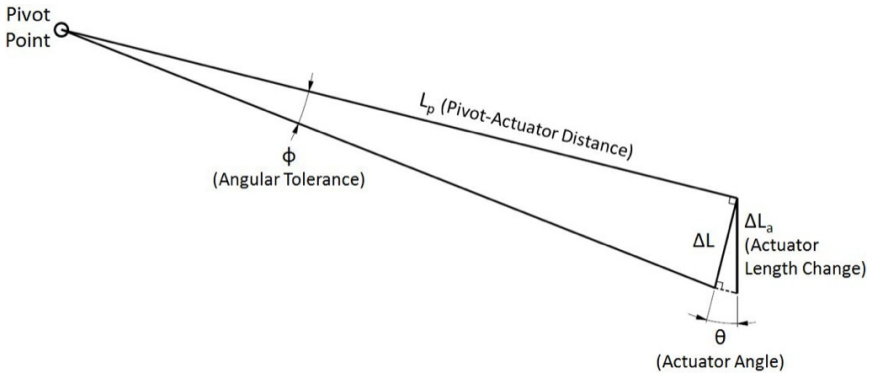

Figure 9.2: Schematic diagram showing the various parameters used in Equations 9.1 through 9.6.

normal to the pivot-actuator line by:

$$\Delta L = \Delta L_\mathrm{a} \cos\theta. \tag{9.2}$$

Figure 9.2 also shows that ΔL is equal to a change in the angular position of the mount:

$$\Delta L = L_\mathrm{p} \tan\phi. \tag{9.3}$$

Equating Equations 9.2 and 9.3, and then including Equation 9.1:

$$L_\mathrm{p} \tan\phi = \Delta L_\mathrm{a} \cos\theta, \tag{9.4}$$
$$L_\mathrm{p} \tan\phi = L_\mathrm{a} \alpha \Delta T \cos\theta. \tag{9.5}$$

After rearranging:

$$\Delta T = \frac{L_\mathrm{p} \tan\phi}{L_\mathrm{a} \alpha \cos\theta}. \tag{9.6}$$

Equation 9.6 can then be used to determine the allowable temperature change given mount design parameters (L_p, L_a, α, θ) and the 1 m/s tolerance on the angular change (ϕ) of the optic.

The results of applying Equation 9.6 to the mounts with adjustable turn, tilt, and clocking rotational degrees of freedom are shown in Tables 9.2, 9.3 and 9.4 respectively.

The table values show the tilt axis is by far the most sensitive rotational degree of freedom, with an allowable temperature change of only 0.01°C. This is to be expected, as the échelle orders are arranged vertically with respect to the optical table, and a tilt adjustment moves the spectrum along the échelle orders.

Table 9.2: Temperature changes that result in a mount moving to the 1 m/s turn tolerance value for each mount with an adjustable turn axis. This rotation (about a vertical axis) moves the spectrum along the cross dispersion direction.

Component	**Turn 1 m/s Tolerance** [°]	**Allowable Temperature Change** [°C]
External Input Relay	0.0001	1.84
Input Fold	0.0001	0.47
Primary Collimator	0.000005	0.41
Échelle	0.00001	0.26
Secondary Collimator	0.005	19.91
Camera Fold	0.01	47.22
Detector and Window	0.025	137.80
	Min:	0.26

Table 9.3: Temperature changes that result in a mount moving to the 1 m/s tilt tolerance value for each mount with an adjustable tilt axis. This rotation (about a horizontal axis) moves the spectrum along the échelle dispersion direction.

Component	**Tilt 1 m/s Tolerance** [°]	**Allowable Temperature Change** [°C]
External Input Relay	0.00001	0.18
Input Fold	0.00001	0.05
Primary Collimator	0.00000025	0.01
Échelle	0.0000005	0.03
Secondary Collimator	0.000002	0.06
Camera Fold	0.0000025	0.01
Detector and Window	0.001	8.12
	Min:	0.01

Table 9.4: Temperature change that results in the primary collimator clocking adjustment moving to the 1 m/s tilt tolerance value. The primary collimator mount is the only mount with an adjustable clocking degree of freedom.

Component	**Clocking 1 m/s Tolerance** [°]	**Allowable Temperature Change** [°C]
Primary Collimator	0.000005	0.14
	Min:	0.14

While 0.01°C is a very small temperature change, the rotational influences of changing actuator length can be completely removed by designing appropriate locking mechanisms into the mounts. Such mechanisms could allow the actuators to be used for alignment, but then allow the actuators to be drawn back after the locks were applied. With such a system, the expansion and contraction of the actuators would have no effect on the stability of the instrument.

9.2.2.2 Translational Movements

Of the three translational degrees of freedom, changes in the height of the optical elements have the greatest effect on radial velocity stability. This is owing to the échelle orders being oriented perpendicular to the optical table top. However, the importance is not an absolute height change, but rather a differential change in height among the optical elements. To help ensure a consistent response to temperature changes, all mechanical components that set the height of an optical element have been made entirely of aluminium. Care was also taken to ensure that the internal and external optical tables, (as well as the feet that support them), were constructed to be as identical as possible.

There will, however, be a slight difference among the heights of the mounts due to the manufacturing tolerances. However, taking the tightest height tolerance equating to a 1 m/s shift (0.00001 mm), and the sum of the two worst height alignment tolerances (0.5 mm, see Section 4.2.5.1), the allowable temperature change equals 1.78°C. This is a large value and could be easily achieved by a thermally-stable enclosure surrounding the spectrograph.

With regard to the horizontal movements dy and dz, an allowable temperature range can be calculated by rearranging the linear expansion equation to solve for temperature. This equation accounts for the distances between the optical elements as well as the thermal expansion coefficients of the optical tables:

$$\Delta T_{\mathrm{dy}} = \frac{\Delta L_{\mathrm{dy}}}{L_{\mathrm{dy}}\alpha_{\mathrm{dy}}}; \tag{9.7}$$

$$\Delta T_{\mathrm{dz}} = \frac{\Delta L_{\mathrm{dz}}}{L_{\mathrm{dz}}\alpha_{\mathrm{dz}}}. \tag{9.8}$$

Here:

$\Delta T_{(\mathrm{dy,dz})}$	change in temperature	[°C];
$\Delta L_{(\mathrm{dy,dz})}$	the 1 m/s tolerance in either dy or dz	[mm];
$L_{(\mathrm{dy,dz})}$	the longest distance between this mount and another in either dy or dz	[mm];
$\alpha_{(\mathrm{dy,dz})}$	coefficient of thermal expansion of the optical table top material	[°C^{-1}].

Figure 9.3 shows the equation parameters diagrammatically.

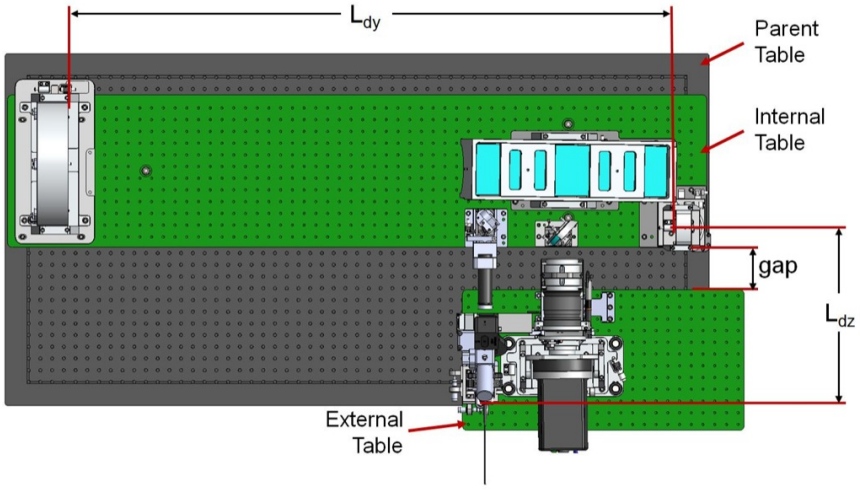

Figure 9.3: Distances measured from the secondary collimator mirror to the furthest optical elements along both the dy and dz degrees of freedom. Note the gap between the internal and external table tops in the dz direction, to which was ascribed the coefficient of linear expansion value of the parent table.

The 1 m/s sensitivity tolerance values calculated within Zemax assume that an optical element is translated while all other optical elements remain stationary. Therefore, the distance $L_{(\mathrm{dy,dz})}$ was determined by measuring the distance between a given optical element and the optical elements the furthest away from it in both the dy and dz directions.

As described in Chapter 6, the KiwiSpec system is supported by three optical tables. The internal table supports the optical mounts within the vacuum chamber; the external table supports the optical mounts outside of the vacuum chamber; and the parent table supports the entire instrument.

With regard to Equations 9.7 and 9.8, the distances between the optical

mounts are set by the optical design. However, the table materials are a free parameter. As mentioned above, the internal and external tables are constructed of the same materials in order to be as similar as possible with regard to thermal expansion in the height direction. However, the parent table may be constructed of a different material than the internal and external tables. The effect of the external table must be considered because as the parent table expands and contracts, it will change the size of the gap between the internal and external tables.

Therefore three materials were investigated for the internal and external tables: 304 stainless steel ($\alpha = 14.7 \times 10^{-6}$ C^{-1}), invar 36 ($\alpha = 1.0 \times 10^{-6}$ C^{-1}), and super invar ($\alpha = 0.3 \times 10^{-6}$ C^{-1}). Two possibilities were considered for the parent table: 416 stainless steel (the composition of the in-air prototype parent table, $\alpha = 8.5 \times 10^{-6}$ C^{-1}), and super invar.[1].

The results for the calculated allowable temperatures for the dy and dz directions are shown in Tables 9.5 and 9.6, and show the not surprising result that super invar tables offer a higher level of temperature stability than stainless steel tables.

9.2.3 Summary and Discussion

This section has investigated the sensitivity of the degrees of freedom of each optical element with regard to movements affecting radial velocity measurements at the 1 m/s level.

As discussed in Section 9.2.2.1, the temperature sensitivity of the rotational degrees of freedom can be removed through appropriate locking mechanisms designed into the mounts. For the translational degrees of freedom, the influence of height changes can be minimized through the consistent use of aluminium in the opto-mechanical mounts. Therefore, the translational movements dy and dz (i.e. movements horizontal to the optical tables) remain as the most sensitive parameters to temperature changes investigated during this analysis.

Tables 9.7 and 9.8 provide a summary of the allowable temperature changes for the dy and dz degrees of freedom, for several situations of optical tables made of stainless steel and super invar. The smallest allowable temperature change in either Table 9.7 or Table 9.8 sets the temperature sensitivity for the six degrees of freedom included in this study.

Within the dy group (Table 9.7), choosing 304 stainless steel tables requires the temperature to be controlled to 0.01°C, which is a difficult value to maintain. Therefore, it would be preferable to choose super invar for the internal and external tables, allowing the temperature sensitivity to increase to 0.73°C.

With respect to the dz group (Table 9.8), the case where all three tables

[1]Coefficient of thermal expansion values are taken from Paquin (1997).

Table 9.5: Calculated dy allowable temperature ranges for optical tables made of three different materials. The calculated temperatures take into account the distance between each optic and the furthest optic from it in the dy direction using Equation 9.7.

	dy		**Allowable Temperature Change**		
Component	**1 m/s Tolerance [mm]**		**304 Stainless [°]**	**Invar 36 [°]**	**Super Invar [°]**
Fibre	0.0001		0.30	6.67	22.22
Relay Collimator Lens	0.0001		0.30	6.67	22.22
External Input Relay	0.0025		0.19	2.73	9.09
Input Vacuum Window	1		74.18	1090.51	3635.04
Relay Focus Lens	0.00025		0.01	0.27	0.91
Input Fold	0.0002		0.01	0.22	0.73
Primary Collimator	0.002		0.10	1.44	4.80
Échelle	1		60.74	892.86	2976.19
Secondary Collimator	0.025		1.22	17.99	59.95
Dichroic	1		57.17	840.34	2801.12
Camera Fold	0.1		6.13	90.09	300.30
Output Vacuum Window	1		61.29	900.90	3003.00
Entire Grism	1		61.29	900.90	3003.00
Hasselblad	0.05		3.06	45.05	150.15
Field Flattening Lens	0.1		6.13	90.09	300.30
Hasselblad and Ff-lens	0.1		6.13	90.09	300.30
Detector and Window	0.01		0.61	9.01	30.03
		Min:	0.01	0.22	0.73

Table 9.6: Calculated dz allowable temperature ranges for internal and external optical tables made of three different materials, and parent tables made of two different materials. The calculated temperatures take into account the distance between each optic and the furthest optic from it in the dz direction using Equation 9.8.

			Allowable Temperature Change					
	dz		**416 Stainless Parent Table**			**Super Invar Parent Table**		
Component	**1 m/s Tolerance [mm]**		**Stainless 304 [°C]**	**Invar 36 [°C]**	**Super Invar [°C]**	**Stainless 304 [°C]**	**Invar 36 [°C]**	**Super Invar [°C]**
Fibre	0.02		34.01	500.00	1666.67	34.01	500.00	1666.67
Relay Collimator Lens	0.02		34.01	500.00	1666.67	34.01	500.00	1666.67
External Input Relay	1		155.73	866.74	1130.45	176.08	2429.25	7017.54
Input Vacuum Window	1		175.33	288.14	297.94	175.33	288.14	297.94
Relay Focus Lens	0.1		18.58	31.91	33.12	18.58	31.91	33.12
Input Fold	0.0002		0.04	0.19	0.23	0.05	0.65	1.80
Primary Collimator	0.00025		0.04	0.21	0.28	0.04	0.59	1.70
Échelle	1		155.73	866.74	1130.45	176.08	2429.25	7017.54
Secondary Collimator	0.075		16.21	72.69	88.44	19.30	258.93	708.22
Dichroic	1		240.52	1000.25	1192.75	292.78	3881.23	10384.22
Camera Fold	0.1		24.05	100.03	119.27	29.28	388.12	1038.42
Output Vacuum Window	1		233.77	3436.43	11454.75	233.77	3436.43	11454.75
Entire Grism	1		319.63	1075.56	1223.39	419.02	5329.07	13280.21
Hasselblad	0.0025		0.62	2.52	2.99	0.76	10.01	26.62
Field Flattening Lens	0.005		0.96	4.67	5.82	1.12	15.21	42.52
Hasselblad and Ff-lens	0.0025		0.55	2.43	2.95	0.65	8.72	23.81
Detector and Window	0.0025		0.47	2.31	2.90	0.54	7.38	20.73
		Min:	0.04	0.19	0.23	0.04	0.59	1.70

are made of super invar is the only situation that results in an allowable temperature change greater than the 0.73°C found for the dy group.

A brief survey of temperatures achievable within the thermal enclosures of other spectrographs helps to put these values into perspective: the FEROS instrument experiences a change in temperature of less than 0.2°C over one night (Kaufer et al., 1999); the HERMES instrument is triple-isolated from its external environment, with the inner room actively stabilized by a heater to within ± 0.01°C (Raskin et al., 2011); SALT HRS employs 'multiple layers of insulation and temperature regulation' with a goal of 0.001°C stability (Bramall et al., 2012); the SOPHIE instrument employs three stages of thermal isolation, with the spectrograph experiencing a 'daily thermal stability better than 0.01°C' (Perruchot et al., 2008); and finally, the HARPS instrument achieves a long term stability of approximately 0.01°C, with the highest stability recorded being on the order of 0.001°C RMS over the course of one day (Mayor et al., 2003). These values highlight what is capable with carefully designed thermal isolation and control, and indicate that by employing super invar tables within KiwiSpec, the allowable 0.73°C variation determined above would certainly be achievable.

As mentioned, this analysis is intended as a first-order look at the temperature requirements of the opto-mechanial elements. While this study investigates each degree of freedom separately, in reality all degrees of freedom will be changing simultaneously. Such a situation is very difficult to model, and traditional tolerancing approaches such as Monte Carlo analysis cannot be used. This is because a Monte Carlo analysis assumes that perturbations occur randomly on either side of a nominal value, whereas the effects of temperature changes are biased to all be in one direction (i.e. all components expand when the temperature increases).

Employing three tables composed of super invar is a prudent choice, as in practice all of the degrees of freedom will contribute to instrument instability simultaneously. While this analysis shows the most sensitive parameter requires temperature changes less than 0.73°C, when the contributions of all parameters are included the allowable temperature change will be much lower. Therefore, although the super invar tables provide a great improvement over stainless steel tables with respect to thermal stability, they do not remove the need for a stable thermal enclosure surrounding the instrument.

Table 9.7: Summary of the allowable temperature changes for 1 m/s stability for the dy translational degree of freedom.

	Internal Table	
	304 Stainless [°C]	**Super Invar [°C]**
dy	0.01	0.73

Table 9.8: Summary of the allowable temperature changes for 1 m/s stability for the dz translational degree of freedom.

	Parent Table	**Internal/External Tables**	
		304 Stainless [°C]	**Super Invar [°C]**
dz	**416 Stainless**	0.04	0.23
	Super Invar	0.04	1.70

9.3 Vacuum Chamber Prototype Stability Summary

Table 9.9 provides a summary of the various analyses and measurements undertaken to determine the stability of the KiwiSpec vacuum chamber prototype. As can be seen within the table, in general the expected values are much smaller than the values required for the 1 m/s radial-velocity precision level. The exception is the 'external temperature' parameter; however, as described in Section 6.4.4 the value reported here is the worst-case scenario (which does not assume the averaging of spectral line movements, something that is done in practice).

9.4 Prototype Stability Tests

This section outlines the stability tests undertaken with the in-air prototype. For these tests, the spectrograph was placed within a thin-walled, uninsulated aluminium room measuring approximately 2 m × 2 m × 2 m.

9.4.1 Environmental Sensors

High precision sensors were selected to monitor temperature, pressure and humidity in the vicinity of the spectrograph.

The device chosen for temperature measurements was a 'PT-104 Platinum RTD Convertor', manufactured by Pico Technology. The PT-104 offers a measurement resolution of 0.001°C, with a precision of 0.01°C and was recommended by the Temperature Standards section of the Measurement Standards Laboratory of New Zealand (MSL). A picture of the device is shown in Figure 9.4.

Figure 9.4: The Pico Technology PT-104 temperature measurement device, with a USB cable and one platinum RTD sensor attached (the white wire).

For temperature sensors, platinum 'PT-100' RTD (resistance temperature detectors) were selected. The 4-wire version of this sensor was chosen as it is the most accurate configuration, in that it allows the PT-104 module to compensate for any differences in the lengths or characteristics of the separate sensor lead wires.

Table 9.9: Summary of the various stability analyses and measurements undertaken for the vacuum chamber prototype.

Stability Parameter	**Section**	**1 ms^{-1} hr^{-1} Requirement**	**Expected Value**	**Comments**
Vacuum chamber pressure	6.4.1	0.0124 mbar hr^{-1}	0.002 mbar hr^{-1}	Based on initial chamber pressure test
Vacuum chamber temperature[a]	6.4.3	3.7°C hr^{-1}	< 0.1°C hr^{-1}	Achievable with an environmental enclosure
External pressure (worst case)	6.4.2	3.8 mbar hr^{-1}	-0.2 mbar hr^{-1}	Based on Paranal data
External temperature (worst case)	6.4.4	0.1°C hr^{-1}	< 0.1°C hr^{-1}	Achievable with an environmental enclosure
Vacuum chamber deflection/ window movements	6.3.2	$< 1.6\,\mu$m (input); $< 26\,\mu$m (output)	$< 0.1\,\mu$m (input); $< 0.5\,\mu$m (output)	Based on FEA analysis of vacuum chamber
Temperature (Mount Movements)	9.2.2.1	-	-	Compensated for by mount designs and locks
Temperature (Mount Heights)	9.2.2.2	1.78°C hr^{-1}	< 0.1°C hr^{-1}	Achievable with an environmental enclosure
Temperature (Table Dimensions)	9.2.2.2	0.73°C hr^{-1}	< 0.1°C hr^{-1}	Assumes three super invar tables and an environmental enclosure

[a]Assumes a vacuum chamber pressure of 1 mbar.

Each PT-104 device allows for the connection of four sensors; for the KiwiSpec prototype two devices were purchased, which allowed for eight temperature sensors to be located throughout the instrument.

Temperature sensors were placed in direct contact with the back surfaces of the primary collimator, the échelle grating substrate and the secondary collimator, and also on top of the grism and CCD detector. Each of these sensors was placed under a piece of foam to ensure the sensor was not being influenced by the air temperature.

Three sensors were also used to monitor air temperatures: one at the primary collimator and one at the échelle grating (both being set at the height of the optical axis), and one outside the KiwiSpec room within the outer laboratory. Figure 9.5 shows the échelle substrate sensor and the échelle air temperature sensor within the in-air prototype.

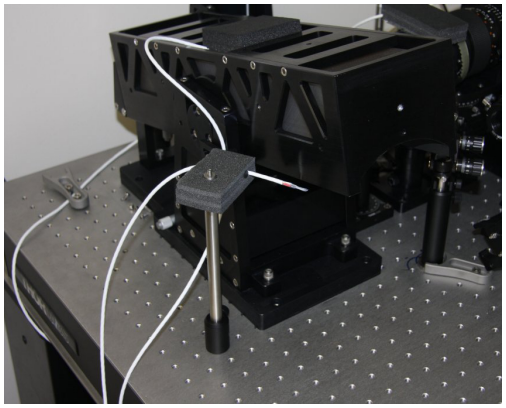

Figure 9.5: Temperature sensors placed near the échelle grating. Shown is the sensor attached to the top of the grating substrate (placed under a piece of closed-cell foam for insulation from air temperature changes). Also shown is a sensor mounted on a post (but isolated from it via a piece of foam), which measured the air temperature at the échelle grating.

Atmospheric pressure and relative humidity measurements were combined within one device, the Vaisala PTU301. This unit, shown in Figure 9.6, is factory-calibrated and was recommended by the Pressure and Humidity Standards sections of MSL. It offers a pressure measurement accuracy of $\pm$ 0.1 mbar (at 20°C) with a repeatability of $\pm$ 0.03 mbar, and a relative humidity accuracy of $\pm$ 1 per cent.

Given that the goal of these tests was to measure radial-velocity stability, the accuracies of the three environmental sensors chosen were converted to equivalent radial-velocity shifts with the NIST-based refractive index calculator (described in detail in Section 6.1.1). Table 9.10 provides this conversion for each of the sensors. Although the converted values indicate the sensors are not as accurate as the spectrograph itself can measure, they represent the highest-accuracy sensors found for reasonable cost (i.e. the temperature and pressure/humidity measurement systems each cost several thousand US dollars).

Figure 9.6: The Vaisala PT301 atmospheric pressure and relative humidity sensor. The humidity probe is the long tube extending from the bottom of the device.

Table 9.10: The sensor accuracies expressed as a radial velocity shift due to a change in the refractive index of air.

Sensor	Accuracy	Equivalent RV Shift
Temperature	$\pm 0.01°C$	± 2.9 m/s
Atmospheric Pressure	± 0.1 mbar	∓ 8.1 m/s
Relative Humidity	$\pm 1\%$	± 2.5 m/s

9.4.2 Temperature Sensor Calibration

During the stability tests of the in-air prototype, the temperature sensors were not calibrated as the interest at the time was the variation in temperature and not absolute measurements. In retrospect, the sensors should have been calibrated as then a more accurate calculation of the refractive index of air could have been made. Therefore, the temperature sensors will be calibrated by MSL before the stability tests of the vacuum chamber prototype.

Without calibration, each of the sensors measures an offset from the correct temperature. To determine this offset, the eight KiwiSpec temperature sensors and an additional calibrated sensor were located side-by-side, and placed between two large, thick layers of foam for insulation, (the intent being to immerse all of the sensors within a constant-temperature environment). The results are shown in Figure 9.7, which shows the offset measured by each sensor. The maximum offset between one of the KiwiSpec sensors and the separate calibrated sensor is $+0.13°$, which equates to a $+37$ m/s radial velocity shift based on a refractive index of air change. However, as will be seen in Section 9.4.4.2, this offset did not influence the test results as refractive index of air changes were not the limiting factor in the stability of the instrument. For the vacuum chamber prototype stability tests, the move to calibrated sensors will remove this offset from the measurements.

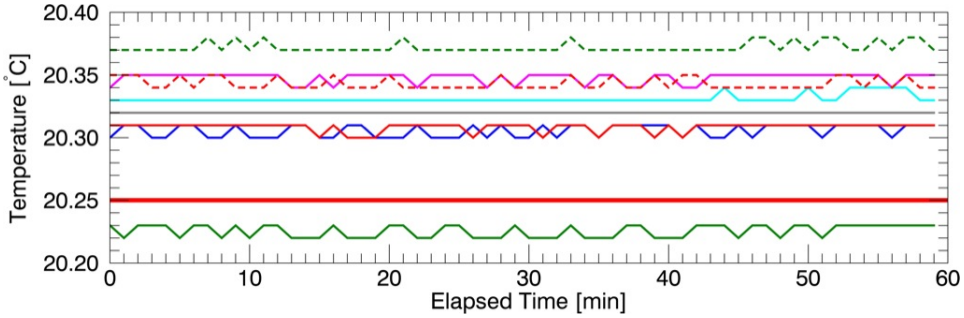

Figure 9.7: Output values from the eight temperature sensors, which for this one-hour period were located side-by-side and placed between two thick layers of foam insulation for temperature stability. Therefore, all eight sensors experienced the same temperature conditions, and hence indicate the measurement offset of each sensor. The thick red line indicates the temperature reported by a separate, calibrated temperature sensor co-located with the KiwiSpec sensors during this time period.

9.4.3 Temperature Stability of Laboratory

Initial tests showed that temperature changes in the outer laboratory were influencing the temperature within the smaller spectrograph room. Although the (uninsulated) aluminium walls of the smaller spectrograph room provided somewhat of a buffering effect to small-scale changes, the overall temperature trends carried through to the instrument.

The effect of the air conditioning unit on the temperature of the outer laboratory is shown in Figure 9.8. The temperature oscillations in the left hand side of the figure clearly show the strong effect of the air conditioning unit cycling on and off. Every hour, the temperature increases by approximately 1°C and then falls by 1°C. Also shown in the figure is how the temperature stabilized after the air conditioning unit was shut down.

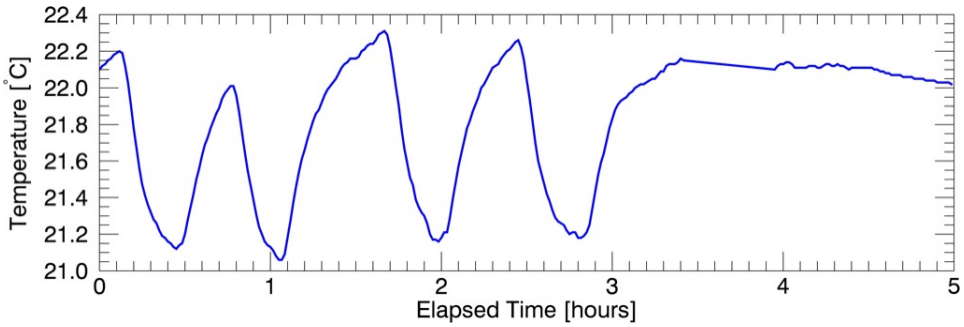

Figure 9.8: The effect of the air conditioning unit on the temperature variation in the outer laboratory. The air conditioning unit was switched off at approximately 3.5 hours.

With the air conditioning unit turned off, as shown in Figure 9.9, the room experienced a 1°C total variation over a period of 24 hours. This passive, gently-changing temperature variation is much preferred to the sharp temperature changes created by the air conditioning control system.

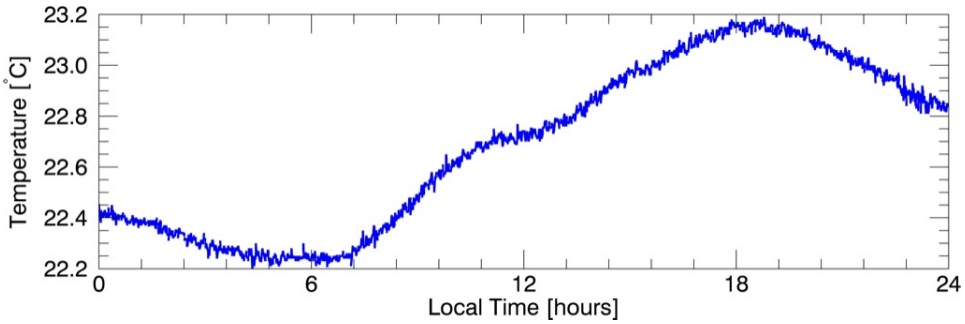

Figure 9.9: The diurnal temperature variability of the outer laboratory. The plot shows temperature data over a full day (starting at local midnight). For this measurement, the stainless steel cover was removed from the sensor, making it more sensitive to slight variations in temperature (hence the small variations).

9.4.4 In-Air Prototype - Laboratory Tests

A series of tests were undertaken with the in-air prototype to determine the response of the instrument to (naturally) varying environmental conditions. During these tests, a continuous series of thorium-argon spectra were taken while the environmental conditions were monitored and logged. The spectra were then analysed to determine the relative movements of the thorium-argon emission lines throughout the test, with respect to the position of the lines in the first spectrum of the series.

Several stability test runs of different durations were undertaken; the results of one 12-hr long test are shown here as being representative of the stability of the in-air prototype.

During the tests, thorium-argon spectra were recorded at approximately 2-min intervals. The taking of spectra was completely automated through the KiwiSpec software, which allowed the scripting of a sequence of images, and also recorded all temperature, humidity and atmospheric pressure data to the image headers. The graphical user interface (GUI) of the KiwiSpec software is shown in Figure 9.10. This software system was developed by the author to control and monitor the spectrograph (although the code behind the GUI was written by Shaun Hurd of kanDO Innovation).

Figure 9.10: The KiwiSpec software user interface.

9.4.4.1 Refractive Index of Air Stability

As introduced in Section 6.1.1, changes in the refractive index of air (caused by changing environmental conditions) can mimic radial velocity shifts for a spectrograph operating in air.

The environmental conditions that occurred during a 12-hr long stability test with the KiwiSpec in-air prototype are shown in Figure 9.11. The top three subfigures show separately the variations in temperature, atmospheric pressure and relative humidity during the test. The bottom subfigure employs the NIST-based refractive index calculator to convert the environmental changes to equivalent radial-velocity shifts, for each parameter changing individually (with the other parameters constant), and for the combined effect with all parameters changing simultaneously.

The bottom subfigure of Figure 9.11 provides some insight into how environmental changes affect the stability of an in-air spectrograph:

- Changes in relative humidity have a small effect on radial-velocity stability;
- The overall shape of the 'combined' curve follows the inverse of the pressure curve (as a positive pressure change equates to a negative radial-velocity shift);
- However, the 'combined' curve does not exactly follow the pressure curve, but is rather offset from it owing to the effects of changing temperature;
- Given the relative strengths shown in Figure 6.2, one would expect temperature changes to have a stronger effect. However, the relative change in temperature during the test was much smaller than the relative change in pressure, and hence the two effects are of similar magnitude;
- The effects of pressure and temperature interact with each other: at times the effects counteract (i.e. between 1000 and 1500 h UTC); at times they nullify (i.e. at 1500 h UTC); and at times they reinforce (i.e. after 1900 h UTC).

Note that the 'combined' curve in Figure 9.11 is predictive, and is based on refractive index of air changes only. In practice, mechanical changes within the instrument will also affect the stability of the spectrograph (i.e. movements of mounts or optics owing to thermal expansion or contraction).

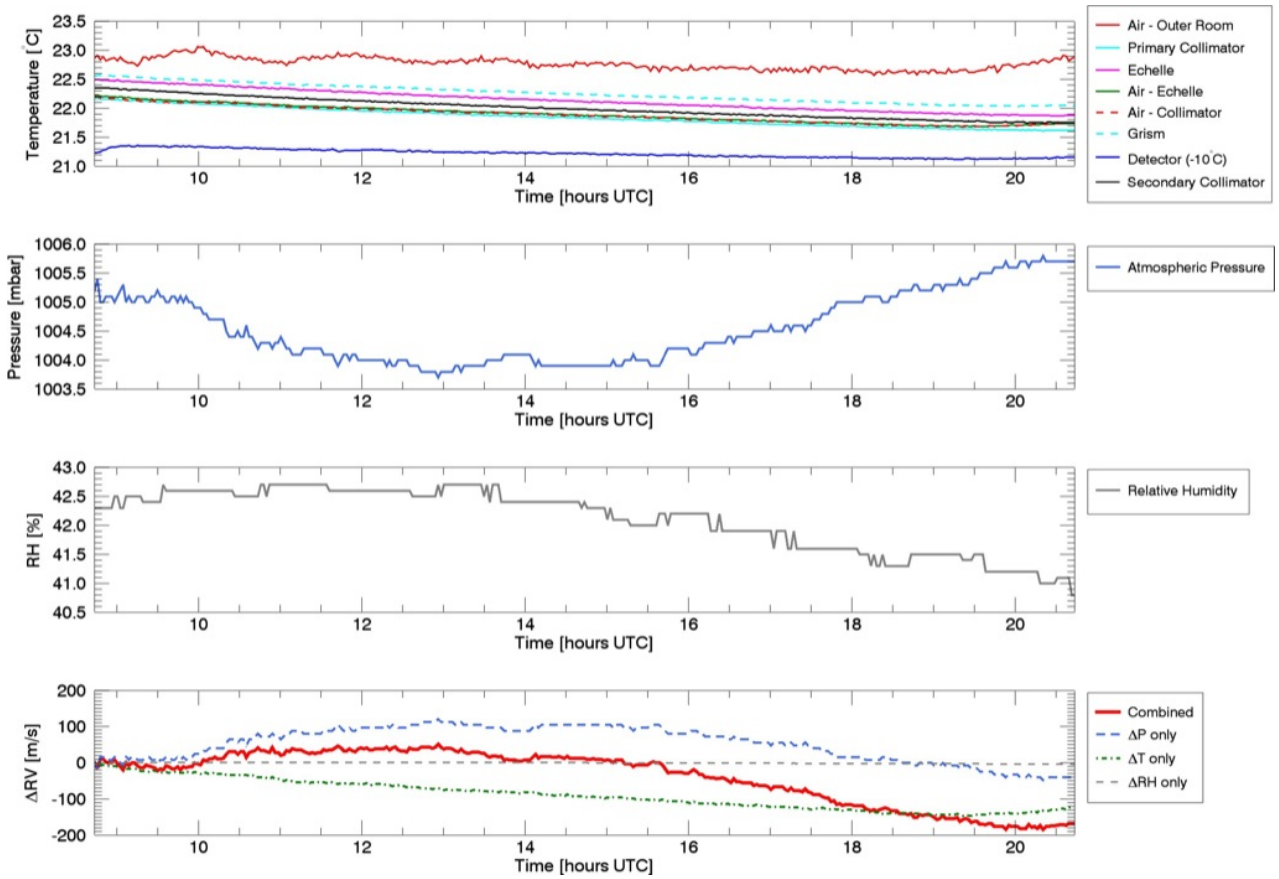

Figure 9.11: Predictive plot. The 'combined' line represents the best stability that the instrument could deliver while sitting in-air. The 'Air-Échelle' temperature measurements were employed for the 'ΔT only' and 'Combined' data in the bottom subfigure.

9.4.4.2 Measured Line Movements

Figure 9.12 shows the measured movements of the thorium-argon lines during the same stability test, as well as the temperature and pressure measurements for comparison. The line movements in the échelle dispersion direction have been converted from pixels to an equivalent radial velocity shift via the relationship that 1 pixel equals approximately 1000 m/s (as shown in Section 2.5.2).

Figure 9.12a shows only two temperature sensors: one representative of the mount and optical element temperatures, and one representative of the air temperature at the height of the optical axis above the table. The échelle substrate sensor correlated well with the other sensors placed on optics or mounts, and the échelle air sensor correlated well with the other air sensor within the spectrograph. This can be seen in the top subfigure of Figure 9.11, which includes the measurements from all of the temperature sensors.

Comparing Figure 9.12c with the movements predicted by refractive index changes shows that the shapes of the two curves do not match, and that the measured lines in the échelle dispersion direction moved approximately ten times more than the movements predicted by refractive index changes alone. Given the striking resemblance between the échelle dispersion thorium-argon line movements (Figure 9.12c) and the temperature change of the mounts (Figure 9.12a), the correlation between measured line movements and temperature was further investigated.

Figure 9.13 shows how the échelle and cross-dispersion line movements correlate with the temperature of the optical mounts (represented by the échelle substrate temperature). A best-fit line in the form of a second-degree polynomial is also included for both the échelle and cross-dispersion cases, as well as plots showing the residuals about the best-fit line for each case.

As Figure 9.13 shows, for the échelle dispersion direction there is a very clear correlation between the line movements and the temperature of the mechanical mounts and optics. Therefore, temperature effects were the predominant source of instability of the in-air prototype.

This result matches the findings of Section 9.2.2.2, which indicated that supporting the instrument on stainless steel tables would not provide the required temperature stability, and that super invar tables should be employed. As that analysis showed, the expansion and contraction of the optical tables have a significant effect on instrumental stability: with all three tables made of stainless steel (which approximates to the in-air prototype situation), the temperature would need to be controlled to 0.01°C to achieve 1 m/s radial-velocity stability. Given that during the stability test period the temperature varied by 0.63°C, it is not surprising that temperature is strongly affecting stability.

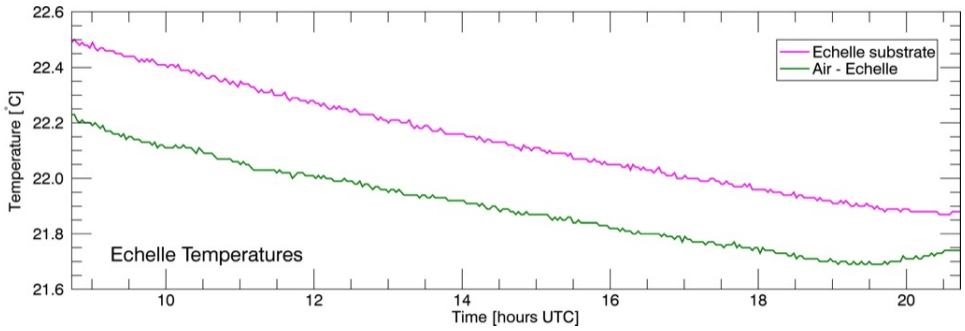

(a) Temperature variation in the vicinity of the échelle during the stability test.

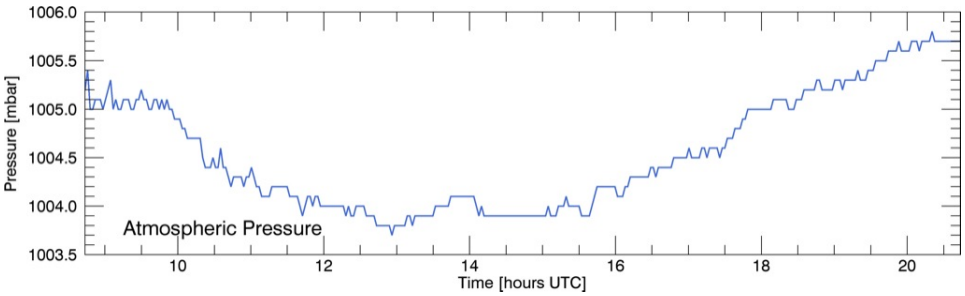

(b) Atmospheric pressure variation during the stability test.

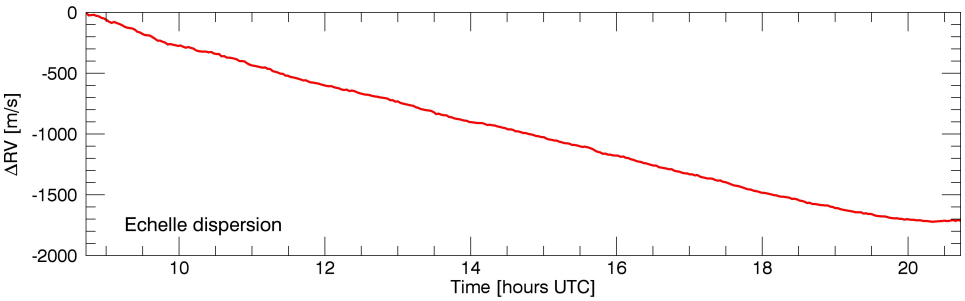

(c) Measured line movements in the échelle dispersion direction.

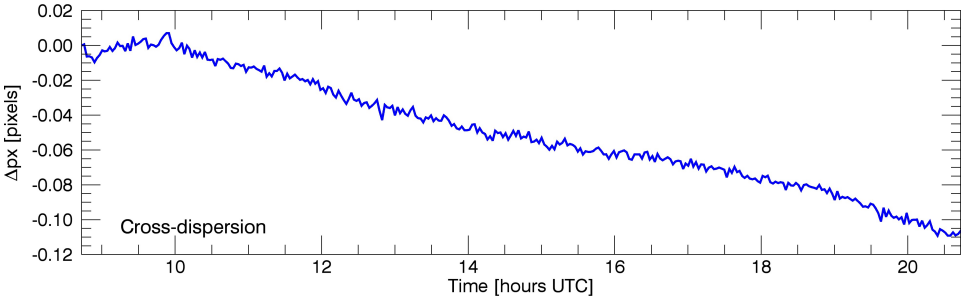

(d) Measured line movements in the cross-dispersion direction.

Figure 9.12: Data from a 12-hr long stability test, during which thorium-argon spectra were recorded every 2 min. Data are from the same stability test shown in Figure 9.11. The fine detail visible in the cross-dispersion plot is also present within the échelle dispersion data, but is hidden in the échelle plot because of the larger y-axis range.

In addition to the material of the optical tables, other design elements of the in-air prototoype were prone to introduce temperature instabilities. These included the design of the input relay system (which was cantilevered off a single kinematic stage) and the use of both aluminium and stainless steel within the height supports of the optical elements (which would lead to a differential height change between optical elements as the temperature varied). The opto-mechanical design of the vacuum chamber prototype corrected both of these issues.

Within Figure 9.13, the residual plots both show an oscillation about the best-fit line, with an apparent inversion of the profile between the échelle and cross-dispersion cases. Given that the 'combined' curve of Figure 9.11 also shows an oscillation, as a test these predicted data were removed from the measured line data to ensure that the oscillation was not due to refractive index of air changes. However, the oscillation within the residuals remained, and therefore it is not clear what is causing the oscillation (or the inversion).

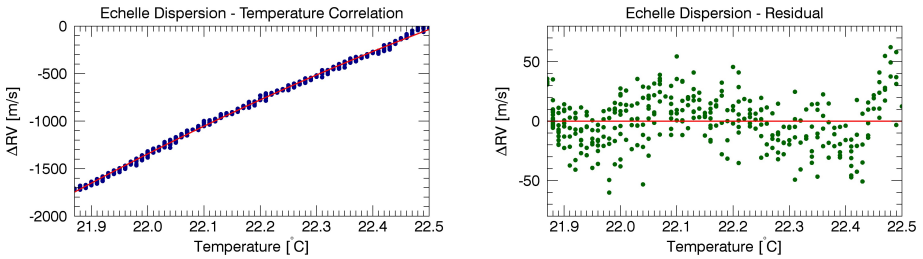

(a) Correlation of thorium-argon line movements with temperature in the échelle dispersion direction. The red line is a second-order polynomial fit to the data.

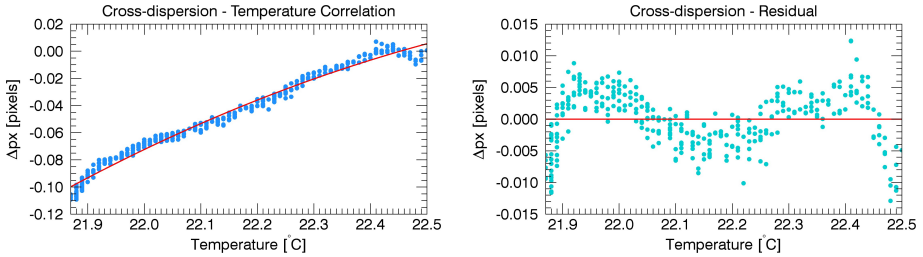

(b) Correlation of thorium-argon line movements with temperature in the cross-dispersion direction. The red line is a second-order polynomial fit to the data.

Figure 9.13: Correlation between line movements and temperature for both the échelle and cross-dispersion directions. These plots compare line movements against the échelle substrate temperature, which is representative of the temperatures of the other optical mounts.

9.4.5 In-Air Prototype - On-Sky Tests

Although the laboratory stability tests shown above demonstrate that the in-air prototype was not stable with temperature, during use with a telescope an iodine reference cell can be used to monitor the instrumental stability. This technique was employed during the on-sky testing period at Mt John University Observatory. Several radial velocity standard stars were observed with the intent of measuring the radial velocity capability of the instrument during an on-sky observing run. For these observations, an iodine cell was placed within the fibre feed module on the telescope, and the spectrograph itself was used in-air without any environmental controls, although it was placed within an insulated room in the observatory.

While the iodine reference cell partially removes the need for absolute stability from the spectrograph, it places a heavy demand on the reduction software to dis-entangle the iodine absorption lines from the stellar spectrum. As such, the velocity analysis was not undertaken by the author, but was performed by Mike Endl using the Austral radial velocity package (Endl et al., 2000). The spectra were reduced by Stuart Barnes.

Although the author was not responsible for the analysis of the spectra, the results from two radial velocity targets, HD75289 and δ Pavonis, are shown here as indicators of the in-air prototype's capability and stability during an observing run.

Figure 9.14 shows the phased and fitted KiwiSpec radial velocity data for the star HD75289, showing the clear detection of known extra-solar planet HD75289b. A total of twenty-eight spectra of this star were captured over seven nights, with a gap of only one night in the dataset. Figure 9.14 includes the results of a keplerian orbit fit to the KiwiSpec data. Udry et al. (2000) report a minimum mass of 0.42 $M_{\rm Jup}$ and a period of 3.51 days for this planet, and the derived parameters from the KiwiSpec observations are very well correlated with the results reported by those authors.

As an indicator of the night-to-night stability, the best four nights of δ Pavonis data are shown in Figure 9.15. The RMS of all observations is 3.8 m/s, while the variation of the mean of each night's set of data is close to 1.0 m/s. For comparison, the HERCULES spectrograph (also on the 1-m McLellan telescope), can achieve a 3.9 m/s measurement precision with the same iodine cell. Given that the HERCULES instrument is within a vacuum chamber, such a level of precision should be maintainable over a longer time period than that achieved with the in-air prototype, which was subject to varying environmental conditions.

These results, while demonstrating the radial velocity capability of the in-air prototype, also highlight the power of the iodine reference cell technique. That is, the addition of an iodine cell allowed the in-air prototype (with its strong temperature dependence on stability) to achieve radial velocity precisions on the order of several metres per second.

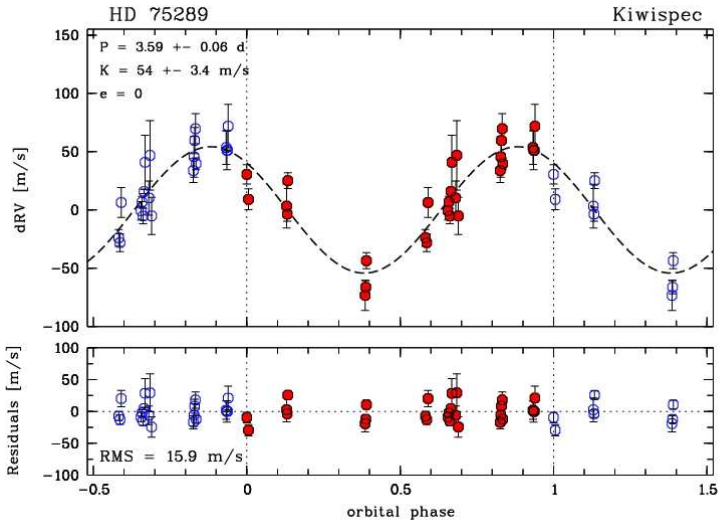

Figure 9.14: The KiwiSpec radial velocity observations of HD75289 showing the clear detection of the known extra-solar planet HD75289b. The blue data points are duplicates of the red data points, employed to illustrate more than one complete cycle within the figure. This analysis was performed by Mike Endl for the KiwiSpec project.

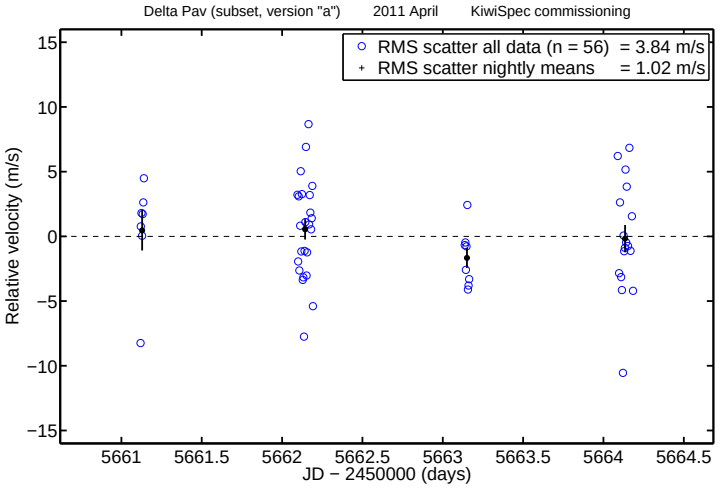

Figure 9.15: KiwiSpec δ Pavonis radial velocity observations over four nights during the on-sky testing period. This analysis was performed by Mike Endl for the KiwiSpec project.

9.4.6 Vacuum Chamber Prototype - Laboratory Tests

At the time of writing, the vacuum chamber prototype has not yet been tested for stability. This is primarily for two reasons: the material and construction of the optical tables and outgassing issues caused by the optical table within the vacuum chamber.

Given the results of the temperature sensitivity analysis in Section 9.2, and the findings from the in-air prototype stability tests, it is obvious that stainless steel optical tables will not provide the level of stability desired. Therefore, although the stainless steel tables were already in hand, the decision was made to change to super invar tables. Initially these were going to be similar in design to the current stainless steel tables (that is, with an internal honeycomb structure).

However, while testing the internal optical table within the vacuum chamber, it was noticed that the table had a serious outgassing issue that would not allow the chamber pressure to stabilize. A plot of the measured pressure stability is shown in Figure 9.16. As seen in the figure, the table outgassing rate is many times greater than the stability achieved with the empty chamber, or the predicted 1 m/s stability rate. Although not shown in the figure, after three days the outgassing rate fell below the 1 m/s rate, but was still much worse than the stability achieved with the empty chamber. Note also that the table had already been under vacuum for over two weeks at this point.

This outgassing issue has implications not only for the stability of the instrument, but also for practical or operational reasons. That is, if the chamber needs to be opened at any point, the instrument may require an unacceptable period of several weeks to return to a stable pressure level.

To ensure the outgassing was not due to contaminants, when the table was initially put under vacuum, a small stainless steel mirror was also placed within the chamber as a sample collector. After several days under vacuum, the chamber was vented to atmosphere and the mirror was sent out for an

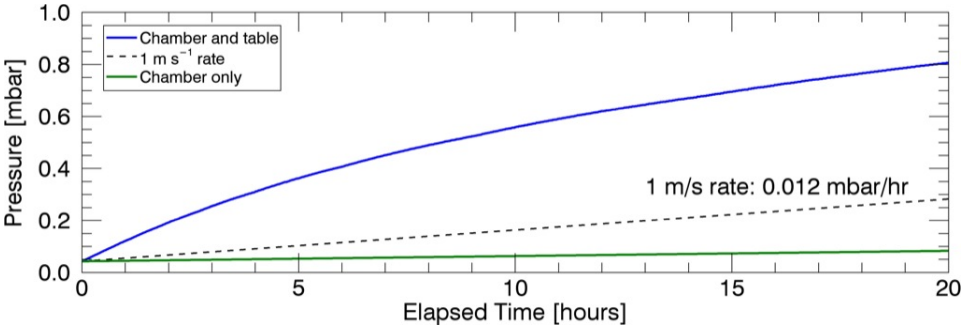

Figure 9.16: The measured pressure stability of the empty vacuum chamber, and of the chamber containing the stainless steel optical table. The 1 m/s rate is based on a refractive index of air change due to a change in pressure.

elemental analysis of the mirror surface with an electron microscope. That analysis did not return any evidence of contamination, indicating that it was not the presence of oils or cutting fluids degrading the vacuum.

Leaks in the vacuum chamber system have also been ruled out, as the chamber itself (with nothing inside) had been placed under vacuum several times and did not produce this level of pressure increase.

Given the internal honeycomb construction of the table (with a myriad of air pockets), it is assumed that trapped air was slowly being released into the chamber when it was under vacuum. Therefore, the decision was made to change from an internal honeycomb table construction to a solid piece of super invar to remove the outgassing issue entirely. At the time of writing, this solid invar table is being designed.

Steps are also underway to improve the temperature stability of the spectrograph's environment. To this end, a thermal enclosure has been constructed to surround the instrument, as shown in Figure 9.17. The purpose of this room is to isolate the spectrograph thermally from the outer laboratory.

Figure 9.17: The thermal enclosure surrounding the KiwiSpec vacuum chamber prototype. The room measures 3400 × 2200 × 2100 mm and is constructed of 100-mm thick polystyrene panels with metal skins. Shown to the left of the door is the KiwiSpec computer and electronics rack, and to the right of the door is the water chiller for the CCD detector.

It is also expected that the vacuum chamber, grism and camera will be surrounded by a smaller enclosure of insulating panels to isolate them from the heat produced by the detector, the iodine cell and the exposure meter. Given the lack of heat sources and the high thermal mass of the vacuum chamber within this smaller enclosure, the instrument should experience very stable temperatures. Similar multi-room approaches towards temperature stability have been used with success in other spectrograph installations, as described in Section 9.2.3. At the time of writing tests are being planned to determine if some form of heat exchanger will be require to remove the heat from the detector, iodine cell and exposure meter.

Once the new super invar tables are in hand, the vacuum chamber system will be fully assembled, aligned and tested. The test procedure will follow the same method and analysis outlined for the in-air prototype, that is, to measure the amount of movement of thorium-argon emission lines while monitoring the environmental changes of temperature, atmospheric pressure and humidity.

Chapter 10

Conclusion

This document has described the design, analysis, construction and testing of KiwiSpec, a fibre-fed, high resolution astronomical spectrograph of an asymmetric white pupil design. The instrument employs an R4, 31.6 groove mm^{-1} échelle grating for primary dispersion and a 725 lines mm^{-1} volume phase holographic (VPH) based grism for cross-dispersion. Two versions of the prototype were designed and constructed: an 'in-air' prototype, and a prototype featuring a vacuum chamber (to increase the stability of the instrument). Photographs of the two prototypes are shown in Figure 10.1.

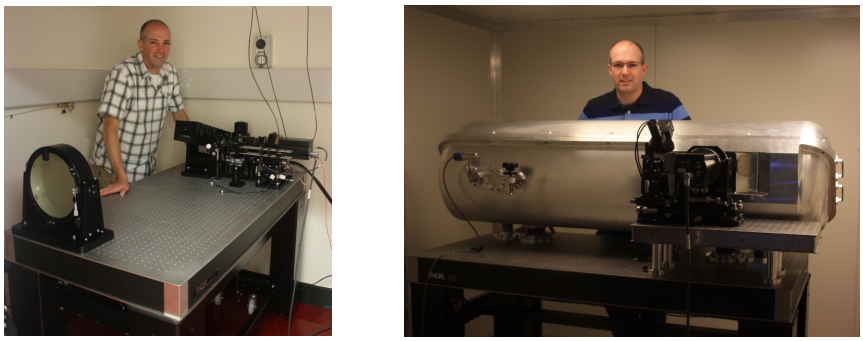

(a) The in-air prototype. (b) The vacuum chamber prototype.

Figure 10.1: The author with the two versions of the KiwiSpec prototype.

Within this document, Chapter 1 introduced the instrument, including an overview of the optical design and the white pupil concept. Also presented were the parameters employed for the prototype configuration, and a description of how the instrument could be easily adapted to include multiple channels (thereby increasing the wavelength coverage of the instrument). The KiwiSpec instrument was also put into historical context through a description of the evolution of échelle-based high resolution spectrographs designed for high stability.

Chapter 2 provided the theoretical basis of high-resolution astronomical spectrographs, with an emphasis on cross-dispersed échelle instruments.

Chapter 3 introduced several aspects of optical design pertaining to the prototype system. Included was a discussion on the choice of the asymmetry factor in white pupil spectrographs, which influences the amount of linear dispersion and has implications for the optical design of the camera. Also described were: the design of the input relay system (which re-images the fibre exit on the entrance slit of the spectrograph); a discussion of the effects of fibre length on efficiency; the effects of fibre diameter on efficiency and resolving power; an analysis of the stray-light potential from VPH orders adjacent to the VPH blaze order; and finally a description of the calibration lamp system used for testing the prototype instrument.

Chapter 4 described the tolerancing of the optical design. The findings of that study indicated that the prototype configuration was straightforward to manufacture, assemble and align (which was found to be the case in practice). Also discussed was how the tolerancing results drove the opto-mechanical design of the instrument, by indicating which parameters were most sensitive and which elements required adjustments for use during assembly and alignment. The final section in the chapter discussed the tolerancing of the iodine cell, which in the KiwiSpec design was placed within the input relay system. The intent was to ensure that the cell could be moved into and out of the light path without deviating the beam.

Chapter 5 detailed the opto-mechanical design of both the in-air and vacuum chamber prototypes. Each of the optical mounts were described in turn, and also discussed were the échelle grating mounting orientation and the focus method used for the instrument.

Chapter 6 described the vacuum chamber system, including: justification for the overall design approach; determination of the vacuum window thicknesses; analysis of the amount of window movement allowed with respect to radial-velocity stability; and an overview of the chamber design, manufacture and initial testing. Also included were four analyses which investigated the allowable temperature and pressure changes within and outside of the vacuum chamber with respect to radial-velocity stability. These analyses found that, with respect to stability of the refractive index of air: it is not the *absolute* vacuum chamber pressure that is important, but rather a *change* in the pressure level; normally-occurring atmospheric pressure changes should not affect the stability of the components outside of the vacuum chamber; by choosing a moderate vacuum pressure level the temperature requirements inside the vacuum chamber are easily met; and the temperature stability required by the components outside the vacuum chamber is an achievable value.

Chapter 7 discussed various aspects surrounding instrumental efficiency. Measured spectral efficiencies of various optical components were presented, as well as a description of the efficiency test designed and performed for the VPH gratings. The theoretical model developed to determine the expected efficiency of the instrument was described, including results for the as-built

prototype and an improved version of the prototype with high-efficiency coatings. The chapter concluded with a description of the measured efficiency of the instrument during an on-sky testing period with the 1-m McLellan telescope at Mt John University Observatory. A maximum efficiency of 5 per cent was achieved. However, as described within the text, that should be taken as a lower boundary of what the design is capable of.

Chapter 8 introduced the two locations studied as possible locations for the exposure meter, and the analysis undertaken to determine the optimal location (which included a zero-order reflectivity measurement of the KiwiSpec échelle grating).

Chapter 9 described various aspects regarding the stability of the instrument. The mechanical stability required to achieve metre-per-second stability was investigated, and the results indicated: that the designs of the optical mounts were important to avoid mount movements with temperature changes; and that the material choice for the optical tables was very important due to expansion and contraction effects with temperature changes. The analysis results showed that the KiwiSpec optical tables should be made of super invar, a situation which allows a much more forgiving temperature variability than tables made of stainless steel. Also discussed were stability tests undertaken with the in-air prototype, which monitored spectral line movements and compared them against environmental changes. It was found that the stability of the in-air prototype had a strong temperature dependence. Although not yet confirmed through testing, it is expected that the various sources of this temperature dependence have been largely removed from the vacuum chamber prototype design. The chapter also described the radial velocity based observations undertaken during the on-sky testing period (with an iodine reference cell in place), and described the testing plan for the vacuum chamber prototype.

This project has demonstrated KiwiSpec to be a very capable high resolution astronomical spectrograph, and the addition of the vacuum chamber to the system promises an increase in instrumental stability. With a view to the future, moving to high-efficiency optical coatings and custom-designed camera and input relay systems has the potential to offer a significant increase in performance over the achievements of the prototype.

Appendix A

NIST-modified Edlén Refractive Index of Air Calculator

An IDL-based version of the National Institute of Standards and Technology (NIST) 'Engineering Metrology Toolbox Refractive Index of Air Calculator'[1]. This tool is based on a modified[2] version of the Edlén equation (Edlén, 1966), which calculates the refractive index of air for a set of temperature, pressure and humidity values.

```
1  pro NIST_wavelength_calculator_Edlen
2
3  ;inputs: lambda_vacuum_nm, t_C, pressure_kPa, RH
4  ;outputs: lambda_air_nm, n
5
6  ;valid wavelength range is 300 to 1700 nm
7  ;valid air temp range is -40 to 100 C
8  ;valid pressure range is 10 to 140 kPa
9  ;valid humidity range is 0 to 100%
10
11 ;convert the pressure from kPa to Pa
12   pressure_Pa = pressure_kPa * 1000D
13
14 ;- - - - - - - - - - - - - - - - - - - - - - - - - - - - - - - - - -
15 ;calculate the saturation vapour pressure over water (psv)
16
17   ;constants array
18     K= DBLARR(11)
19     K= [0.0D, 1.16705214528E+03, -7.24213167032E+05,
20          -1.70738469401E+01, 1.20208247025E+04,
21          -3.23255503223E+06, 1.49151086135E+01,
22          -4.82326573616E+03, 4.05113405421E+05,
23          -2.38555575678E-01, 6.50175348448E+02]
```

[1] Online tool: `http://emtoolbox.nist.gov/Wavelength/Edlen.asp`
[2] See documentation at:
`http://emtoolbox.nist.gov/Wavelength/Documentation.asp#References`

```
24
25   ;convert temperature to Kelvin
26     T_K = T_C + 273.15D
27
28   ;various calculations
29     Omega = T_K + K[9] / (T_K - K[10])
30     A = Omega^2 + K[1] * Omega + K[2]
31     B = K[3] * Omega^2 + K[4] * Omega + K[5]
32     C = K[6] * Omega^2 + K[7] * Omega + K[8]
33     X = -B + SQRT(B^2 - (4 * A * C))
34
35     psv = 1.0E6 * ((2.0D * C / X)^4)
36 ;- - - - - - - - - - - - - - - - - - - - - - - - - - - - - - - - - - -
37 ;calculate partial pressure given the relative humidity
38   p_v = (RH / 100.0) * psv
39
40 ;constants
41   A = 8342.54D
42   B = 2406147D
43   C = 15998D
44   D = 96095.43D
45   E = 0.601D
46   F = 0.00972D
47   G = 0.003661D
48
49 ;convert the laser vacuum wavelength to micrometers
50   lambda_vacuum_um = lambda_vacuum_nm / 1000D
51   S = 1D / (lambda_vacuum_um^2)
52
53 ;calculate intermediate results at
54 ; air pressure (pressure_Pa),
55 ; water vapour partial pressure (p_v),
56 ; and temperature (t_C):
57   n_s = 1D + 1.0E-8, $
58           * (A + B / (130D - S) + C / (38.9D - S))
59   X = (1D + 1.0E-8 * (E - F * t_C) * pressure_Pa), $
60       / (1D + G * t_C)
61   n_tp = 1D + pressure_Pa * (n_s - 1D) * X / D
62
63 ;calculate the index of refraction of air
64   n = n_tp - 1.0E-10 * (292.75D / (t_C + 273.15D)), $
65       *(3.7345D - 0.0401D * S) * p_v
66
67 ;calculate the wavelength in air
68   lambda_air_nm = lambda_vacuum_nm / n
69
70 end ;main
```

Bibliography

Adams, J. J., G. J. Hill, and P. J. MacQueen (2008). Volume phase holographic grating performance on the VIRUS-P instrument. In *Society of Photo-Optical Instrumentation Engineers (SPIE) Conference Series*, volume 7014 of *Society of Photo-Optical Instrumentation Engineers (SPIE) Conference Series*.

Adams, W. S. (1912). The three-prism stellar spectrograph of the Mount Wilson Solar Observatory. *ApJ*, **35**, 163–182.

Adams, W. S. (1941). Some Results with the Coudé Spectrograph of the Mount Wilson Observatory. *ApJ*, **93**, 11.

Allen, C.W. (1973). *Astrophysical Quantities*. Athlone Press.

Allen, C.W. and A.N. Cox (2000). *Allen's Astrophysical Quantities*. Springer.

Anderson, J. A. (1948). Optics of the 200-inch Hale Telescope. *PASP*, **60**, 221.

Angel, J. R. P., M. T. Adams, T. A. Boroson, and R. L. Moore (1977). A very large optical telescope array linked with fused silica fibers. *ApJ*, **218**, 776–782.

ASTM E 595 (1993). Standard test method for total mass loss and collected volatile condensable materials from outgassing in a vacuum environment [astm e 595-93]. Technical report, American Society for Testing and Materials (ASTM).

Baranne, A. (1965). Un nouveau montage spectrographique. *C.R. Acad. Sc. Paris*, **260**, 3283–3286.

Baranne, A. and M. Duchesne (1972). Le spectrographe coudé "Echel.E.C.152" (Montage à pupille blanche pour caméra électronique). In S. Laustsen and A. Reiz, editors, *Auxiliary Instrumentation for Large Telescopes*, pp. 241–245.

Baranne, A., D. Queloz, M. Mayor, G. Adrianzyk, G. Knispel, D. Kohler, D. Lacroix, J.-P. Meunier, G. Rimbaud, and A. Vin (1996). ELODIE: A spectrograph for accurate radial velocity measurements. *A&AS*, **119**, 373–390.

Barden, S. C., J. A. Arns, and W. S. Colburn (1998). Volume-phase holographic gratings and their potential for astronomical applications. In S. D'Odorico, editor, *Society of Photo-Optical Instrumentation Engineers (SPIE) Conference Series*, volume 3355 of *Society of Photo-Optical Instrumentation Engineers (SPIE) Conference Series*, pp. 866–876.

Barden, S. C., J. A. Arns, W. S. Colburn, and J. B. Williams (2000). Volume-Phase Holographic Gratings and the Efficiency of Three Simple Volume-Phase Holographic Gratings. *PASP*, **112**, 809–820.

Barnes, S. (2004). *The design and performance of high resolution échelle spectrographs in astronomy.* Ph.D. dissertation, University of Canterbury, Christchurch, New Zealand.

Barnes, S. I., P. L. Cottrell, M. D. Albrow, N. Frost, G. Graham, G. Kershaw, R. Ritchie, D. Jones, R. Sharples, D. Bramall, J. Schmoll, P. Luke, P. Clark, L. Tyas, D. A. H. Buckley, and J. Brink (2008). The optical design of the Southern African Large Telescope high resolution spectrograph: SALT HRS. In *Society of Photo-Optical Instrumentation Engineers (SPIE) Conference Series*, volume 7014 of *Society of Photo-Optical Instrumentation Engineers (SPIE) Conference Series*.

Bowen, I. S. (1952). The Spectrographic Equipment of the 200-inch Hale Telescope. *ApJ*, **116**, 1.

Bramall, D. G., J. Schmoll, L. M. G. Tyas, P. Clark, E. Younger, R. M. Sharples, N. A. Dipper, S. G. Ryan, D. A. H. Buckley, and J. Brink (2012). The SALT HRS spectrograph: instrument integration and laboratory test results. In *Society of Photo-Optical Instrumentation Engineers (SPIE) Conference Series*, volume 8446 of *Society of Photo-Optical Instrumentation Engineers (SPIE) Conference Series*.

Butler, R. P., G. W. Marcy, E. Williams, C. McCarthy, P. Dosanjh, and S. S. Vogt (1996). Attaining Doppler Precision of 3 m s^{-1}. *PASP*, **108**, 500.

Campbell, B. and G. A. H. Walker (1979). Precision radial velocities with an absorption cell. *PASP*, **91**, 540–545.

Campbell, B., G. A. H. Walker, and S. Yang (1988). A search for substellar companions to solar-type stars. *ApJ*, **331**, 902–921.

Castilho, B. V., B. Delabre, and C. D. Gneiding (2004). A new concept for echelle spectrographs: the SOAR Telescope Echelle Spectrograph. In A. F. M. Moorwood and M. Iye, editors, *Society of Photo-Optical Instrumentation Engineers (SPIE) Conference Series*, volume 5492 of *Society of Photo-Optical Instrumentation Engineers (SPIE) Conference Series*, pp. 433–444.

Chonis, T. S., G. J. Hill, J. C. Clemens, B. Dunlap, and H. Lee (2012). Methods for evaluating the performance of volume phase holographic gratings for the VIRUS spectrograph array. In *Society of Photo-Optical Instrumentation Engineers (SPIE) Conference Series*, volume 8446 of *Society of Photo-Optical Instrumentation Engineers (SPIE) Conference Series*.

Cosentino, R., C. Lovis, F. Pepe, A. Collier Cameron, D. W. Latham, E. Molinari, S. Udry, N. Bezawada, M. Black, A. Born, N. Buchschacher, D. Charbonneau, P. Figueira, M. Fleury, A. Galli, A. Gallie, X. Gao, A. Ghedina, C. Gonzalez, M. Gonzalez, J. Guerra, D. Henry, K. Horne, I. Hughes, D. Kelly, M. Lodi, D. Lunney, C. Maire, M. Mayor, G. Micela, M. P. Ordway, J. Peacock, D. Phillips, G. Piotto, D. Pollacco, D. Queloz, K. Rice, C. Riverol, L. Riverol, J. San Juan, D. Sasselov, D. Segransan, A. Sozzetti, D. Sosnowska, B. Stobie, A. Szentgyorgyi, A. Vick, and L. Weber (2012). Harps-N: the new planet hunter at TNG. In *Society of Photo-Optical Instrumentation Engineers (SPIE) Conference Series*, volume 8446 of *Society of Photo-Optical Instrumentation Engineers (SPIE) Conference Series*.

Diego, F. and D. D. Walker (1985). On the possibility of increasing the throughput of astronomical spectrographs by overfilling the dispersing element. *MNRAS*, **217**, 347–354.

Diego, F., A. C. Fish, M. J. Barlow, I. A. Crawford, J. Spyromilio, M. Dryburgh, D. Brooks, I. D. Howarth, and D. D. Walker (1995). The Ultra-High-Resolution Facility at the Anglo-Australian Telescope. *MNRAS*, **272**, 323–332.

Dumusque, X., F. Pepe, C. Lovis, D. Ségransan, J. Sahlmann, W. Benz, F. Bouchy, M. Mayor, D. Queloz, N. Santos, and S. Udry (2012). An Earth-mass planet orbiting α Centauri B. *Nature*, **491**, 207–211.

Edlén, B. (1966). The refractive index of air. *Metrologia*, **2**, 71–80.

Endl, M., M. Kürster, and S. Els (2000). The planet search program at the ESO Coudé Echelle spectrometer. I. Data modeling technique and radial velocity precision tests. *A&A*, **362**, 585–594.

Filippenko, A. V. (1982). The importance of atmospheric differential refraction in spectrophotometry. *PASP*, **94**, 715–721.

Fischer, R. E., B. Tadic-Galeb, and P. R. Yoder (2008). *Optical System Design*. SPIE Press, 2nd edition.

Giordano, P. (1997). Dust contamination and in-situ cleaning of ground-based telescope optics: the VLT approach. In A. L. Ardeberg, editor, *Society of Photo-Optical Instrumentation Engineers (SPIE) Conference Series*, volume 2871 of *Society of Photo-Optical Instrumentation Engineers (SPIE) Conference Series*, pp. 416–423.

Hamuy, M., A. R. Walker, N. B. Suntzeff, P. Gigoux, S. R. Heathcote, and M. M. Phillips (1992). Southern spectrophotometric standards. *PASP*, **104**, 533–552.

Hamuy, M., N. B. Suntzeff, S. R. Heathcote, A. R. Walker, P. Gigoux, and M. M. Phillips (1994). Southern spectrophotometric standards, 2. *PASP*, **106**, 566–589.

Harris, Nigel S. (2005). *Modern Vacuum Practice*. Nigel S. Harris, 3rd edition.

Harrison, G. R. (1949). The production of diffraction gratings: II. Design of echelle gratings and spectrographs. *Journal of the Optical Society of America (1917-1983)*, **39**, 522.

Harrison, G. R., J. E. Archer, and J. Camus (1952). A fixed-focus broad-range echelle spectrograph of high speed and resolving power. *J. Opt. Soc. Am.*, **42**(10), 706–709.

Haynes, D. M., R. Haynes, J. C. Olaya, and S. G. Leon-Saval (2012). Optical fibre tapers: focal reduction and magnification. In *Society of Photo-Optical Instrumentation Engineers (SPIE) Conference Series*, volume 8450 of *Society of Photo-Optical Instrumentation Engineers (SPIE) Conference Series*.

Hearnshaw, J. (2009). *Astronomical Spectrographs and their History*. Cambridge University Press.

Hearnshaw, J.B., S.I. Barnes, G.M. Kershaw, N. Frost, G. Graham, R. Ritchie, and G.R. Nankivell (2002). The HERCULES échelle spectrograph at Mt John. *Experimental Astronomy*, **13**(2), 59–76.

Herbert, J. J. (2006). Techniques for deriving optimal bondlines for athermal bonded mounts. In *Society of Photo-Optical Instrumentation Engineers (SPIE) Conference Series*, volume 6288 of *Society of Photo-Optical Instrumentation Engineers (SPIE) Conference Series*.

Horton, A., M. Goodwin, B. Baumgartner, and T. Feger (2011). The effect of core geometry on focal ratio degradation in optical fibres for astronomy. In *Quantum Electronics Conference Lasers and Electro-Optics (CLEO/IQEC/PACIFIC RIM), 2011*, pp. 1919–1921.

Hoya Optics Division (2010). Optical glass. http://www.hoyaoptics.com.

Kaufer, A., B. Wolf, J. Andersen, and L. Pasquini (1997). FEROS, the fiber-fed extended range optical spectrograph for the ESO 1.52-m telescope. *The Messenger*, **89**, 1–4.

Kaufer, A., O. Stahl, S. Tubbesing, P. Nrregaard, G. Avila, P. Francois, L. Pasquini, and A. Pizzella (1999). Commissioning FEROS, the new high-resolution spectrograph at La-Silla. *The Messenger*, **95**, 8–12.

Kelt, A., A. Harris, P. Jorden, and S. Tulloch (2006). Optimised CCD Antireflection Coating. In J. E. Beletic, J. W. Beletic, and P. Amico, editors, *Scientific Detectors for Astronomy 2005*, p. 369.

Kibrick, R. I., D. A. Clarke, W. T. S. Deich, and D. Tucker (2006). A comparison of exposure meter systems for three exoplanet-hunting spectrometers: Hamilton, HIRES and APF. In *Society of Photo-Optical Instrumentation Engineers (SPIE) Conference Series*, volume 6274 of *Society of Photo-Optical Instrumentation Engineers (SPIE) Conference Series*.

King, I. R. (1971). The Profile of a Star Image. *PASP*, **83**, 199.

Lee, H., G. J. Hill, J. L. Marshall, B. L. Vattiat, and D. L. Depoy (2010). Visible Integral-field Replicable Unit Spectrograph (VIRUS) optical tolerance. In *Society of Photo-Optical Instrumentation Engineers (SPIE) Conference Series*, volume 7735 of *Society of Photo-Optical Instrumentation Engineers (SPIE) Conference Series*.

Loewen, E. G. and E. Popov (1997). *Diffraction Gratings and Applications*. Marcel Deckker.

Marcy, G. W. and R. P. Butler (1992). Precision radial velocities with an iodine absorption cell. *PASP*, **104**, 270–277.

Mayor, M., F. Pepe, D. Queloz, F. Bouchy, G. Rupprecht, G. Lo Curto, G. Avila, W. Benz, J.-L. Bertaux, X. Bonfils, T. Dall, H. Dekker, B. Delabre, W. Eckert, M. Fleury, A. Gilliotte, D. Gojak, J. C. Guzman, D. Kohler, J.-L. Lizon, A. Longinotti, C. Lovis, D. Megevand, L. Pasquini, J. Reyes, J.-P. Sivan, D. Sosnowska, R. Soto, S. Udry, A. van Kesteren, L. Weber, and U. Weilenmann (2003). Setting New Standards with HARPS. *The Messenger*, **114**, 20–24.

McMath, R. R. (1956). Solar Spectroscopy with a Vacuum Spectrograph. *ApJ*, **123**, 1.

Melles Griot (1997). *The Melles Griot Catalog (Appendix 5)*. Melles Griot, Irvine, CA.

Merrill, P. W. (1931). A Plane-Grating Spectrograph for the Red and Infra-Red Regions of Stellar Spectra. *ApJ*, **74**, 188.

Moffat, A. F. J. (1969). A Theoretical Investigation of Focal Stellar Images in the Photographic Emulsion and Application to Photographic Photometry. *A&A*, **3**, 455.

Murphy, J. D., P. J. MacQueen, G. J. Hill, F. Grupp, A. Kelz, P. Palunas, M. Roth, and A. Fry (2008). Focal ratio degradation and transmission in VIRUS-P optical fibers. In *Society of Photo-Optical Instrumentation Engineers (SPIE) Conference Series*, volume 7018 of *Society of Photo-Optical Instrumentation Engineers (SPIE) Conference Series*.

Oke, J. B. (1964). Photoelectric Spectrophotometry of Stars Suitable for Standards. *ApJ*, **140**, 689.

Palmer, Christopher and Erwin Loewen (2005). *Diffraction Grating Handbook*. Newport Corporation, Rochester, New York, 6th edition.

Paquin, R. A. (1997). Materials for optical systems. In A. Ahmad, editor, *Handbook of Optomechanical Engineering*. CRC Press.

Parker Hannifin Corporation (2007). *Parker O-ring Handbook*. Parker Hannifin Corporation, Cleveland, OH.

Paykel Engineering (1980). *O-Rings*. Paykel Engineering, Mt Wellington, NZ.

Pedrotti, F. L. and L. S. Pedrotti (1993). *Introduction to Optics*. Prentice Hall, 2nd edition.

Pepe, F., G. Rupprecht, G. Avila, A. Balestra, F. Bouchy, C. Cavadore, W. Eckert, M. Fleury, A. Gillotte, D. Gojak, J. C. Guzman, D. Kohler, J.-L. Lizon, M. Mayor, D. Megevand, D. Queloz, D. Sosnowska, S. Udry, and U. Weilenmann (2003). Performance verification of HARPS: first laboratory results. In M. Iye and A. F. M. Moorwood, editors, *Society of Photo-Optical Instrumentation Engineers (SPIE) Conference Series*, volume 4841 of *Society of Photo-Optical Instrumentation Engineers (SPIE) Conference Series*, pp. 1045–1056.

Perruchot, S., D. Kohler, F. Bouchy, Y. Richaud, P. Richaud, G. Moreaux, M. Merzougui, R. Sottile, L. Hill, G. Knispel, X. Regal, J.-P. Meunier,

S. Ilovaisky, H. Le Coroller, D. Gillet, J. Schmitt, F. Pepe, M. Fleury, D. Sosnowska, P. Vors, D. Mégevand, P. E. Blanc, C. Carol, A. Point, A. Laloge, and J.-C. Brunel (2008). The SOPHIE spectrograph: design and technical key-points for high throughput and high stability. In *Society of Photo-Optical Instrumentation Engineers (SPIE) Conference Series*, volume 7014 of *Society of Photo-Optical Instrumentation Engineers (SPIE) Conference Series*.

Perruchot, S., F. Bouchy, B. Chazelas, R. F. Díaz, G. Hébrard, K. Arnaud, L. Arnold, G. Avila, X. Delfosse, I. Boisse, G. Moreaux, F. Pepe, Y. Richaud, A. Santerne, R. Sottile, and D. Tézier (2011). Higher-precision radial velocity measurements with the SOPHIE spectrograph using octagonal-section fibers. In *Society of Photo-Optical Instrumentation Engineers (SPIE) Conference Series*, volume 8151 of *Society of Photo-Optical Instrumentation Engineers (SPIE) Conference Series*.

Pierce, A. K., R. R. McMath, and O. Mohler (1951). Solar spectroscopy with echelles. *AJ*, **56**, 137.

Pompea, Stephen M. and Robert P. Beault (1995), Bass, Michael, editor, *Handbook of Optics*, volume 2, chapter Black Surfaces for Optical Systems. McGraw-Hill.

Queloz, D., M. Casse, and M. Mayor (1999). The Fiber-Fed Spectrograph, a Tool to Detect Planets. In J. B. Hearnshaw and C. D. Scarfe, editors, *IAU Colloq. 170: Precise Stellar Radial Velocities*, volume 185 of *Astronomical Society of the Pacific Conference Series*, p. 13.

Racine, R. (1996). The Telescope Point Spread Function. *PASP*, **108**, 699.

Ramsey, L. W. (1988). Focal ratio degradation in optical fibers of astronomical interest. In S. C. Barden, editor, *Fiber Optics in Astronomy*, volume 3 of *Astronomical Society of the Pacific Conference Series*, pp. 26–39.

Ramsey, L. W. and D. P. Huenemoerder (1986). A versatile fiber coupled CCD/echelle spectrograph system. In D. L. Crawford, editor, *Society of Photo-Optical Instrumentation Engineers (SPIE) Conference Series*, volume 627 of *Society of Photo-Optical Instrumentation Engineers (SPIE) Conference Series*, pp. 282–290.

Ramsey, L. W., C. Brungardt, D. P. Huenemoerder, and S. Rosenthal (1985). The Penn State Fiber Coupled-CCD Spectrograph System. In *Bulletin of the American Astronomical Society*, volume 17 of *Bulletin of the American Astronomical Society*, p. 574.

Raskin, G., H. van Winckel, H. Hensberge, A. Jorissen, H. Lehmann, C. Waelkens, G. Avila, J.-P. de Cuyper, P. Degroote, R. Dubosson, L. Dumortier, Y. Frmat, U. Laux, B. Michaud, J. Morren, J. Perez Padilla,

W. Pessemier, S. Prins, K. Smolders, S. van Eck, and J. Winkler (2011). HERMES: a high-resolution fibre-fed spectrograph for the Mercator telescope. *A&A*, **526**, A69.

Rowland, H. A. (1882). Preliminary notice of the results accomplished in the manufacture and theory of gratings for optical purposes. *The Observatory*, **5**, 224–228.

Schroeder, D.J. (2000). *Astronomical Optics*. Academic Press.

Schroeder, D. J. and R. L. Hilliard (1980). Echelle efficiencies - Theory and experiment. *ApOpt*, **19**, 2833–2841.

Schwab, C., J. F. P. Spronck, A. Tokovinin, and D. A. Fischer (2010). Design of the CHIRON high-resolution spectrometer at CTIO. In *Society of Photo-Optical Instrumentation Engineers (SPIE) Conference Series*, volume 7735 of *Society of Photo-Optical Instrumentation Engineers (SPIE) Conference Series*.

Schwertz, K.M. and J.H. Burge (2012). *Field Guide to Optomechanical Design and Analysis*. Field Guide Series. SPIE.

Sens-Tech Limited (2010). *P25USB User Manual*. Sens-Tech Limited, Langley, UK.

Smith, G. H. (2007). *Practical Computer-Aided Lens Design*. Willman-Bell, 2nd edition.

Smith, W. J. (2000). *Modern Optical Engineering*. McGraw-Hill, New York, NY, 3rd edition.

Smith, W. J. (2005). *Modern Lens Design*. McGraw-Hill, 2nd edition.

Stetson, P.B., L.E. Davis, and D.R. Crabtree (1990). Future development of the DAOPHOT crowded-field photometry package. In G.H.Jacoby, editor, *CCDs in astronomy*, volume 8 of *Astronomical Society of the Pacific Conference Series*, pp. 289–304.

Strassmeier, K. G., M. Woche, I. Ilyin, E. Popow, S.-M. Bauer, F. Dionies, T. Fechner, M. Weber, A. Hofmann, J. Storm, R. Materne, W. Bittner, J. Bartus, T. Granzer, C. Denker, T. Carroll, M. Kopf, I. DiVarano, E. Beckert, and M. Lesser (2008). PEPSI: the Potsdam Echelle Polarimetric and Spectroscopic Instrument for the LBT. In *Society of Photo-Optical Instrumentation Engineers (SPIE) Conference Series*, volume 7014 of *Society of Photo-Optical Instrumentation Engineers (SPIE) Conference Series*.

Strong, J. (1934). Evaporated Aluminum Films for Astronomical Mirrors. *PASP*, **46**, 18.

Szentgyorgyi, A., G. Furesz, P. Cheimets, M. Conroy, R. Eng, D. Fabricant, R. Fata, T. Gauron, J. Geary, B. McLeod, J. Zajac, S. Amato, H. Bergner, N. Caldwell, A. Dupree, R. Goddard, E. Johnston, S. Meibom, D. Mink, M. Pieri, J. Roll, S. Tokarz, W. Wyatt, H. Epps, L. Hartmann, and S. Meszaros (2011). Hectochelle: A Multiobject Optical Echelle Spectrograph for the MMT. *PASP*, **123**, 1188–1209.

Tüg, H., N. M. White, and G. W. Lockwood (1977). Absolute energy distributions of Alpha Lyrae and 109 Virginis from 3295 A to 9040 A. *A&A*, **61**, 679–684.

Tull, R. G. (1972). The coudé spectrograph and échelle scanner of the 2.7 m telescope at McDonald Observatory. In S. Laustsen and A. Reiz, editors, *Auxiliary Instrumentation for Large Telescopes*, pp. 259–274.

Udry, S., M. Mayor, D. Naef, F. Pepe, D. Queloz, N. C. Santos, M. Burnet, B. Confino, and C. Melo (2000). The CORALIE survey for southern extrasolar planets. II. The short-period planetary companions to HD 75289 and HD 130322. *A&A*, **356**, 590–598.

Walker, D. D. and F. Diego (1985). Design philosophy of the forthcoming echelle spectrographs for the AAT and LPO. *MNRAS*, **217**, 355–365.

Walker, G. (1987). *Astronomical Observations: An Optical Perspective*. Cambridge University Press.

Wright, J. T. and B. S. Gaudi (2013), Oswalt, T. D., L. M. French, and P. Kalas, editors, *Exoplanet Detection Methods*, p. 489. Springer.

Yoder, P. R. (2006). *Opto-Mechanical Systems Design*. CRC Press, 3rd edition.

Yoder, P. R. (2008). *Mounting Optics in Optical Instruments*. SPIE Press, 2nd edition.